12 Bijlage B: Seismische Risico Analyse

De winning van aardgas gaat gepaard met een daling van de druk in de ondergrond met als gevolg een verandering van de gesteentespanningen. Deze verandering van spanning kan leiden tot plotselinge bewegingen langs bestaande breuken, waardoor mogelijk een lichte aardbeving kan plaatsvinden. In Nederland is/wordt uit ongeveer 140 olie- en gasvelden op het vasteland geproduceerd. Boven ongeveer 20% van de velden zijn bevingen geregistreerd. Boven 11 velden zijn bevingen geregistreerd die ook duidelijk aan het oppervlak voelbaar waren (Magnitude meer dan 2,0 op de schaal van Richter).

Stap 1: Inschatten risicopotentieel voor de verschillende voorkomens. Voor het inschatten van het risicopotentieel is uitgegaan van de maximale drukdaling volgens het “high case” productieprofiel[14].

De kans op beven van een olie- of gasvoorkomen
In de studie ‘Deterministische Hazard Analyse voor Geïnduceerde Seismiciteit (DHAIS)[15] is onderzocht welke eigenschappen (geologische, productietechnische en geomechanische eigenschappen) van olie- en gasvoorkomens invloed hebben op het wel of niet optreden van aardbevingen. In 2012 is een update van deze studie uitgevoerd, waarin alle nieuwe data zijn meegenomen tot mei 2010[16]. Aan de hand van de volgende parameters van een olie- of gasvoorkomen wordt de kans op beven van dat voorkomen bepaald:

- DP/Pini: De ratio van drukval (DP) en initiële druk (Pini) in het reservoir;
- E: de verhouding tussen de Young’s moduli (stijfheidsmoduli) van de ‘overburden’ en het reservoirgesteente;

$$E = \frac{E_{burden}}{E_{reservoir}}$$

- B: een maat voor de breukdichtheid van het reservoir.

$$B = \frac{breukoppervlakte^{3/2}}{brutogesteentevolume} = \frac{l_b^{3/2} \cdot h^{3/2}}{A \cdot h} = \frac{l_b^{3/2} \cdot \sqrt{h}}{A}$$

Waarbij:

l_b = De totale breuklengte van de intra reservoir breuken en de randbreuken van het voorkomen in meters;
h = De maximale dikte van de gaskolom van het voorkomen in meters;
A = De oppervlakte van het voorkomen gemeten binnen de gas-water-contact-dieptecontour (in vierkante meters);

---

[14] Het hoog scenario productieprofiel is gebruikt om de druk te bereken in het veld. Om een conservatieve schatting te geven van de mogelijke bovengrondse gevolgen is in dit geval gekozen om de druk te middelen voor het gehele veld.
[15] TNO-rapport NITG 04-171-C. Van Eijs, 2004. Deterministische hazard analyse voor geïnduceerde seismiciteit
[16] TNO-rapport 2012 R10198. Van Thienen, 2012. Deterministische hazard analyse voor geïnduceerde seismiciteit in Nederland.

De combinatie van de parameterwaarden geven een kans op beven voor een bepaald voorkomen gedurende de productietijd.

Reeds bevende voorkomens	
$DP/P_{ini} \geq 28\%$	B > 0,86 en E ≥ 1,34: P_h = 0.42 ± 0.08
	B > 0,86 en 1,01 ≤ E ≤ 1,33: P_l = 0.19 ± 0.05
	B < 0,86 en/of E < 1,01: verwaarloosbare kans
$DP/P_{ini} < 28\%$	Verwaarloosbare kans

De waarden die zijn gebruikt in de bepaling van de DHAIS-kans zijn gegeven in Tabel 12-1.

Tabel 12-1: Invoergegevens voor de bepaling van de DHAIS en de DHAIS kansen

Voorkomen	Reservoir dikte / gaskolom (m)[17]	Initiële druk (bar)	Totale drukdaling volgens hoog-scenario (bar)	Totale breuk-lengte (km)	Reservoir opper-vlakte (km^2)	Maximale waar-genomen aardbeving	Aantal aard-bevingen per jaar	DHAIS E[18]	DHAIS B	DHAIS kans
Ternaard	112	557	181	23,7	18,5	geen	geen	1,28	2,08	19%

Realistisch sterkste beving

Naast de kans op beven, wordt ook een theoretische waarde voor de “realistisch sterkste beving” (Mmax) bepaald. Er worden twee methoden gebruikt om de Mmax waarde te bepalen: op basis van breukgeometrie en op basis van energiebalans. In de Seismisch Risico Analyse leidraad worden beide methoden gebruikt. Voor de berekeningen van de Mmax is uitgegaan van de standaardwaarden voor de “stress drop” en “partitie coëfficiënt” die gegeven zijn in de leidraad (respectievelijk 5 MPa en 0,01). De veldspecifieke waarden die benodigd zijn voor de berekeningen en de uitkomsten voor de Mmax staan vermeld in Tabel 12-2.

Tabel 12-2: Invoergegevens voor de bepaling van de Mmax, en de Mmax waarden volgens de twee methoden.

Voorkomen	Langste breuklengte (km) [19]	Poisson's ratio[20]	Breukhoogte (m)	Mmax energiebalans	Mmax breukslip
Ternaard	6,5	0,2	112	3,4	3,7

Stap 2: Risico matrix

Voor het voorkomen Ternaard is het nodig gebleken om de risicomatrix te gebruiken (“Stap 2” van de SRA). Voor elke factor die bepaald is voor de onder- en bovengrond wordt een score gegeven waarbij de som van de scores een positie geeft in de risico matrix.

---

[17] Voor de DHAIS berekening wordt zowel de hoogte van de gaskolom als de totale reservoir dikte beschouwd. Het minimum van deze twee wordt gekozen voor de berekening van de “B” waarde zoals voorgeschreven door de DHAIS methodiek

[18] Young’s moduli ratio volgens TNO rapport: Deterministische hazard analyse voor geïnduceerde Seismiciteit, NITG 04-171-C. Voor nieuwe velden wordt de ratio van een analoog veld met dezelfde reservoir seal combinatie gebruikt

[19] Langste breuklengte is aangegeven op de kaart in bijlage C met blauwe pijl

[20] Poisson’s ratio gebaseerd op gemiddelde waarde voor gecementeerde zandsteen op basis van kernplugmetingen

In dit deel van de bijlage worden de figuren en tabellen getoond die gebruikt zijn om tot een risicobeoordeling te komen. Figuur 12-1, Figuur 12-2, Figuur 12-3 tonen de situaties voor respectievelijk “Bevolkingsdichtheid”, “Industriële inrichtingen”, “Speciale gebouwen en vitale infrastructuur” en ”Dijken”. Figuur 12-4 toont de kaart van de grondsoorten in de ondiepe ondergrond kaart om de mate van opslingering te bepalen. Tabel 12-3 A en B toont de evaluatie en scores voor de invloedfactoren. De risicomatrix is afgebeeld in Figuur 8-4.

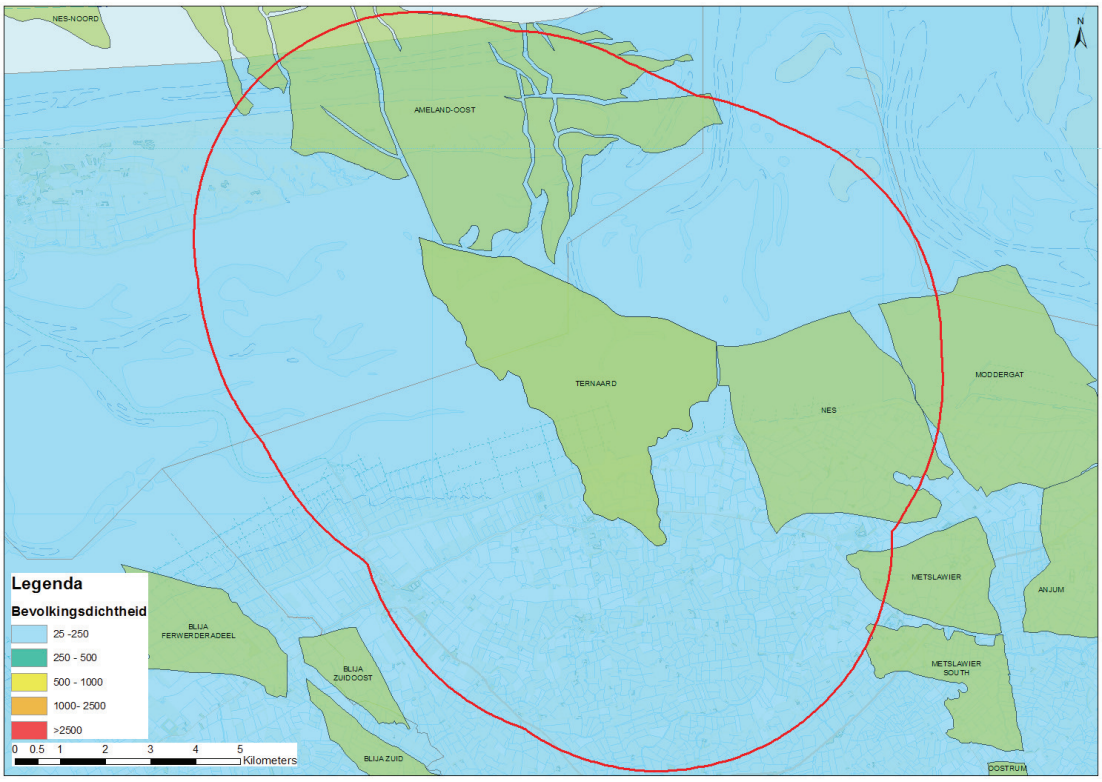

Figuur 12-1: Overzicht van de bevolkingsdichtheid boven het Ternaard veld.

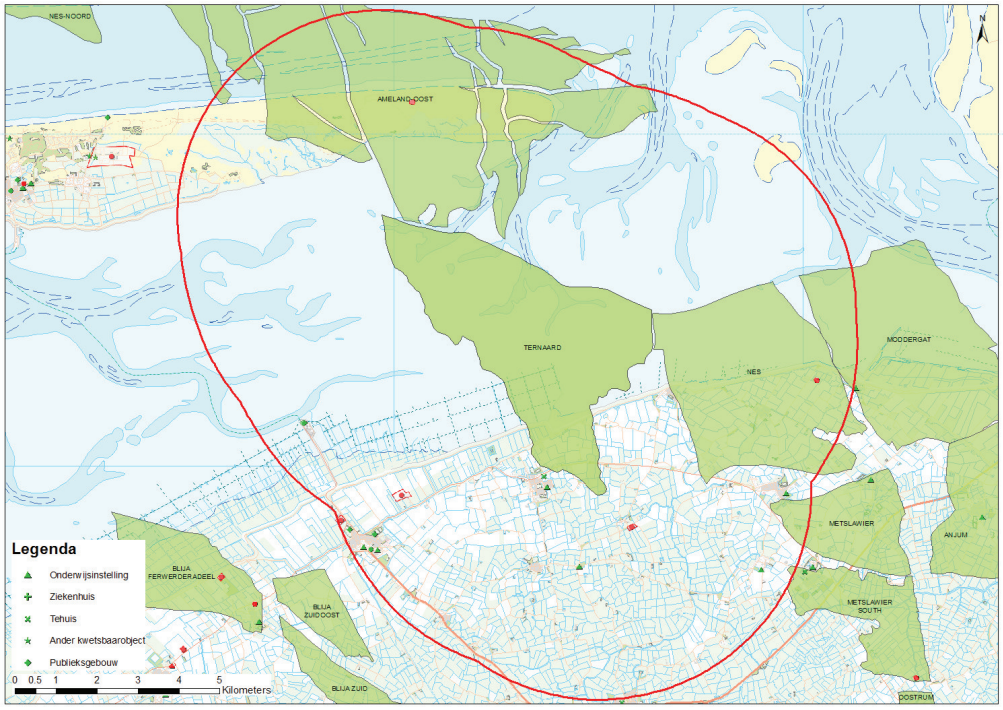

Figuur 12-2: Overzicht van de industriële inrichtingen (rode punt), ziekenhuizen (groene plus) onderwijsinstellingen (groene driehoek), tehuizen (groene x) en publieksgebouwen (groene ruit) boven het Ternaard veld. De rode cirkel geeft de 5 km straal rond het Ternaard veld aan die relevant is voor de SRA.

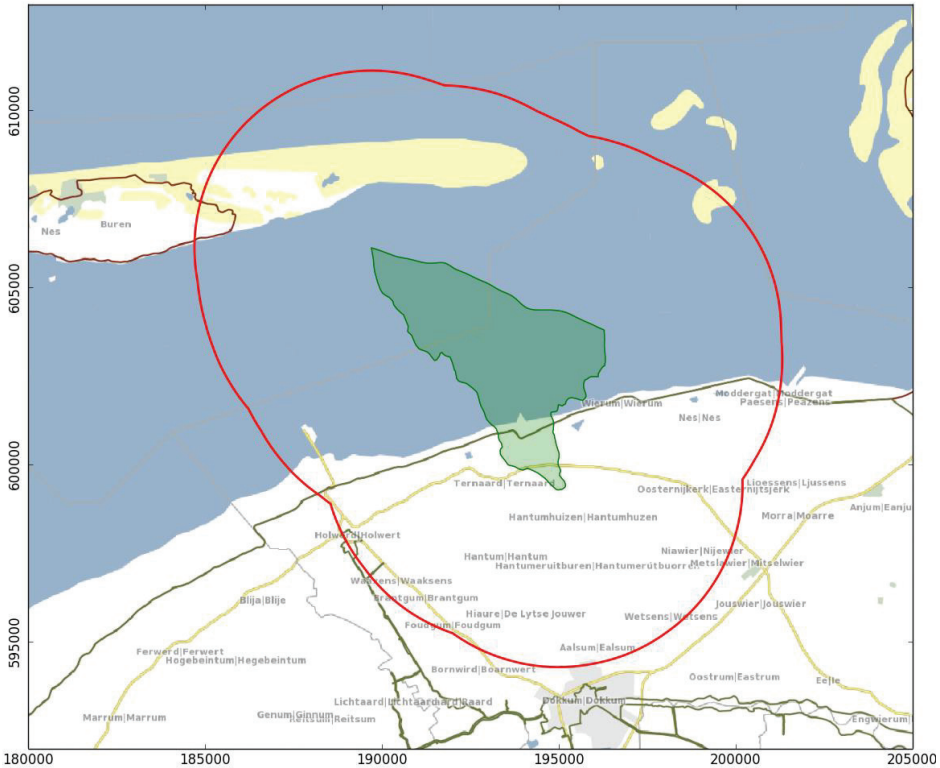

Figuur 12-3: Overzicht van de dijken (bruin: primaire dijken, groen: secundaire dijken). De rode cirkel geeft de 5 km straal rond het Ternaard veld aan die relevant is voor de SRA.

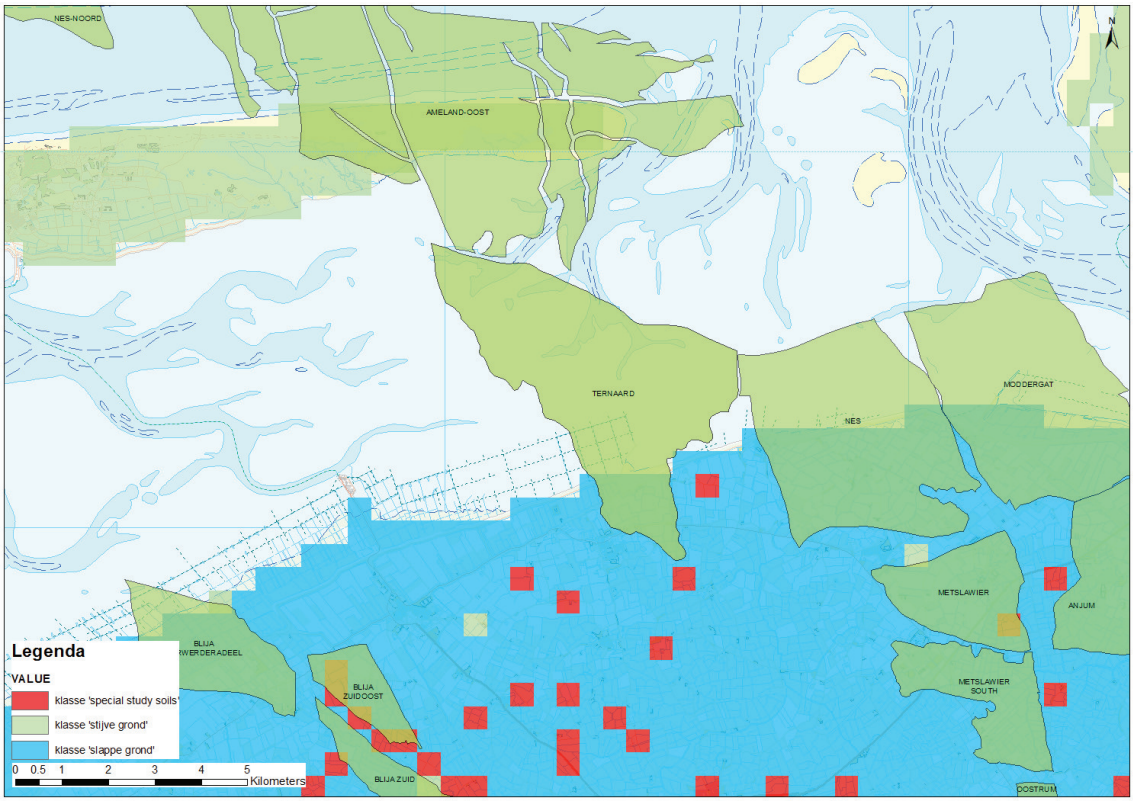

Figuur 12-4: Overzicht van de grondsoorten in de ondiepe ondergrond om de mate van opslingering te bepalen

Uit de analyse op basis van bovenstaande figuren volgen de scores voor de verschillende factoren. Tabel 12-3 geeft de evaluatie en bijbehorende scores voor Ternaard.

Tabel 12-3 Kwantitatieve evaluaties (A) en daaruit voortkomende scores (B) voor de invloedfactoren onder- en bovengrond

A

Voorkomen	Dhais	Mmax	Analoge velden	Opslingering[21]	Bevolkingsdichtheid (aantal inwoners per km2)	Industriële inrichting	Speciale gebouwen en vitale infrastructuur	Dijken
Ternaard	P=19%	1 methode 3,6 - 4,0	Boven de lijn Amsterdam - Arnhem	30 - 60% slappe grond	< 250	1 boven het veld en/of meerdere binnen 5 km rond het veld.	1 school, tehuis en/of publieksgebouw boven het veld of meerdere binnen 5 km rond het veld.	Primaire dijken boven het veld

B

	score invloedfactoren ondergrond					score invloedfactoren bovengrond					
Voorkomen	Kans op beven of waargenomen bevingen	Magnitude	Ligging voorkomen	Opslingering	Genormaliseerde totaalscore ondergrond	Bevolkings dichtheid	Industriele inrichtingen	Speciale gebouwen en vitale infrastructuur	Dijken	Genormaliseerde totaalscore bovengrond	Categorie
Ternaard	1	2	2	2	0,5	0	3	2	4	0,56	I

[21] Aangenomen is dat de bodem onder de Waddenzee vooral uit zand is opgebouwd, waarmee deze bodem onder de klasse “stijve grond” valt.

1 FEBRUARI 2016

METHODIEK VOOR RISICOANALYSE OMTRENT GEÏNDUCEERDE BEVINGEN DOOR GASWINNING

TIJDELIJKE LEIDRAAD VOOR ADRESSERING MBB. 24.1.P, VERSIE 1.2

STAATSTOEZICHT OP DE MIJNEN
Postbus 24037, 2490 AA, Den Haag

INHOUDSOPGAVE

Inhoud

Inleiding

ACHTERGROND

Op grond van de Mijnbouwwet moet sinds 1 januari 2003 een seismische risico analyse omtrent bodemtrillingen als gevolg van de winning in het winningsplan worden opgenomen. In de memorie van toelichting op dit artikel wordt opgemerkt dat het verkenningsonderzoek naar risico's plaatsvindt op het niveau van afzonderlijke velden, maar ook op een brede basis waarbij de maatschappijen en onderzoeksinstellingen gezamenlijk onderzoek verrichten. Mede in dit verband zijn door TNO en KNMI verschillende studies verricht naar de seismische hazard door geïnduceerde aardbevingen. De resultaten van deze studies zijn samengevat en geïntegreerd in het TNO/KNMI integratie-rapport '*Seismisch hazard van geïnduceerde aardbevingen. Integratie van deelstudies*' [1].

In reactie op het OVV-rapport 'Aardbevingsrisico's in Groningen' [2] heeft het kabinet aangegeven dat in de winningsplannen "mijnbouwondernemingen veiligheidsrisico's expliciet in kaart moeten brengen". Hiermee wil de minister borgen dat veiligheid een volwaardige plaats krijgt in de belangenafweging bij de besluitvorming.

Aangezien het in kaart brengen van veiligheidsrisico's verder gaat dan alleen de seismische hazard waarop tot nu toe de focus heeft gelegen, heeft de Minister van Economische Zaken het Staatstoezicht op de Mijnen gevraagd om, in afwachting van een door de maatschappijen en onderzoeksinstellingen te ontwikkelen definitieve leidraad voor het adresseren van het seismisch risico, met een gedragen tijdelijke leidraad voor het analyseren van de risico's ten gevolge van door gaswinning geïnduceerde aardbevingen te komen. Dit document geeft invulling aan dit verzoek.

UITGANGSPUNTEN

In deze tijdelijke leidraad is uitgegaan van bestaande onderzoeksresultaten. Voor de invulling van de methodologie in de leidraad is zoveel mogelijk gebruik gemaakt van kwantificeerbare grootheden uit bestaande analyses en informatiebronnen. Deze leidraad kan in de toekomst op basis van nieuwe inzichten en onderzoeken worden aangepast of vervangen.

AFBAKENING

Deze leidraad geeft alleen invulling aan het in kaart brengen van het seismisch risico (=kans x effect) zoals vereist in het winningsplan (Mijnbouwbesluit artikel 24.1p). **Het is niet de brede risicobeoordeling die is voorzien in het wetsvoorstel tot wijzing van de Mijnbouwwet (versterking veiligheidsbelang en regie). Ook de duiding van de risico's (wat betekend de uitkomst van de in deze leidraad opgenomen methodologie bv. in termen van o.a. te verwachten schade; Mbb. 24.1.q) is géén onderdeel van deze leidraad en dient door de mijnbouwmaatschappij in het winningsplan te worden opgenomen.** Ten aanzien van de maatregelen om bodembeweging (Mbb 24.1r) dan wel schade ten gevolge van bodembeweging (Mbb 24.1s) te voorkomen of te beperken worden in de leidraad **slechts randvoorwaarden voor de monitoring en risicobeheersing** aangegeven.

PROCESS

Staatstoezicht op de Mijnen heeft mede op basis van internationale literatuur en gebruiken een concept voor deze leidraad ontwikkeld [3] en nader uitgewerkt. Deze uitwerking is afgestemd met de Nederlandse Aardolie Maatschappij BV (als grootste landoperator) en kennisinstituut TNO. Vervolgens is de methodologie besproken

binnen het Technisch Platform Aardbevingen (TPA), waarin zowel de mijnbouwondernemingen als kennisinstellingen vertegenwoordigd zijn.

Seismisch risico analyse

De methodologie in deze leidraad is erop gericht om in drie stappen onderscheid te maken tussen velden met een verschillend seismisch risicoprofiel. Hiervoor is een getrapte strategie geadopteerd bestaande uit drie stappen. Deze strategie wordt weergegeven in Figuur 1. Op basis van de uitkomsten van de verschillende stappen worden vervolgstappen genomen.

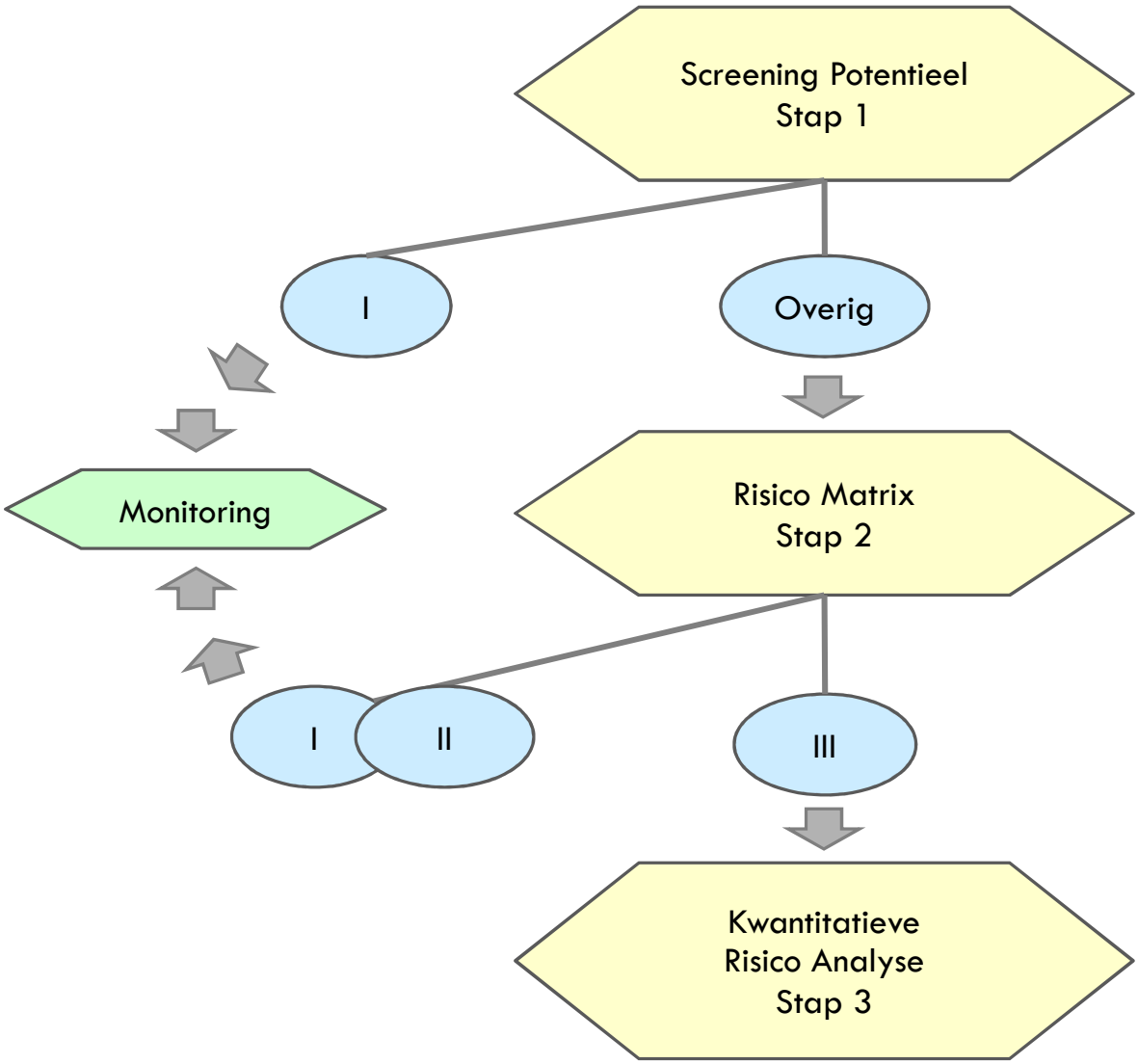

Figuur 1: Weergave van de verschillende stappen in de seismisch risico analyse.

STAP 1: SCREENING POTENTIEEL

Allereerst wordt het potentiële vermogen van het gasveld om aardbevingen te genereren bepaald. In de studie 'Deterministische hazard analyse voor geïnduceerde seismiciteit in Nederland' [4,5] zijn, op basis van historische waarnemingen, statistische correlaties bepaald tussen parameters voor veld- en productiekenmerken

en het optreden van geïnduceerde bevingen. Op basis van deze correlaties kan de waarschijnlijkheid dat bevingen geïnduceerd worden door gasproductie, worden bepaald (Bijlage 1).

Daarnaast wordt op basis van de in het veld aanwezige breuken en op basis van de compactie een inschatting gemaakt van de sterkste beving waar realistisch gezien rekening mee moet worden gehouden. De methodologie voor deze berekeningen staan in Bijlage 2.

Voor velden die op basis van deze berekeningen een verwaarloosbare kans hebben om geïnduceerde bevingen te genereren of waar geen bevingen sterker dan M_l=2,5 op de schaal van Richter zijn te verwachten, zijn geen aanvullende onderzoekstappen noodzakelijk en volstaat monitoring d.m.v. het bestaande KNMI netwerk. Voor de overige velden wordt overgegaan tot de tweede stap in de analyse.

Figuur 2 geeft een overzicht van de beslisstructuur in stap 1.

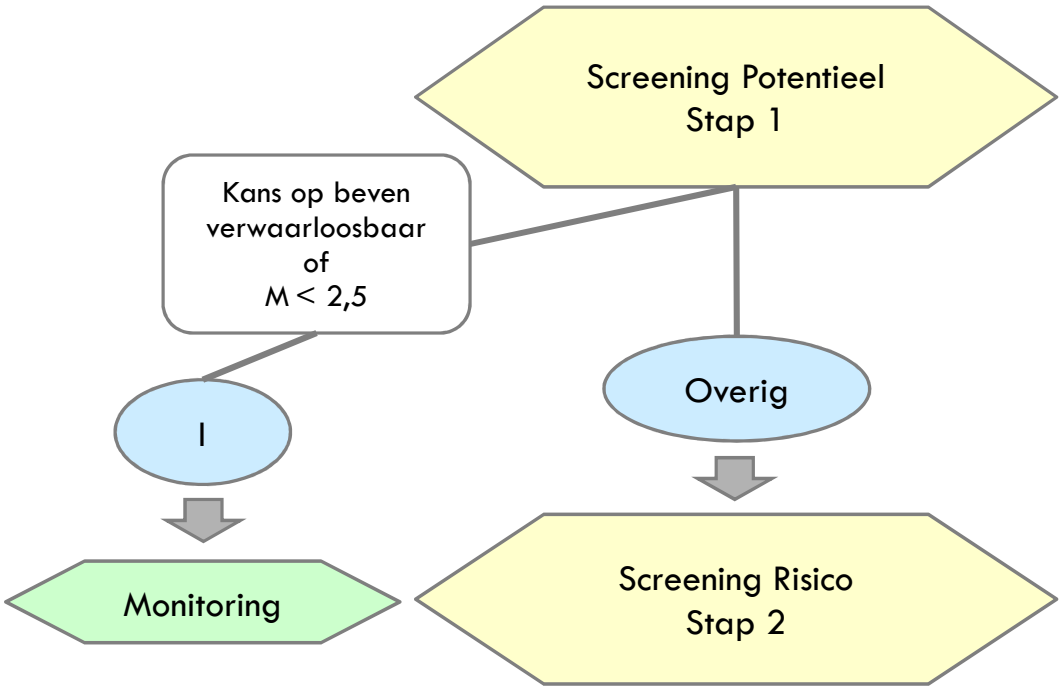

Figuur 2. Weergave van de beslisstructuur in stap1.

STAP 2: RISICO MATRIX

In stap 2 wordt op basis van een risico matrix benadering het risico van geïnduceerde aardbevingen verder gekwalificeerd. Figuur 3 geeft een schematische weergave van de verschillende factoren die bepalen of een geïnduceerde beving kan resulteren in een sterke grondbeweging (de invloedfactoren ondergrond) en de verschillende factoren die invloed hebben op de grootte van de mogelijke gevolgen (de invloedfactoren bovengrond).

In de risico matrix analyse worden de verschillende factoren zoveel mogelijk kwantitatief geanalyseerd en op basis van de uitkomst per factor gerankt (Bijlage 3). Over de scores van de individuele factoren wordt gesommeerd, zodat een totaalscore voor zowel de invloedfactoren ondergrond als de invloedfactoren bovengrond wordt bepaald. Deze worden genormaliseerd met het maximaal te behalen aantal punten voor

ondergrond cq. bovengrond en in de risico matrix tegen elkaar uitgezet waarmee kwalitatief een risicocategorie wordt bepaald (Figuur 4).

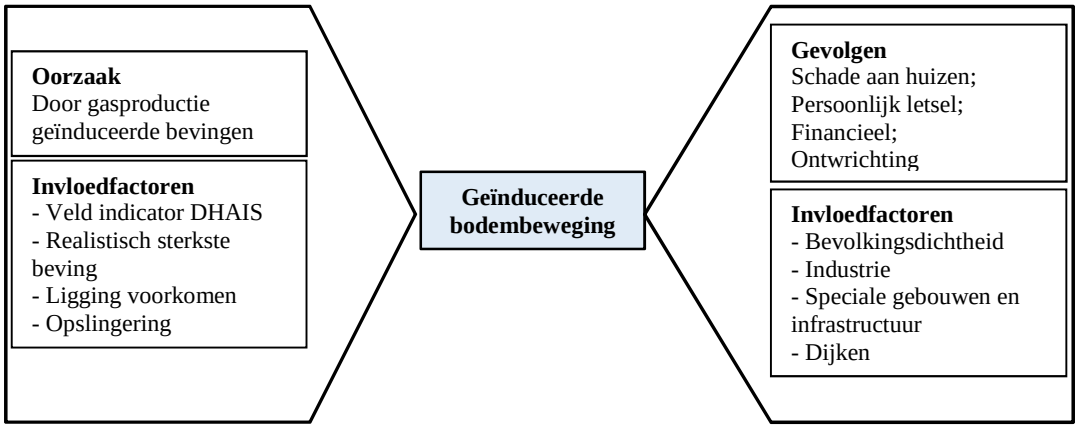

Figuur 3. Schematische weergave van de bedreigingen en gevolgen van geïnduceerde bevingen en de verschillende invloedfactoren die daarbij een rol spelen.

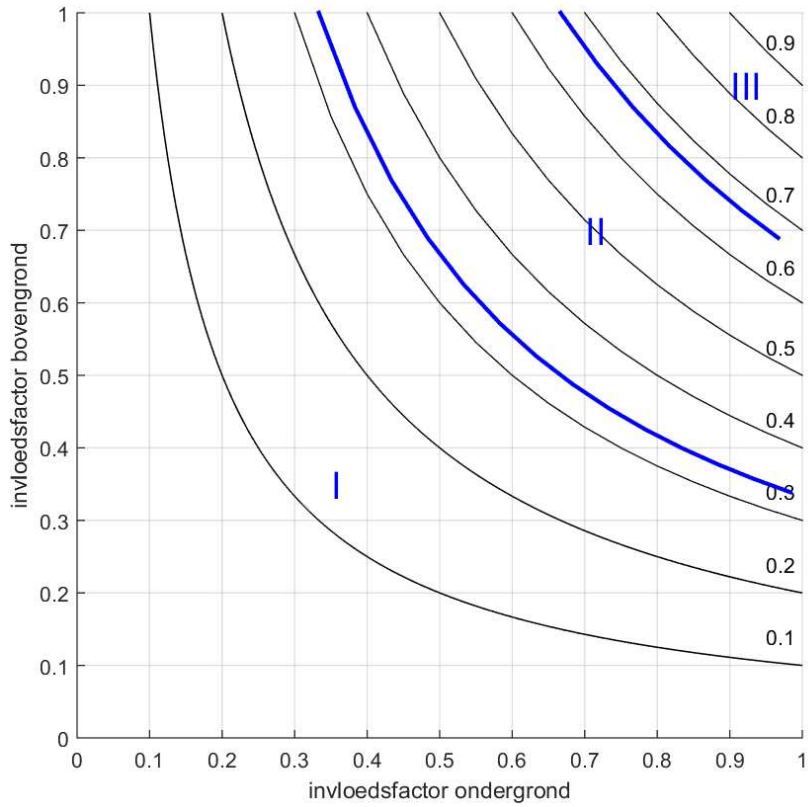

Figuur 4. De risico matrix. De zwarte lijnen zijn lijnen van gelijk genormaliseerd risico. De verdeling in categorieën is simpelweg gedaan op basis van 1/3 en 2/3 van het genormaliseerde risico.

De locatie in de risicomatrix is afhankelijk van de combinatie van de scores voor de invloedfactoren ondergrond en de invloedfactoren bovengrond. De duiding van het risico o.a. in termen van de mogelijke

schade is sterk afhankelijk van deze combinatie en de specifieke factoren waarvoor een hoge/lage score is bepaald. Er is geen algemene duiding per risicocategorie. De duiding kan alleen per voorkomen op basis van de uitkomsten van de analyse gegeven worden[1].

Voor velden waarvan op basis van de risico matrix analyses het seismisch risico door gasdepletie in de categorieën I en II vallen, zijn v.w.b. de screening geen verdere vervolgstappen nodig. Velden in categorie III vervolgen met stap 3.

STAP 3: KWANTITATIEVE RISICOANALYSE

De methodologie voor een kwantitatieve seismisch risicoanalyse in termen van individueel en maatschappelijk risico is ten dele uitgewerkt voor het Groningen gasveld [6, 7, 8, 9]. Indien andere velden in categorie III terecht komen zal het seismisch risico op een vergelijkbare wijze moeten worden gekwantificeerd..

[1] En vormt derhalve geen onderdeel van deze leidraad.

IMPLICATIES

Implicaties

Aan de inschatting van het risiconiveau voor mogelijke geïnduceerde bevingen bij gaswinning worden de volgende monitoringsverplichtingen, beheersmaatregelen en onderzoeksverplichtingen verbonden:

Categorie I:

- Monitoring met het huidige geofoon en accelerometer netwerk van het KNMI.

Categorie II:

- Duiding van de uitkomst van de risicomatrix analyse (Mbw 34.g en Mbb. 24.1.q)
- Monitoring met een minimale cataloguscompleetheid in de omgeving van het veld van magnitude 1,5,
- Monitoring in de omgeving van het veld aanvullen met accelerometers op de geofoonlocaties,
- Implementeren generiek seismisch-risicobeheersplan[2].

Categorie III:

- Monitoring met een minimale cataloguscompleetheid vanaf magnitude 0,5,
- Monitoring aanvullen met accelerometers op de geofoonlocaties,
- Monitoring van trillingen in huizen,
- Onderzoeksprogramma[3],
- Specifiek risicobeheersplan op basis van een Meet- en Regelprotocol.[4]

[2] Een plan waarin de operator de maatregelen beschrijft welke genomen worden bij het optreden van bevingen met een bepaalde sterkte cq. grondversnelling.
[3] Krijgt nadere invulling op basis van de oorzaak van het hoge risico.
[4] Met het Meet- en Regelprotocol wordt (half)jaarlijks getoetst en gerapporteerd of het risico nog binnen vastgestelde acceptabele grenzen blijft en bij (dreigende) overschrijding welke maatregelen getroffen worden om deze (dreigende) overschrijding te mitigeren..

REFERENTIES

Referenties

[1] TNO, 2012, *Seismisch hazard van geïnduceerde aardbevingen; Integratie van deelstudies*, TNO-rapport 2012 R11139 (www.nlog.nl).

[2] OVV, 2015, Aardbevingsrisico's in Groningen; Onderzoek naar de rol van veiligheid van burgers in de besluitvorming over de gaswinning (1959-2014).

[3] Muntendam-Bos, A.G., J.P.A. Roest en J.A. de Waal, 2015, *A guideline for assessing seismic risk induced by gas extraction in the Netherlands*, The Leading Edge, 34(6), 672-677, doi: 10.1190/tle34060672.1.

[4] TNO, 2004, *Deterministische hazard analyse voor geïnduceerde seismiciteit*, TNO-rapport NITG 04-171-C

[5] TNO, 2012, *Deterministische hazard analyse voor geïnduceerde seismiciteit in Nederland*, TNO-rapport 2012 R10198 (www.nlog.nl).

[6] Hazard and Risk Assessment for Induced Seismicity in Groningen – Interim Update November 2015, NAM, 7 November 2015.

[7] Een voorstel voor een toetsingsmethodiek voor mens-geïnduceerde aardbevingen in Groningen, Prof. Pieter van Gelder, TU Delft, Faculteit TBM, 16 november 2015.

[8] Seismisch risico Groningenveld; beoordeling en advies, SodM, December 2015.

[9] Handelingsperspectief voor Groningen, Eindadvies van de adviescommissie 'Omgaan met risico's van geïnduceerde aardbevingen', december 2015.

Bijlage 1

DETERMINISTISCHE HAZARD ANALYSE VOOR GEÏNDUCEERDE SEISMICITEIT IN NEDERLAND [4]

Deze studie gebruikt gegevens over seismiciteit (bron: www.knmi.nl), drukdata en eigenschappen van de voorkomens. Aan de hand van de volgende parameters van een olie- of gasvoorkomen wordt de kans bepaald dat zich, op enig moment gedurende de productie van een voorkomen, een beving voordoet:

- DP/Pini: De ratio van drukval (DP) en initiële druk (Pini) in het reservoir;
- E: de verhouding tussen de Young's moduli (stijfheidsmoduli) van de 'overburden' -en het reservoirgesteente;
- B: een maat voor de breukdichtheid van het reservoir, gedefinieerd als:

$$B = \frac{breukoppervlakte^{3/2}}{brutogesteentevolume} = \frac{l_b{}^{3/2}\, h^{3/2}}{A\, h} = \frac{l_b{}^{3/2}\, h^{1/2}}{A}$$

met h de maximale dikte van de gaskolom van het voorkomen is, l_b de totale breuklengte van de intra-reservoir breuken en de randbreuken van het voorkomen en A het oppervlakte (gemeten binnen de GWC dieptecontour) van het voorkomen [m^2].

De kans-klassen worden hieronder weergegeven (met P_h de kans op beven van het olie-gasvoorkomen):

Reeds bevende voorkomens	
$DP/P_{ini} \geq 28\%$	B > 0,86 en E ≥ 1,34: P_h = 0.42 ± 0.08
	B > 0,86 en 1,01 ≤ E ≤ 1,33: P_l = 0.19 ± 0.05
	B < 0,86 en/of E < 1,01: verwaarloosbare kans
$DP/P_{ini} < 28\%$	Verwaarloosbare kans

De analyse geeft geen informatie over de vraag hoe groot de frequentie en magnitude van een eventuele beving zou kunnen zijn.

Bijlage 2

Bepaling sterkte realistisch sterkste beving

Er worden twee methoden gebruikt om de sterkte van de realistisch sterkste beving te bepalen: op basis van breukgeometrie en op basis van energiebalans. Beide methoden kennen grote aannamen en onzekerheden. In deze Seismisch Risico Analyse leidraad worden daarom beide methoden gebruikt.

Methode 1: breukgeometrie

De hoeveelheid energie die vrijkomt bij een beving en daarmee de sterkte van een beving schaalt met het breukoppervlak dat beweegt. De grootte van een breuk is daarmee limiterend voor de sterkste beving die op die breuk kan plaatsvinden. Deze relatie wordt gegeven door (Kanamori, 2001; Stein en Wysession, 2006):

$$M_0 = GAu = \frac{3\pi}{8}\Delta\sigma(w^2 L)$$

Waarbij M_0 het seismisch moment (maat voor de hoeveelheid energie) is dat bij een beving vrijkomt, G de schuifmodulus, A het breukoppervlak waarover beweging plaatsvind, u de gemiddelde slip (verplaatsing) op de breuk, $\Delta\sigma$ stress drop, oftewel de spanning die tijdens een beving is gerelaxeerd, w de hoogte en L de lengte van de breuk. De relatie tussen het seismisch moment (M_0) en de magnitude (M) van een beving wordt gegeven door (Hanks and Kanamori, 1979):

$$log_{10}\, M_0 = 9.1 + 1.5M$$

Voor tektonische bevingen varieert de stress drop tussen de 1MPa (10 bar) en 10 MPa (100 bar) (Abercrombie, 1995). Voor de meeste geïnduceerde bevingen komt de stress drop niet boven de 5MPa (50 bar) uit. Voor de bepaling van de sterkste realistisch mogelijke beving kan hiervan worden uitgegaan. Een stress drop van 1MPa geeft een 0,5 magnitude punt lagere magnitude, een stress drop van 10MPa een verhoging met 0,2 magnitude punt.

De grootte van de breukoppervlakken waarover slip kan plaatsvinden is voor geïnduceerde bevingen moeilijk vast te stellen. Op basis van geomechanische modellen (Roest & Kuilman, 1994; Mulders, 2003; Muntendam-Bos et al, 2008) is bekend dat de spanningstoename door depletie vooral op het breukoppervlak in het reservoir optreedt, met een lichte spanningstoename op de breuk net buiten het reservoir. Voor de bepaling van een realistische sterkste beving wordt voor het breukoppervlak uitgegaan van het breukoppervlak dat aan het reservoir grenst. Het is echter niet uitgesloten dat ook grotere bewegingen op het oppervlak buiten het reservoir kunnen optreden.

De schuifmodulus (G) kan worden bepaald op basis van de Young's modulus (E) en de Poisson Ratio (υ):

$$G = \frac{E}{2(1+\upsilon)}$$

Methode 2: Energiebalans

Voor geïnduceerde aardbevingen geldt dat slechts een deel van de energie die er door de activiteit – in dit geval onttrekking van olie of gas – opgebouwd wordt tijdens een beving vrij kan komen. Deze relatie is empirisch bepaald. Op basis van Kostrov (1974) hebben Bourne et al. (2014) voor Groningen afgeleid:

BIJLAGE 2

$$M_{0,T}(t) \cong \frac{4\mu}{3}\alpha|\Delta V(t)|$$

Waarbij $M_{0,T}(t)$ het seismisch moment is dat maximaal vrij kan komen, μ de schuifmodulus en $\Delta V(t)$ de volume verandering in het reservoir ten gevolge van de compactie door gasonttrekkking. De fractie van de door compactie opgebouwde energie die seismisch vrij kan komen wordt gegeven door de zogenaamde partitie-coëfficiënt α. De relatie tussen het seismisch moment (M_0) en de magnitude (M) van een beving wordt gegeven door (Hanks and Kanamori, 1979):

$$log_{10}\, M_0 = 9.1 + 1.5M$$

Door de logaritmische relatie tussen seismisch moment en magnitude gaat de sterkste beving gepaard met de helft van het totale seismische moment. De sterkte van deze beving wordt dan gegeven door:

$$M = \frac{2}{3}(log_{10}\left(\frac{2\mu}{3}\alpha|\Delta V(t)|\right) - 9.1)$$

De partitie coëfficiënt α is empirisch bepaald. Voor de bepaling van de sterkste realistisch te verwachten beving wordt een partitie coëfficiënt van 0,01 aangenomen, oftewel 1% van de energie die wordt opgebouwd kan vrijkomen in de sterkste beving. Dit komt overeen met de grootste waarde die geobserveerd is voor enkele velden in Noord-Nederland[5]. Ter vergelijking: voor het Groningen gasveld wordt tot nu toe een waarde voor de partitie coëfficiënt van 0,0005 geobserveerd (Bourne er al, 2014). De gevoeligheid voor de partitie coëfficiënt in de analyse is aanzienlijk: een factor 10 hogere of lagere partitie coëfficiënt geeft een verhoging cq. verlaging van de sterkste magnitude met 0,7 magnitude punt.

Referenties:

Abercrombie, R.E. (1995), *Earthquake source scaling relationships from -1 to 5 Ml using seismograms recorded at 2.5 km depth*, J. Geophys. Res. 100.

Bourne, S.J., S.J. Oates, J. van Elk, and D. Doornhof (2014), *A seismological model for earthquakes induced by fluid extraction from a subsurface reservoir*, J. Geophys. Res. 119(2), 8991-9015, doi:10.1002/2014JB011663.

Hanks, T., and H. Kanamori (1979), *Moment magnitude scale*, J. Geophys. Res. 84, 2348-2350.

Kanamori, H. (2001), *Energy budget of earthquakes and seismic efficiency*, in Earthquake Thermodynamics and Phase Transformations in the Earth's Interior, edited by R. Teisseyre, pp.293-305, Academic, Wlatham, Mass.

Kostrov, V.V. (1974), *Seismic moment and energie of earthquakes and seismic flow of rocks*, Izv. Acad. Sci. USSR Phys. Solid Earth, Eng. Transl., 1, 23-44.

Mulders, F.M.M. (2003), Modelling of stress development and fault slip in and around a producing gas reservoir, Phd. Thesis Technical University Delft, IOS Press.

Muntendam-Bos, A.G. et al. (2008), *Bergermeer Seismicity Study*, TNO Report 2008-UR1071/B, 6 November 2008.

Roest, J.P.A., and W. Kuilman (1994), *Geomechanical analysis of small earthquakes at Eleveld gas reservoir*, Eurock '94, 573 – 580.

[5] De 1% wordt voor 1 veld in de analyse gerealiseerd indien de energie uit alle opgetreden bevingen samen genomen wordt.

Bijlage 3

RISICO MATRIX ANALYSE

In de risico matrix analyse worden de belangrijkste invloedfactoren ondergrond en bovengrond beschouwd en geclassificeerd. Op basis van de classificatie wordt een puntenwaarde toegekend. De toegekende puntenwaarden voor de invloedfactoren worden vervolgens gesommeerd en genormaliseerd om de puntenwaarde voor de ondergrond en bovengrond te bepalen.

In de risicomatrix wordt de combinatie van de puntenwaarden voor boven- en ondergrond met een stip aangegeven. Uit de locatie van het punt in de matrix volgt de risicoclassificatie.

Hieronder worden de verschillende invloedfactoren besproken.

Invloedfactoren ondergrond

De invloedfactoren en de classificatie voor deze factoren worden gegeven in Tabel 1. De manier waarop de classificatie bepaald moet worden, is hieronder beschreven.

1. Kans op het induceren van bevingen:
   De kans dat bevingen geïnduceerd worden wordt bepaald op basis van de DHAIS analyse. Deze analyse is in niveau 1 al uitgevoerd. Het resultaat kan direct worden gebruikt in de classificatie.
2. De sterkste beving waar realistisch rekening mee moet worden gehouden:
   De magnitude van de sterkste beving waar realistisch rekening mee moet worden gehouden wordt berekend in niveau 1 volgens de methodieken beschreven in Bijlage 2. Het resultaat kan direct worden gebruikt in de classificatie.
3. Ligging voorkomen:
   In het noorden van Nederland (inclusief Noord-Holland) ligt een dikke laag Zechstein zout wat vaak de afsluitende laag is van de aanwezige gas voorkomens. Zout op een diepte van ~3km gedraagt zich vloeibaar en zal stromen om de spanningen in het zout te relaxeren. Hierdoor wordt extra spanning opgebouwd net boven en onder een dikke laag zout. Sinds de start van de gaswinning is het nooit voorgekomen dat er geïnduceerde bevingen optraden in velden ten zuiden van de lijn Amsterdam-Arnhem, waar de Zechstein zoutafzettingen ontbreken.
4. Lokale opslingering:
   In [1] zijn de ondiepe grondsoorten en de daaraan verbonden opslingering in kaart gebracht. Het te analyseren gasveld dient op de kaart te worden geprojecteerd en het percentage van het veld boven de verschillende grondsoorten te worden geanalyseerd. Op basis van de bepaalde percentages kan de factor opslingering worden geclassificeerd.

Om de bedreiging te bepalen worden de puntenwaarden behorende bij de classificatie van de vier factoren gesommeerd en genormaliseerd met het maximaal te behalen aantal punten (=14).

Invloedfactoren bovengrond

De gevolgfactoren en de classificatie voor deze factoren worden gegeven in Tabel 2. De manier waarop de classificatie bepaald moet worden, is hieronder beschreven. Algemene opmerking hierbij is dat een 5 km bufferzone genomen wordt vanaf de rand van het veld. De reden hiervoor is dat bevingen op de randbreuken van een veld binnen deze afstand nog significante grondbewegingen kunnen veroorzaken.

1. Bevolkingsdichtheid & bebouwing:
   De bevolkingsdichtheid, oftewel het aantal inwoners per km^2, kan worden bepaald door het oppervlakte

van het veld binnen de verschillende gemeenten waaronder het veld gelegen is in kaart te brengen. Op de bevolkingsdichtheidkaart (CBS Statline)) kan per gemeente de gemiddelde bevolkingsdichtheid worden afgelezen. Op basis van het oppervlakte binnen de verschillende gemeenten kan vervolgens een gewogen gemiddelde voor de bevolkingsdichtheid boven het gasveld worden bepaald, welke geclassificeerd kan worden. Voor hele keine velden kan eventueel ook de ´bevolkingsdichtheid per buurt' worden gebruikt (CBS Statline). Daarnaast wordt in deze categorie ook rekening gehouden met de aanwezige bebouwing. Het type bebouwing speelt een belangrijke rol, maar is moeilijk te specificeren. Het is wel vast te stellen of er wijken met flats/appartementencomplexen aanwezig zijn. Dit is in deze categorie verwerkt.

2. Industriële inrichtingen:
   Op http://www.risicokaart.nl kan de aanwezigheid van industriële inrichtingen boven en rond het veld worden geïnventariseerd en kan deze factor worden geclassificeerd.
3. Speciale gebouwen en vitale infrastructuur:
   Op http://www.risicokaart.nl kan de aanwezigheid van scholen, ziekenhuizen, tehuizen en publieke gebouwen waar veel mensen samenkomen in kaart worden gebracht en kan deze factor worden geclassificeerd.
4. Dijken:
   De aanwezigheid van primaire en/of secundaire dijken kan op http://www.risicokaart.nl in kaart worden gebracht.

Om de gevolgen te bepalen worden de puntenwaarden behorende bij de classificatie van de vijf factoren gesommeerd en genormaliseerd met het maximaal te behalen aantal punten (=16).

BIJLAGE 3

Tabel 1. Classificering van de invloedfactoren ondergrond.

	DHAIS	M	Ligging voorkomen	Opslingering
5		Alle methodes >4,5		
4	Bevend veld > 5 bevingen per jaar van M≥ 1,5	1 methode > 4,5 én/of Alle methodes 4,1 – 4,5		
3	Bevend veld < 5 bevingen per jaar van M≥ 1,5	1 methode 4,1 – 4,5 én/of Alle methodes 3,6 – 4,0		>60% slappe grond ($V_{s,30}$ =< 200m/s) en/of >30% grondsoort die extra gevoelig zijn voor amplificatie, zoals veenlagen dikker dan 3m en slappe veenlagen met een dikte van 1m-3m gelegen op een stijve ondergrond.
2	P=42% Of Bevend veld M < 1,5	1 methode 3,6 – 4,0 én/of Alle methodes 3,1 – 3,5	Boven de lijn Amsterdam-Arnhem	30-60% slappe grond ($V_{s,30}$ =< 200m/s) en/of 15-30% grondsoort die extra gevoelig zijn voor amplificatie, zoals veenlagen dikker dan 3m en slappe veenlagen met een dikte van 1m-3m gelegen op een stijve ondergrond.
1	P=19%	1 methode 3,1 – 3,5 én/of Alle methodes 2,6 – 3,0		10-30% slappe grond ($V_{s,30}$ =< 200m/s) en/of 5-15% grondsoort die extra gevoelig zijn voor amplificatie, zoals veenlagen dikker dan 3m en slappe veenlagen met een dikte van 1m-3m gelegen op een stijve ondergrond.
0		1 methode 2,6 – 3,0 én/of Alle methodes ≤ 2,5	Onder de lijn Amsterdam-Arnhem	<10 % slappe grond ($V_{s,30}$ =< 200m/s) en/of < 5% grondsoort die extra gevoelig zijn voor amplificatie, zoals veenlagen dikker dan 3m en slappe veenlagen met een dikte van 1m-3m gelegen op een stijve ondergrond.

BIJLAGE 3

Tabel 2. Classificering van de invloedfactoren bovengrond

	Bevolkings-dichtheid (aantal inwoners per km^2)	**Industriële inrichtingen**	**Speciale gebouwen En vitale infrastructuur**	**Dijken**
4	> 2500	Meerdere direct boven het veld	Meerder ziekenhuizen en/of energievoorzieningen direct boven het veld	Primaire dijken boven het veld
3	1000-2500 en/of 500-1000 met wijken bestaande uit flats/appartementencomplexen binnen 5 km rond het veld	1 boven het veld en/of meerdere binnen 5 km rond het veld.	1 ziekenhuis en/of energievoorziening direct boven het veld of meerdere binnen 5 km rond het veld. Meerdere scholen, tehuizen en/of publieksgebouwen direct boven het veld	Primaire dijken binnen 5 km rond het veld en/of secundaire dijken boven het veld
2	500-1000 en/of 250-500 met wijken bestaande uit flats/appartementencomplexen binnen 5 km rond het veld	1 binnen 5 km rond het veld.	1 school, tehuis en/of publieksgebouw boven het veld of meerdere binnen 5 km rond het veld.	Secundaire dijken binnen 5 km rond het veld
1	250-500 en/of <250 met wijken bestaande uit flats/appartementencomplexen binnen 5 km rond het veld		1 school, tehuis en/of publieksgebouw binnen 5 km rond het veld.	
0	< 250	Geen binnen 5 km rond het veld	Geen boven en/of binnen 5 km rond het veld	Geen dijken binnen 5 km rond het veld

Inschatting van het risico op schade aan de Waddendijk door mogelijke seismische activiteit van het Ternaard gasveld

NAM, april 2019.

Als onderdeel van de Milieu Effect Rapportage voor het Ternaard gasveld is het risico op schade, door mogelijke seismische activiteit aan de waddendijk nabij Ternaard, bepaald. Deze dijkenstudie is in maart 2019 afgerond met als resultaat het onderliggende engels-talige rapport;

"*Estimate of seismic activity of the Ternaard gasfield and deformation risk assessment for the adjacent primary levee, The Netherlands*"

Om de mogelijke effecten van aardbevingen op de waddendijk in Friesland beter te begrijpen heeft de NAM de firma GR8Geo een analyse laten doen naar de mogelijke effecten van bevingen op de waddendijk nabij Ternaard. De methodes van onderzoek in een eerder gedane studie naar de dijk Eemshave-Delfzijl zijn ook gebruikt voor de Friese studie. Deze studie methodes, zijn goed bevonden door een panel van internationale experts en is geaccepteerd door het Ministerie van Infrastructuur en Milieu (zie notitie van Deltares[1] en ook de brief van het Ministerie van Infrastructuur en Milieu[2]).

In het eerste gedeelte van het GR8Geo rapport over de Friese waddendijk is, als basis en uit conservatisme, een aardbeving gebruikt met een magnitude die groter is dan de maximale magnitude zoals gedocumenteerd in het winningsplan. Meerdere Ground Motion Prediction Equiations (GMPE) zijn gebruikt om de relatie tussen de beving en versnellingen van de grond, in het dijklichaam te berekenen en waarbij de uitkomsten vergeleken zijn met de uitkomsten voor de Eemshaven-Delfzijldijk. Belangrijk in deze berekening zijn de gedetailleerde geotechnische data van het dijklichaam bij Ternaard, die verstrekt zijn door het Wetterskip Fryslân. De analyse wijst uit dat de effecten van een beving met een magnitude van M=3,9 en zelfs van een beving met de hoogste potentiele magnitude ooit bepaald voor een klein gasveld in Nederland, zeer klein zijn.

In het laatste deel is onderzocht wat de impact zou kunnen zijn van de beweging op het vloeigedrag van de grond en stabiliteit in en van de dijk. Hiervoor is een grote hoeveelheid data van sonderingen in combinatie met gedetailleerde geomterische beschrijvingen van de dijk gebruikt in een gedetailleerd model voor de dijk. Een belangrijke parameter hierbij is de Liquifaction Potential Index (LPI) voor de verschillende grondsoorten. Deze LPI-waarden blijken zeer laag te zijn (LPI ligt tussen 0 en 0,73). Liquifactie kan alleen ontstaan bij een veel hogere waarde (LPI=5). De verdere analyse naar de mogelijke deformatie van zachte kleiformaties bracht ook geen reden voor vervolg studies.

Samenvattend kan er gesteld worden dat het onwaarschijnlijk is dat een beving, zelfs met zeer conservatieve waarden voor de maximale magnitude van de beving, zal leiden tot schade aan de Waddendijk boven het Ternaard gasveld.

[1] Deltares, Memo : Eemshaven Delfzijl – Uitgangspunten voor een aardbevingsbestendig ontwerp, Juni 2017

[2] Ministerie van Infrastructuur en Milieu , Brief aan Waterschap Noorderzijlvest, juli 2017.

ESTIMATE OF SEISMIC ACTIVITY OF THE TERNAARD GAS FIELD AND DEFORMATION RISK ASSESSMENT FOR THE ADJACENT PRIMARY LEVEE, THE NETHERLANDS

Prepared for:
Nederlandse Aardolie Maatschappij B.V.

February 2019
Project No. P2019.0002

GR8 GEO Private Company | Dimitrakopoulou 79 | 11741 Athens, Greece | +30 210 922 2186 | www.gr8-geo.com

DOCUMENT CONTROL SHEET

PROJECT	:	Estimate of Seismic Activity of the Ternaard Gas Field and Deformation Risk Assessment for the Adjacent Primary Levee, the Netherlands
PREPARED BY	:	GR8 GEO Dimitrakopoulou 79, 11741 Athens, Greece
PREPARED FOR	:	Nederlandse Aardolie Maatschappij B.V.
PROJECT NO	:	P2019.0002
DATE	:	06/03/2019
Issue	:	01

Issue No	Date	Prepared By	Checked By	Approved By
01	06/03/2019	PG	AG	JC

GR GEO

Dimitrakopoulou 79
11741 Athens, Greece
T: +30 210 922 2186

March 06, 2019
Project No. 2019.0002

Nederlandse Aardolie Maatschappij B.V.
Postbus 28000
9400 HH ASSEN
The Netherlands

Attention: Mr. Ruud van Boom

Subject: Estimate of Seismic Activity of the Ternaard Gas Field and Deformation Risk Assessment for the Adjacent Primary Levee

Dear Mr. van Boom:

The Nederlandse Aardolie Maatschappij B.V., referred to here as NAM, has retained the services of GR8 GEO to develop estimates of seismic activity due to the gas production in Ternaard gas field and assess the risks for major infrastructure such as the primary levee.

As part of the above study, GR8 GEO conducted Deterministic Seismic Hazard Analyses and evaluated the levee deformation potential also considering the findings of recent studies on the dynamic performance assessment of the Eemshaven-Delfzijl levee in the nearby Groningen field.

It has been a pleasure working with you on this project. We look forward to the opportunity to provide continued support to your team as the project progresses.

Sincerely,

GR8 GEO

Jacob Chacko
Principal Engineer

CONTENTS

TABLES

FIGURES

Page

APPENDICES

1.0 INTRODUCTION

1.1 BACKGROUND

As part of the Environmental Impact Assessment Study for the Ternaard gas field development NAM is estimating the risks for major infrastructure such as the primary levee due to potential gas-extraction induced seismic activity. The area of interest is shown on Figure 1. The main focus areas, the Blija-Ferwerderadeel and Ternaard gas fields, are marked with the blue circles.

GR8 GEO was requested to derive an estimate of seismic demand resulting from the Friesland gas field (i.e. in the form of spectral accelerations) and compare it with the seismic demand from the nearby (and much bigger) Groningen field. The relative seismic demands and the performance estimates from the previously studied Eemshaven-Delfzijl levee near Groningen are to be used as indicators of the Friesland primary levee deformation potential.

This report presents the findings of the deterministic seismic hazard analyses performed to develop estimates of the seismic demand resulting from the Friesland gas field and the levee deformation potential evaluations for the primary levee north of Ternaard.

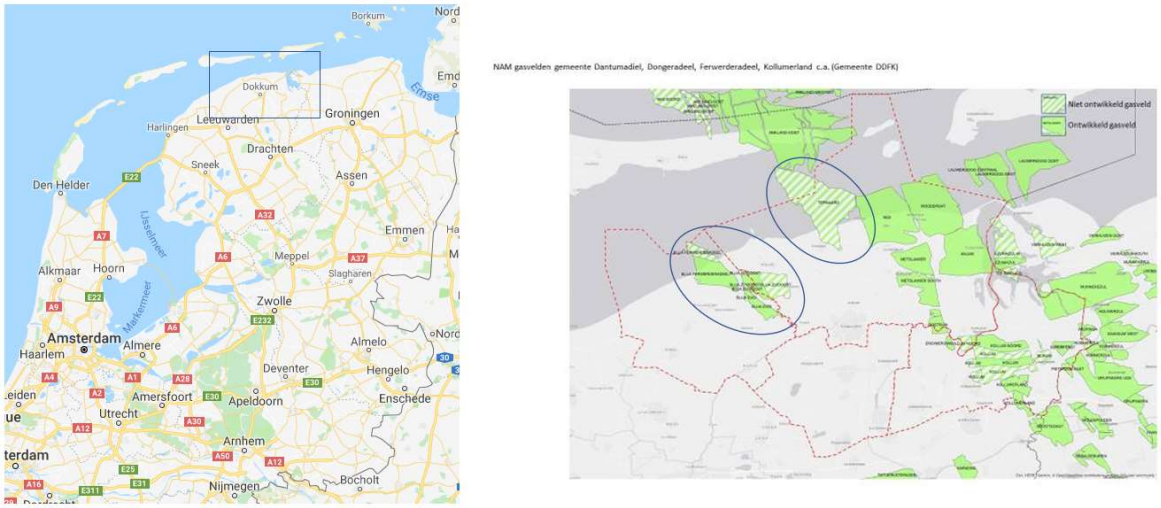

Figure 1. Ternaard Gas Field

1.2 KEY PERSONNEL

Key personnel associated with this study are identified in the following table.

Table 1. Key Project Personnel

CLIENT	NAME
Project Manager, NAM	Ruud van Boom
GR8 GEO	**NAME**
Technical Reviewer	Jacob Chacko
Project Manager	Amalia Giannakou
Deterministic Seismic Hazard Assessment	Amalia Giannakou, Vasileios Drosos
Evaluation of Levee Deformation Potential	Panagiotis Georgarakos

1.3 REPORT ORGANIZATION

The report is organized in four main sections. Following this introductory section:

- Section 2 presents the results of the deterministic seismic hazard analyses
- Section 3 presents the evaluations of the levee deformation potential
- Section 4 summarizes the main conclusions
- Section 5 lists the references

2.0 DETERMINISTIC SEISMIC HAZARD ANALYSES

2.1 MAXIMUM MAGNITUDE ESTIMATES

Maximum magnitude, M_{max}, estimates were developed by NAM following the guidelines outlined by the State Supervision of Mines (2016). According to these guidelines two methods are used to develop estimates of maximum magnitude based on fault geometry and energy balance.

- The method based on fault geometry assumes that the amount of energy released during an earthquake and thus the earthquake magnitude is a function of the fault area that ruptures. The maximum earthquake magnitude is therefore limited by the size of the rupture. The Kanamori (2001) and Stein and Wysession (2006) relationships were used to estimate the maximum seismic moment that is released during an earthquake, the shear modulus, the rupture area, the average slip (displacement) of the fault, the stress drop, the height and the length of the rupture.
- The method based on energy balance assumes that for induced earthquakes, only part of the energy generated by gas extraction activity can be released during an earthquake. Bourne et al. (2014) based on Kostrov (1974) have developed an empirical relationship between the maximum seismic moment that can be released, the shear modulus and the volume change in the reservoir as a result of the compaction due to gas extraction for Groningen.

The maximum magnitude is then estimated from the maximum seismic moment using the relationship by Hanks and Kanamori (1979).

Since these methods are associated with significant assumptions and uncertainties, both were used in the estimation of maximum magnitude. The results are summarized in Table 2.

Table 2. Maximum Magnitude Estimates

Field	Maximum Fault Length (km)	Poisson's Ratio	Fault Throw (m)	M_{max} Energy Balance Method	M_{max} Fault Geometry Method
Blija-Ferwerderadeel	2.7	0.25	98	3.2	3.4
Blija-Zuid	4.3	0.25	87	2.7	3.5
Blija-Zuidoost	2.5	0.25	115	3.3	3.5
Ternaard	6.5	0.2	112	3.4	3.7

Based on the above deterministic seismic hazard analyses were performed for an earthquake scenario with an M_{max} of 3.9.

2.2 SITE GEOLOGY

Cross sections that show the primary geologic units in Friesland were generated from Dinoloket using the DGMdeep v4.0 model (that extends to more than 6 km depth) and the DGM v2.2 (that focuses on the upper 300 to 600 meters) to obtain an overview of the site conditions at the Friesland gas field and how they compare to the conditions at the Groningen gas field.

Figure 2 shows a deep cross section from DGMdeep v4.0 model that extends from the Friesland gas field (i.e. from the levee north of Ternaard) to the Groningen gas field (i.e. to the levee

west of Eemshaven). As shown on this figure the top of the gas reservoir (denoted with RO in the cross section on Figure 2) is located at about 3.7 km depth at Friesland with an upwards slope towards the northeast where it is encountered at about 3.0 km depth near Eemshaven.

In addition, as shown on Figure 2, it looks like the area near Ternaard is underlain by a salt diapir from the Zechstein Formation (denoted as ZE on Figures 2 and 3, pink colour), the top of which is about 800 meters deep near Ternaard. By contrast, the Zechstein formation is typically about 1.8-2 km deep in the Groningen Field. As a consequence the base of North Sea supergroup (denoted as NL_NM on Figures 2 and 3, orange colour), which represents the reference bedrock in the Groningen v5 GMM (Bommer et al 2018), is encountered at depths varying from 450 to 1200 m, compared to about 800 to 900 m depth which is where it is typically encountered in the Groningen Field.

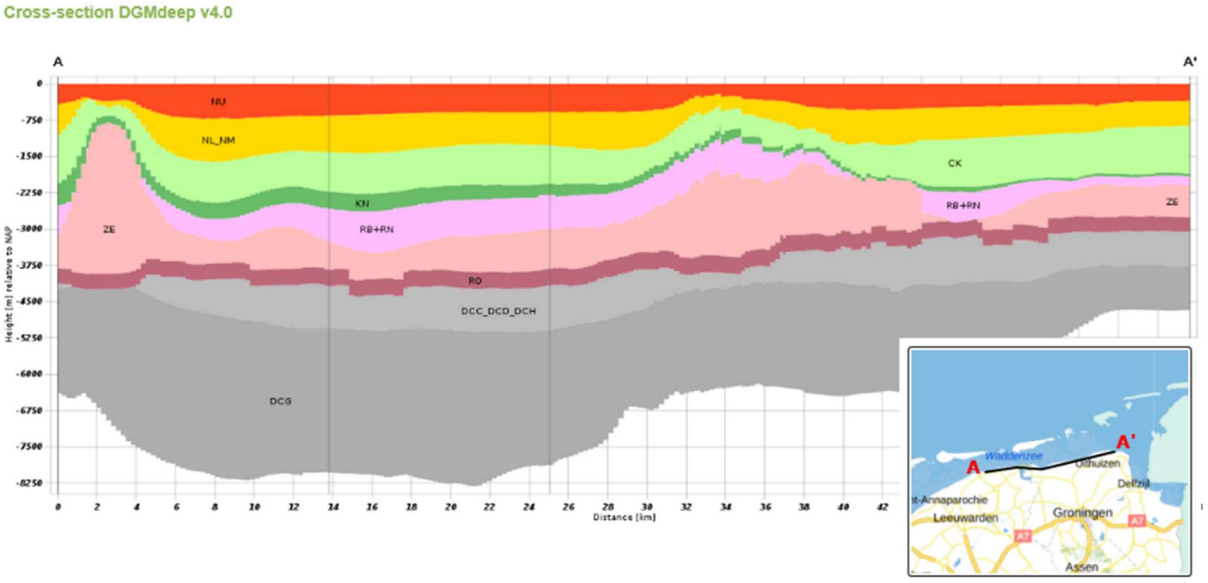

Figure 2. Deep Cross Section extending from Ternaard to west of Eemshaven along the primary levees, DGMdeep v4.0 model, Dinoloket

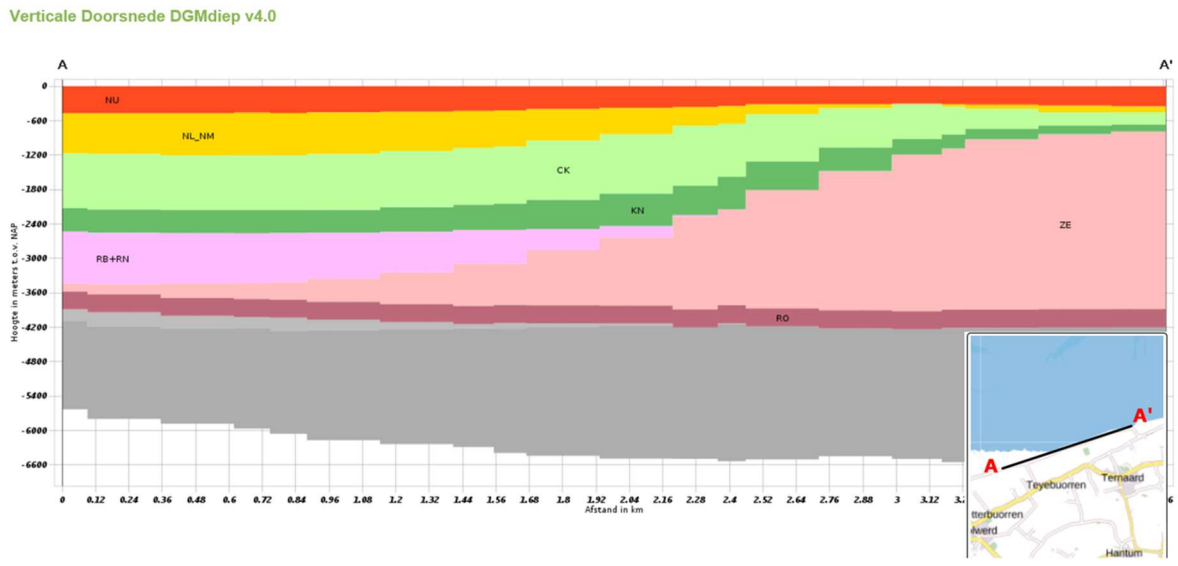

Figure 3. Deep Cross Section near Ternaard primary levee, DGMdeep v4.0 model, Dinoloket

Figure 4 includes a cross section from the DGM v2.2 model focusing on the upper 500 meters that extends from the Friesland gas field (i.e. from the levee north of Ternaard) to the Groningen gas field (i.e. to the levee west of Eemshaven), upper illustration, and cross sections from the same model along the primary levee near Ternaard and along the primary levee between Eemshaven and Delfzijl in the Groningen gas field.

The geologic units included in the DGM v2.2 model are part of the Upper North Sea Group from DGMdeep v4.0 model (NU is Figures 2a and 2b, red colour). As shown on this figure roughly the same sequence of geologic units is encountered in Friesland and in Groningen gas fields although the thicknesses of the individual formations vary between the two fields along the primary levees. The Upper North Sea Group includes the Miocence marine clays of the Brenda Formation (BR on Figure 4), overlain by Pliocene marine delta slope deposits of the Oosterhout Formation (OO on Figure 4). The uppermost deposits within the group of Pleistocene age include the Peize Formation (PZWA on Figure 4), Appelscha Formation (AP on Figure 4) and Urk Formation (UR on Figure 3) fluvial deposits, overlain by Peelo Formation (PE on Figure 4) glacial deposits and Eem Formation (EE on Figure 4) marine deposits (Kruiver et al 2017). The Pleistocene deposits are overlain by a sequence of Holocene soft clays and loose to medium dense sands (HL on Figure 4).

As shown on Figure 4, the Holocene deposits appears to be thinner in Friesland than under the primary levees near the Groningen field, and the top of Pleistocene is also encountered at shallower depths in Friesland than in the Groningen field. Geotechnical cross sections along the levee near Ternaard were provided by the Waterboard and are included in Appendix A. As shown on these sections the levees are underlain by a Holocene sequence of soft clays, peats and medium dense sands that extend down to El. -5 m to -10 m NAP where the top of Pleistocene deposits consisting of stiff clays and denser sands is encountered.

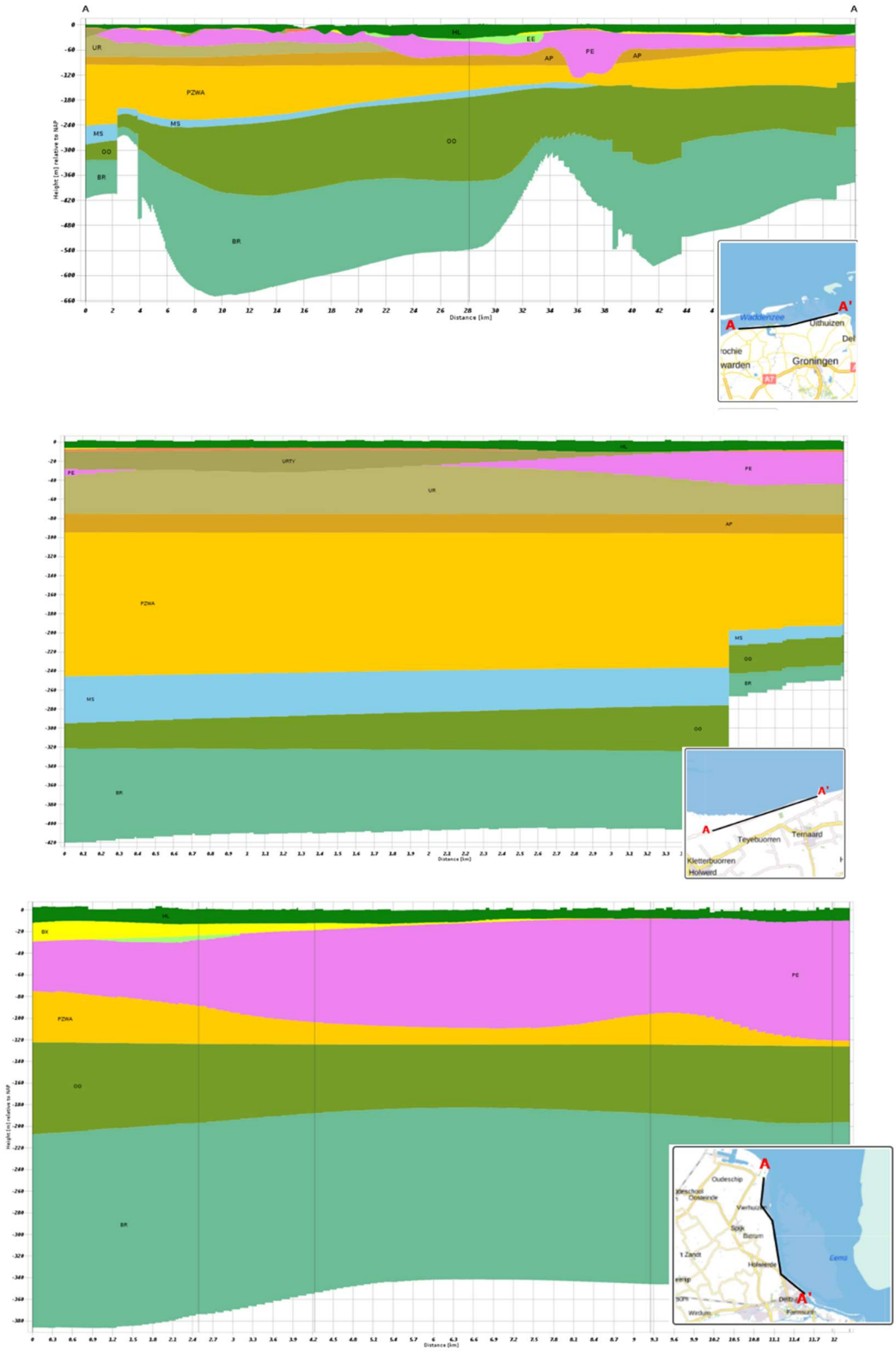

Figure 4. Cross Sections from DGM v2.2 model: along the primary levees from Ternaard to west of Eemshaven (upper illustration), along the primary levees near Ternaard (middle illustration), along the primary levees between Eemshaven and Delfzijl (lower illustration)

2.3 SELECTION OF EMPIRICAL ATTENUATION RELATIONSHIPS

The attenuation of seismic waves from a seismic source to the site is modeled using ground motion prediction equations (GMPEs). These empirical relationships should model the type of seismic source rupture mechanism as well as the regional geology and seismotectonic setting to properly estimate site-specific earthquake ground motion amplitudes.

Most of the GMPEs typically used in seismic hazard assessments generally focus on relatively large events (M>5.0) although the current state-of-the-art tends to consider small events (M>3) when developing GMPEs in order to better calibrate the magnitude scaling (i.e. Next Generation Attenuation West 2 project, Bozorgnia et al., 2014).

Induced earthquakes are likely to be of smaller magnitude and shallower focal depth than the tectonic earthquakes for which most GMPEs are derived, which also results in the wave propagation paths being more strongly influenced by the heterogeneous properties of the uppermost portion of the crust. This results in more accentuated regional differences in ground motion characteristics compared to tectonic earthquakes which is particularly the case for the Groningen gas field (and potentially even more for the Friesland gas field) given the presence of a high velocity salt layer above the reservoir which exerts a pronounced effect on seismic wave propagation (Kraaijpoel and Dost 2013).

A ground motion model for gas-extraction-induced seismicity in the Groningen field has been developed by Bommer et al (2016, 2018). The model was calibrated to local recordings of small-magnitude events (up to M 3.6) and captures the epistemic uncertainty in the extrapolation to larger magnitude considered in the assessment of the resulting hazard and risk for the Groningen field. In order to reflect the conditions in the field, the model first predicts accelerations at the bottom of the North Sea supergroup (NS_B) approximately 800 m below the surface and then convolves these motions with frequency-dependent nonlinear amplification factors assigned to zones across the Groningen field.

Farhadi et al (2018) presented a relatively short list of ground-motion models (GMMs) not established from datasets strictly made of induced events most suitable for induced-seismicity application in Central and Eastern North America (CENA). The models were tested against a dataset of induced earthquakes composed of 2414 time histories from 384 CENA induced events with hypocentral distances below 50 km and moment magnitudes from 3.5 to 5.8. Candidate GMMs were selected from two categories, including purely empirical models developed from the Next Generation Attenuation-West2 (NGAWest2) database and indigenous models of CENA. Some models performed better in certain frequencies than others, and no single model was the best over the entire frequency range. Overall, three models including Abrahamson et al. (2014), Chiou and Youngs (2014), and Atkinson (2015) GMMs outperformed other models.

Douglas et al. (2013) developed GMPEs based on empirical data from ground-motion datasets of induced and natural seismicity from geothermal activities (in Basel, Geysers, Hengill, Roswinkel, Soultz, and Voerendaal), and stochastic simulations.

Table 3 summarizes the main characteristics of the GMPEs considered in this study.

For the Douglas et al. (2013) GMPE the function based on stochastic simulations was selected for a scenario with a path attenuation factor Q=200, a site attenuation factor κ=0.02 sec, and a stress drop parameter of 100 bars, which are the closest parameters to those defined for the Groningen v5 GMM simulations in Bommer et al. (2018) (Q=220, κ=0.01 sec, and a stress parameter of 50 to 100

bars for magnitudes less than 3.4). For the aleatory variability, the between-event standard deviation (τ) was used and was estimated as the average value proposed for the Basel and Soultz geothermal fields. For periods longer than 0.5 s, extrapolation of sigma was done assuming same values as at 0.5s.

Table 3. Characteristics of the GMPEs considered in this study

GMPE	M range	R range (km)	Vs30	Period range
GMPE Groningen V5 GMM Bommer et al. (2018)	M_w 2.6-3.6 extrapolated to M_{max} of about 6.5 using stochastic simulations	0-20	Reference bedrock 1400 m/s Amplification Functions for Vs30 values between 160 to 280 m/s	PGV and SA from 0.01 to 5.0 s
Abrahamson et al. (2014)	M_w 3.0 - 8.5	0-300	200 - 1500 m/s	PGV and SA from 0.01 to 10.0 s
Chiou and Youngs (2014)	M_w 3.0 - 8.5	0-300	200 - 1500 m/s	PGV and SA from 0.01 to 10.0 s
Atkinson (2015)	M_w 3.0-6.0	0-40	760 m/s	PGV and SA from 0.01 to 5.0 s
Douglas et al. (2013)	M_w 1.0-4.0	0-20	1100 m/s	PGV and SA from 0.01 to 10.0 s

2.4 DETERMINISTIC SEISMIC HAZARD APPROACH

2.4.1 Overview

The goal of the deterministic seismic hazard assessment (DSHA) is to develop estimates of seismic demand that can be compared to the levels of seismic demand used in the dynamic levee stability evaluations for the Eemshaven primary levee (Fugro 2017) near Groningen (Segment 6-6, Figure 5), which has the same allowable probability of flooding as the primary levee north of Ternaard (i.e. 1/1000 years).

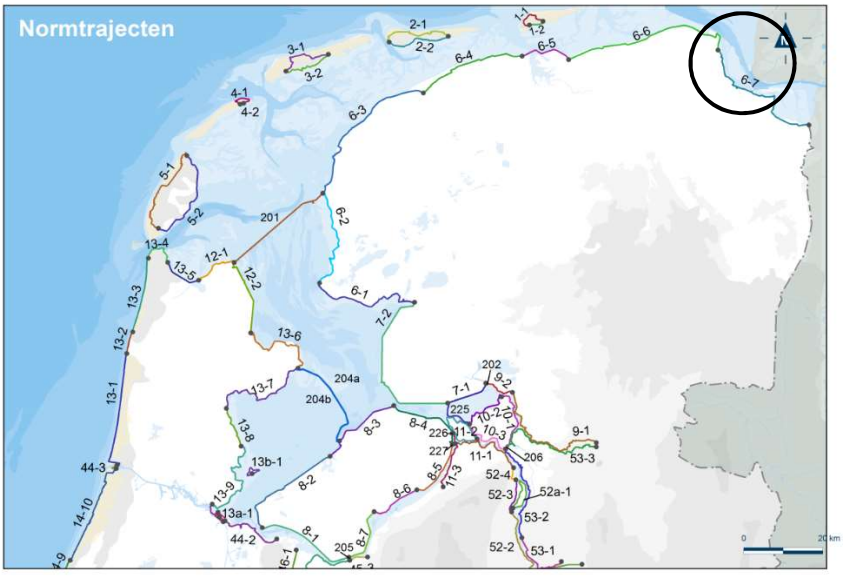

Figure 5. Overview of segments in the Flood Protection Act (in Dutch: Waterwet).

A code calibration study for the primary flood defenses at Eemshaven-Delfzijl was undertaken (Jongejan et al 2017) to derive design parameters for the dynamic stability evaluations of the Eemshaven-Delfzijl primary levee that resulted in a 1100-year design return period for Segment 6-6.

The seismic demand was estimated at a stiff soil horizon level located near the top of Pleistocene deposits and was compared to the acceleration response spectrum used as input at the base of the numerical models in the dynamic stability evaluations for Eemshaven levee. Estimates of shear wave velocity within the Pleistocene deposits along the primary levee near Ternaard were developed using the average of the empirical correlations with CPT data of Rix & Stokoe (1991), Mayne & Rix (1995), Andrus et al. (2007), and Robertson (2009) summarized in Table 4.

Table 4. Empirical Correlations for Shear Wave Velocity

Reference	Soil Type	Correlated Parameters	Correlations
Mayne and Rix (1995)	Clay	• Cone tip resistance, q_c	$V_s = 1.75(q_c)^{0.627}$ where V_s is in m/s and q_c is in kPa
Rix and Stokoe (1991)	Quartz Sands	• Cone tip resistance, q_c • Effective vertical stress, σ'_v	$G_{max} = 1634(q_c)^{0.25}(\sigma'_v)^{0.375}$ where G_{max}, q_c and σ'_v are in kPa; and $V_s = (G_{max}/\rho)^{0.5}$ in m/s
Andrus et al. (2007)	All	• Cone tip resistance corrected for pore pressure effects, q_t • Depth, z • Soil behavior type index, I_c • Age scaling factor (SF)	$V_s = 2.62(q_t)^{0.395}(I_c)^{0.912}(z)^{0.124}SF$ where V_s is in m/s, q_t in kPa, I_c is dimensionless, z is in m, and SF = 1.12 for Pleistocene soils and 0.90 for Holocene soils;
Robertson (2009)	All	• Cone tip resistance corrected for pore pressure effects, q_t • Total stress, σ_v • Soil behavior type index, I_c	$V_s = [10^{(0.55\,Ic + 1.68)}(q_t - \sigma_v)/P_a]^{0.5}$ where V_s is in m/s, q_t and σ_v in kPa, I_c is dimensionless, and P_a is the atmospheric pressure

The interpreted shear wave velocity from CPT data within the Pleistocene deposits is shown on Figure 6. Also shown on this figure is the idealized shear wave velocity profile within the Pleistocene deposits considered in this study. Based on this a Vs30 of about 260 m/s was used in the evaluations of seismic demand applicable near the top of Pleistocene deposits.

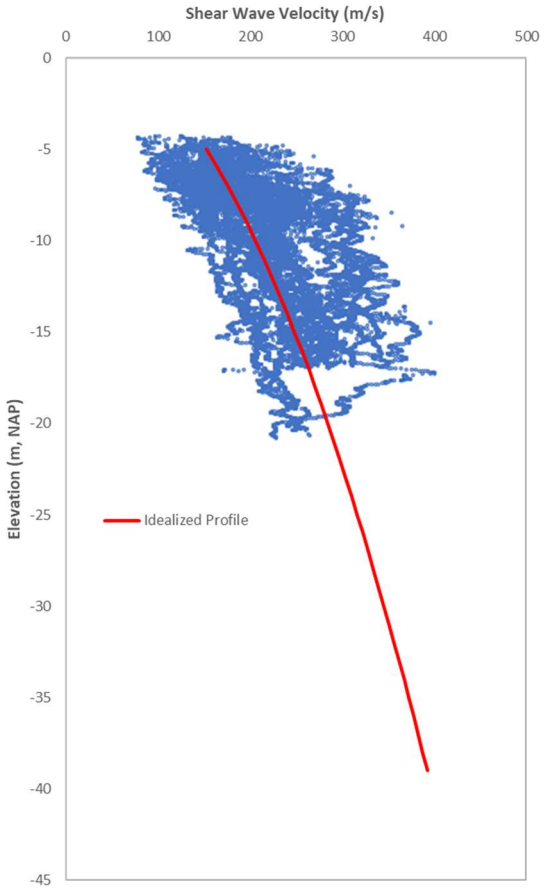

Figure 6. Shear Wave Velocity from Interpreted CPT data within Pleistocene deposists underlying the primary levee north of Ternaard.

The following approach was adopted for the deterministic seismic hazard evaluation for Friesland gas field:

- Estimates of reference bedrock horizontal acceleration response spectra were developed using the selected GMPEs for a deterministic scenario of Mw=3.9, R=3 km.
- Similar to the v5 GMM (Bommer et al. 2018) the bottom of the North Sea supergroup (NS_B) was selected as reference bedrock with an assumed Vs30 of 1400 m/s.
- For the Atkinson (2015) and Douglas (2013) GMPEs that only provide spectral accelerations for Vs30 values of 760 m/s and 1100 m/s, respectively, the linear site amplification function term by Boore et al. (2014) was used to adjust the GMPEs to a common reference V_{s30} of 1400 m/s.
- Due to the largely similar geologic units encountered above 800 meters depth between Groningen and Friesland the v5 GMM nonlinear site amplification function was used to estimate horizontal acceleration response spectra at the top of Pleistocene (Vs30 ~ 260 m/s, Zone 308 from v5 GMM)

2.4.2 Estimating "Reasonably Conservative" Number of Standard Deviations (Sigmas) for Use in DSHA

The input seismic demand in the Eemshaven primary levee stability assessment was derived from probabilistic seismic hazard analyses using the v2 GMM (Bommer 2016) and was associated with an 1100-year return period. In the deterministic approach adopted for the seismic demand at Friesland field, the selected GMPEs are weighted and used to estimate spectral accelerations resulting from a maximum magnitude event as a function of the number of standard deviations from the median prediction. In order to assess what is a reasonably "conservative" value or range of values to be compared with the Eemshaven-Delfzijl levee demands, a deterministic seismic hazard analyses was performed using the v5 GMM (Bommer 2018) and an earthquake scenario with magnitude M_w 5 at a distance of 10 km, which corresponds to the controlling scenario based on PSHA deagreggation results at the Eemshaven levee location with the v2 GMM. Median, median plus one sigma and median plus two sigma acceleration response spectra are estimated at the stiff soil horizon corresponding to the base of the numerical model used in the Eemshaven levee stability evaluations and compared with the probabilistic acceleration response spectra used in the Eemshaven-Delfzijl stability analyses (Fugro 2017). The comparison is presented on Figure 7. Also plotted on this figure with a grey dashed line is the fundamental period of the Eemshaven levee including SSI effects which was estimated to be about 0.7 second (Jongejan et al 2017). Since the v5 GMM is expected to result in lower spectral accelerations compared to the v2 GMM due to reduction in gas production rates and also differences between the two models, the median plus one and median plus two sigma spectra are expected to provide a reasonably "conservative" range of values to be compared with the Eemshaven-Delfzijl levee demands.

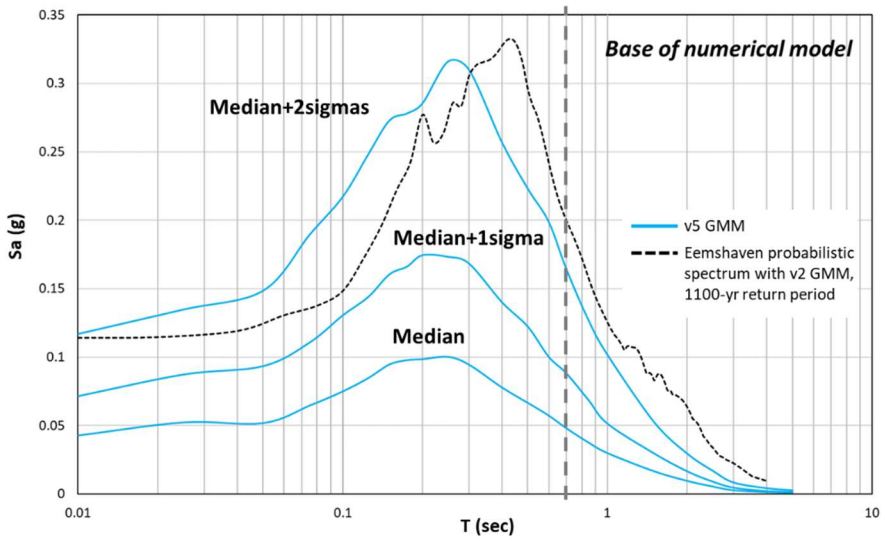

Figure 7. Comparison of deterministic spectra for a M=5 at R=10 km scenario using v5 GMM with probabilistic spectra using v2 GMM corresponding to a return period of 1100-years at the base of the numerical model used for the dynamic stability evaluations at Eemshaven levee.

2.4.3 Comparative GMPE Scaling

The spectral trends of the selected 5 GMPEs summarized in Table 3 are visually inspected from trellis plots for different earthquake scenarios. Trellis plots can help capture unexpected trends and identify the general behavior of ground-motion estimates in multi-dimensional space (magnitude,

source-to-site distance, structural period). In this respect, trellis plots provide an effective insight into the GMPEs while assessing their general trends for site-specific seismic hazard assessment.

The aim of the trellis plots is to help identify outliers with clearly nonphysical behavior but also to help guide the selection of models to capture epistemic uncertainty. The plots were prepared for rock site conditions (Vs30=1400 m/s) and for the median, median plus one sigma and median plus two sigma predictions and shown on Figures 8 (median prediction), 9 (median plus one sigma prediction) and 10 (median plus two sigma prediction). The selected magnitude and distance values are Mw 3.0, 3.9, 5.0 and R = 3km, 5km, 10km. The trellis diagrams are plotted for periods up to T = 5.0s.

A comparison of Figures 8 to 10 indicates that the predictions of Atkinson (2015) and Douglas (2013) GMPEs are considerably higher than the predictions of v5 GMM (2018), Abrahamson et al (2014) and Chiou and Youngs (2014) especially for magnitudes larger than 3 and larger sigmas. It is noted that while Douglas et al (2013) results in considerably higher predictions at structural periods less than 0.1 s for all magnitudes and standard deviations considered, the Atkinson (2015) GMPE predictions become significantly higher when the standard deviation term is included in the model. Perhaps due to the availability of more robust data sets, the standard deviation term in the Groningen-specific v5 GMM and the NGA-West 2 models are likely better constrained than in Atkinson (2015) and Douglas (2013).

One additional observation from Figures 8 to 10 is that the two NGA-West 2 GMPEs result in similar predictions compared with the rest of the models considered so the consideration of both GMPEs instead of only one of the two does not increase the overall uncertainty.

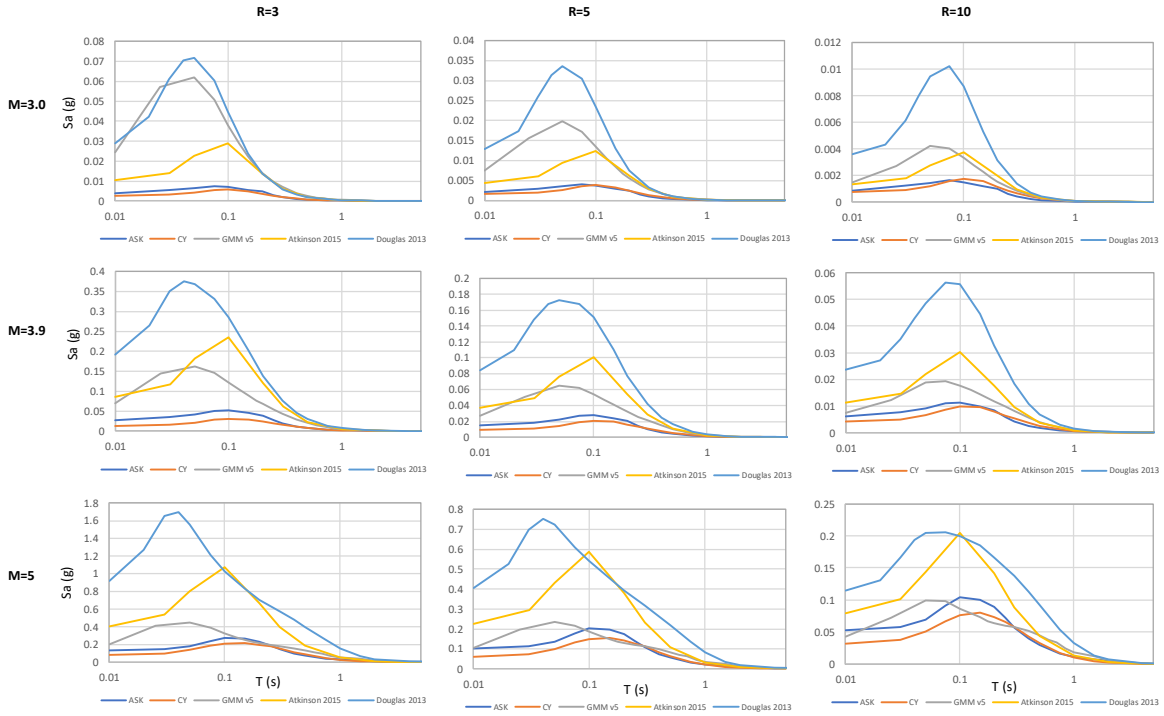

Figure 8. Trellis plot for acceleration response spectra of the selected GMPEs (median estimates and V_{S30}=1400m/s).

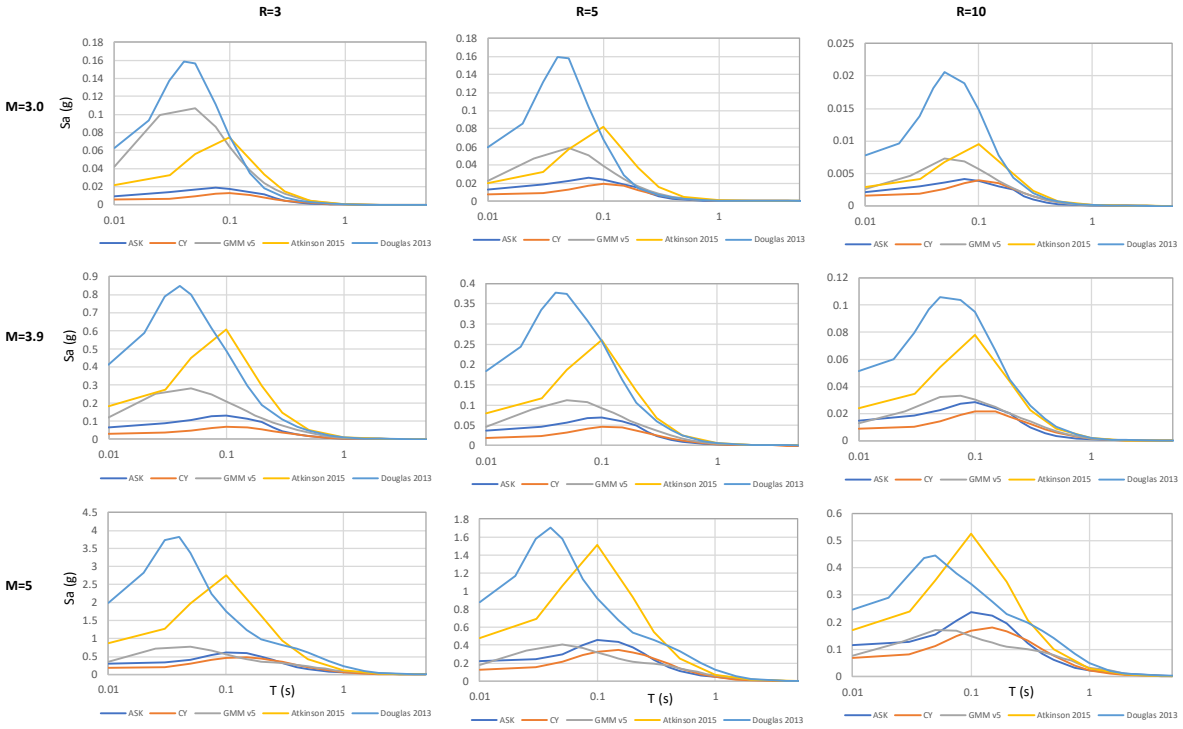

Figure 9. Trellis plot for acceleration response spectra of the selected GMPEs (median plus one sigma estimates and V_{S30}=1400m/s).

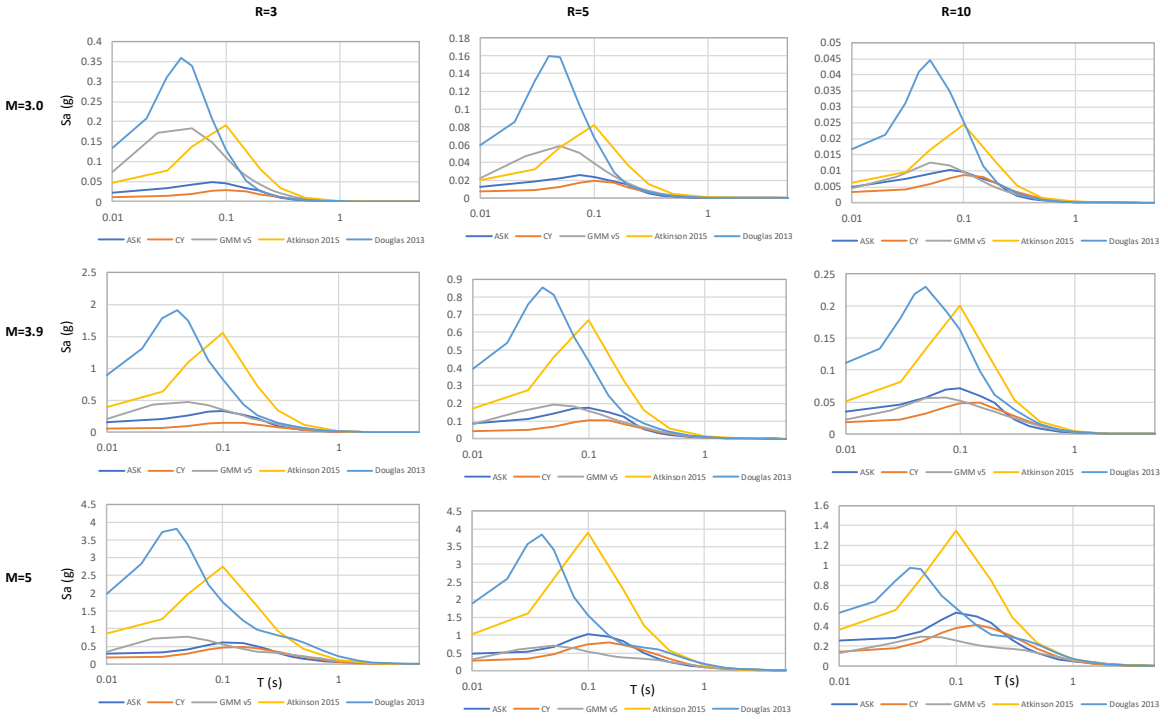

Figure 10. Trellis plot for acceleration response spectra of the selected GMPEs (median plus two sigma estimates and V_{S30}=1400m/s).

Based on the discussions above the following weights were applied on the GMPEs:

- Groningen V5 GMM Bommer et al. (2018): weight 0.6
- Abrahamson et al. (2014): weight 0.2
- Atkinson (2015): 0.1
- Douglas et al. (2013): 0.1

2.5 RESULTS

Results of the DSHA at stiff soil horizon (near the top of Pleistocene) for an earthquake scenario with M=3.9 and R=3km using the weighted average of the GMPEs for the median, median plus 1 sigma and median plus 2 sigma are presented on Figure 11. Also shown on the same figure for comparison is the response spectrum corresponding to 1100-year return period that was used at the base of the numerical model for the Eemshaven levee (black dashed line) as well as the fundamental period of the Eemshaven levee (dashed grey line) including SSI effects which was estimated to be about 0.7 second (Jongejan et al 2017). As shown on this figure the seismic demand at Friesland in the period range of interest (i.e. about 0.7 s) is considerably smaller than the input seismic demand used in the dynamic stability evaluations of the Eemshaven levee for the level of uncertainty considered in this study.

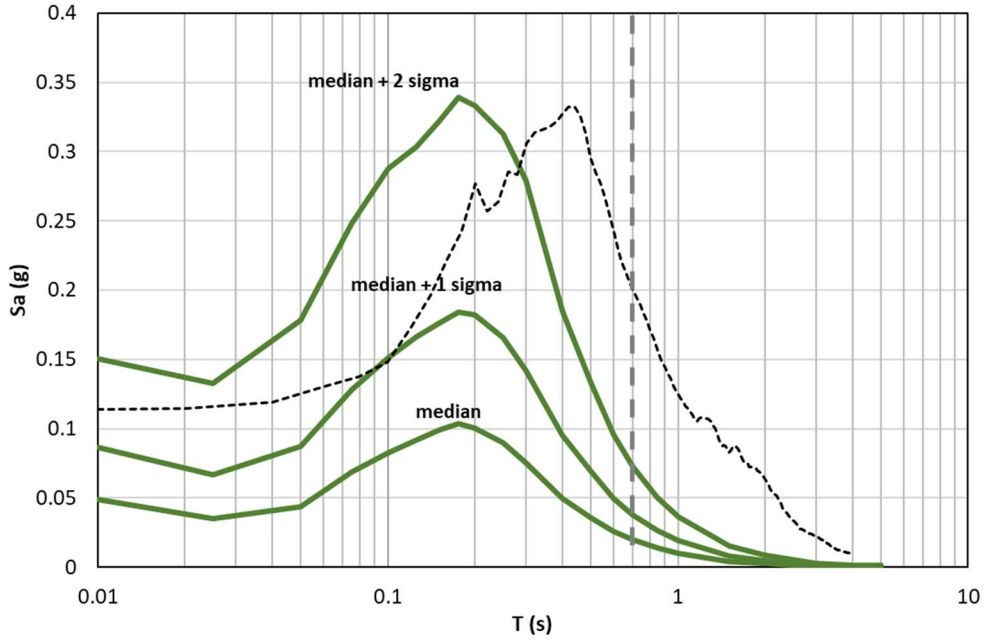

Figure 11. Comparison of deterministic spectra for a M=3.9 at R=3 km scenario using the weighted average of selected GMPEs for different values of standard deviations with probabilistic spectra using v2 GMM corresponding to a return period of 1100-years at the base of the numerical model used for the dynamic stability evaluations at Eemshaven levee.

In addition results for an upper bound M_{max} scenario of 4.1 (representative of the upper bound of maximum magnitude of small size fields in the Netherlands) are also presented in Figure 12. As for the DSHA results of the M=3.9 at R=3 km scenario discussed above, the seismic demand for this scenarios in the period range of interest (i.e. about 0.7 s) is smaller than the input seismic demand used in the dynamic stability evaluations of the Eemshaven levee for the level of uncertainty considered in this study

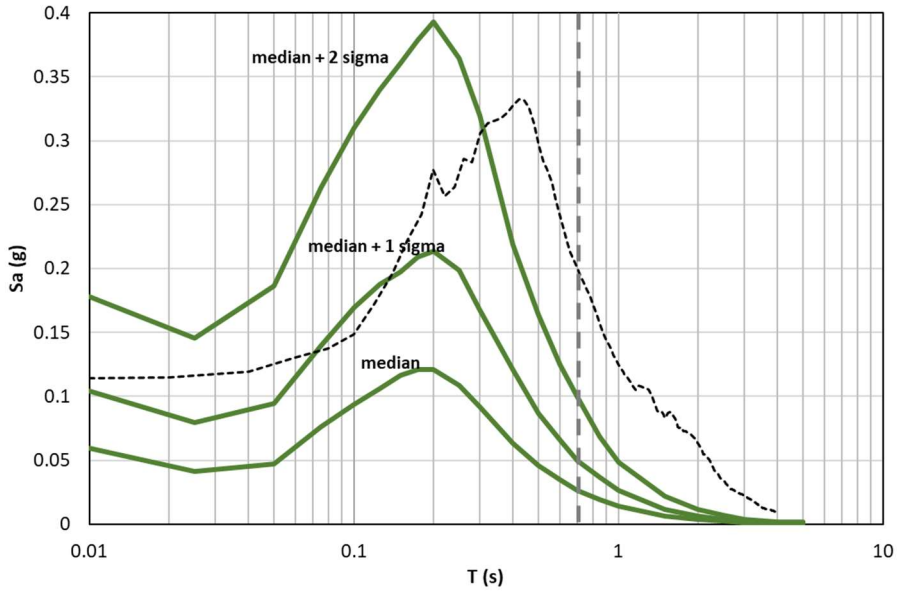

Figure 12. Comparison of deterministic spectra for a M=4.1 at R=3 km scenario using the weighted average of selected GMPEs with probabilistic spectra using v2 GMM corresponding to a return period of 1100-years at the base of the numerical model used for the dynamic stability evaluations at Eemshaven levee.

3.0 EVALUATION OF PRIMARY LEVEE DEFORMATION POTENTIAL

An estimate of seismic demand resulting from the Friesland gas field (i.e. in the form of spectral accelerations) was developed deterministically as described in the previous section and was compared with the seismic demand from the nearby (and much bigger) Groningen field. In this section: a) the available site-specific geotechnical data at the primary levee near Teenaard were used to: perform a screening level assessments of strength loss of the underlying Holocene deposits and b) the performance estimates from the previously studied Eemshaven-Delfzijl levee in Groningen gas field (Fugro 2017) were used as indicators of the Friesland primary levee deformation potential.

3.1 AVAILABLE DATA

The following data were provided for the evaluation of primary levee deformation potential near Ternaard:

- 67 CPTs in digital format by Wiertsema & Partners (2016) shown on Figure 13
- 32 scanned CPT graphs (1973)
- Longitudinal geotechnical cross sections with layer interpretations along the levee from km 41.2 to km 47.8 (included in Appendix A); and
- Drawings illustrating the levee geometry

Figure 13. Available explorations along the primary levee north of Ternaard.

3.2 GEOTECHNICAL SITE CONDITIONS

Geotechnical cross sections along the levee near Ternaard were provided by the Waterboard and are included in Appendix A. As shown on these sections the levees are underlain by a Holocene sequence of soft clays, peats and medium dense sands that extend down to El. -5 m to -10 m NAP where the top of Pleistocene deposits consisting of stiff clays and denser sands is encountered.

The thickness of the Holocene deposits appears to be relatively smaller in Friesland than under the Eemshaven-Delfzijl primary levee in the Groningen field, where the top of Pleistocene was encountered at about El. -13 m NAP.

In addition, both the lateral extent and thickness of medium dense Holocene sand deposits encountered beneath the Friesland primary levee are limited compared to the coarse-grained deposits encountered under the Eemshaven-Delfzijl primary levee within the Holocene sequence.

3.3 PRIMARY LEVEE GEOMETRY

Figure 14 shows a comparison of the levee geometries between the primary levee at km 45+400 near Ternaard and the primary levee at km 38+000 near Eemshaven (both having the same allowable probability of flooding of 1/1000 years). As shown on this figure the levee height and overall geometry is similar between the two sections.

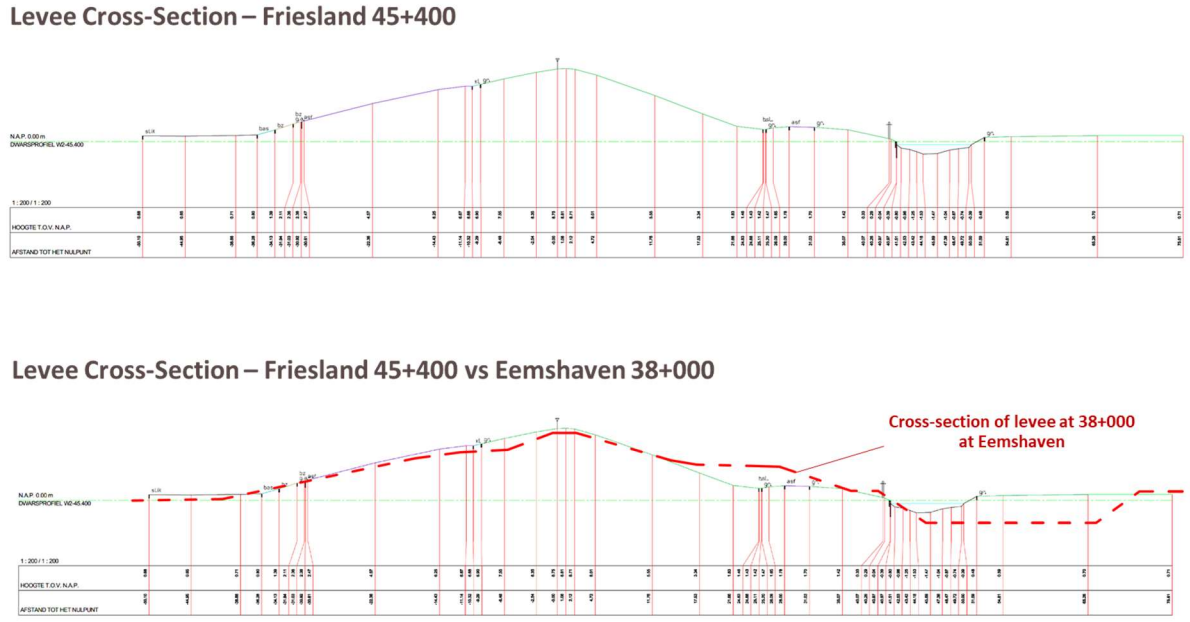

Figure 14. Comparison of primary levee geometries near Ternaard and near Eemshaaven with the same allowable probability of flooding of 1/1000 years.

3.4 EVALUATION OF LIQUEFACTION TRIGGERING POTENTIAL OF COARSE-GRAINED DEPOSITS

Evaluations of liquefaction triggering potential of coarse-grained deposits underlying the Friesland primary levee were performed using: a) the same screening methodology developed and applied in the Eemshaven-Delfzijl levee (Expert Panel, 2016), b) the deterministic ground motion estimate described in Section 2.0 for the median plus 2 standard deviations and c) the Groningen-specific Green et al (2018) simplified triggering procedure that has also been adopted in the current NPR9998 guidelines.

Using these criteria, we performed liquefaction triggering hazard assessments along approximately 6.6 km of the primary levee north of Ternaard using available geotechnical data (67 CPTs) provided to us in an electronic format.

For the Eemshaven-Delfzijl levee, the Expert Panel (2016) report recommended a two-phase approach for seismic stability evaluations. In Phase 1, simplified procedures based on available CPT data are used to estimate the potential liquefaction severity at each point where CPT data are available. In addition to evaluations of factors of safety at each CPT location, it was recommended that liquefaction severity be characterized using the Liquefaction Potential Index (LPI). If the Phase 1 analyses show a significant risk of liquefaction-related damage (typically associated with LPI values

larger than 5 as was also demonstrated for the Eemshaven-Delfzijl levee by Kolk et al 2017), it was recommended that a secondary phase (Phase 2) involving detailed, nonlinear, effective stress analysis of levee sections that do not pass the preliminary screening are initiated.

3.4.1 Basis of Evaluation

The liquefaction analyses presented herein are based on:

- Cyclic stress ratios (CSR) estimated from Peak Ground Acceleration (PGA) using the Green et al (2018) empirical procedure;
- Cyclic resistance of the coarse-grained deposits evaluated from Cone Penetration Test (CPT) data using the Green et al (2018) empirical procedure.

3.4.2 Cyclic Demand

The evaluation of the seismically induced demand or cyclic stress ratio (CSR) was estimated using a PGA estimate from the deterministic hazard analyses described in Section 2.0. According to Jongejan et al (2017) code calibration study, the design earthquake return period for the Eemshaven primary levee which has the same probability of flooding as the Friesland levee is 1100 years. Since the estimates of seismic demand for the Friesland levee were developed deterministically, the median + 2 standard deviation estimate of PGA was conservatively used in the evaluations resulting in a PGA value of 0.15g (see further discussion in Section 2.0). The estimated maximum earthquake magnitude of 3.9 was used for the triggering evaluations.

3.4.3 Cyclic Resistance

The CPT data were used to evaluate the liquefaction resistance or cyclic resistance ratio (CRR) of the liquefiable layers. The factor of safety (FoS) against liquefaction was then calculated as the ratio of the CRR to the CSR (FoS = CRR/CSR). Liquefaction potential evaluations were conducted using the Green et al (2018) procedure.

We note that the Green et al (2018) Groningen specific method is largely based on the Boulanger and Idriss (2014) method with the exception of:

(i) the r_d factor, which is defined from regression analyses of site response analyses results from Groningen-specific soil profiles and

(ii) the MSF factor which is derived based on an energy approach

Thin Layer Correction. In some cases, a thin layer correction factor is applied to the raw cone tip resistance using methods described in Youd et al. (2001). This correction was applied if a thin sand layer existed immediately above a softer clay or silt layer.

Fines Correction. The measured tip resistances were corrected for fines content and normalized to an overburden pressure of 1 atmosphere (~0.1 MPa). The fines content and associated corrections were estimated from CPT data using the procedure suggested by Boulanger and Idriss (2014) using C_{FC}=0.

The Ground water table (GWT) was assumed at +0.50m NAP.

3.4.4 Evaluation of Liquefaction Potential Index

The estimated Factor of Safety against liquefaction shows the liquefaction potential of a soil layer at a particular depth; however, it may not reflect the degree of liquefaction severity over the

entire depth of a soil column. Iwasaki et al. (1978) introduced a liquefaction potential index (LPI) to estimate the potential for liquefaction to cause foundation and structural damage.

LPI at a site is calculated by integration of FoS along the soil column up to 20m depth. A weighting function is added to give more weight to the layers closer to the ground surface.

The LPI is expressed as follows:

$$\int_0^{20m} F.w(z)dz$$

Where;

$F \quad = 1 - FoS, for\ FoS \leq 1$

$F \quad = 0\ for,\ FoS > 1$

$W(z) \quad = 10 - 0.5z,\ where\ z\ is\ depth\ in\ meters$

LPI is intended to demonstrate liquefaction severity during seismic events, and LPI ≥ 5 is generally considered as a threshold for the surface manifestation of liquefaction. In addition, numerical analyses performed for the Eemshaven-Delfzijl levee for various scenarios associated with different LPI values showed that the deformation potential of the levee for LPI values less than 5 was low (Kolk et al 2017). An example of levee crest settlement versus LPI estimated from dynamic numerical evaluations for the Eemshaven primary levee is shown on Figure 15.

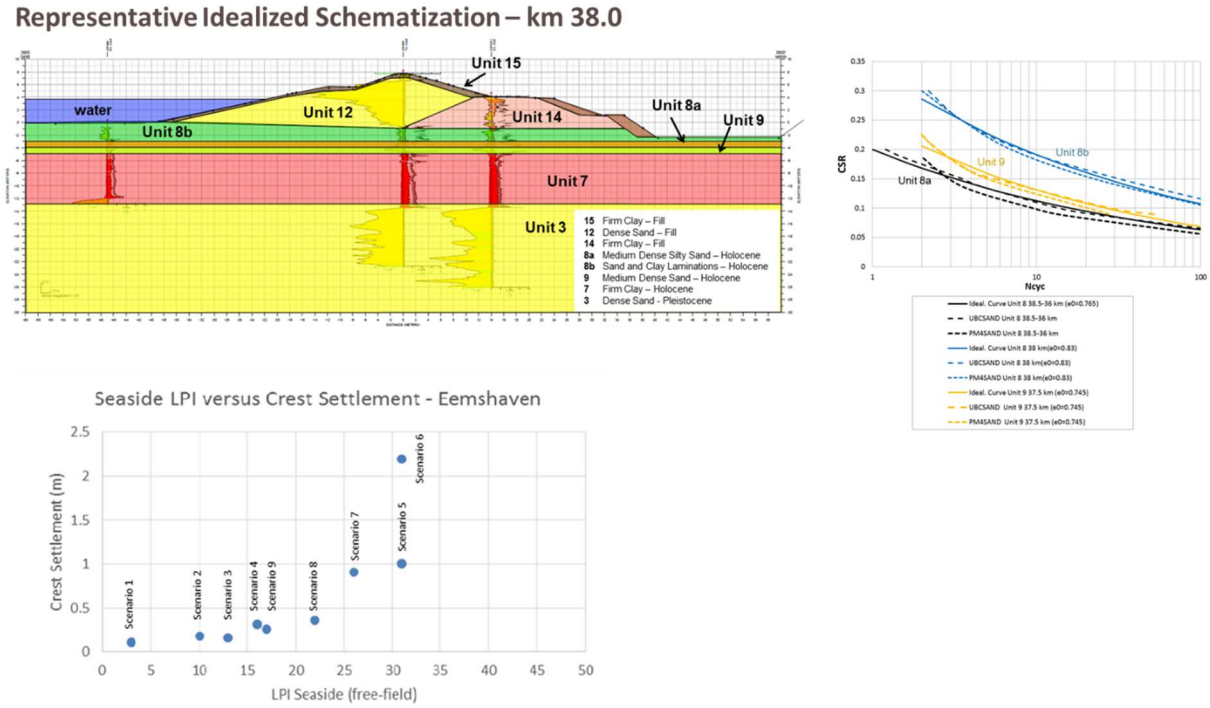

Figure 15. Example of levee crest settlement versus LPI estimated from dynamic numerical evaluations for the Eemshaven primary levee (Kolk et al 2017).

3.4.5 Results

CPTs along the Friesland primary levee were analyzed using the procedures described above. Figure 16 shows the estimated LPI values along the levee. The analyses showed that LPI values are

either equal to zero or have very close to it for the vast majority of the CPTs analyzed with couple of exceptions where the LPI values are about 0.7, which is still a very low value.

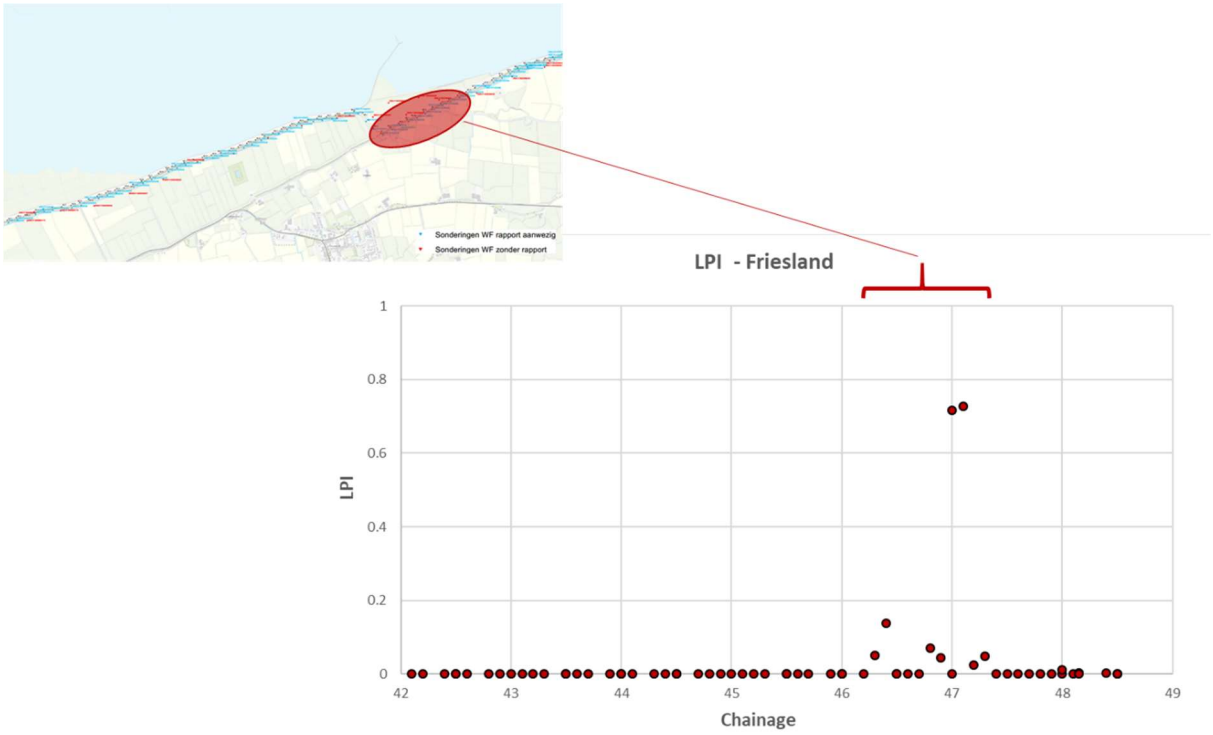

Figure 16. Estimated LPI values along Friesland levee.

Figures 17 and 18 present typical results for a CPT with LPI=0 and a CPT with the maximum estimated LPI value of 0.73. On these figures the tip resistance is shown as a black line on the first graph. The area between the CPT measured tip resistance and the CPT axis is colored according to the zones of Robertson (1990) classification chart shown on Figures 19. Also shown on each plot is the estimated tip resistance that would be required (based on the Green et al 2018 procedure) to achieve a factor of safety of 1.0 for the assumed earthquake scenario. In general, layers and zones where the tip resistance required to preclude the occurrence of liquefaction (i.e. resulting in FS of 1) is larger than the measured tip resistance are considered liquefiable. Where the resistance required to prevent liquefaction is larger than the measured resistance, the zone that represents the deficiency is shaded blue. In the second graph the friction ratio is presented. The third graph presents soil behavior index (I_c) with a black line and the zones of Robertson (1990) classification chart. In the fourth graph the calculated CSR and CRR values are plotted and the fifth graph shows the factor of safety at each depth with black dots. At depths where the estimated FoS is greater than 4, we assign the value 4, so that it plots within the limits of this graph.

Results from liquefaction evaluation analyses of all CPT data are presented in Appendix B.

The liquefaction triggering evaluation results indicate that the liquefaction triggering potential of the sandy materials underlying the Friesland primary levee is low.

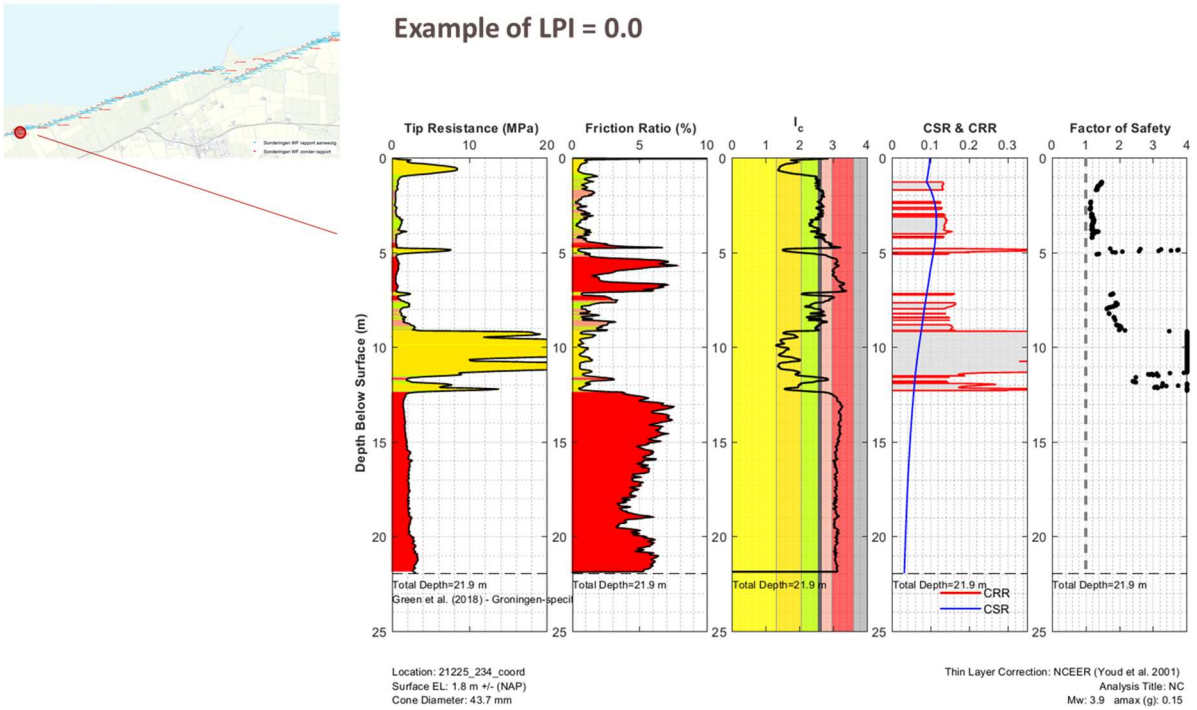

Figure 17. Example CPT liquefaction triggering log for a CPT with LPI=0.

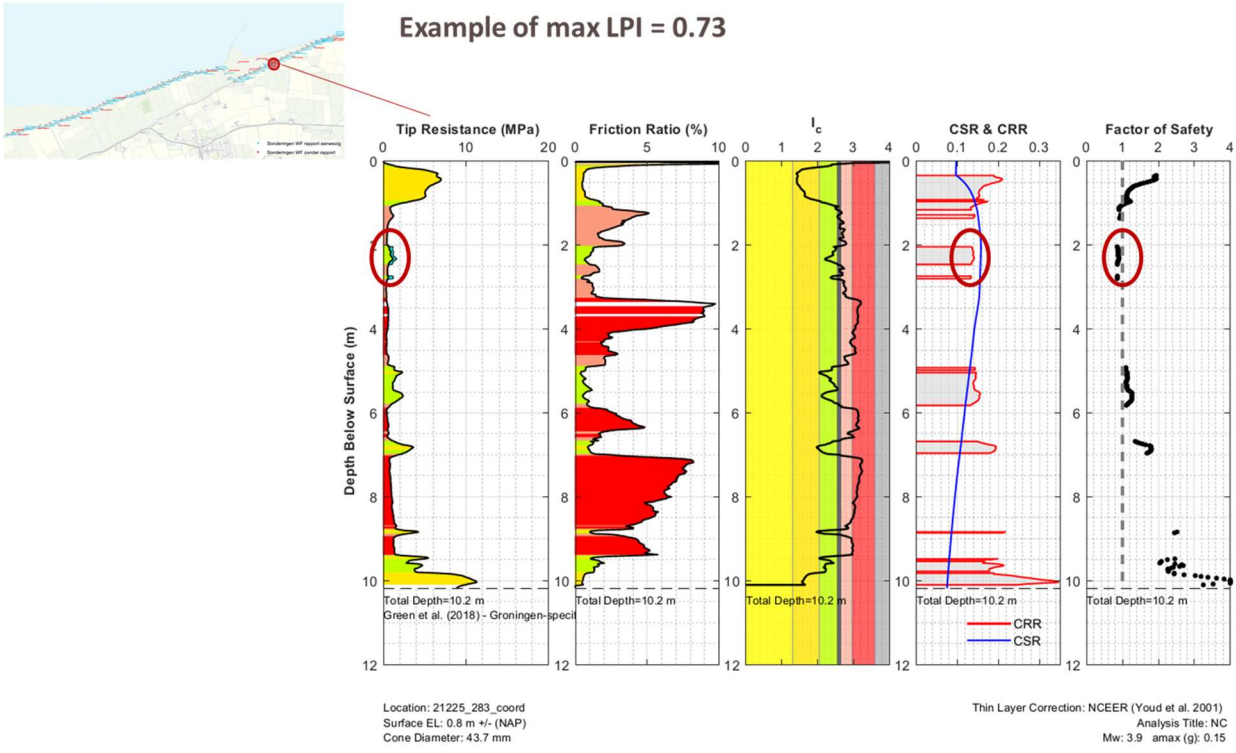

Figure 18. Example CPT liquefaction triggering log for a CPT with LPI=0.73.

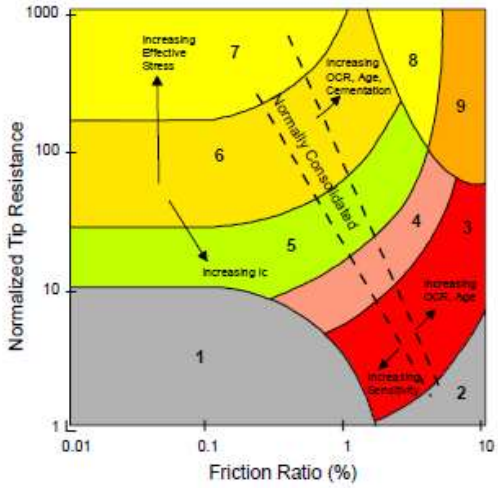

Zone	Soil Behavior Type
1	Sensitive Fine-grained
2	Peats
3	Silty Clay to Clay
4	Clayey Silt to Silty Clay
5	Silty Sand to Sandy Silt
6	Clean Sand to Silty Sand
7	Gravelly Sand to Dense Sand
8	Very Stiff Sand to Clayey Sand*
9	Very Stiff Fine-Grained*

*heavily overconsolidated or cemented

Figure 19. Robertson (1990) Classification Chart.

3.5 EVALUATION OF CYCLIC SOFTENING POTENTIAL OF FINE-GRAINED DEPOSITS

To evaluate the potential presence of soft clay layers along the levee, we estimate the undrained shear strength (Su) of the fine-grained layers from all the CPTs available using an N_k factor of 15. Figure 20 presents the Su values that are estimated to be below 40 kPa (red dots) and 20 kPa (black circles). As shown on this figure relatively soft clay layers with Su<20kPa are present under the levee.

For the evaluation of cyclic softening potential of fine-grained deposits a similar approach as the one adopted for the Eemskanaal levee was adopted (Georgarakos et al 2017). According to this approach the Factor of Safety against cyclic softening proposed by Idriss and Boulanger (2008) is first calculated for the Holocene soft clay layers according to the following expression:

$$\mathrm{FS} = \frac{CRR_M}{CSR_M}$$

where $CSR_M = \mathbf{0.65}\ \frac{\tau_{peak}}{\sigma'_{vc}}$ is the cyclic shear stress ratio, and

$CRR_M = \mathbf{0.80}\ \frac{s_u}{\sigma'_{vc}}\ \boldsymbol{MSF\ K_a}$ is the cyclic resistance ratio of the soil.

MSF is the magnitude scaling factor and K_a is a static shear stress correction factor (Idriss and Boulanger 2008). Then, the FS values within the Holocene fine-grained deposits are integrated to take into account both the thickness and the degree of potential softening of the soft soil, resulting in a scalar measure that is referred to as Cyclic Softening Potential Index (CSPI). This index is intended to be an approximate soft clay analogue of Liquefaction Potential Index (LPI).

$$CSPI = \int_0^{H_{holocene}} (1 - FS)\, dz$$

The estimated CSPI values along the Friesland levee are shown on Figure 21 (left plot). As shown on this figure the CSPI values are 0 for the majority of the CPTs (indicating lack of softening potential under the design event) with the exception of 1 CPT with a CSPI value of 0.5 which is still

low. For comparison the estimated CSPI values along Eemshaven-Delfzijl levees are plotted on the right plot of Figure 21 which show higher values of up to 3 (which are still associated with low levee deformations).

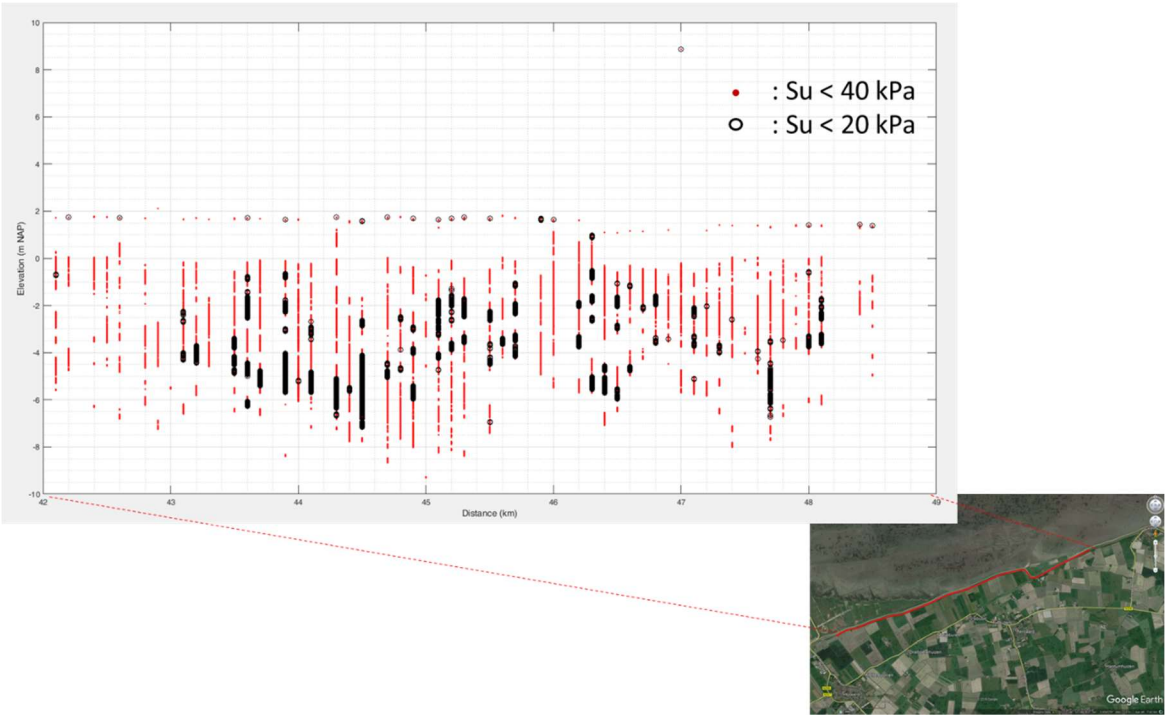

Figure 20. Estimated Su values for all the CPTs along the. Red dots correspond to S_u less than 40 kPa, and black circles correspond to S_u less than 20 kPa.

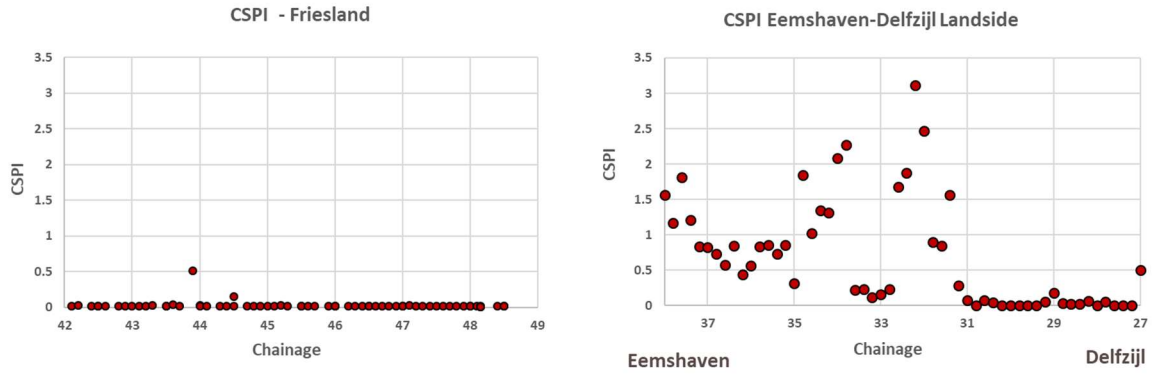

Figure 21. Estimated CSPI values along Friesland (left) and Eemshaven-Delfzijl (right) levee.

4.0 SUMMARY AND CONCLUSIONS

As part of the Environmental Impact Assessment Study for the Ternaard gas field development NAM is estimating the risks for major infrastructure such as the primary levee due to potential gas-extraction induced seismic activity.

Deterministic seismic hazard assessment (DSHA) were performed to develop estimates of seismic demand at the Friesland gas field that were then compared to the levels of seismic demand used in the dynamic levee stability evaluations for the Segment 6-6 primary levee in Groningen gas field near Eemshaven, which has the same allowable annual probability of flooding as the primary levee north of Ternaard (i.e. 1/1000). The relative seismic demands and the performance estimates from the previously studied Eemshaven-Delfzijl levee near Groningen were used as indicators of the Friesland primary levee deformation potential.

4.1 DETERMINISTIC SEISMIC HAZARD ANALYSES

The seismic demand was estimated at a stiff soil horizon level located near the top of Pleistocene deposits (about El. -10 m NAP) and was compared to the acceleration response spectrum used as input at the base of the numerical models in the dynamic stability evaluations for Eemshaven levee (about El. -30 NAP).

A review of regional geologic models from Dinoloket showed that roughly the same sequence of geologic units is encountered in Friesland and in Groningen gas fields although the thicknesses of the individual formations vary between the two fields along the primary levees. Estimates of reference bedrock horizontal acceleration response spectra were developed using four GMPEs (Groningen v5 GMM by Bommer et al. 2018 with a weight of 0.6; Abrahamson et al. 2014 NGA West-2 with a weight of 0.2; Atkinson 2015 with a weight of 0.1; and Douglas et al. 2013 with a weight of 0.1) for a deterministic scenario of Mw=3.9, R=3 km. Maximum magnitude, M_{max}, estimates were developed by NAM following the guidelines outlined by the State Supervision of Mines (2016).

Similar to the v5 GMM (Bommer et al. 2018) the bottom of the North Sea supergroup (NS_B) was selected as reference bedrock with an assumed Vs30 of 1400 m/s. For the Atkinson (2015) and Douglas (2013) GMPEs that only provide spectral accelerations for Vs30 values of 760 m/s and 1100 m/s, respectively, the linear site amplification function term by Boore et al. (2014) was used to adjust the GMPEs to a common reference V_{s30} of 1400 m/s. Due to the largely similar geologic units encountered above 800 meters depth between Groningen and Friesland the v5 GMM nonlinear site amplification function was used to estimate horizontal acceleration response spectra at the top of Pleistocene (Vs30 ~ 260 m/s, Zone 308 from v5 GMM)

The input seismic demand in the Eemshaven primary levee stability assessment was derived from probabilistic seismic hazard analyses using the v2 GMM (Bommer 2016) and was associated with an 1100-year return period. In the deterministic approach adopted for the seismic demand at the Friesland field, estimates of spectral accelerations resulting from a maximum magnitude event are derived as a function of the number of standard deviations from the median prediction. In order to assess what is a reasonably “conservative” value or range of values to be compared with the Eemshaven-Delfzijl levee demands, a deterministic seismic hazard analyses was performed using the v5 GMM (Bommer 2018) and an earthquake scenario with magnitude M_w 5 at a distance of 10 km, which corresponds to the controlling scenario based on PSHA deagreggation results at the Eemshaven levee location with the v2 GMM. Based on this the median plus one and median plus two sigma

spectral acceleration values were found to provide a reasonably “conservative” range of values to be compared with the Eemshaven-Delfzijl levee demands.

Analyses results indicated that the estimated seismic demand at Friesland for predictions of up to 2 standard deviations above the median is considerably smaller than the input seismic demand used in the dynamic stability evaluations of the Eemshaven levee in the period range of interest (i.e. about 0.7 s).

4.2 EVALUATION OF PRIMARY LEVEE DEFORMATION POTENTIAL

Available site-specific geotechnical data at the primary levee near Teenaard were used to perform screening level assessments of strength loss of the underlying Holocene deposits and the performance estimates from the previously studied Eemshaven-Delfzijl levee in Groningen gas field (Fugro 2017) were used as indicators of the Friesland primary levee deformation potential.

Liquefaction triggering evaluations of coarse-grained deposits underlying the Friesland primary levee were performed using the same screening methodology developed and applied in the Eemshaven-Delfzijl levee (Expert Panel, 2016), the deterministic seismic hazard estimate for the median plus 2 standard deviations prediction and also considering the Groningen-specific Green et al (2018) simplified triggering procedure that has also been adopted in the current NPR9998 guidelines. Results indicate very low liquefaction triggering potential of the sandy materials present at the area. This is also indicated by the very low LPI values estimated (0 for most cases and less than 0.8 for all the CPTs analyzed).

As part of the analyses performed for the Eemshaven-Delfzijl levee to establish a relationship between LPI and levee deformations, it was found that for LPI values less than ~5 crest settlements are expected to be small and no further analyses was warranted (Expert Panel 2016; Kolk et al 2017).

In addition, for the evaluation of cyclic softening potential of fine-grained deposits underlying the levee a similar approach as the one adopted for the Eemskanaal levee was used (Georgarakos et al 2017) through the estimation of the Cyclic Softening Potential Index (CSPI). The estimated CSPI values along Friesland levee are 0 or close to 0 indicating low potential for cyclic softening of fine-grained deposits.

Based on the above it appears that the deformation potential of the Friesland primary levee for a scenario earthquake of M_w 3.9 is low and no further analyses are warranted.

5.0 REFERENCES

Abrahamson N.A., Silva W.J., Kamai R. 2014, "Summary of the ASK14 ground motion relation for active crustal regions", Earthquake Spectra, Vol 30, No 3, pp 1025-1055

Andrus, R.D., Mohanan, N.P., Piratheepan, P., Ellis, B.S., and Holzer, T.L. (2007) "Predicting shear-wave velocity from cone penetration resistance", Proc., 4th Inter. Conf. on Earthq. Geotech. Eng., Thessaloniki, Greece

Atkinson (2015), "Ground-Motion Prediction Equation for Small-to-Moderate Events at Short Hypocentral Distances, with Application to Induced-Seismicity Hazards", Bull. Seism. Soc. Am. 105(2A), pp. 981-992.

Bommer, J.J., Edwards B., Kruiver P.P., Rodriguez-Marek A., Stafford P.J., Dost B., Ntinalexis M., Ruigrok E. B., and Spetzler J (2018) "V5 Ground-Motion Model (GMM) for the Groningen Field", March.

Bommer, J.J., Dost, B., Edwards, B., Stafford, P.J., van Elk, J., Doornhof, D. & Ntinalexis, M., (2016). Developing an application-specific ground motion model for induced seismicity. Bulletin of the Seismological Society of America 106: 158–173.

Bommer, J.J., P.J. Stafford, B. Edwards, B. Dost, E. van Dedem, A. Rodriguez-Marek, P. Kruiver, J. van Elk, D. Doornhof & M. Ntinalexis (2017). Framework for a ground-motion model for induced seismic hazard and risk analysis in the Groningen gas field, The Netherlands. Earthquake Spectra 33(2), 481-498.

Boulanger, R. W., and Idriss, I. M. (2014) CPT and SPT Based Liquefaction Triggering Procedures, Report no. UCD/CGM-14/01, University of California, Davis, CA, 138 pp.

Bourne, SJ, SJ Oates, J. van Elk, and D. Doornhof (2014), A seismological model for earthquakes induced by fluid extraction from a subsurface reservoir , J. Geophys. Res. 119 (2), 8991-9015, doi: 10.1002 / 2014JB011663. Hanks, T., and H. Kanamori (1979), Moment magnitude scale , J. Geophys. Res. 84, 2348-2350.

Boore, D.M., Stewart J.P., Seyhan E. and Atkinson G.M. (2014), "NGA-West2 Equations for Predicting PGA, PGV, and 5% Damped PSA for Shallow Crustal Earthquakes", Earthquake Spectra 30(3), pp. 1057-1085.

Bozorgnia Y., Abrahamson N.A., Al Atik L., Ancheta T.D., Atkinson G.M., Baker J.W., Baltay A., Boore D.M., Campbell K.W., Chiou B.S.J., Darragh R., Day S., Donahue J., Graves R.W., Gregor N., Hanks T., Idriss I.M., Kamai R., Kishida T., Kottke A., Mahin S.A., Rezaeian S., Rowshandel B., Seyhan E., Shahi S., Shantz T., Silva W., Spudich P., Stewart J.P., Watson-Lamprey J., Wooddell K., Youngs R., 2014, "NGA-West2 Research Project", Earthquake Spectra, Volume 30, No. 3, pages 973-987.

Chiou B.S.J., and Youngs R.R., 2014, "Update of the Chiou and Youngs NGA Model for the Average Horizontal Component of Peak Ground Motion and Response Spectra", Earthquake Spectra, Vol. 30, No 3, pp 1117-1153.

Douglas, J., Edwards B., Convertito V., Sharma N., Tramelli A., Kraaijpoel D., Mena Cabrera B., Maercklin N. and Troise C. (2013), "Predicting ground motion from induced earthquakes in geothermal areas", Bull. Seismol. Soc. Am. 103(3), pp. 1875–1897.

Expert Panel, 2016. Expert Panel Report, 2 December 2016. Letter addressed to E. van Dijk by Chacko, J. Green, R.A. Kramer, S.L. Towhata, I

Farhadi, A., Pezeshk S., and Khoshnevis N. (2018). Assessing the applicability of ground-motion models for induced seismicity application in central and eastern North America, Bull. Seismol. Soc. Am. 108, no. 4, 2265–2277.

Fugro (2017) Evaluation of Dynamic Stability Using Code Calibrated Design Parameters Eemshaven-Delfzijl Levee The Netherlands, March

Georgarakos P., Drosos V., Tsiaousi D., Dean C., Giannakou A. and Chacko J. (2017) Proposed Screening Methodology for the Identification of Critical Cross-sections along the Eemskanaal Levee, project memorandum prepared for NAM, dated July 31st 2017

Green R.A., Bommer J.J., Stafford P.J., Maurer B.W.,Edwards B.,Kruiver P.P.,Rodriguez-Marek A., de Lange G., Oates S.J., Storck T., Omidi P., Bourne S.J., and van Elk J. 2018. Liquefaction Hazard Pi-lot Study for the Groningen Region of the Netherlands due to Induced Seismicity, prepared for NAM

Jongejan R., Chacko J., Giannakou A., Drosos V., Tasiopoulou P. (2017) Code calibration for coupled, effective stress FEM-assessments of the primary flood defenses at Eemshaven-Delfzijl, Final Report, 28 February

Idriss, I. M., and Boulanger, R. W., (2008), “Soil liquefaction during earthquakes”, Monograph MNO-12, Earthquake Engineering Research Institute, Oakland, CA

Iwasaki, T., Tokida, K., Tatsuko, F., and Yasuda, S.(1978) “A practical method for assessing soil liquefaction potential based on case studies at various sites in Japan, Proceedings of 2nd International Conference on Microzonation, San Francisco, p.885–896.

Kanamori, H. (2001), Energy budget of earthquakes and seismic efficiency , in Earthquake Thermodynamics and Phase Transformations in the Earth's Interior, edited by R. Teisseyre, pp. 293-305, Academic, Wlatham, Mass.

Kolk B., Coelho B., Venmans A., and Giannakou A. (2017) LPI screening for the Eemshaven-Delfzijl levee, prepared for NAM, March

Kraaijpoel, D., and Dost, B., 2013. Implications of salt-related propagation and mode conversion effects on the analysis of induced seismicity, Journal of Seismology 17(1), 95-107.

Kruiver, P. P., E. van Dedem, E. Romijn, G. de Lange, M. Korff, J. Stafleu, J.L. Gunnink., A. Rodriguez-Marek, J.J. Bommer, J. van Elk & D. Doornhof (2017). An integrated shear-wave velocity model for the Groningen gas field, The Netherlands. Bulletin of Earthquake Engineering 15(9), 3555-3580.

Kostrov, VV (1974), Seismic moment and energy or earthquakes and seismic flow of rocks , Izv. Acad. Sci. USSR Phys. Solid Earth, Eng. Transl., 1, 23-44.

Mayne, P.W., and Rix, G.J. (1993), "Gmax-qc Relationships for Clays," Geotechnical Testing Journal, ASTM, Vol. 16, No. 1, pp. 54-60.

Mayne, PW, and Rix, G.J. (1995) “Correlations between shear wave velocity and cone tip resistance in natural clays”, Soils and Foundations, 35(2), pp. 107–110

Rix, G.J., and Stokoe, K.H. (1991) “Correlations of initial Tangent Modulus and Cone Penetration Resistance”, Proc. International Symposium on Calibration Chamber Testing, Huang A.B., Ed., Elsevier Publishing, New York, pp. 351-362

Robertson, P.K. (2009) “Interpretation of cone penetration tests – a unified approach”, Canadian Geotech. J., 46(11), pp. 1337–1355

Robertson, P.K. (1990). Soil classification using the cone penetration test. Canadian Geotechnical J. 27(1), 151–58.

State Supervision of Mines (2016) Methodiek voor risicoanalyse omtrent geïnduceerde bevingen door gaswinning, tijdelijke leidraad voor adressering MBB. 24.1.P, versie 1.2, February 1st (in Dutch)

Youd, T. L., Idriss, I. M., Andrus, R. D., Arango, I., Castro, G., Christian, J. T., Dobry, R., Finn, W. D. L., Harder, L. F., Hynes, M. E., Ishihara, K., Koester, J. P., Liao, S. S. C., Marcuson, W. F., Martin, G. R., Mitchell, J. K., Moriwaki, Y., Power, M. S., Robertson, P. K., Seed, R. B., and Stokoe, K. H. (2001). Liquefaction resistance of soils: summary report from the 1996 NCEER and 1998 NCEER/NSF workshops on evaluation of liquefaction resistance of soils, J. Geotechnical and Geoenvironmental Eng., ASCE 127(10), 817–33.

APPENDIX A

LONGITUDINAL GEOTECHNICAL CROSS SECTIONS

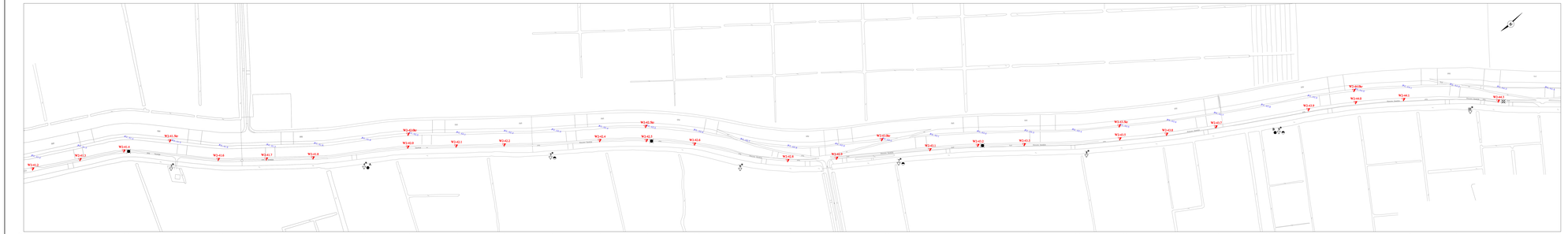

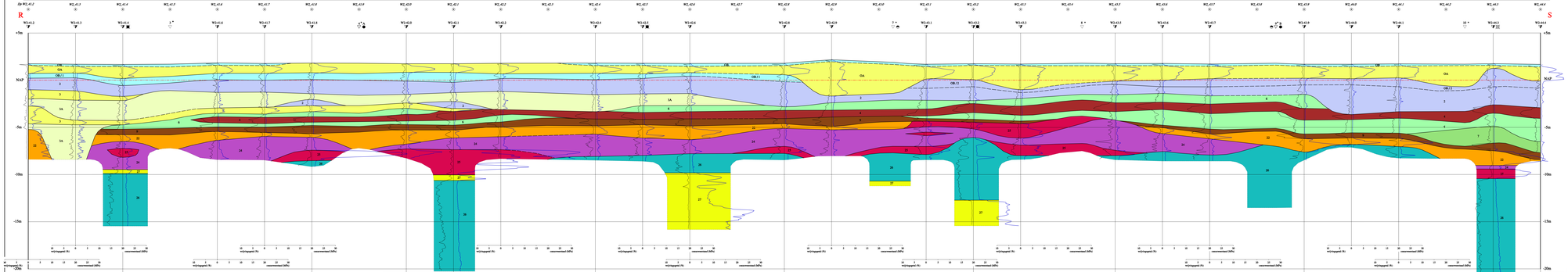

LITHOSTRATIGRAFISCHE LEGENDA				
4A	hoofdzakelijk veen	*Antropogene gronden*		HOLOCEEN
3B	hoofdzakelijk klei			
3C	hoofdzakelijk klei en zand			
1	klei, plaatselijk zandig vaak humeus	*Afzettingen van Duinkerke*	FORMATIE NIEUWKOOP	
2	klei, uiting tot sterk uiting, vaak met dunne zandlagen			
1-2	klei, zandig tot zand, kleirig			
5A	zand met kleilagen			
5B	zand, uiting tot kleirig vaak met veel kleilagen			
5	zand, plaatselijk met enkele kleilagen			
	veen	*Hollandveen*		
6	klei, uiting, vaak humeus	*Afzettingen van Calais*		
7	klei, uiting, vaak met veel zandlagen			
6-8	klei, zandig tot zand, kleirig			
8A	zand, fijn met silt, en kleilagen			
8	zand, plaatselijk enkele kleilagen			
	veen	*Basisveen*		
11	klei, uiting en zandig, vaak humeus (leem)	*FORMATIE VAN TWENTE*		PLEISTOCEEN
	veen			
10A	zand, fijn, matig keurig tot leem, zandig			
10	zand, plaatselijk humeus			
9	klei, zandig en grindig (keileem)	*FORMATIE VAN DRENTE*		
9A	zand, fijn, matig keurig			
9B	zand, zeerklei, plaatselijk grindig			
3A	klei, uiting (gelaagd)	*FORMATIE VAN PEELO*		
27	zand, fijn			

ALGEMENE LEGENDA	
	Middelvroeg sondering
	Middelvroeg boring
	Peilmeetbuis 20mm
	Peilmeetbuis 60mm
	Peilbuis
	Handboring
	Spitsmeetboring
	CO-B609

Schaal profiel: horizontaal 1:2000
verticaal 1:100

1 0 20 40 60 80 100m

Grens steenkar

KAARTBLAD 44 en 45 © Topografische Dienst Emmen SCHAAL 1:25.000

Adviseur:		datum:	2020-08-01
		CO-376710	
VEILIGHEIDSCORRIDOR WADDINGDIJKPOORT			
DIJKVAK 20 VEER OP AMELAND - 't SCHOOR			
GEOTECHNISCH PROFIEL R-S Dp WZ-41.2 tot Dp WZ-44.4		BIJL. G18	

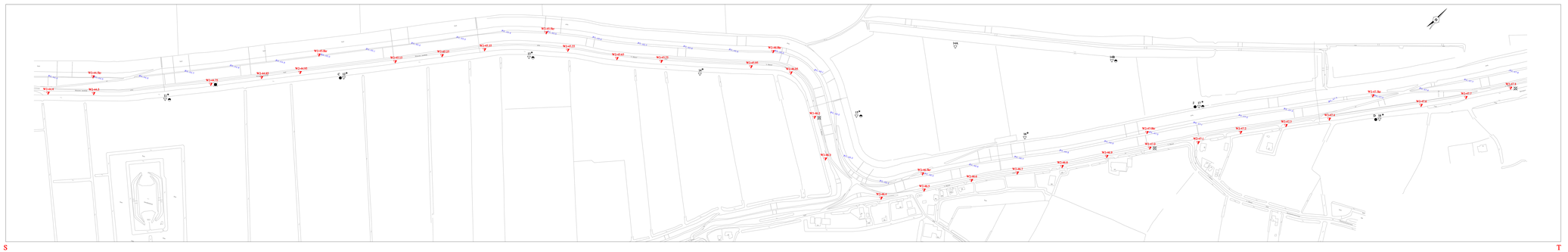

S

T

BINNENDIJKS

LITHOSTRATIGRAFISCHE LEGENDA

1A	hoofdzakelijk zand	*Astrupgroep grondtor*		HOLOCEEN
1B	hoofdzakelijk klei			
1C	hoofdzakelijk klei en zand			
1	klei, plaatselijk zandig; vaak humeus	*Afzettingen van Duinkerke*	*FORMATIE WESTLAND*	
1 - 3	klei, uiterlijk tot zand, kleiig			
1A	zand met kleilagen			
2	zand, uiterlijk tot kleiig; vaak met veel kleilagen			
3	zand, plaatselijk met enkele kleilagen			
	veen	*Hollandveen*		
4	klei, uiterlijk, vaak humeus	*Afzettingen van Calais*		
5	klei, uiterlijk, vaak met veel zandlagen			
4 - 5	klei, zandig tot zand, kleiig			
4A	zand, fijn met silt- en kleilagen			
5	zand, plaatselijk enkele kleilagen			
	veen	*Basisveen*		
6	klei, uiterlijk, vaak humeus	*FORMATIE VAN TWENTE*		PLEISTOCEEN
	veen			
6A	zand, fijn, vaak leemlagen			
7	zand, plaatselijk humeus			
8	klei, zandig en grindig (keileem)	*FORMATIE VAN DRENTE*		
8A	zand, fijn, vaak leemlagen			
9	zand, middel, plaatselijk grindig			
21	klei, uiterlijk (pekklei)	*FORMATIE VAN PEELO*		
27	zand, fijn			
27A	zand, uiterlijk tot kleiig			

ALGEMENE LEGENDA

- Middelzware sondering
- Zware sondering
- Begrenssondering 20mm
- Begrenssondering 40mm
- Peilbuizing
- Peilbuis
- Ophoogbelasting
- CO-0669

School profiel: horizontaal 1:2000
verticaal 1:100

0 100 150 200 250 300m
schaal meters

Cores steenkool

KAARTBLAD 5B en 5D

© Topografische Dienst Emmen

SCHAAL 1:25.000

Tekniek WIG 135 mm			
GeoDelft	Postbus 69, 2600 AB Delft Stieltjesweg 1, 2628 CK Delft	Telefoon (015) 269 30 00 Telefax (015) 261 06 72	Vervolgblad a=n, geschr.=n	datum 2000-08-01
VEILIGHEIDSCOFDIJKLING WADDENZEEDIJKEN DIJKVAK 20 EN 21 VEER OP AMELAND – WIERUM				CO-376710
GEOTECHNISCH PROFIEL S-T Dp W2-44.4 tot Dp W2-47.8				BIJL. G19

APPENDIX B

LIQUEFACTION TRIGGERING CPT LOGS

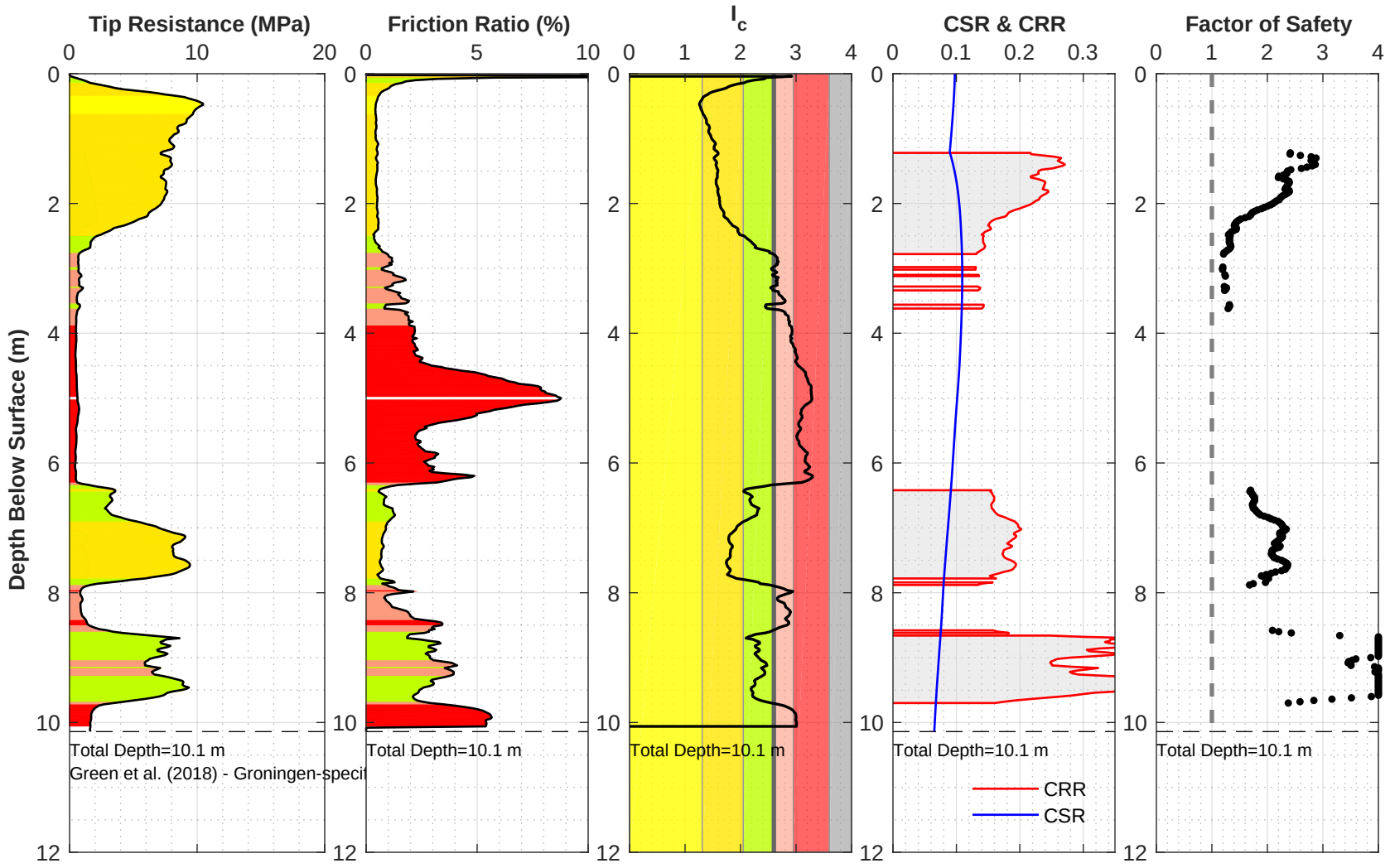

Location: 21225_245_coord
Surface EL: 1.7 m +/- (NAP)
Cone Diameter: 43.7 mm

Thin Layer Correction: NCEER (Youd et al. 2001)
Analysis Title: NC
Mw: 3.9 amax (g): 0.15

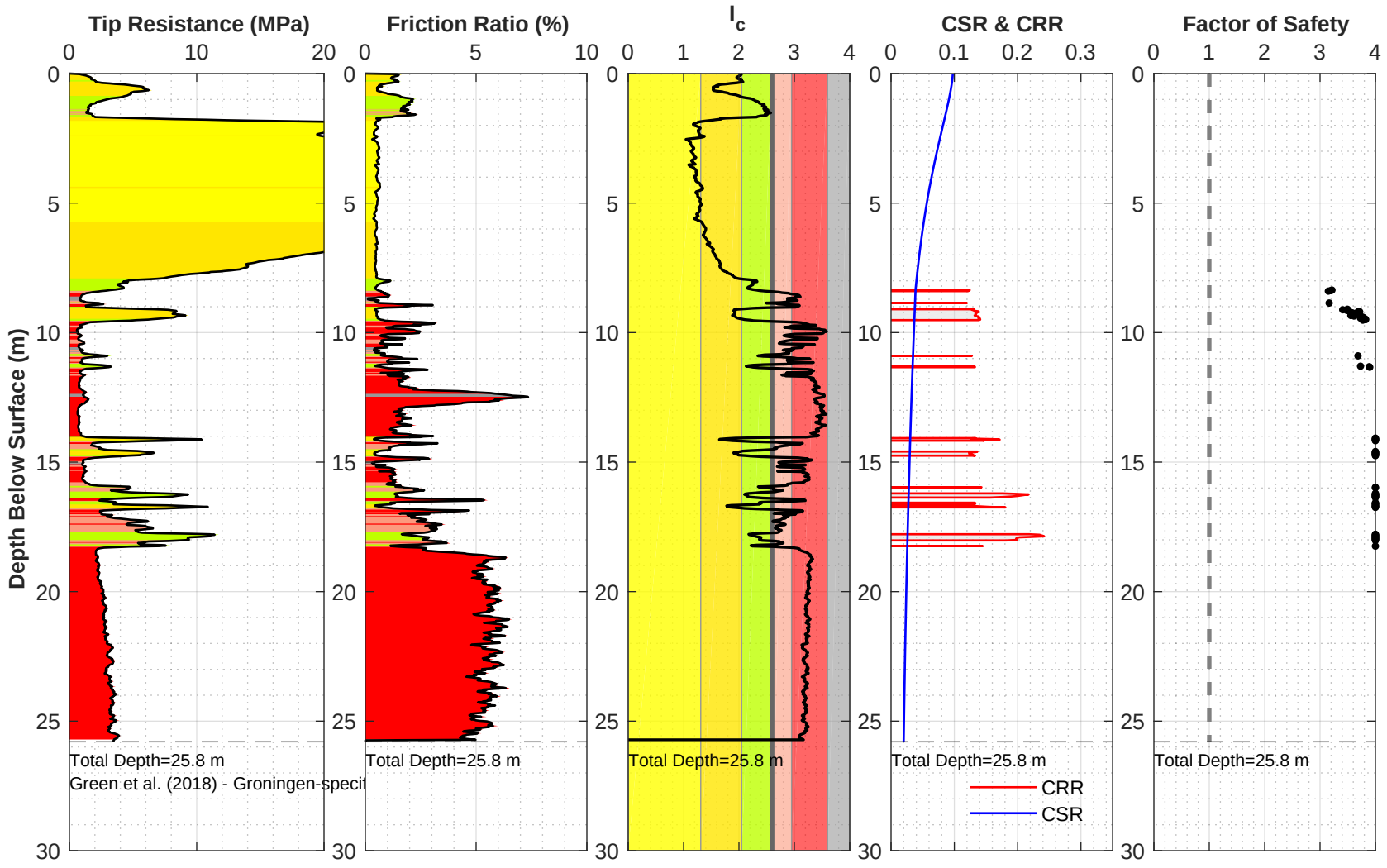

Location: 21225_246_coord
Surface EL: 8.9 m +/- (NAP)
Cone Diameter: 43.7 mm

Thin Layer Correction: NCEER (Youd et al. 2001)
Analysis Title: NC
Mw: 3.9 amax (g): 0.15

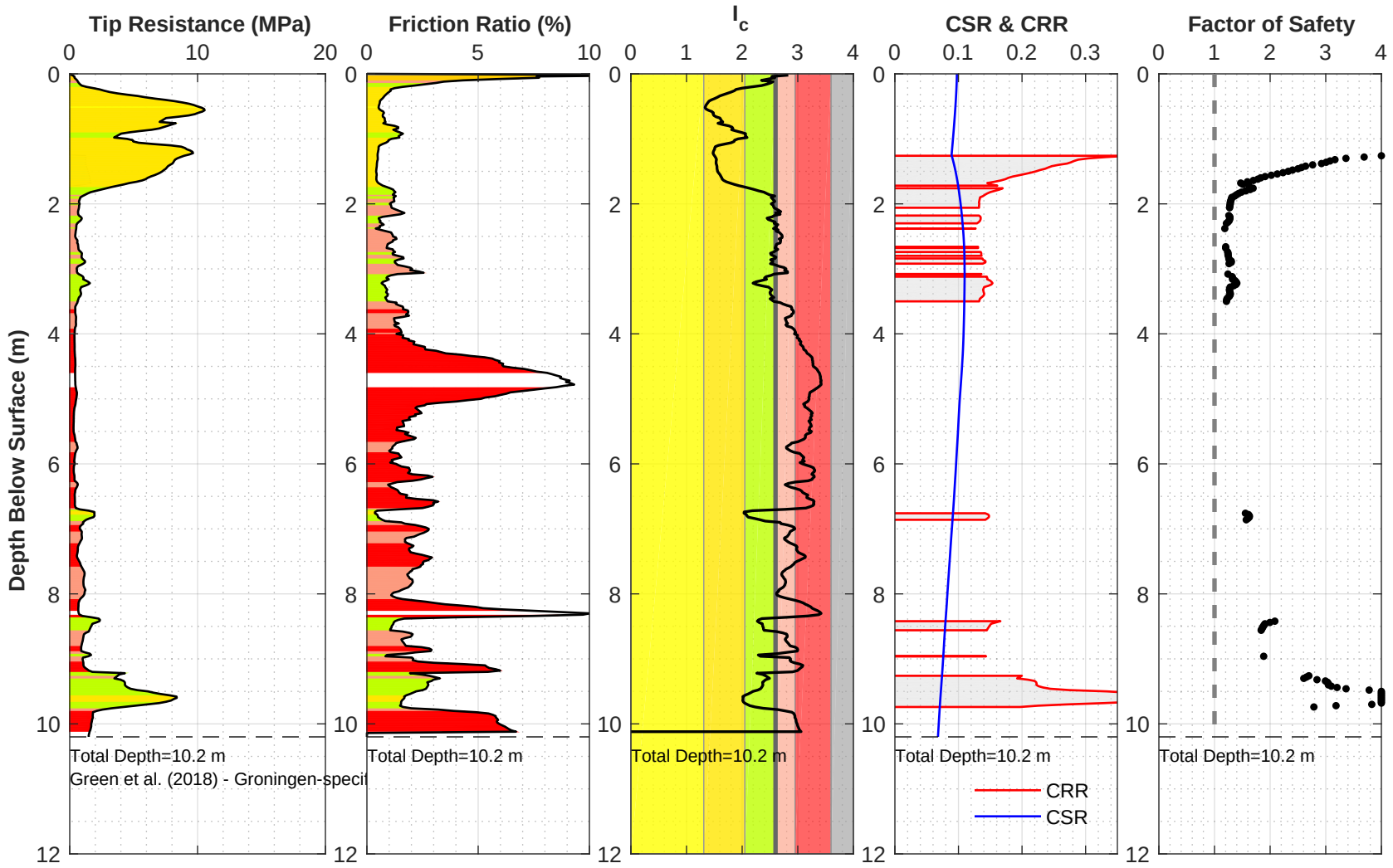

Location: 21225_247_coord
Surface EL: 1.8 m +/- (NAP)
Cone Diameter: 43.7 mm

Thin Layer Correction: NCEER (Youd et al. 2001)
Analysis Title: NC
Mw: 3.9 amax (g): 0.15

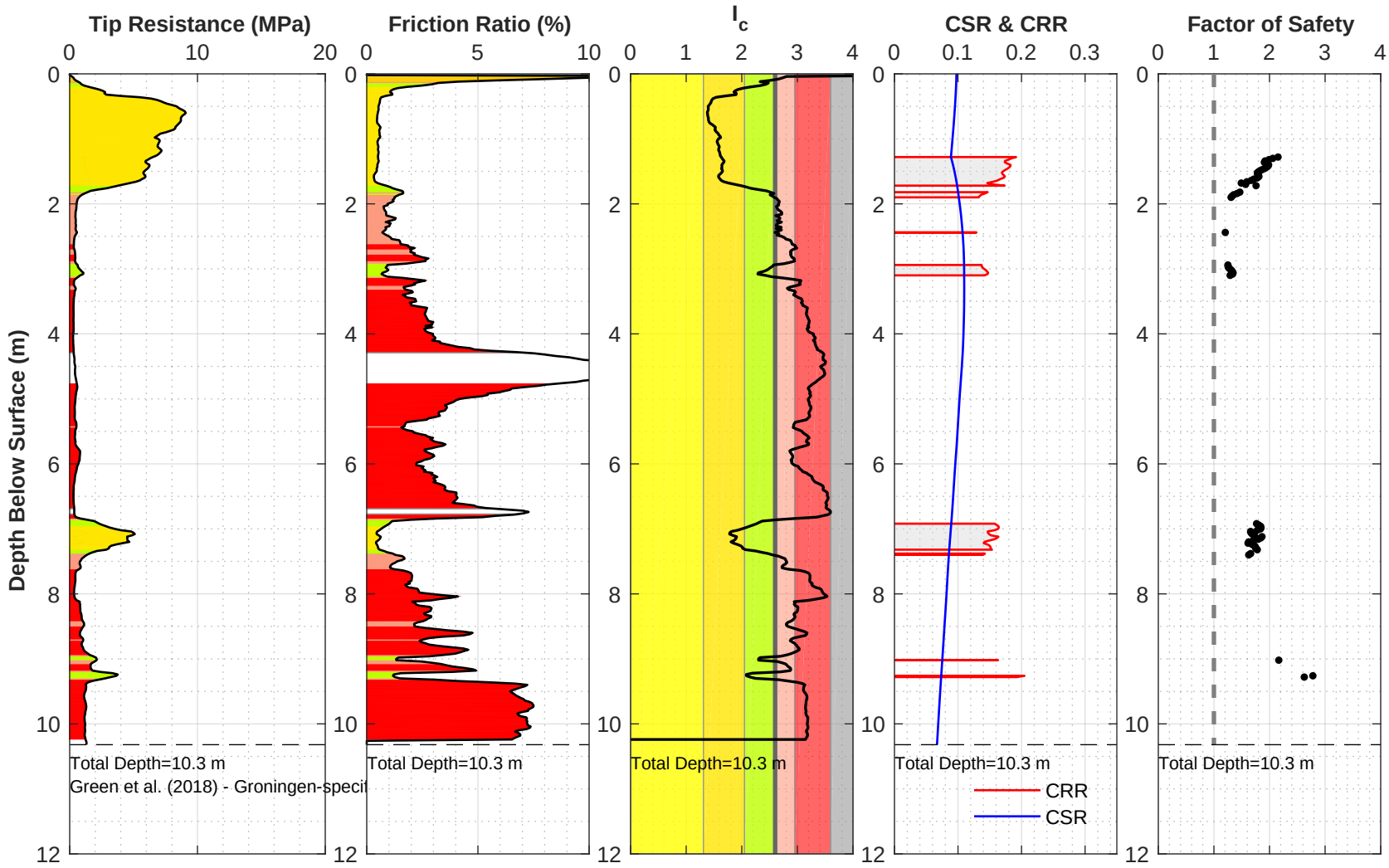

Location: 21225_248_coord
Surface EL: 1.8 m +/- (NAP)
Cone Diameter: 43.7 mm

Thin Layer Correction: NCEER (Youd et al. 2001)
Analysis Title: NC
Mw: 3.9 amax (g): 0.15

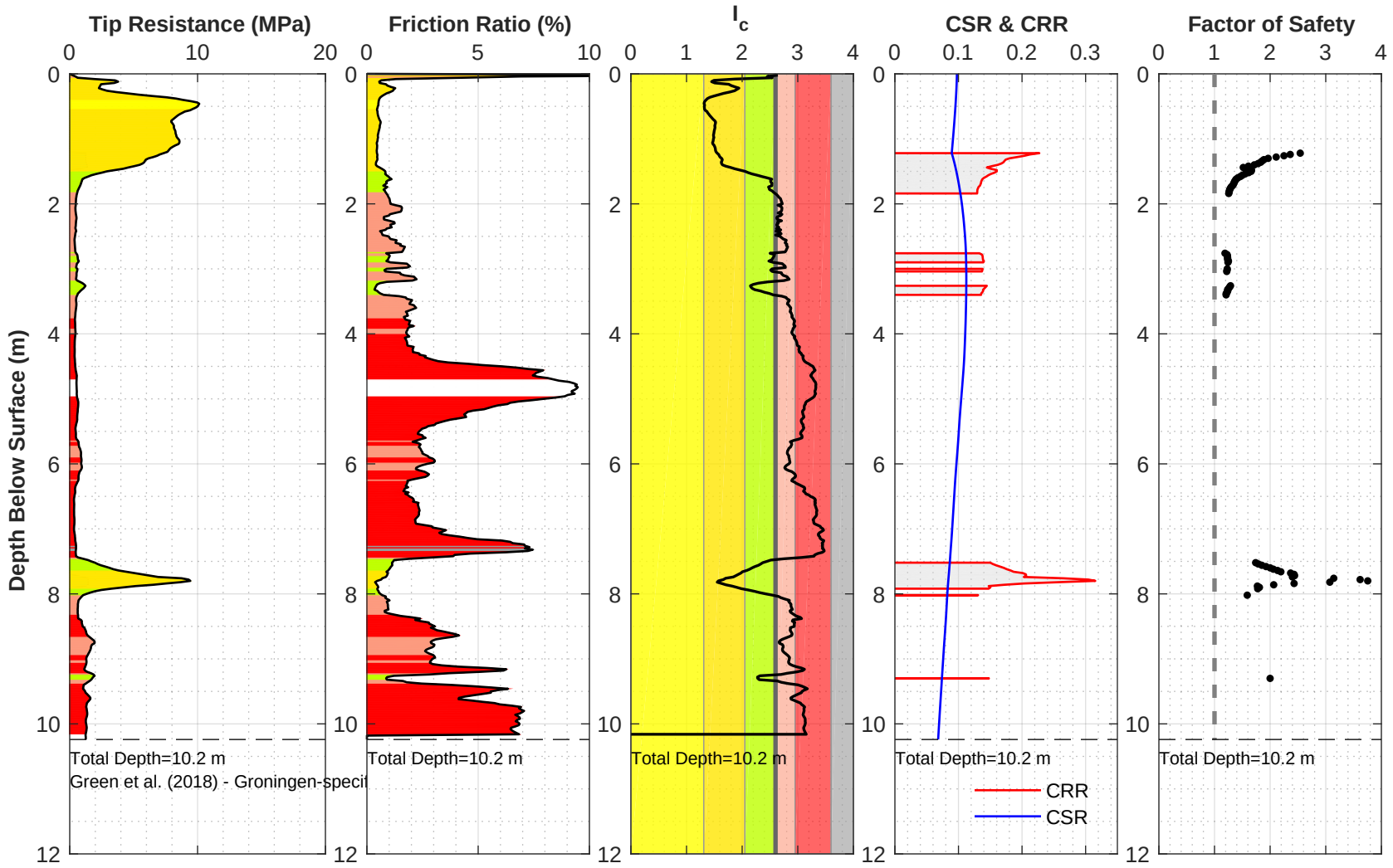

Location: 21225_249_coord
Surface EL: 1.7 m +/- (NAP)
Cone Diameter: 43.7 mm

Thin Layer Correction: NCEER (Youd et al. 2001)
Analysis Title: NC
Mw: 3.9 amax (g): 0.15

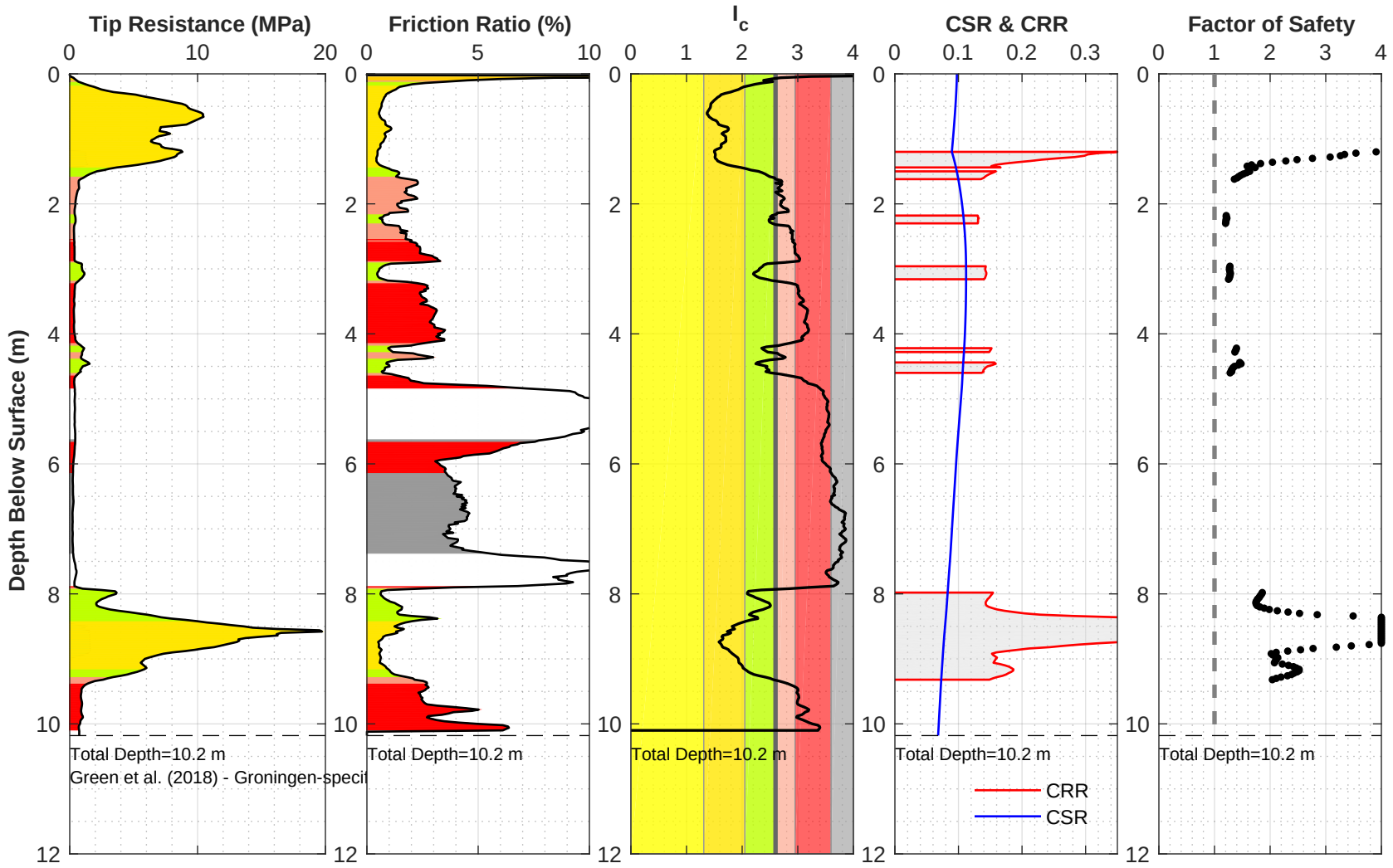

Location: 21225_250_coord
Surface EL: 1.7 m +/- (NAP)
Cone Diameter: 43.7 mm

Thin Layer Correction: NCEER (Youd et al. 2001)
Analysis Title: NC
Mw: 3.9 amax (g): 0.15

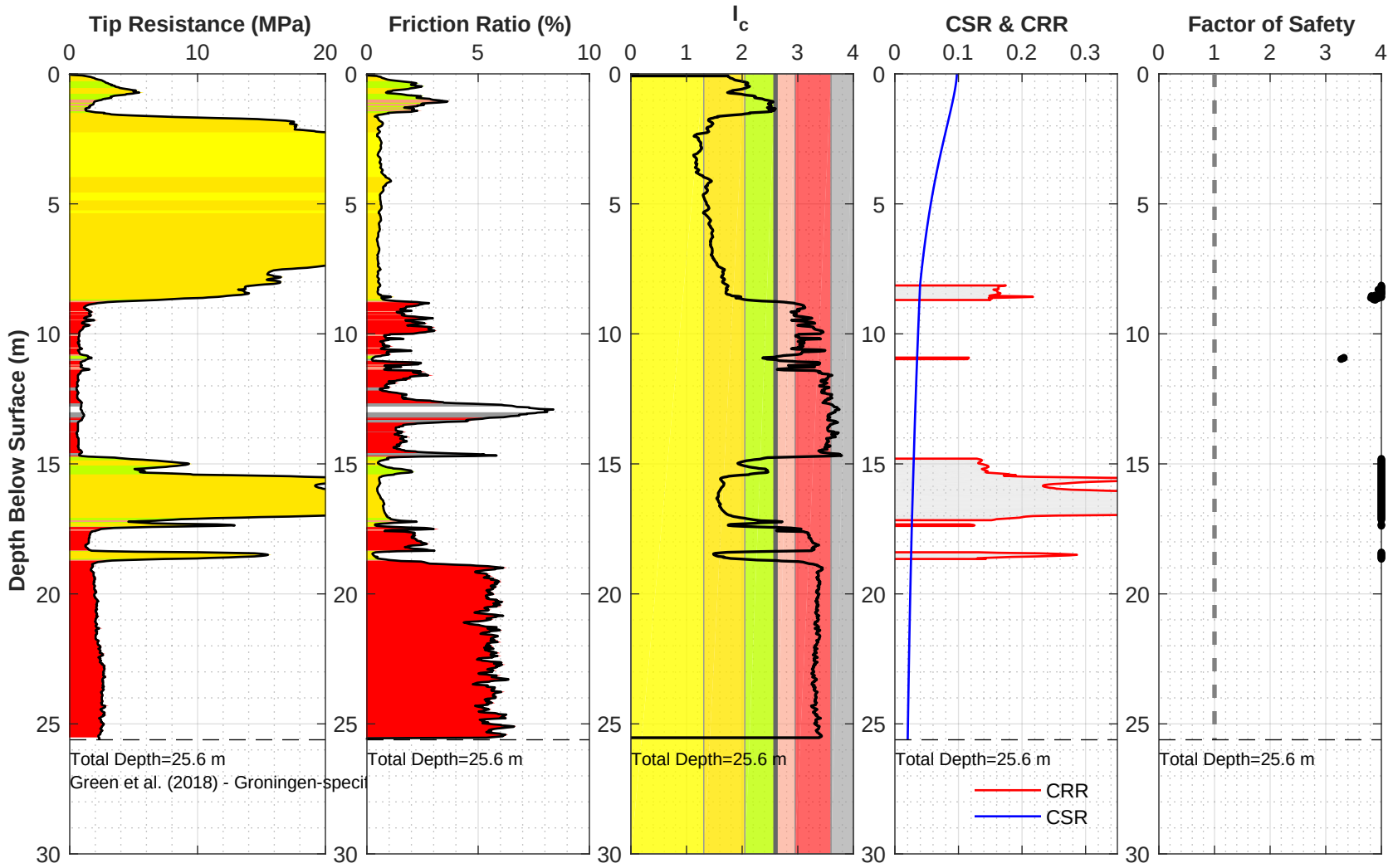

Location: 21225_251_coord
Surface EL: 8.6 m +/- (NAP)
Cone Diameter: 43.7 mm

Thin Layer Correction: NCEER (Youd et al. 2001)
Analysis Title: NC
Mw: 3.9 amax (g): 0.15

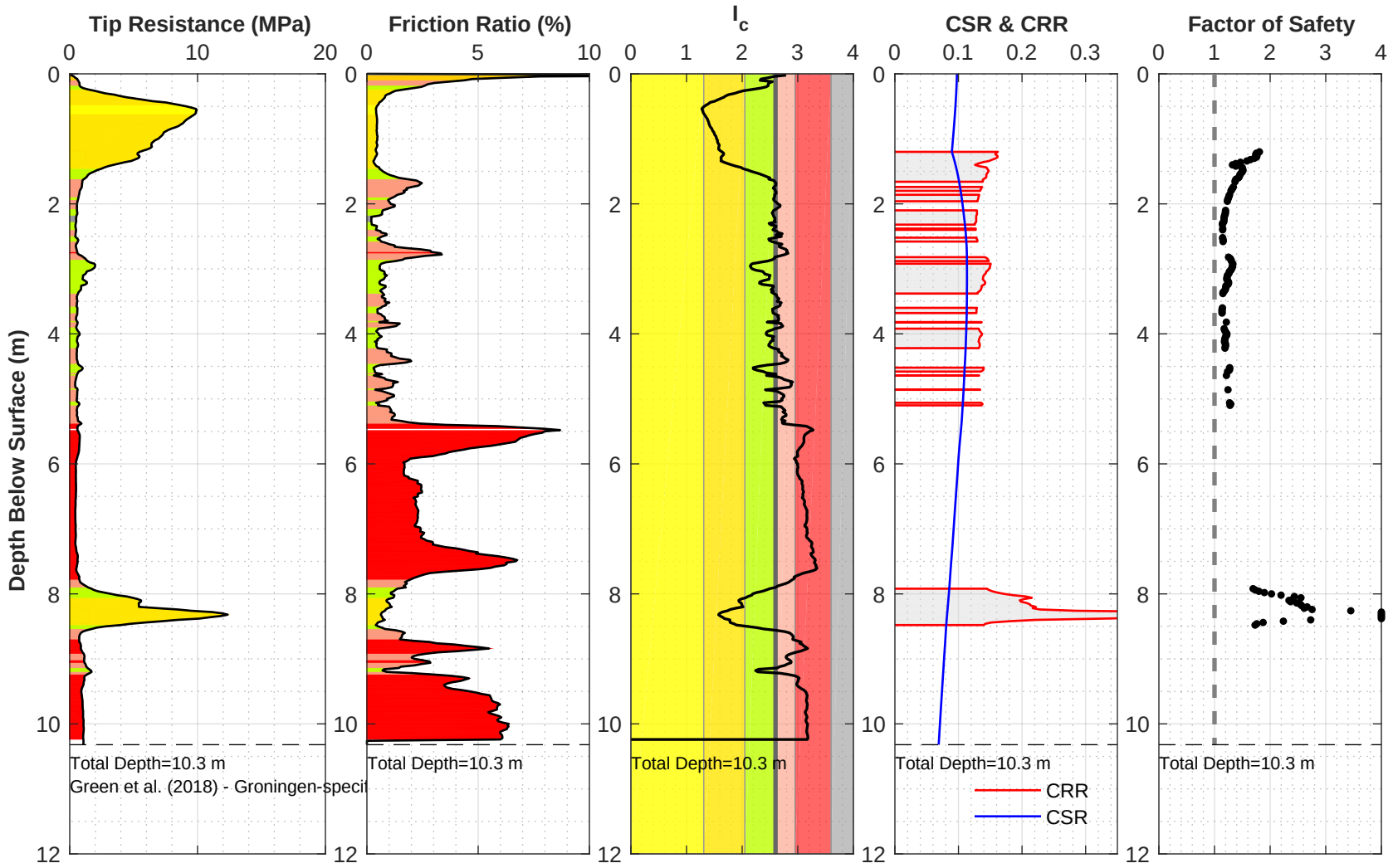

Location: 21225_252_coord
Surface EL: 1.7 m +/- (NAP)
Cone Diameter: 43.7 mm

Thin Layer Correction: NCEER (Youd et al. 2001)
Analysis Title: NC
Mw: 3.9 amax (g): 0.15

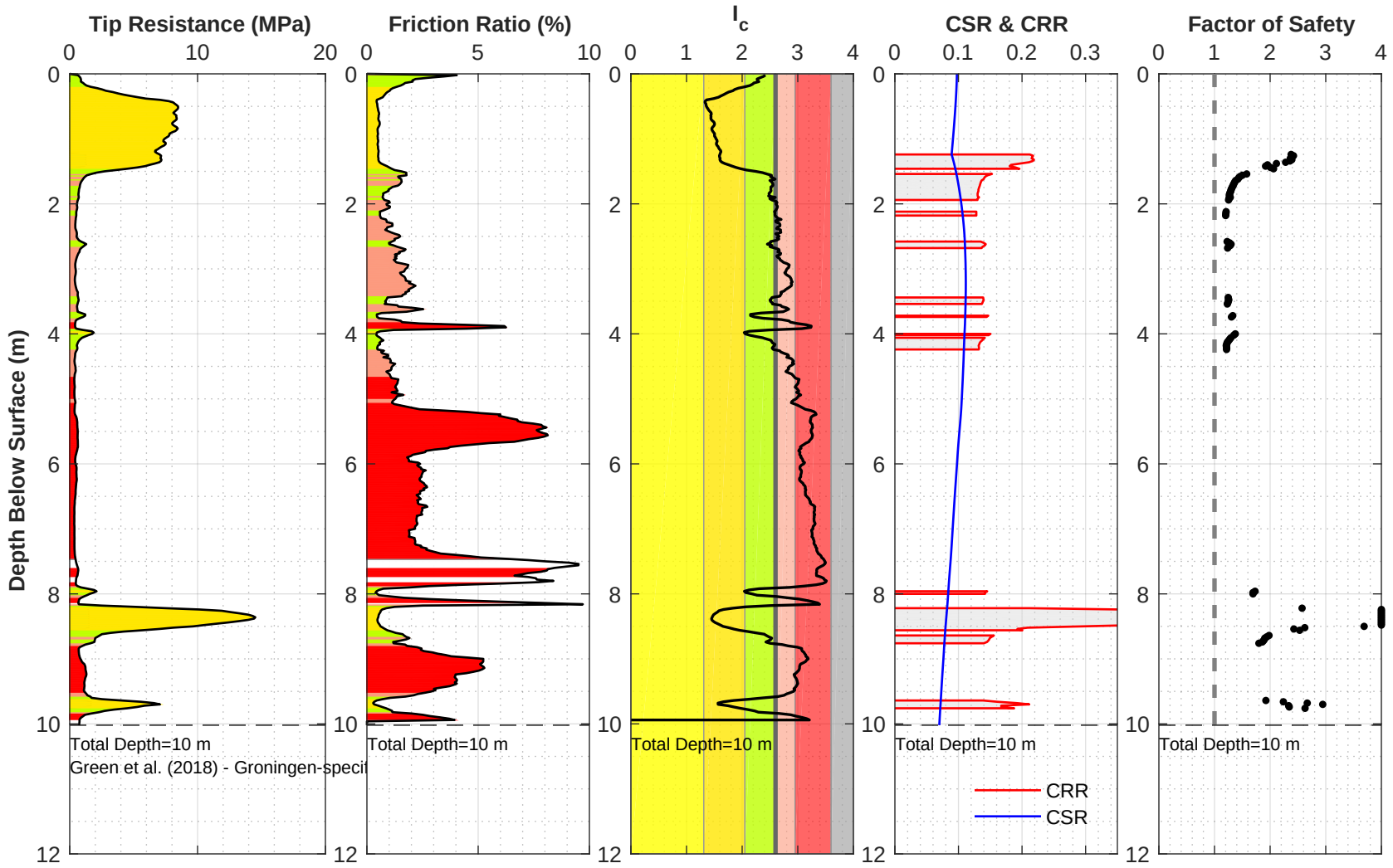

Location: 21225_253_coord
Surface EL: 1.7 m +/- (NAP)
Cone Diameter: 43.7 mm

Thin Layer Correction: NCEER (Youd et al. 2001)
Analysis Title: NC
Mw: 3.9 amax (g): 0.15

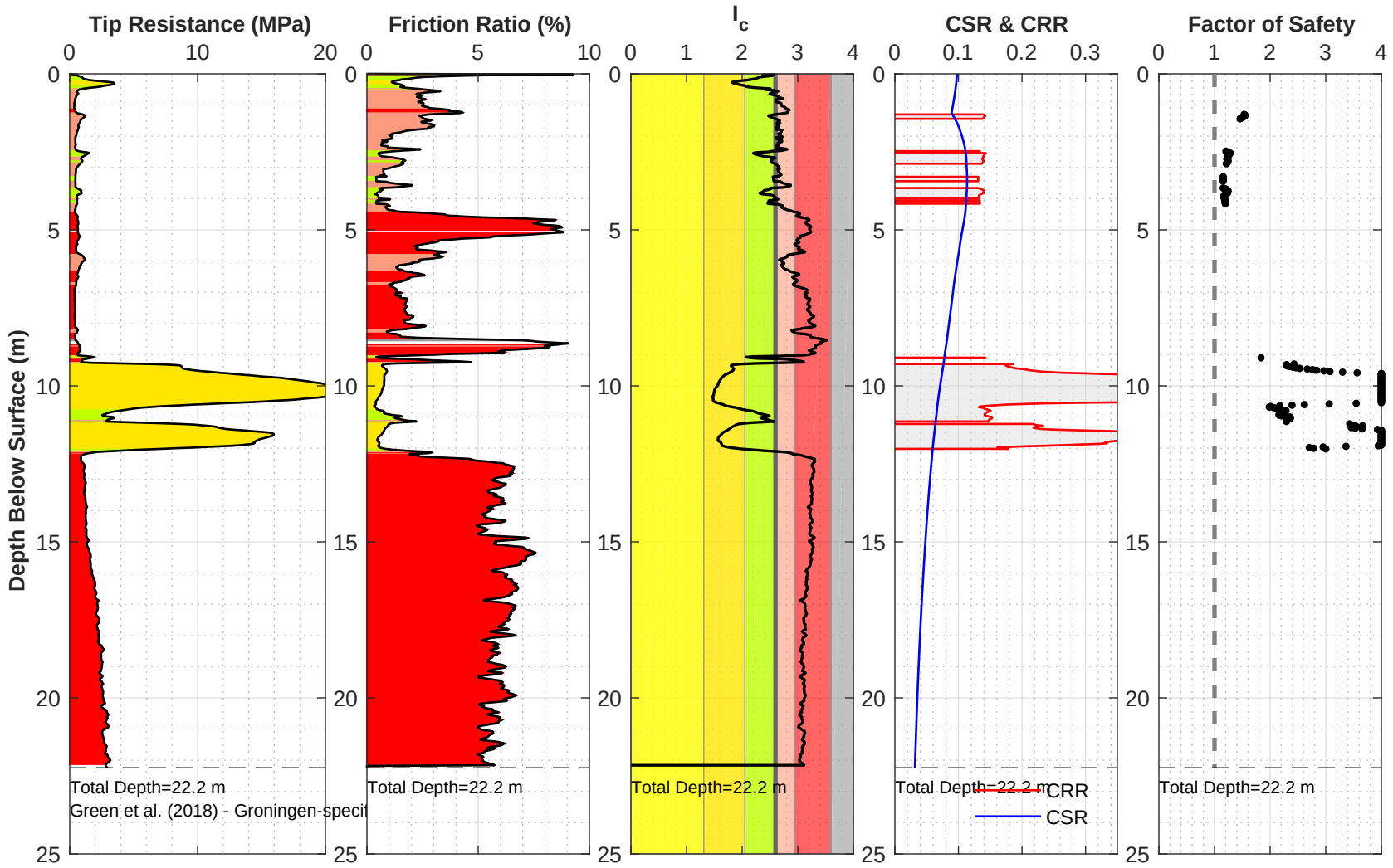

Location: 21225_254_coord
Surface EL: 1.8 m +/- (NAP)
Cone Diameter: 43.7 mm

Thin Layer Correction: NCEER (Youd et al. 2001)
Analysis Title: NC
Mw: 3.9 amax (g): 0.15

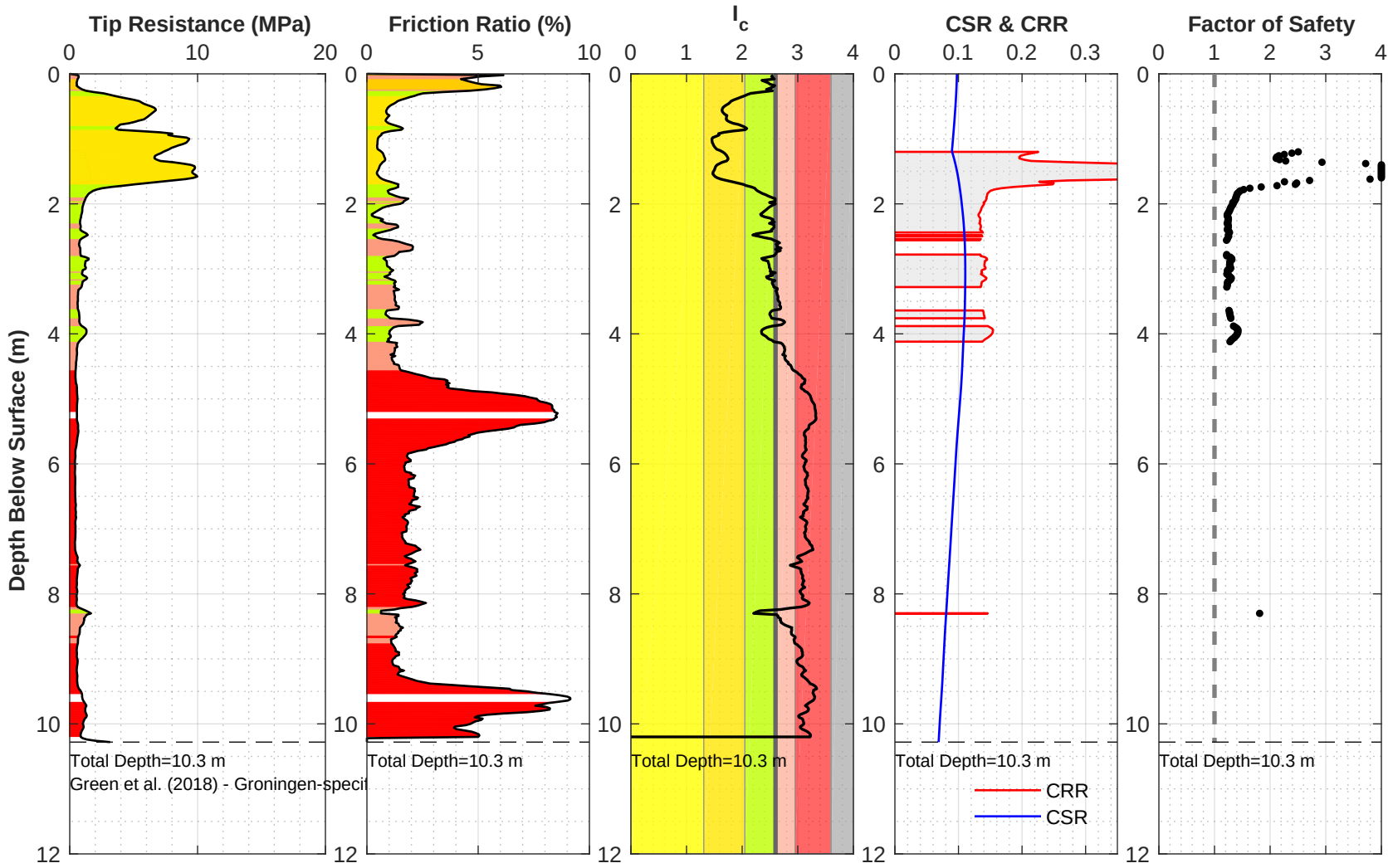

Location: 21225_255_coord
Surface EL: 1.7 m +/- (NAP)
Cone Diameter: 43.7 mm

Thin Layer Correction: NCEER (Youd et al. 2001)
Analysis Title: NC
Mw: 3.9 amax (g): 0.15

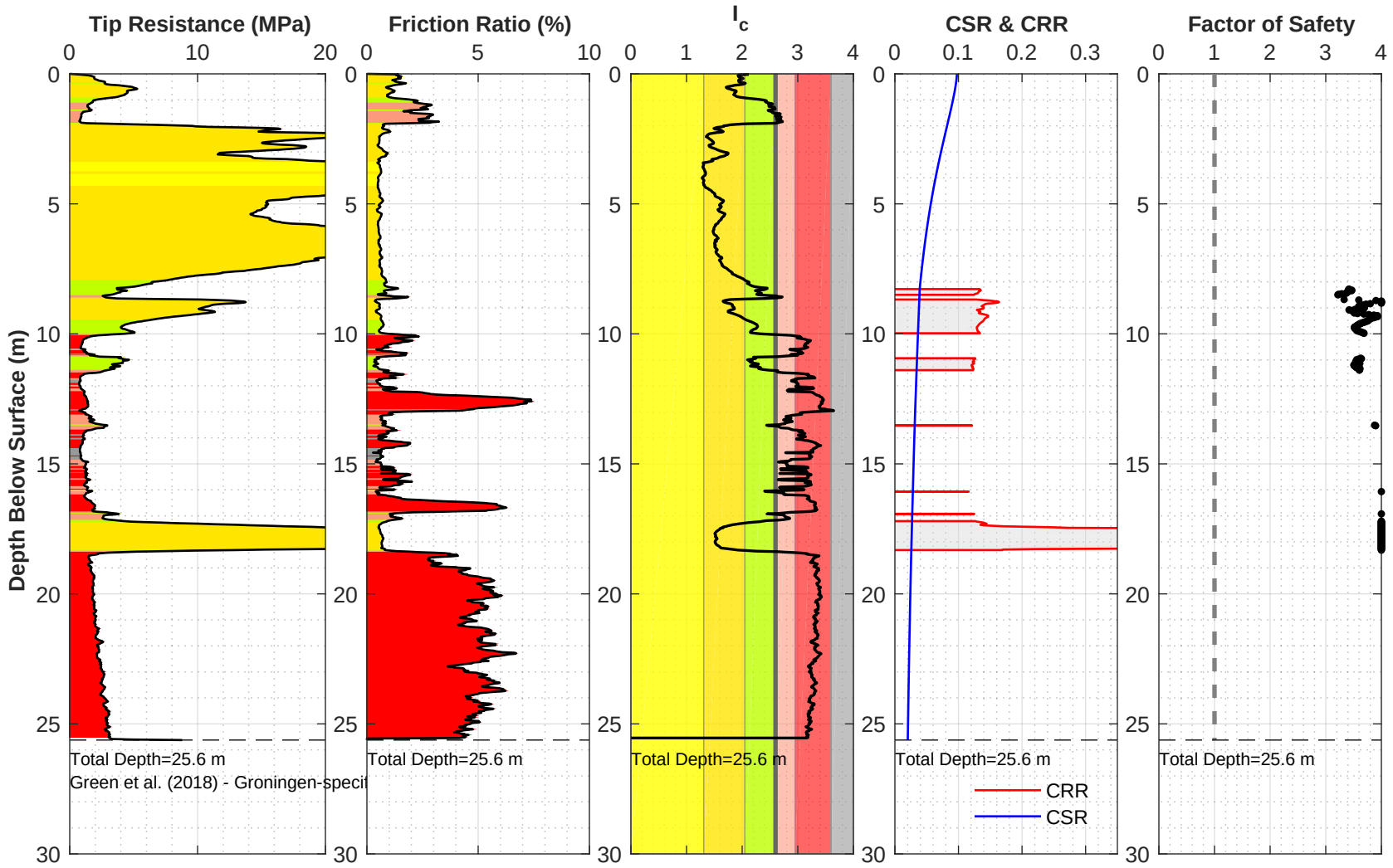

Location: 21225_256_coord
Surface EL: 8.8 m +/- (NAP)
Cone Diameter: 43.7 mm

Thin Layer Correction: NCEER (Youd et al. 2001)
Analysis Title: NC
Mw: 3.9 amax (g): 0.15

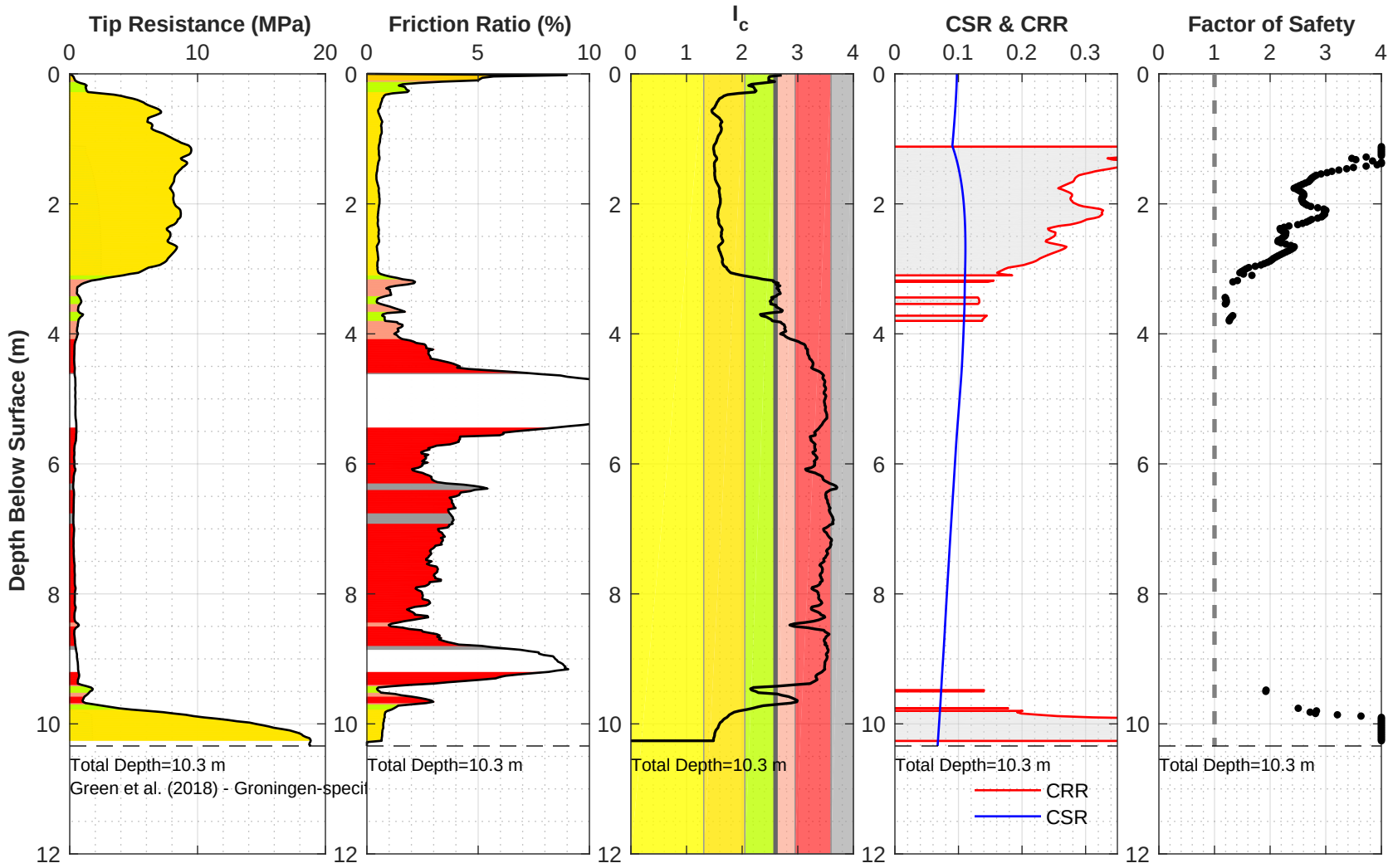

Location: 21225_257_coord
Surface EL: 1.6 m +/- (NAP)
Cone Diameter: 43.7 mm

Thin Layer Correction: NCEER (Youd et al. 2001)
Analysis Title: NC
Mw: 3.9 amax (g): 0.15

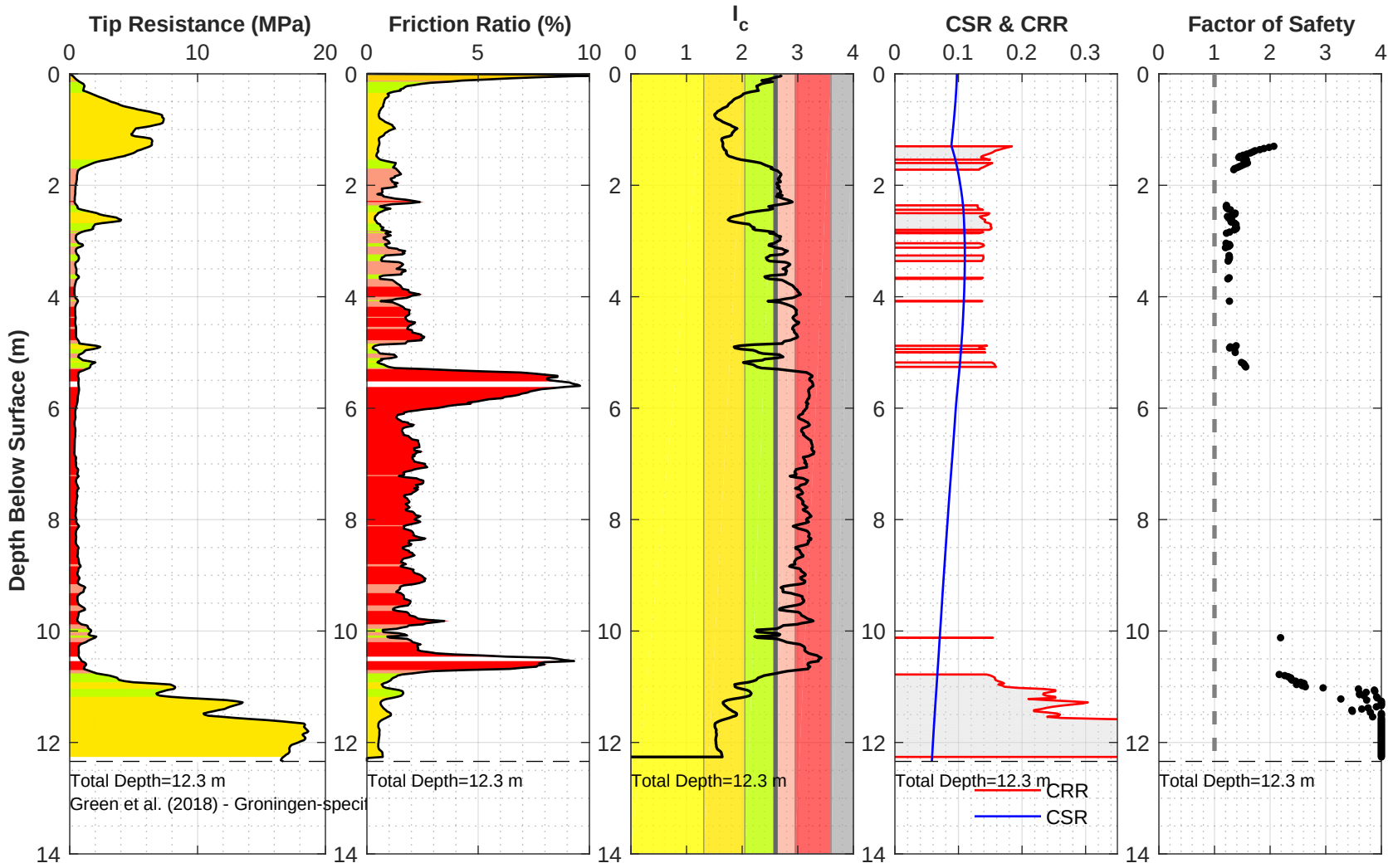

Location: 21225_258_coord
Surface EL: 1.8 m +/- (NAP)
Cone Diameter: 43.7 mm

Thin Layer Correction: NCEER (Youd et al. 2001)
Analysis Title: NC
Mw: 3.9 amax (g): 0.15

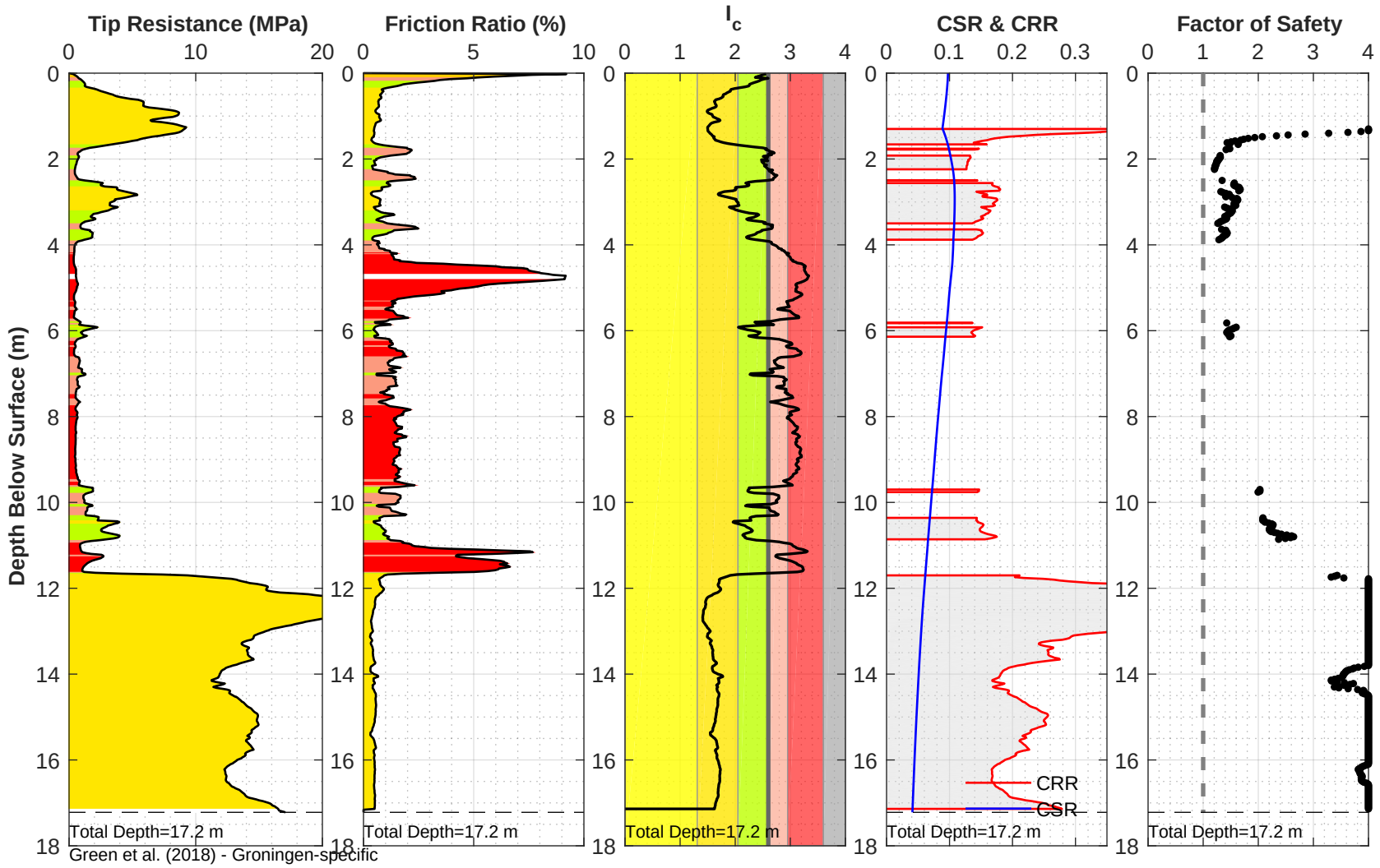

Location: 21225_259_coord
Surface EL: 1.8 m +/- (NAP)
Cone Diameter: 43.7 mm

Thin Layer Correction: NCEER (Youd et al. 2001)
Analysis Title: NC
Mw: 3.9 amax (g): 0.15

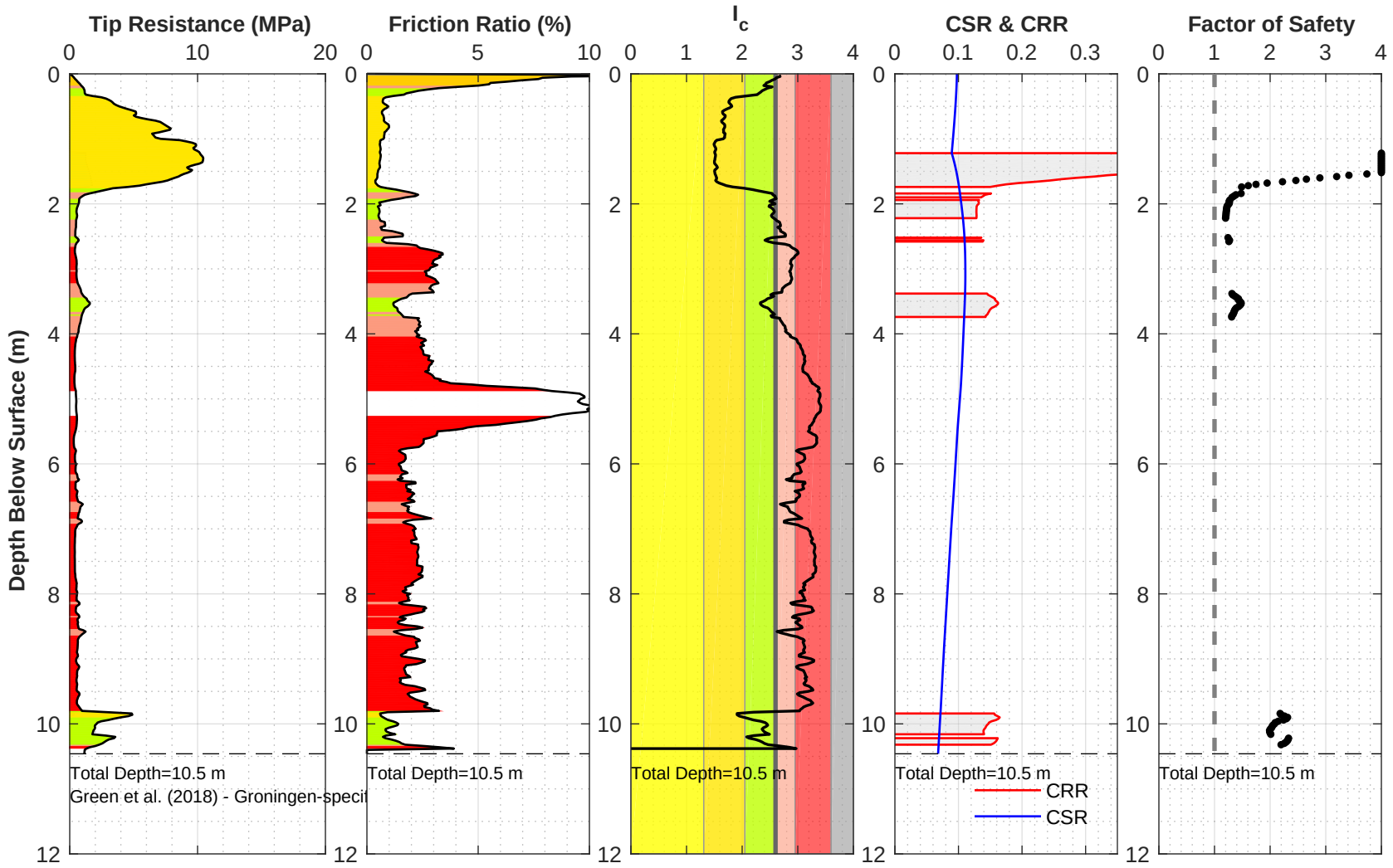

Location: 21225_260_coord
Surface EL: 1.7 m +/- (NAP)
Cone Diameter: 43.7 mm

Thin Layer Correction: NCEER (Youd et al. 2001)
Analysis Title: NC
Mw: 3.9 amax (g): 0.15

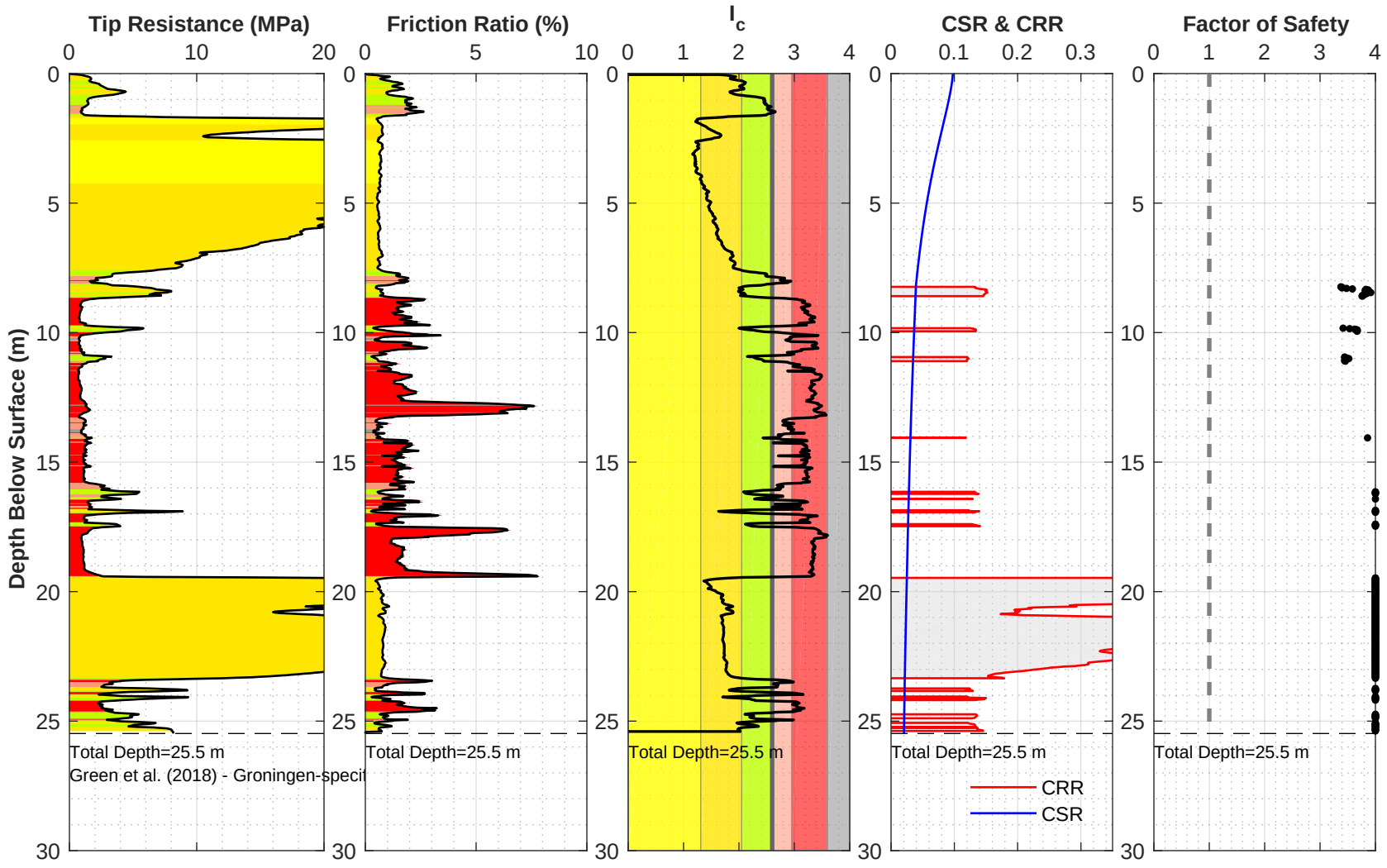

Location: 21225_261_coord
Surface EL: 8.7 m +/- (NAP)
Cone Diameter: 43.7 mm

Thin Layer Correction: NCEER (Youd et al. 2001)
Analysis Title: NC
Mw: 3.9 amax (g): 0.15

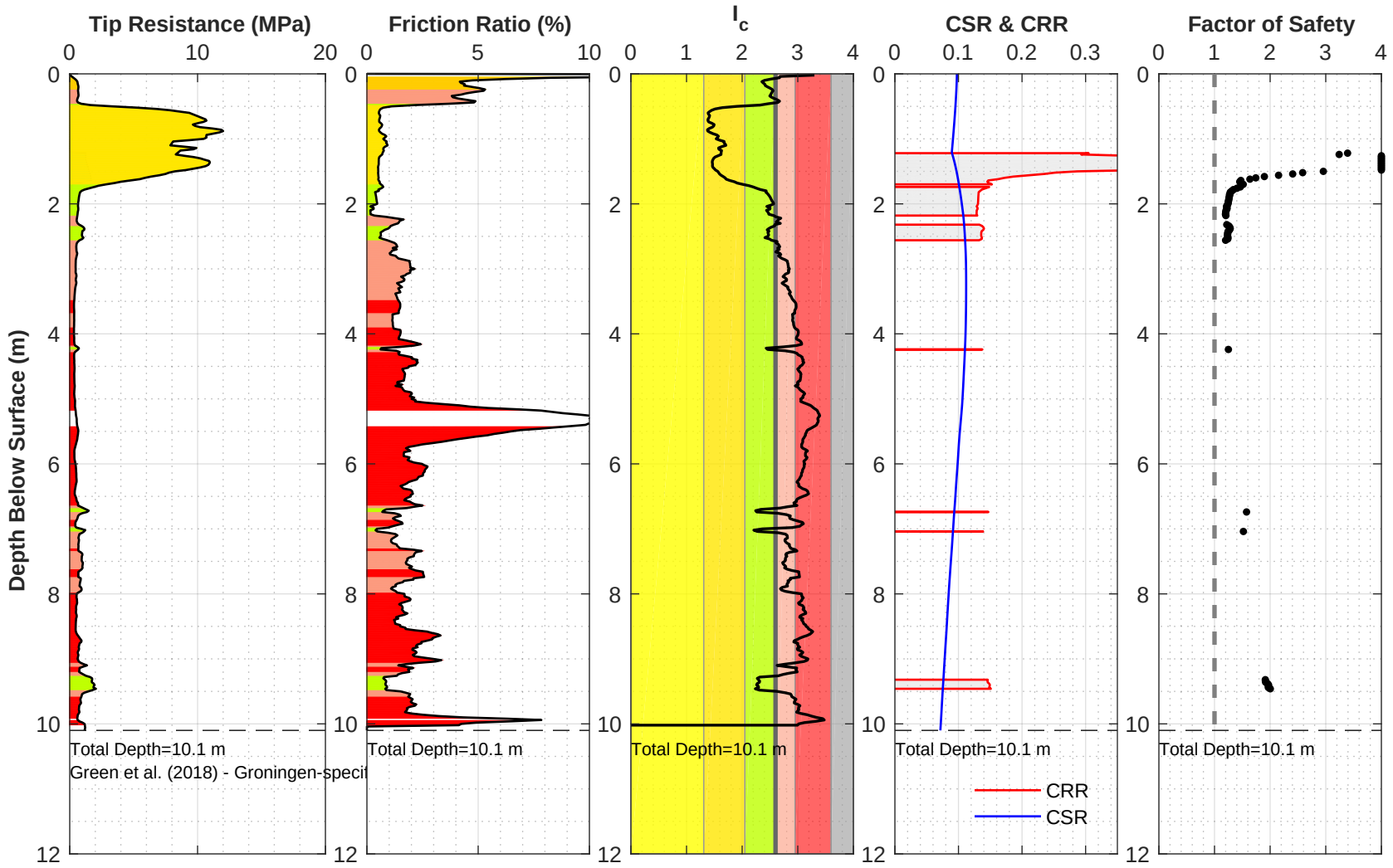

Location: 21225_262_coord
Surface EL: 1.7 m +/- (NAP)
Cone Diameter: 43.7 mm

Thin Layer Correction: NCEER (Youd et al. 2001)
Analysis Title: NC
Mw: 3.9 amax (g): 0.15

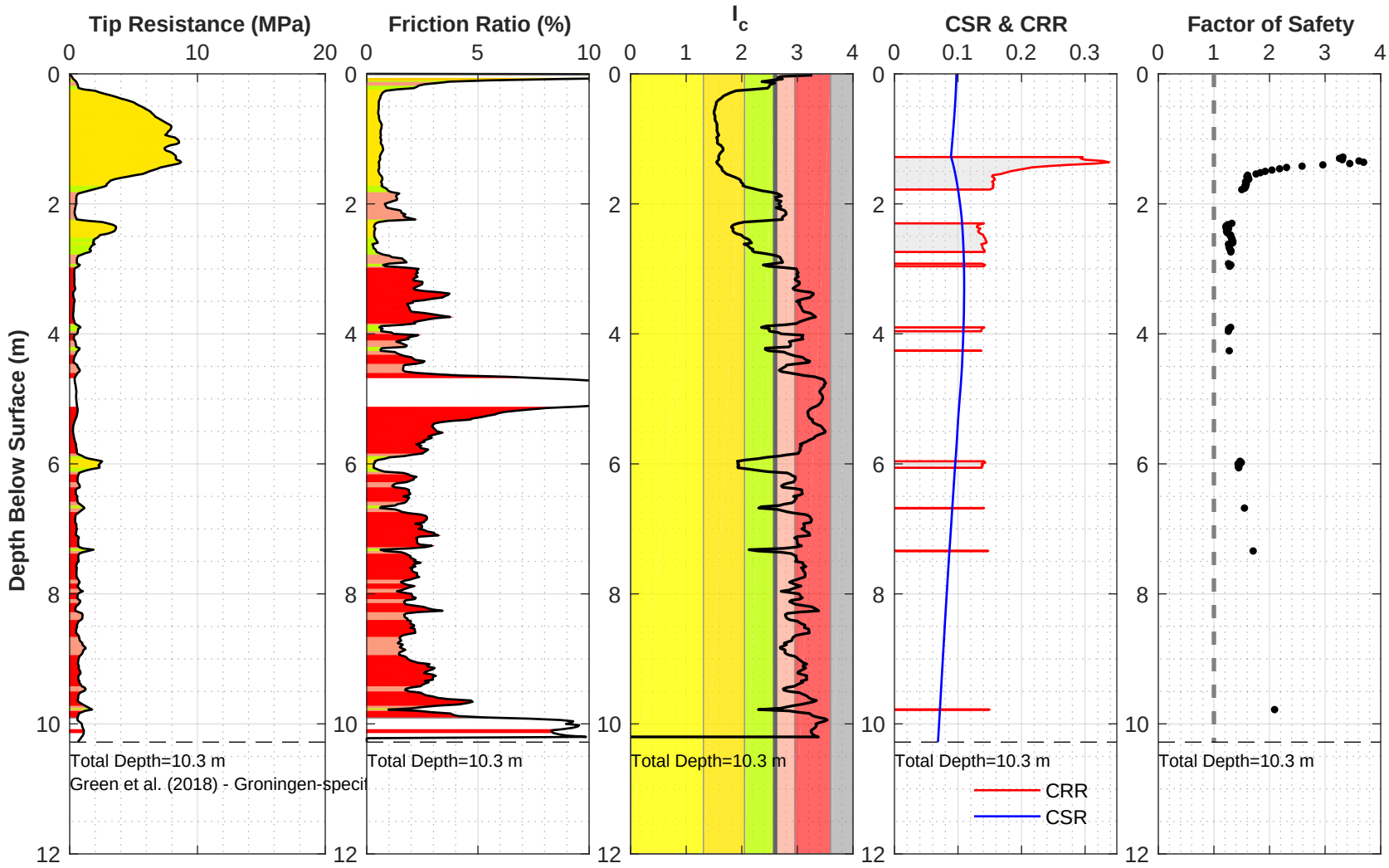

Location: 21225_263_coord
Surface EL: 1.8 m +/- (NAP)
Cone Diameter: 43.7 mm

Thin Layer Correction: NCEER (Youd et al. 2001)
Analysis Title: NC
Mw: 3.9 amax (g): 0.15

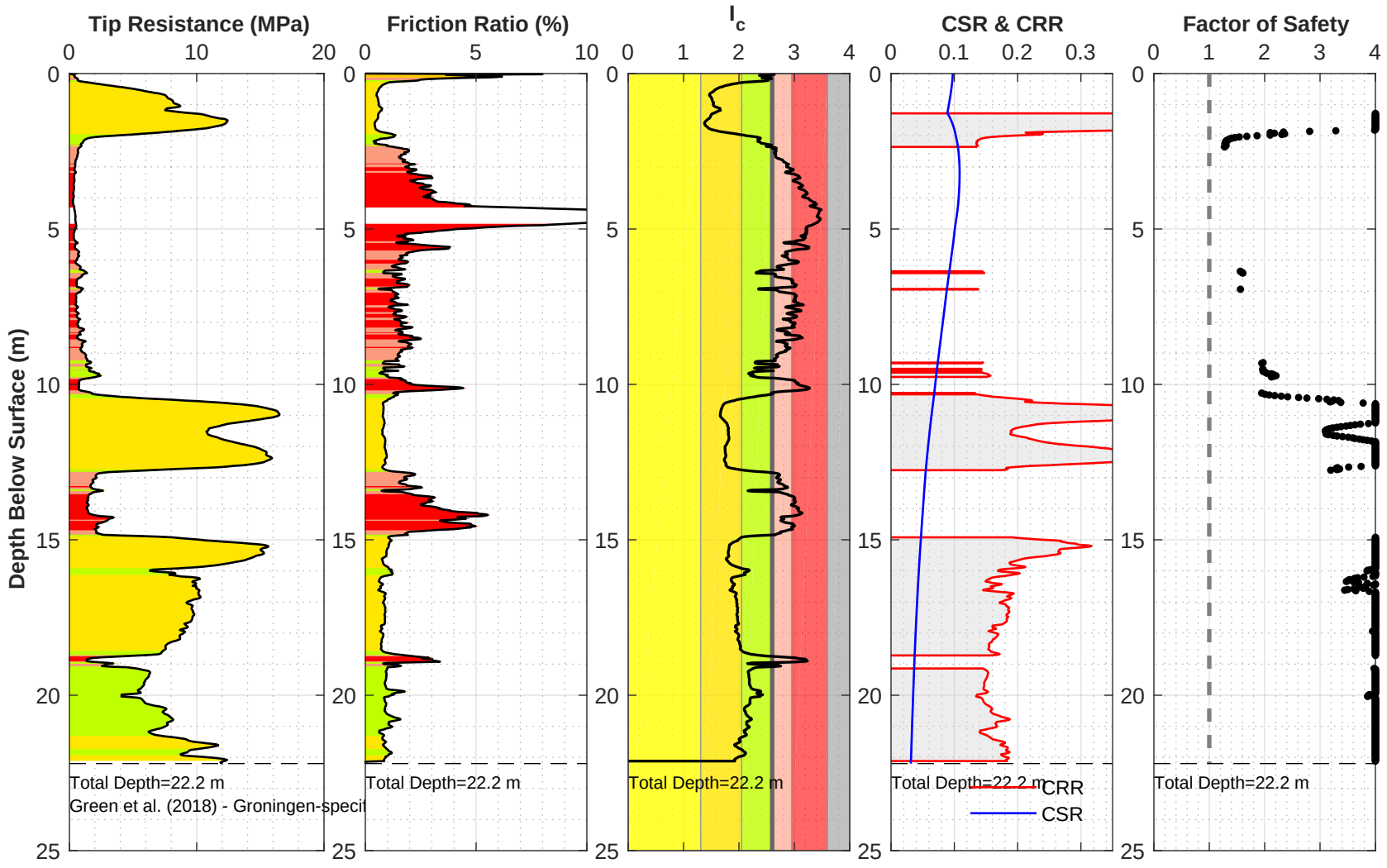

Location: 21225_264_coord
Surface EL: 1.8 m +/- (NAP)
Cone Diameter: 43.7 mm

Thin Layer Correction: NCEER (Youd et al. 2001)
Analysis Title: NC
Mw: 3.9 amax (g): 0.15

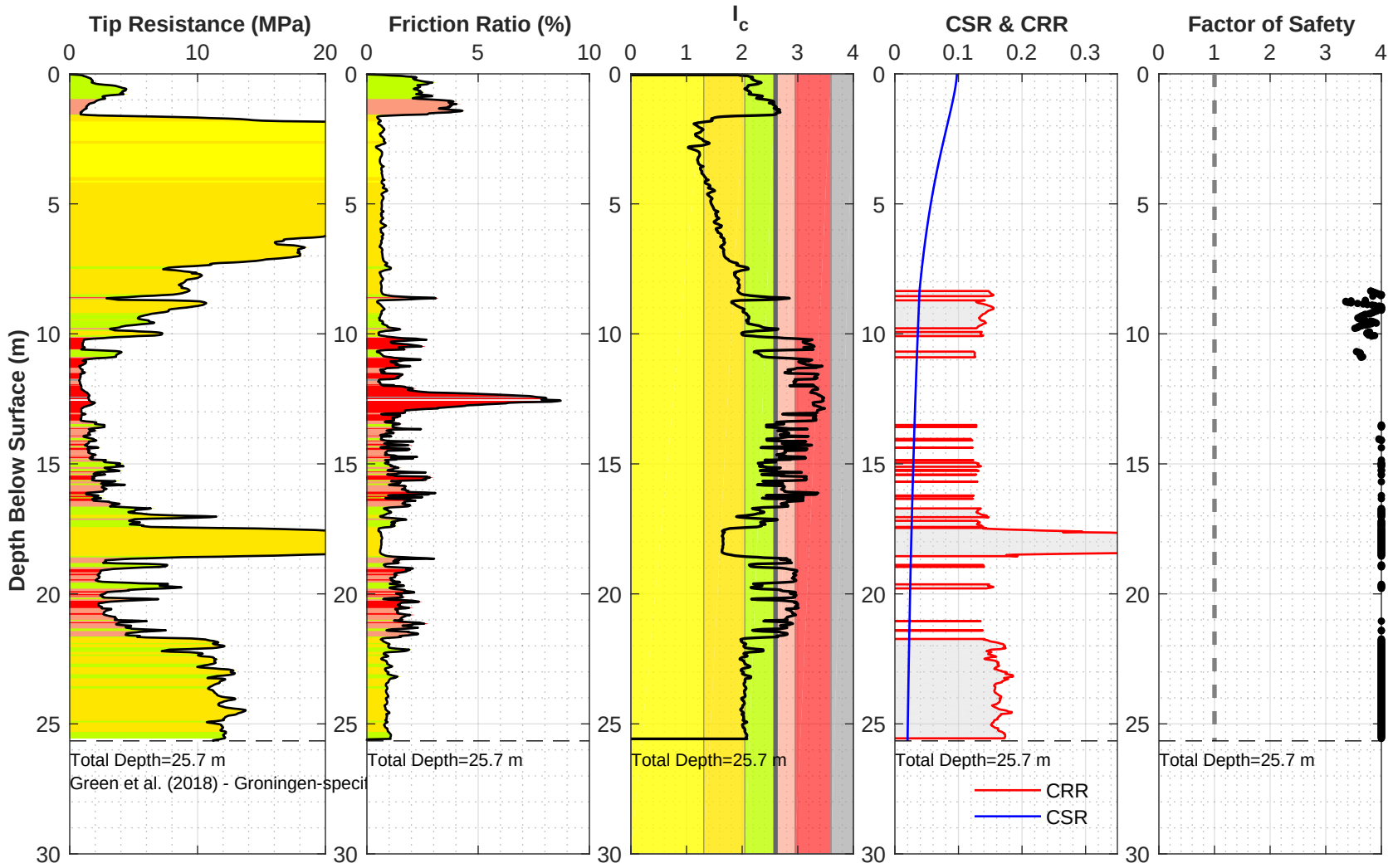

Location: 21225_265_coord
Surface EL: 8.9 m +/- (NAP)
Cone Diameter: 43.7 mm

Thin Layer Correction: NCEER (Youd et al. 2001)
Analysis Title: NC
Mw: 3.9 amax (g): 0.15

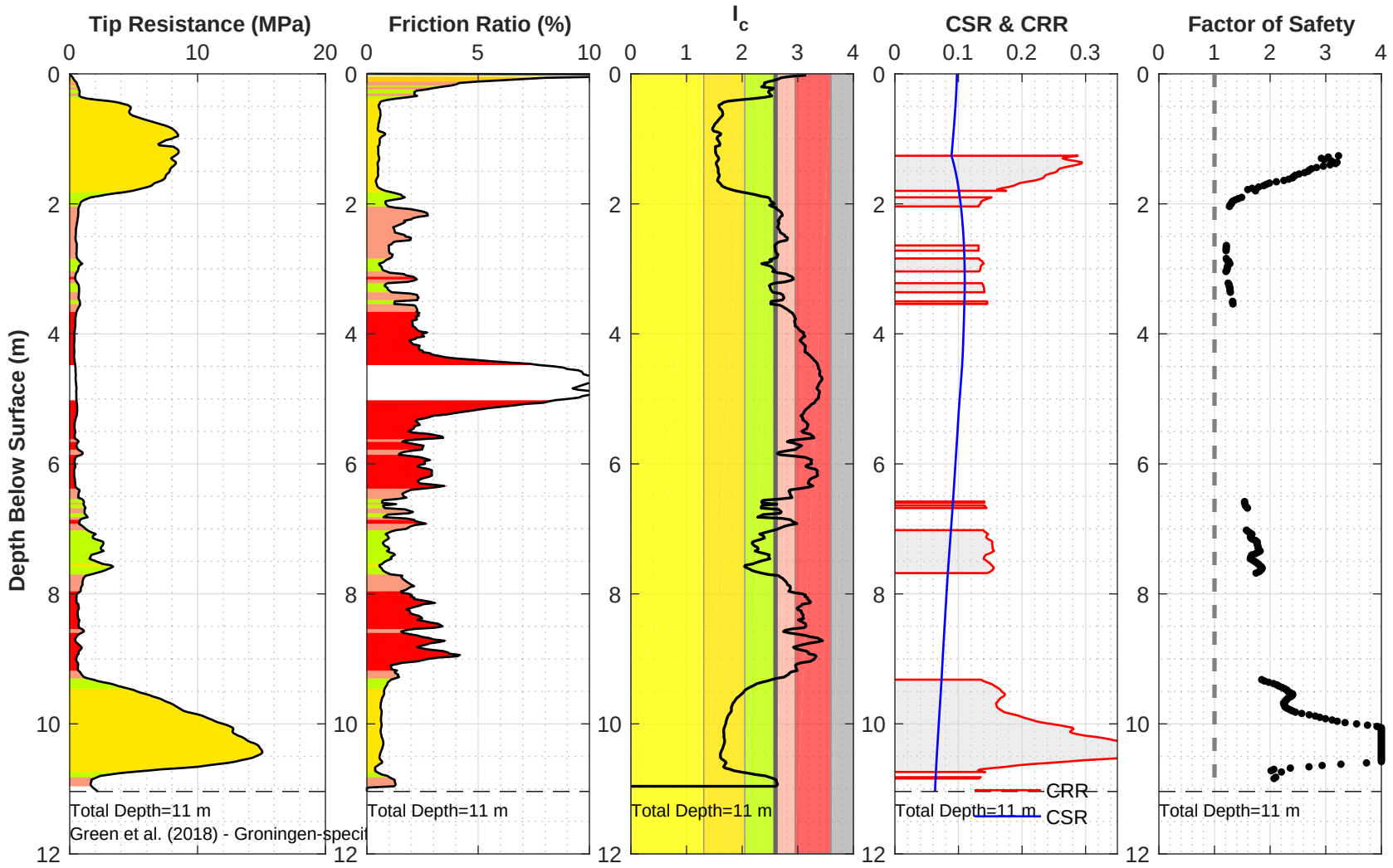

Location: 21225_266_coord
Surface EL: 1.8 m +/- (NAP)
Cone Diameter: 43.7 mm

Thin Layer Correction: NCEER (Youd et al. 2001)
Analysis Title: NC
Mw: 3.9 amax (g): 0.15

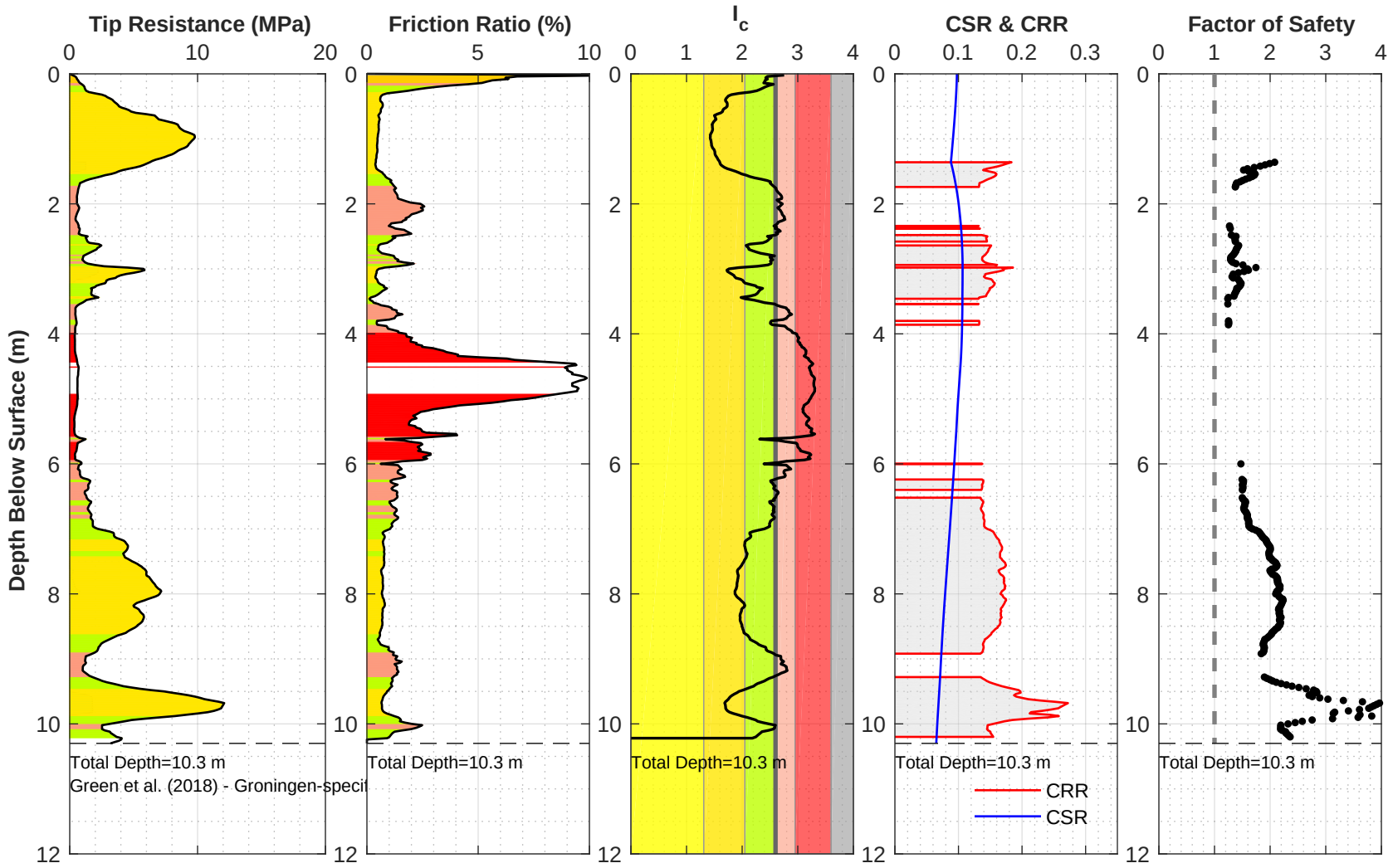

Location: 21225_267_coord
Surface EL: 1.9 m +/- (NAP)
Cone Diameter: 43.7 mm

Thin Layer Correction: NCEER (Youd et al. 2001)
Analysis Title: NC
Mw: 3.9 amax (g): 0.15

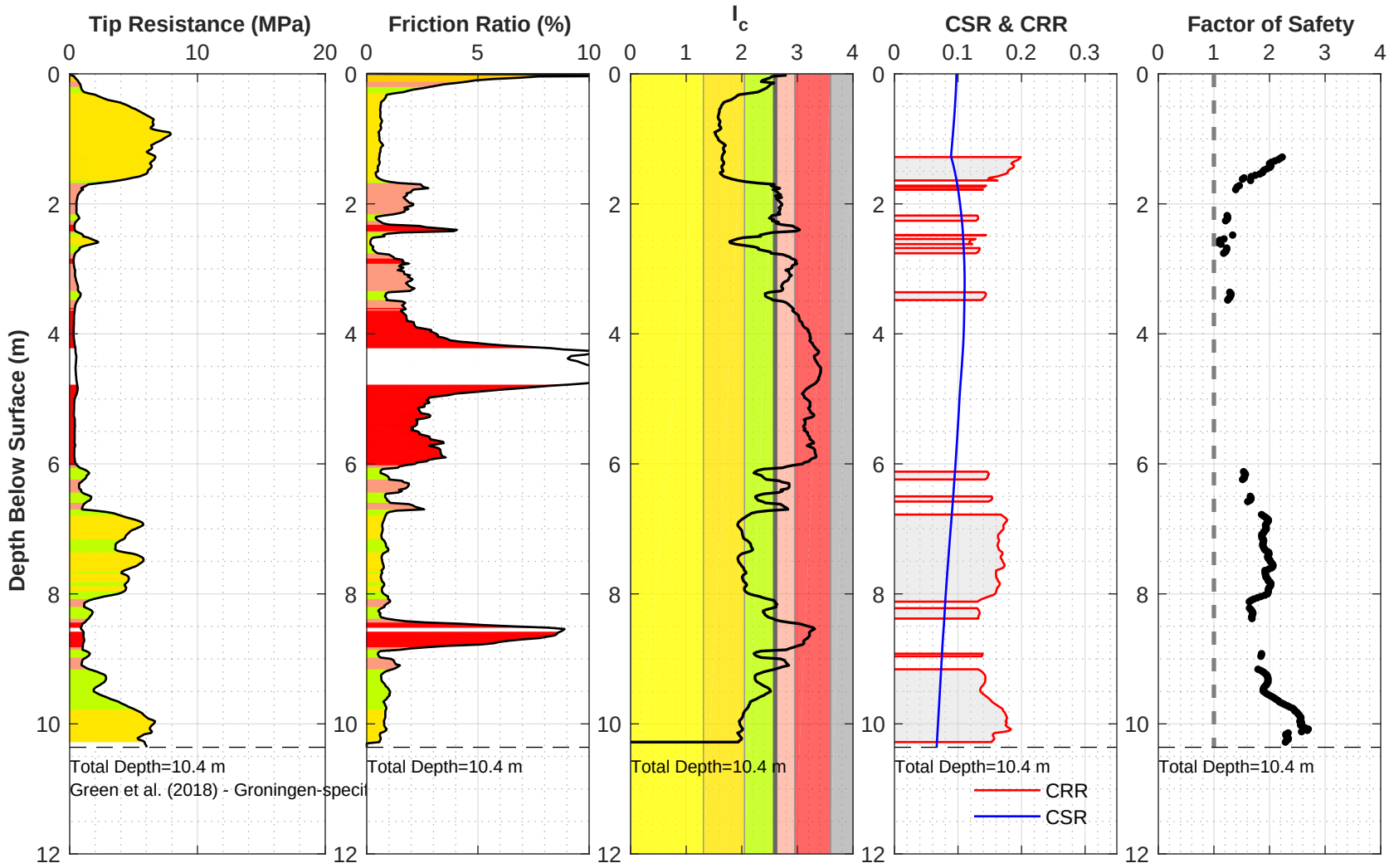

Location: 21225_268_coord
Surface EL: 1.8 m +/- (NAP)
Cone Diameter: 43.7 mm

Thin Layer Correction: NCEER (Youd et al. 2001)
Analysis Title: NC
Mw: 3.9 amax (g): 0.15

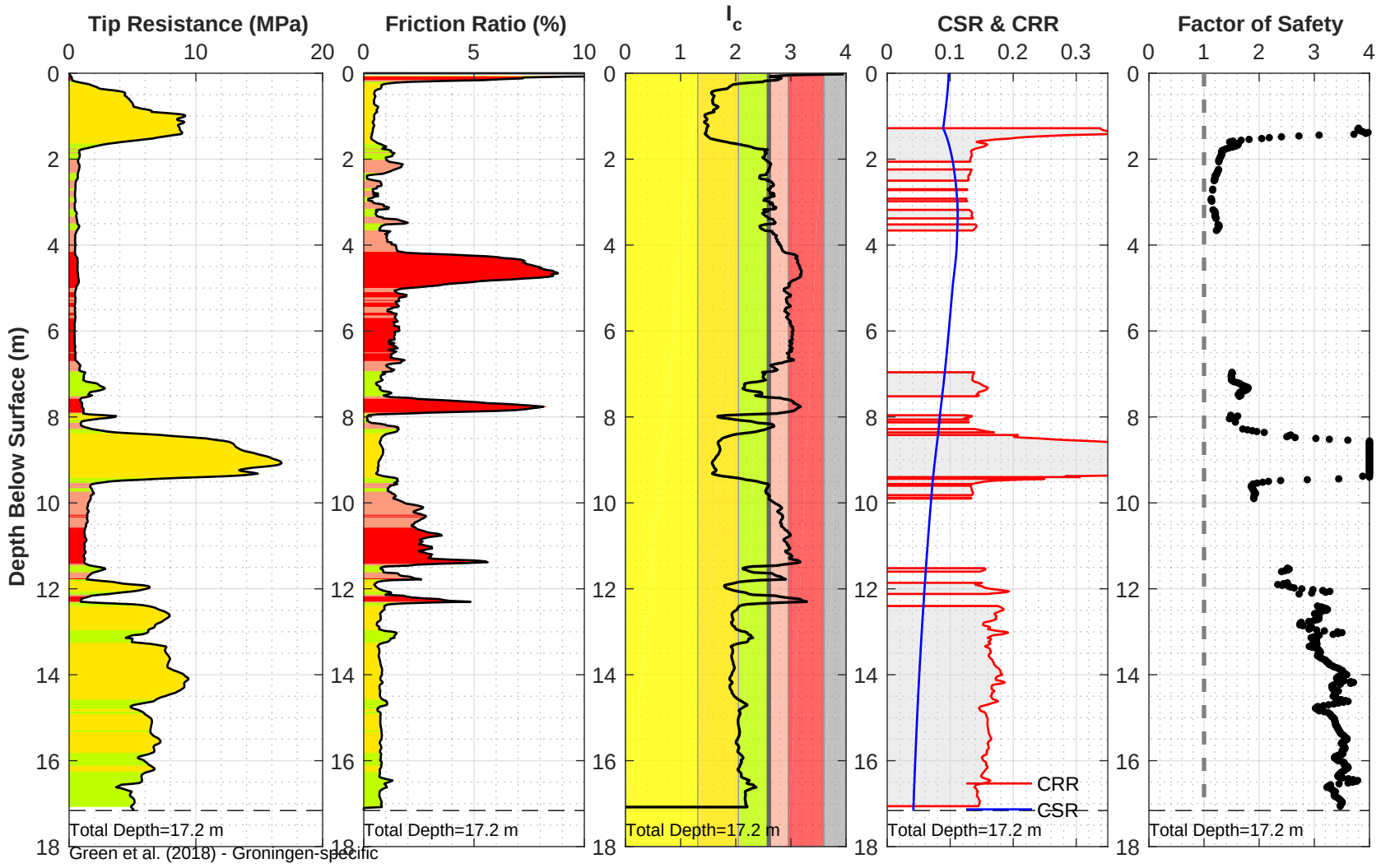

Location: 21225_269_coord
Surface EL: 1.8 m +/- (NAP)
Cone Diameter: 43.7 mm

Thin Layer Correction: NCEER (Youd et al. 2001)
Analysis Title: NC
Mw: 3.9 amax (g): 0.15

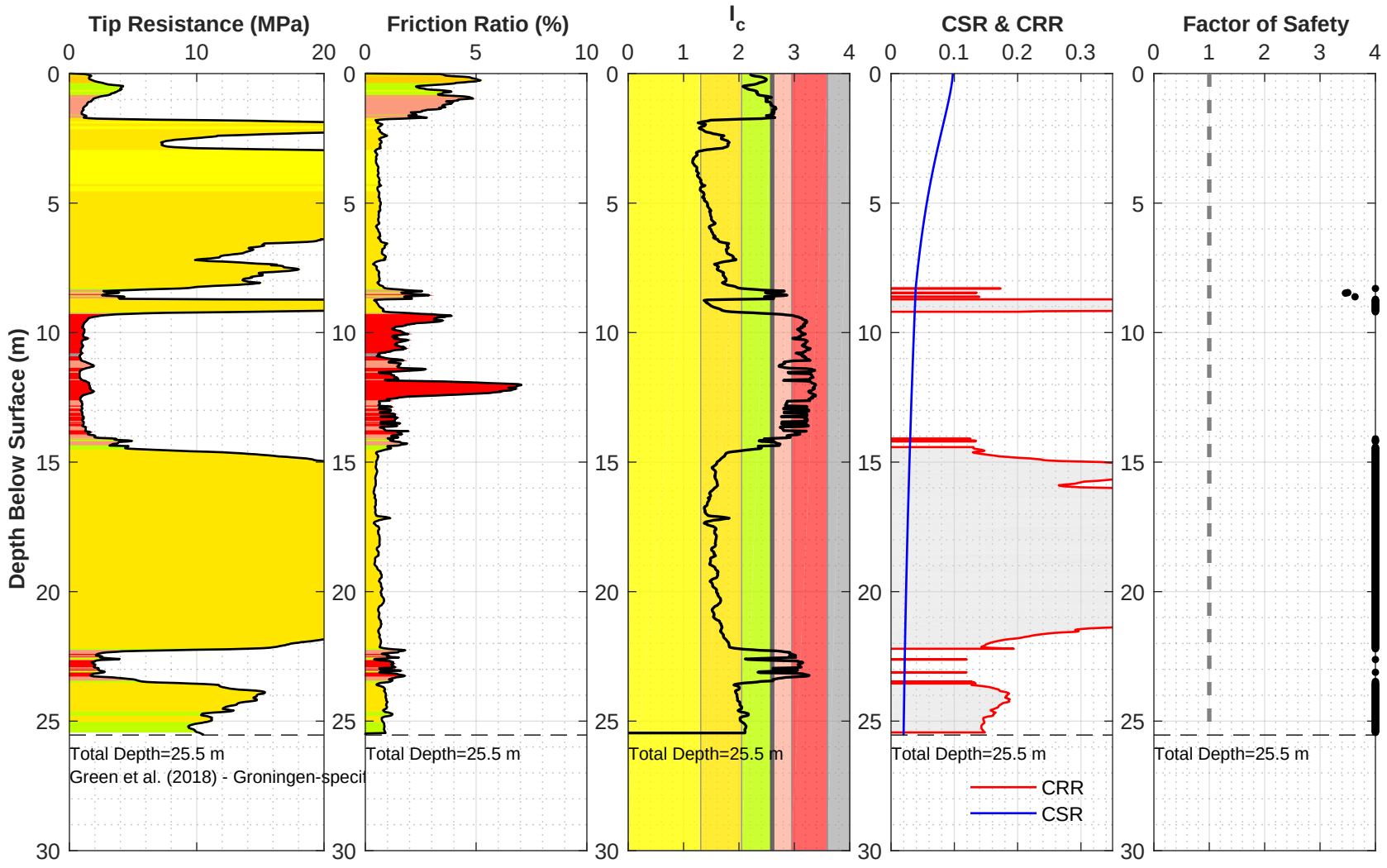

Location: 21225_270_coord
Surface EL: 8.8 m +/- (NAP)
Cone Diameter: 43.7 mm

Thin Layer Correction: NCEER (Youd et al. 2001)
Analysis Title: NC
Mw: 3.9 amax (g): 0.15

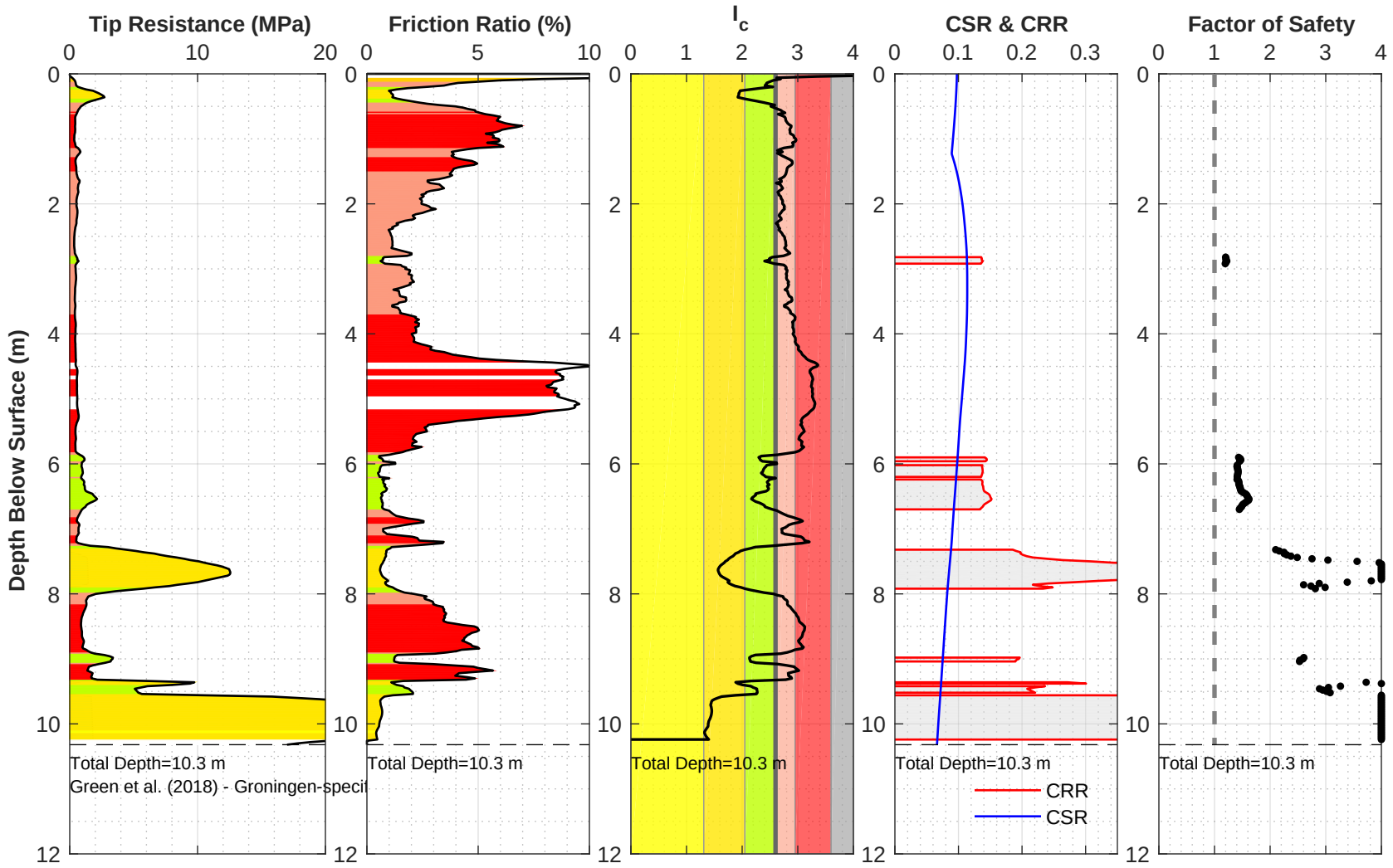

Location: 21225_271_coord
Surface EL: 1.7 m +/- (NAP)
Cone Diameter: 43.7 mm

Thin Layer Correction: NCEER (Youd et al. 2001)
Analysis Title: NC
Mw: 3.9 amax (g): 0.15

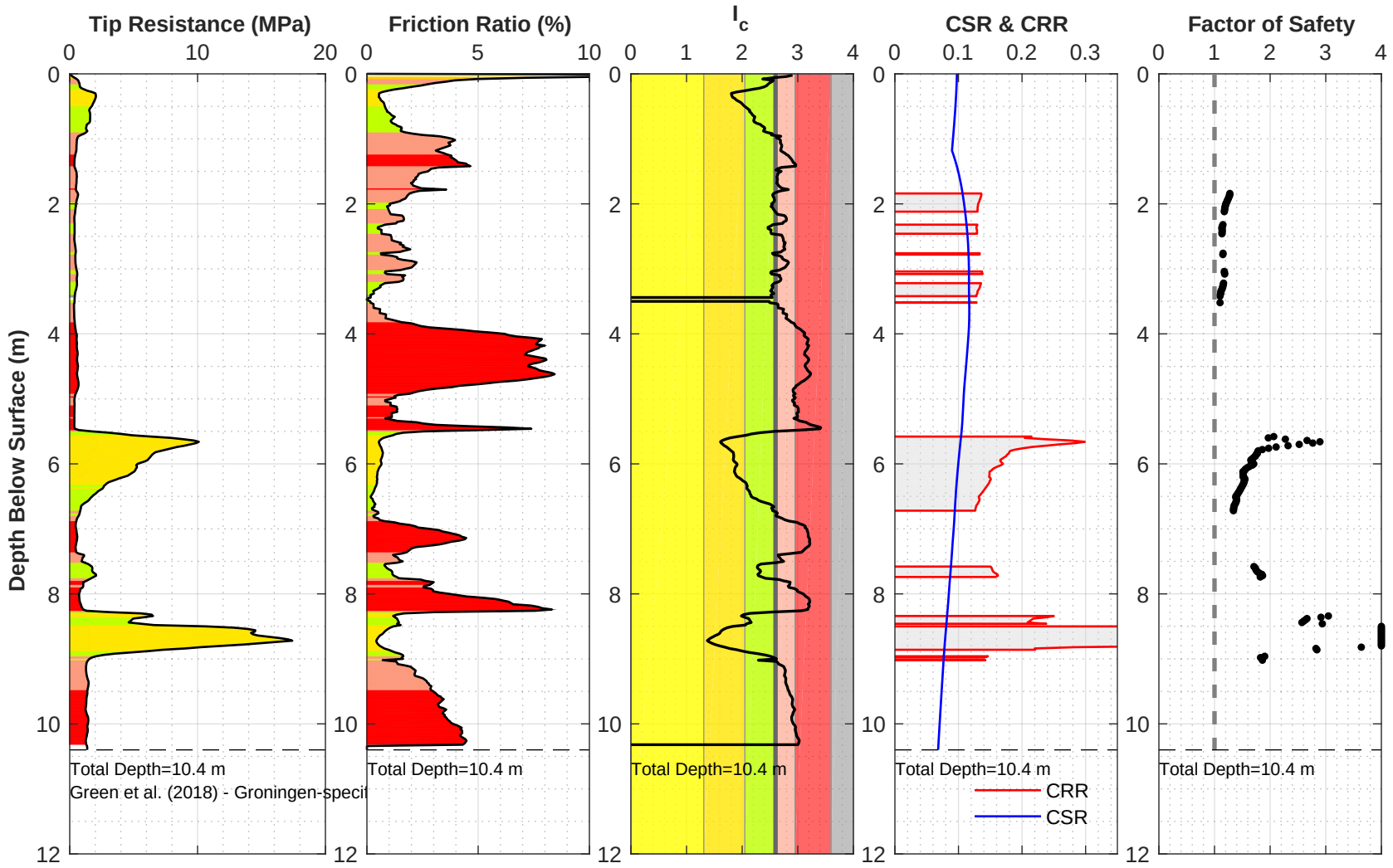

Location: 21225_272_coord
Surface EL: 1.7 m +/- (NAP)
Cone Diameter: 43.7 mm

Thin Layer Correction: NCEER (Youd et al. 2001)
Analysis Title: NC
Mw: 3.9 amax (g): 0.15

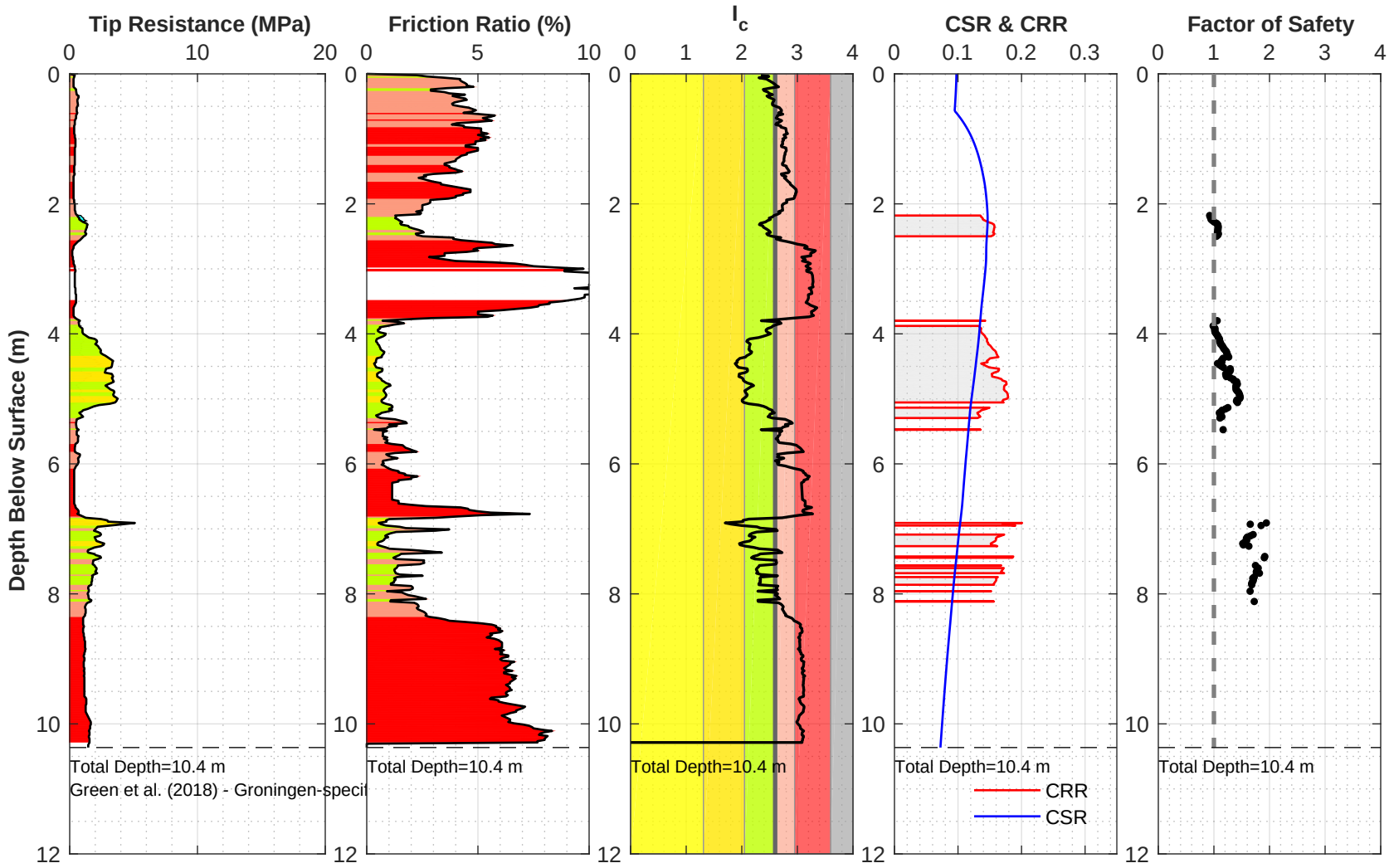

Location: 21225_273_coord
Surface EL: 1.1 m +/- (NAP)
Cone Diameter: 43.7 mm

Thin Layer Correction: NCEER (Youd et al. 2001)
Analysis Title: NC
Mw: 3.9 amax (g): 0.15

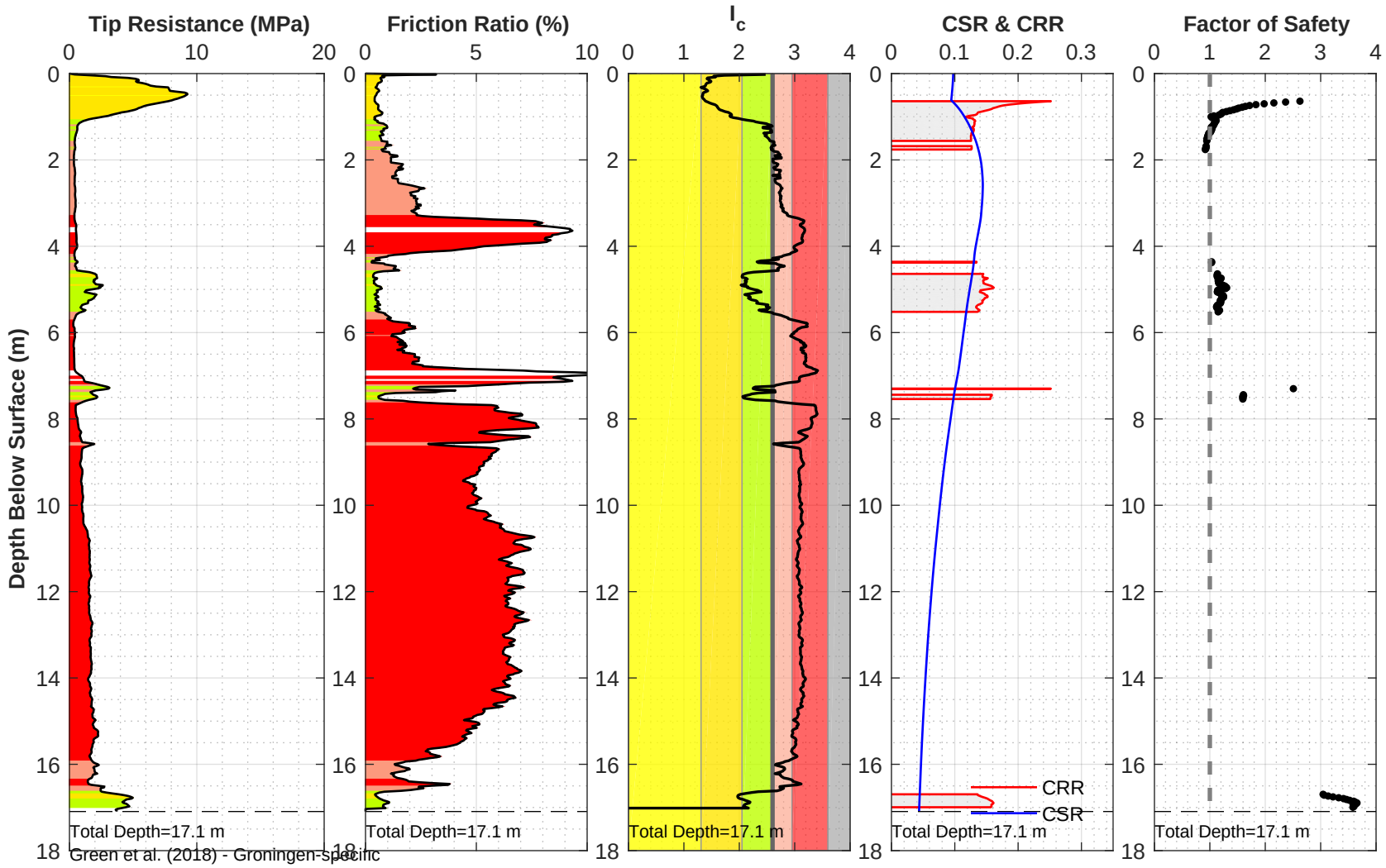

Location: 21225_274_coord
Surface EL: 1.1 m +/- (NAP)
Cone Diameter: 43.7 mm

Thin Layer Correction: NCEER (Youd et al. 2001)
Analysis Title: NC
Mw: 3.9 amax (g): 0.15

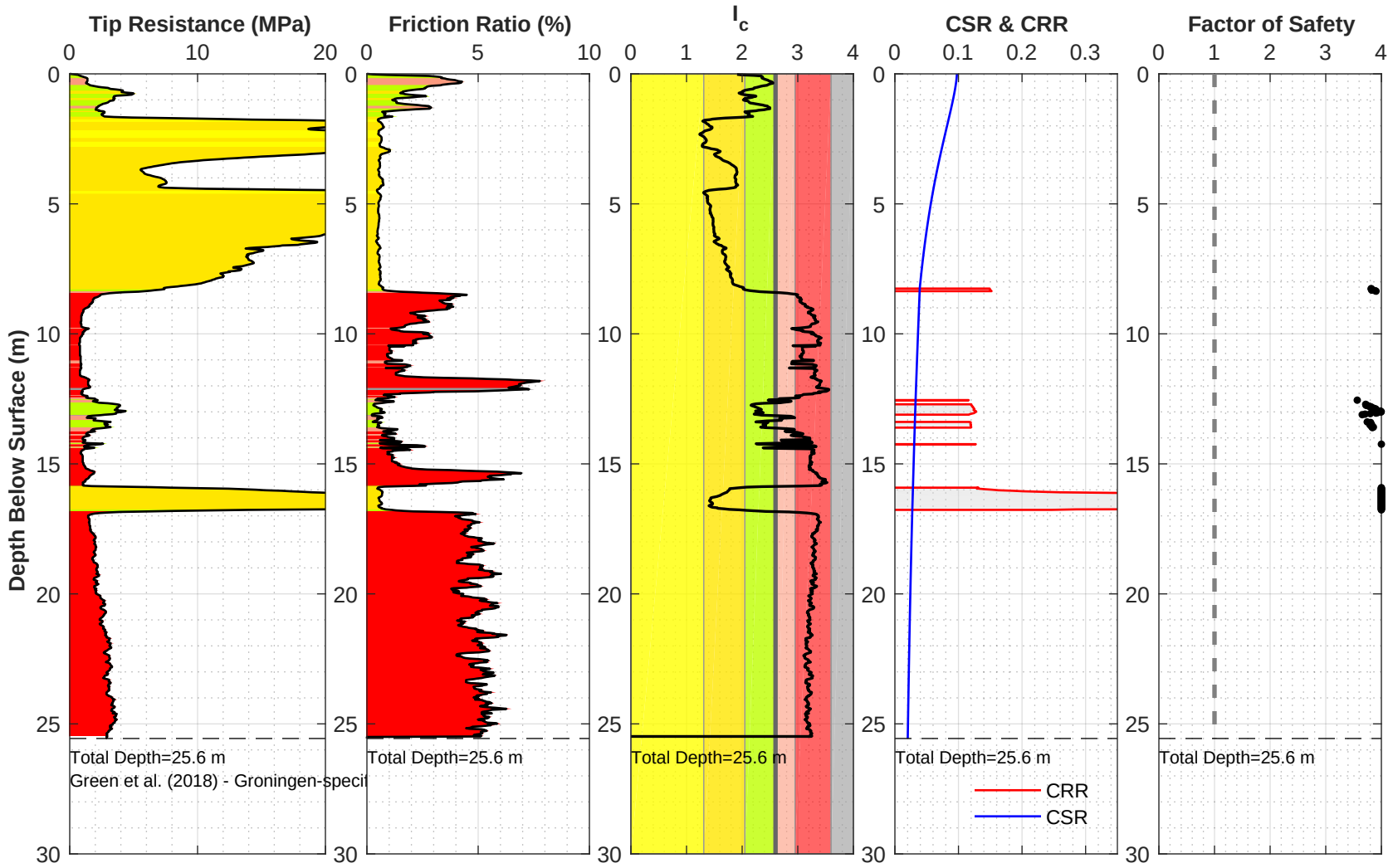

Location: 21225_275_coord
Surface EL: 8.7 m +/- (NAP)
Cone Diameter: 43.7 mm

Thin Layer Correction: NCEER (Youd et al. 2001)
Analysis Title: NC
Mw: 3.9 amax (g): 0.15

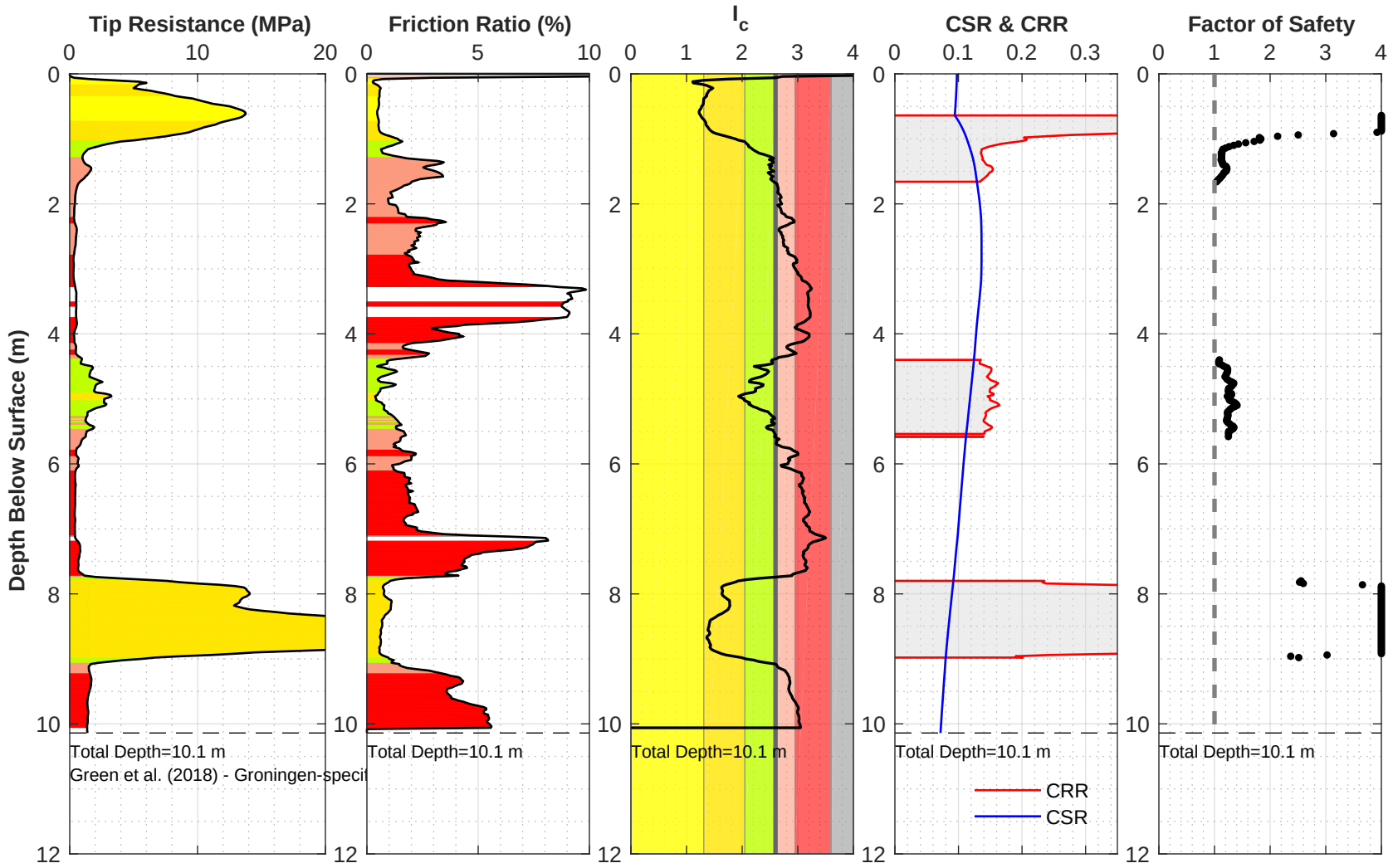

Location: 21225_276_coord
Surface EL: 1.1 m +/- (NAP)
Cone Diameter: 43.7 mm

Thin Layer Correction: NCEER (Youd et al. 2001)
Analysis Title: NC
Mw: 3.9 amax (g): 0.15

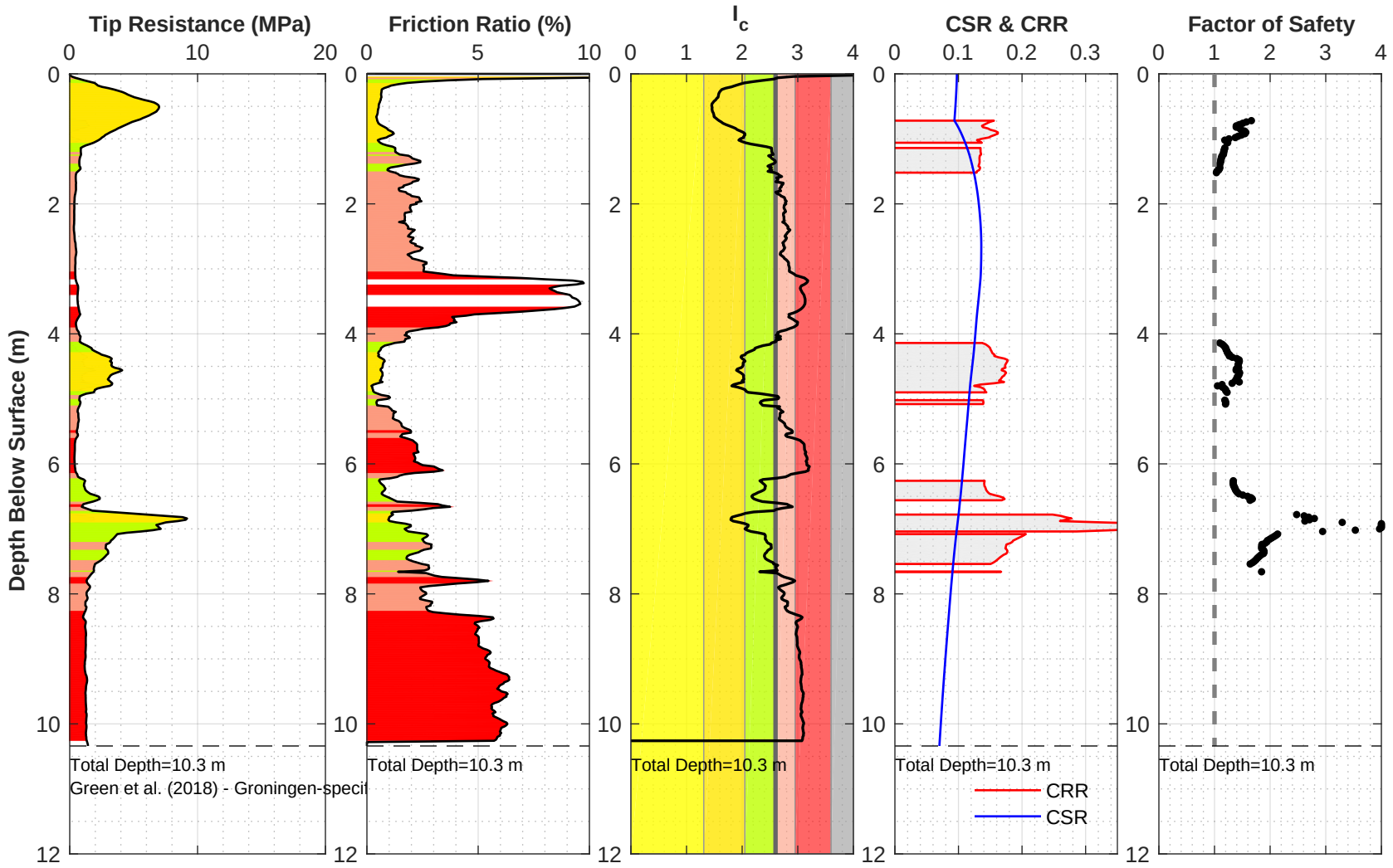

Location: 21225_277_coord
Surface EL: 1.2 m +/- (NAP)
Cone Diameter: 43.7 mm

Thin Layer Correction: NCEER (Youd et al. 2001)
Analysis Title: NC
Mw: 3.9 amax (g): 0.15

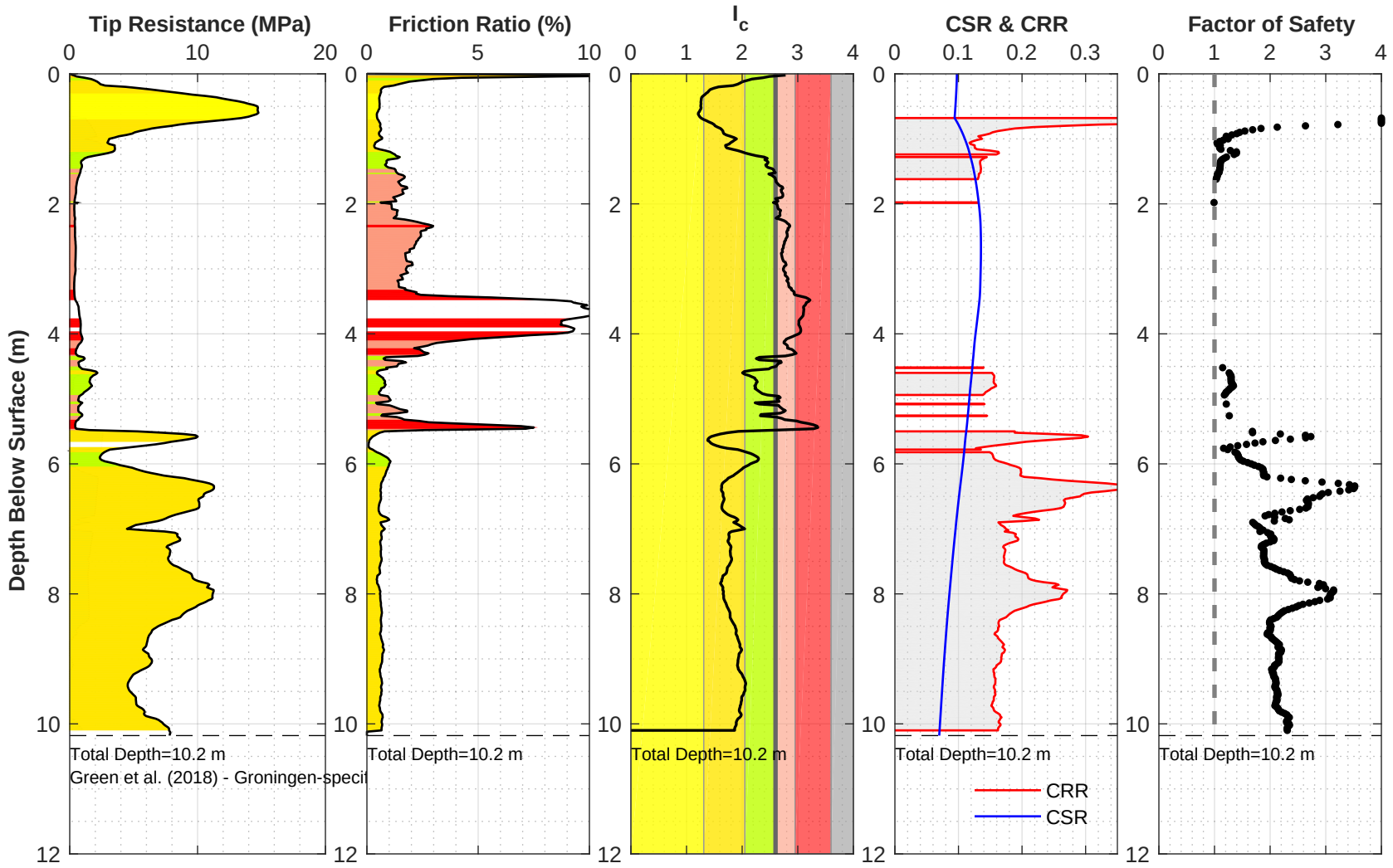

Location: 21225_278_coord
Surface EL: 1.2 m +/- (NAP)
Cone Diameter: 43.7 mm

Thin Layer Correction: NCEER (Youd et al. 2001)
Analysis Title: NC
Mw: 3.9 amax (g): 0.15

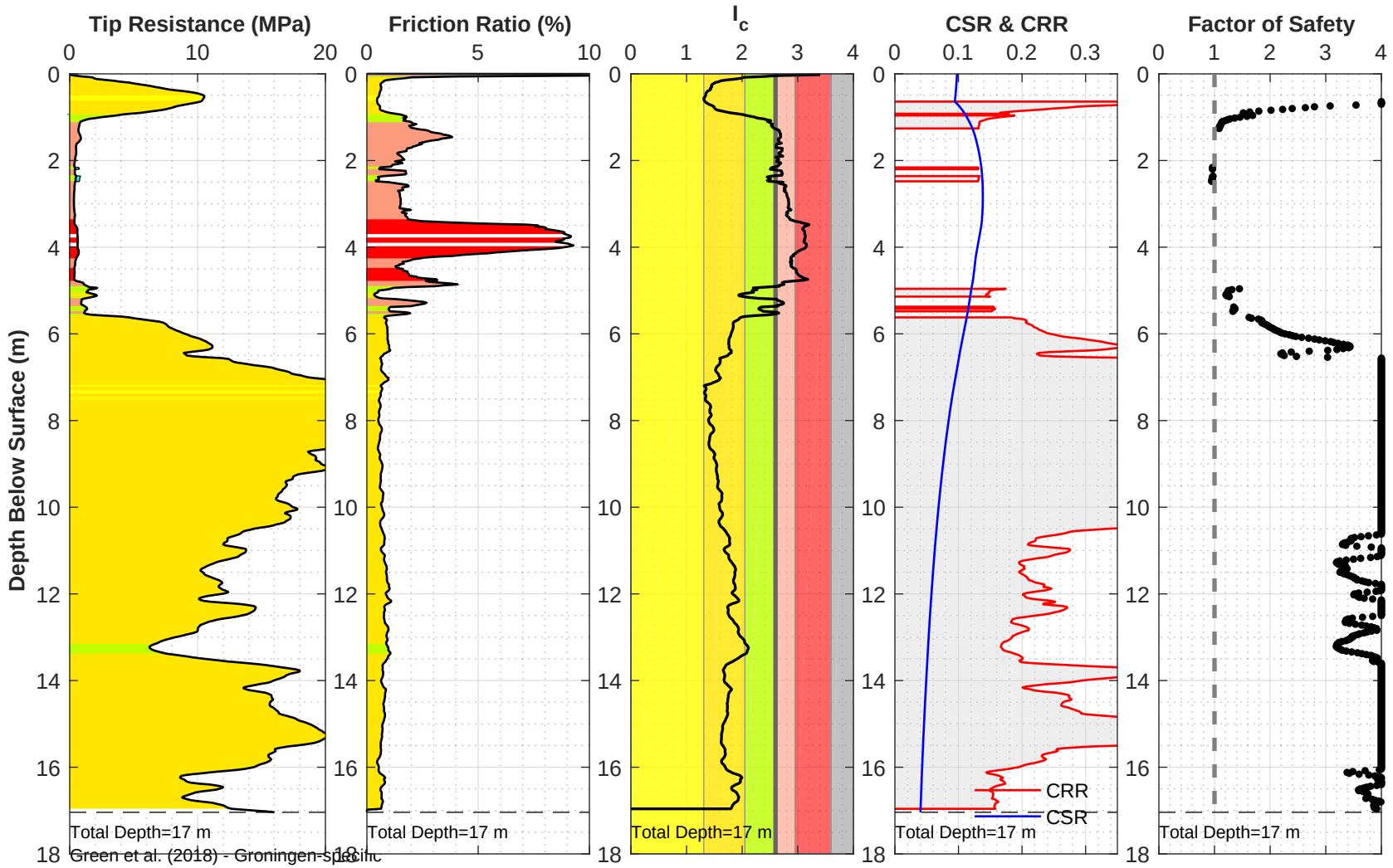

Location: 21225_279_coord
Surface EL: 1.1 m +/- (NAP)
Cone Diameter: 43.7 mm

Thin Layer Correction: NCEER (Youd et al. 2001)
Analysis Title: NC
Mw: 3.9 amax (g): 0.15

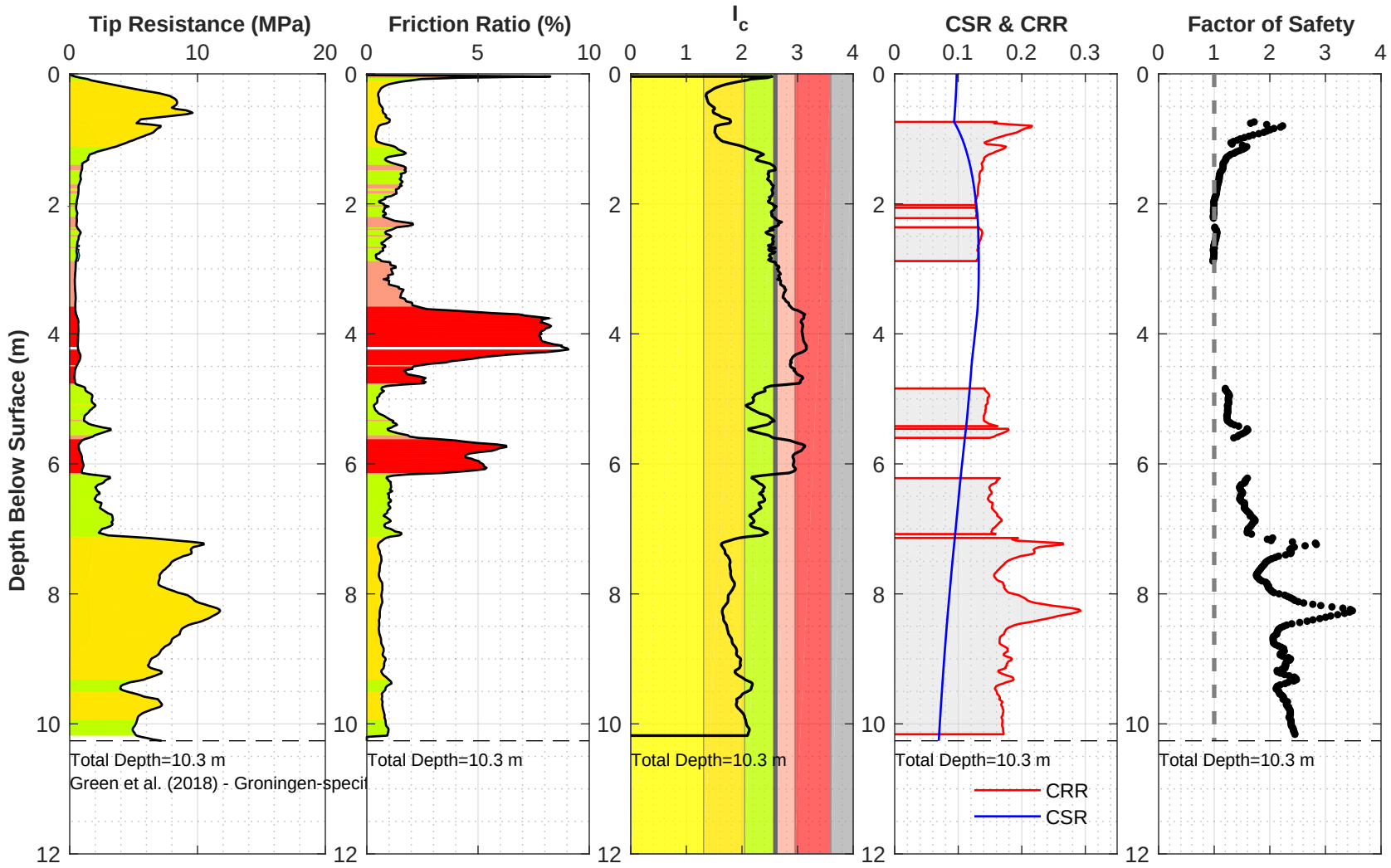

Location: 21225_280_coord
Surface EL: 1.2 m +/- (NAP)
Cone Diameter: 43.7 mm

Thin Layer Correction: NCEER (Youd et al. 2001)
Analysis Title: NC
Mw: 3.9 amax (g): 0.15

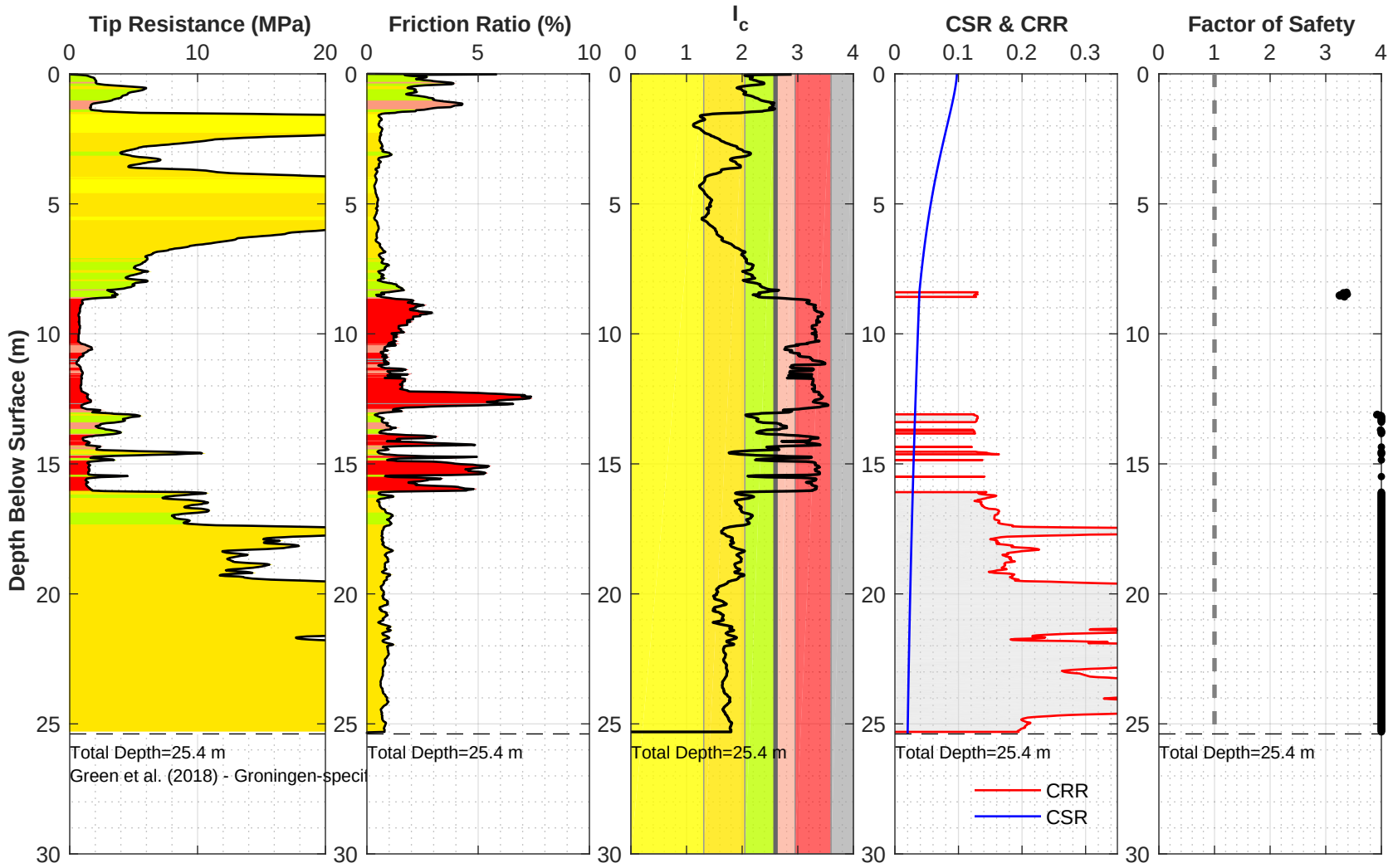

Location: 21225_281_coord
Surface EL: 8.9 m +/- (NAP)
Cone Diameter: 43.7 mm

Thin Layer Correction: NCEER (Youd et al. 2001)
Analysis Title: NC
Mw: 3.9 amax (g): 0.15

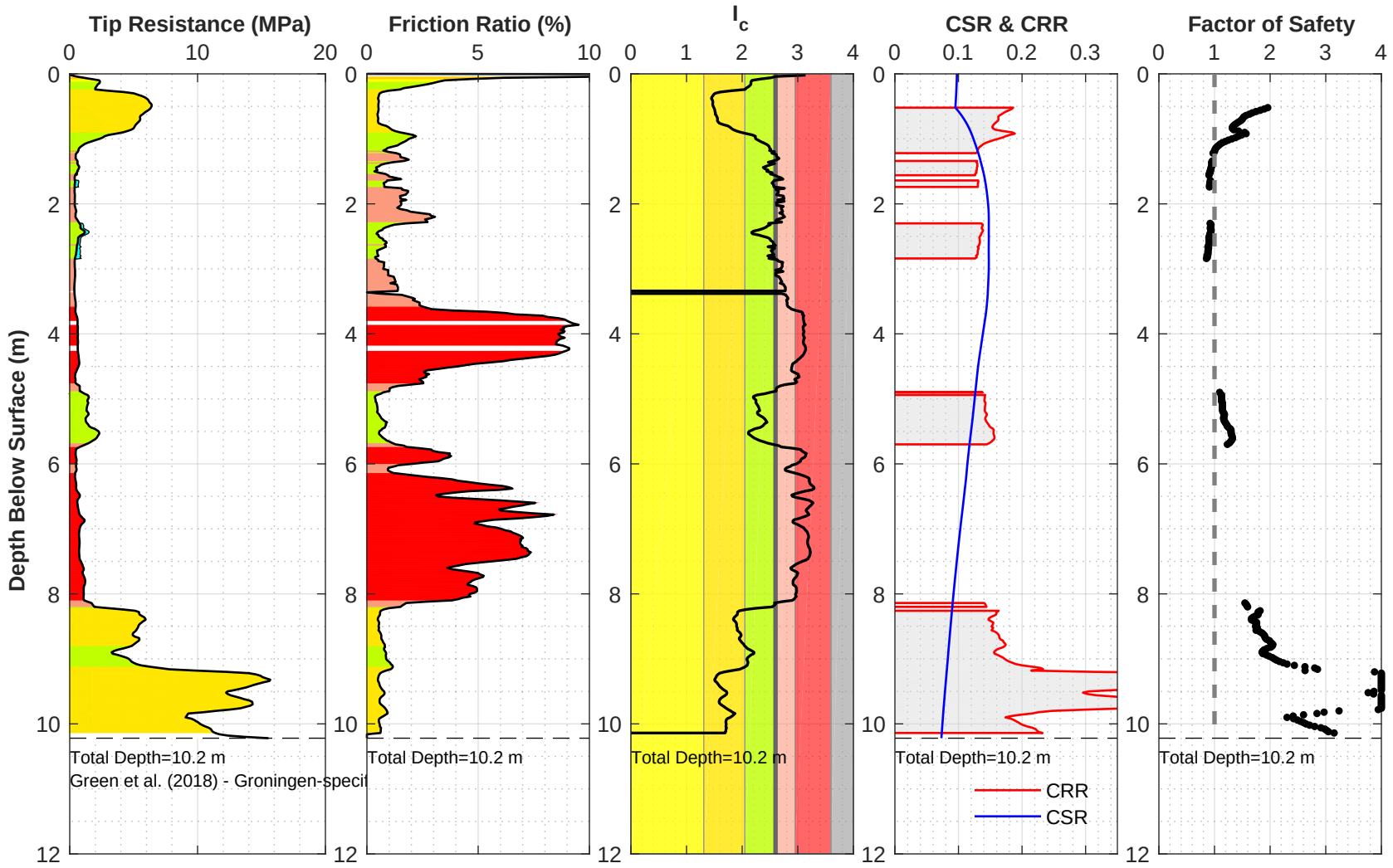

Location: 21225_282_coord
Surface EL: 1 m +/- (NAP)
Cone Diameter: 43.7 mm

Thin Layer Correction: NCEER (Youd et al. 2001)
Analysis Title: NC
Mw: 3.9 amax (g): 0.15

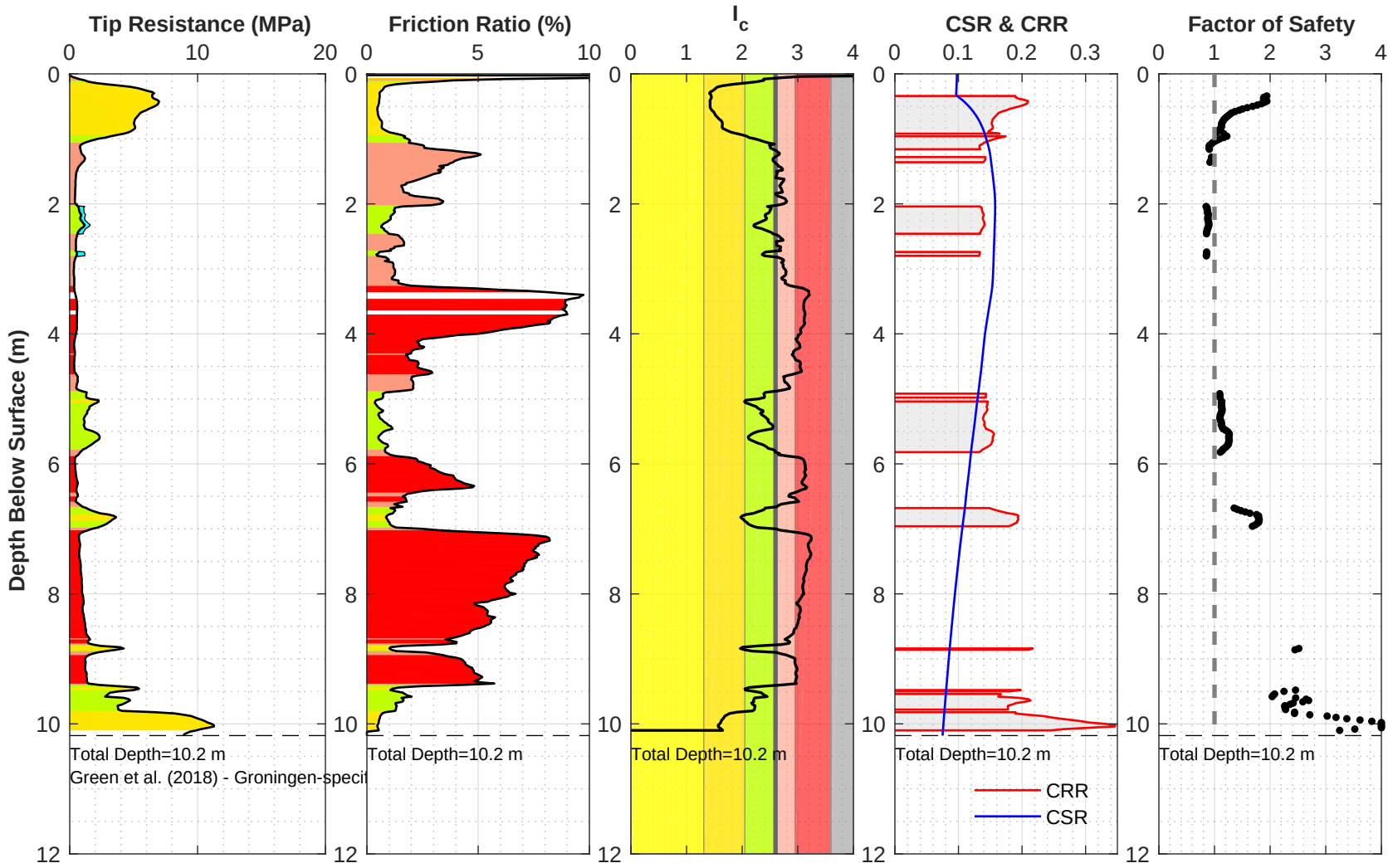

Location: 21225_283_coord
Surface EL: 0.8 m +/- (NAP)
Cone Diameter: 43.7 mm

Thin Layer Correction: NCEER (Youd et al. 2001)
Analysis Title: NC
Mw: 3.9 amax (g): 0.15

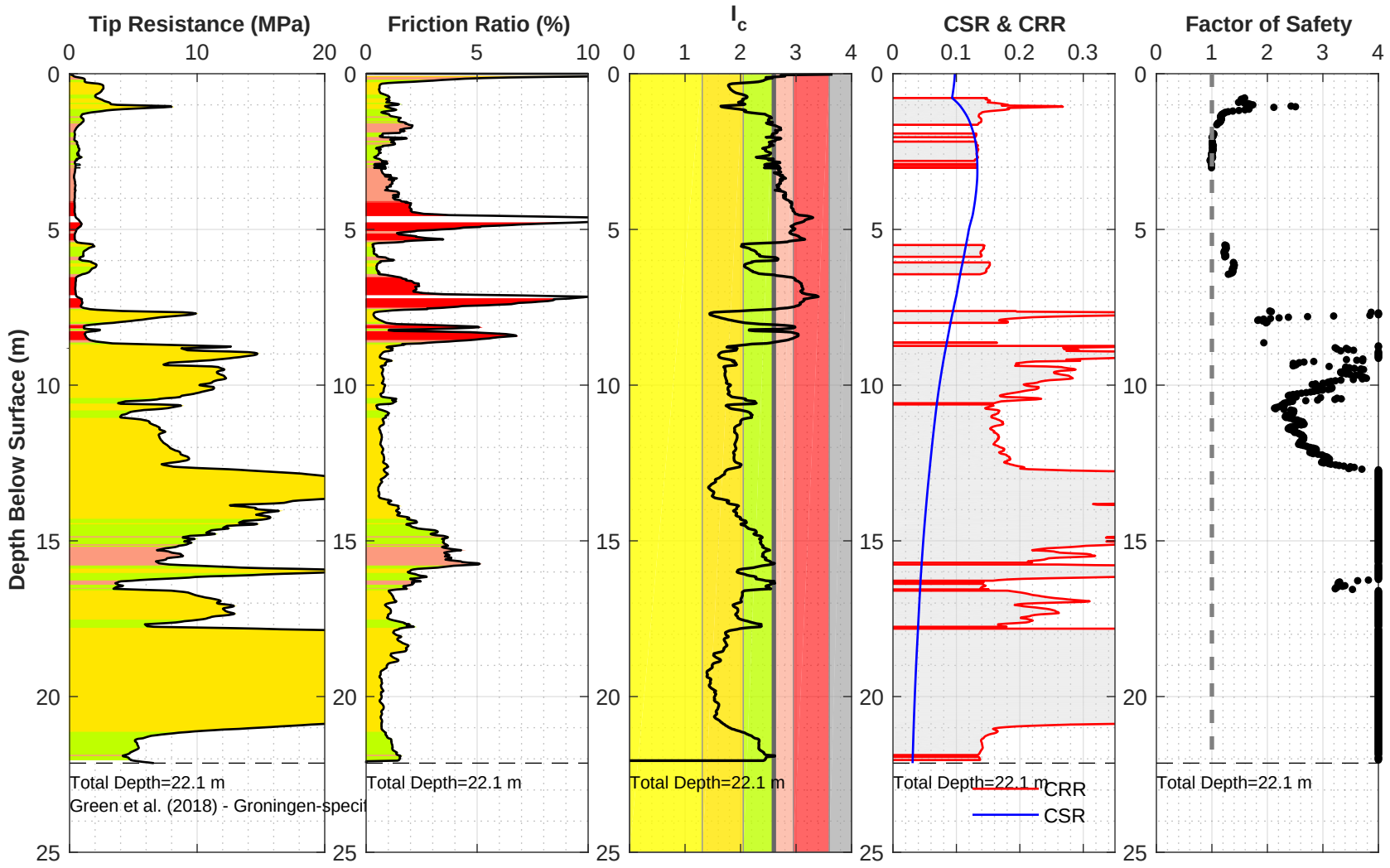

Location: 21225_284_coord
Surface EL: 1.3 m +/- (NAP)
Cone Diameter: 43.7 mm

Thin Layer Correction: NCEER (Youd et al. 2001)
Analysis Title: NC
Mw: 3.9 amax (g): 0.15

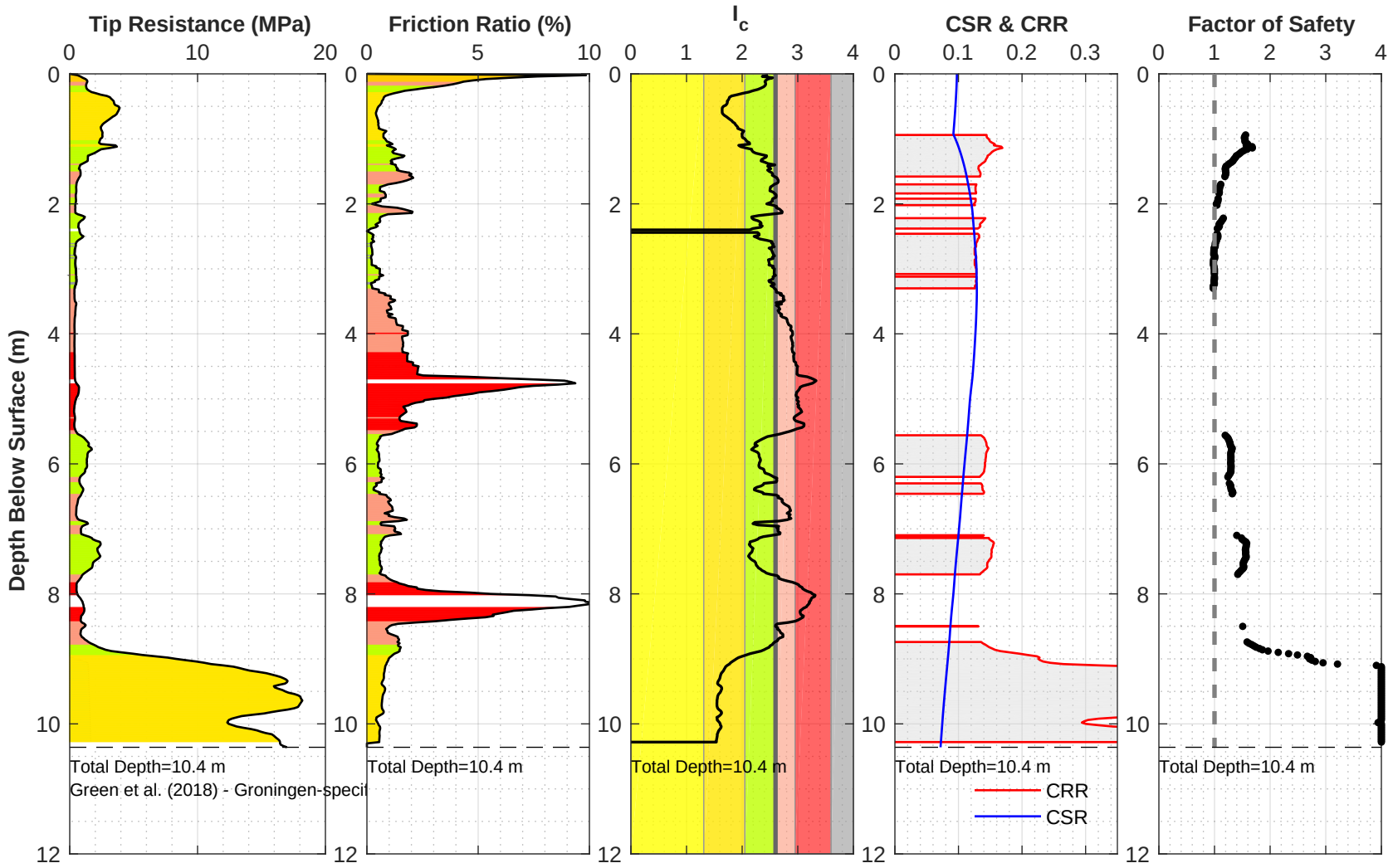

Location: 21225_285_coord
Surface EL: 1.4 m +/- (NAP)
Cone Diameter: 43.7 mm

Thin Layer Correction: NCEER (Youd et al. 2001)
Analysis Title: NC
Mw: 3.9 amax (g): 0.15

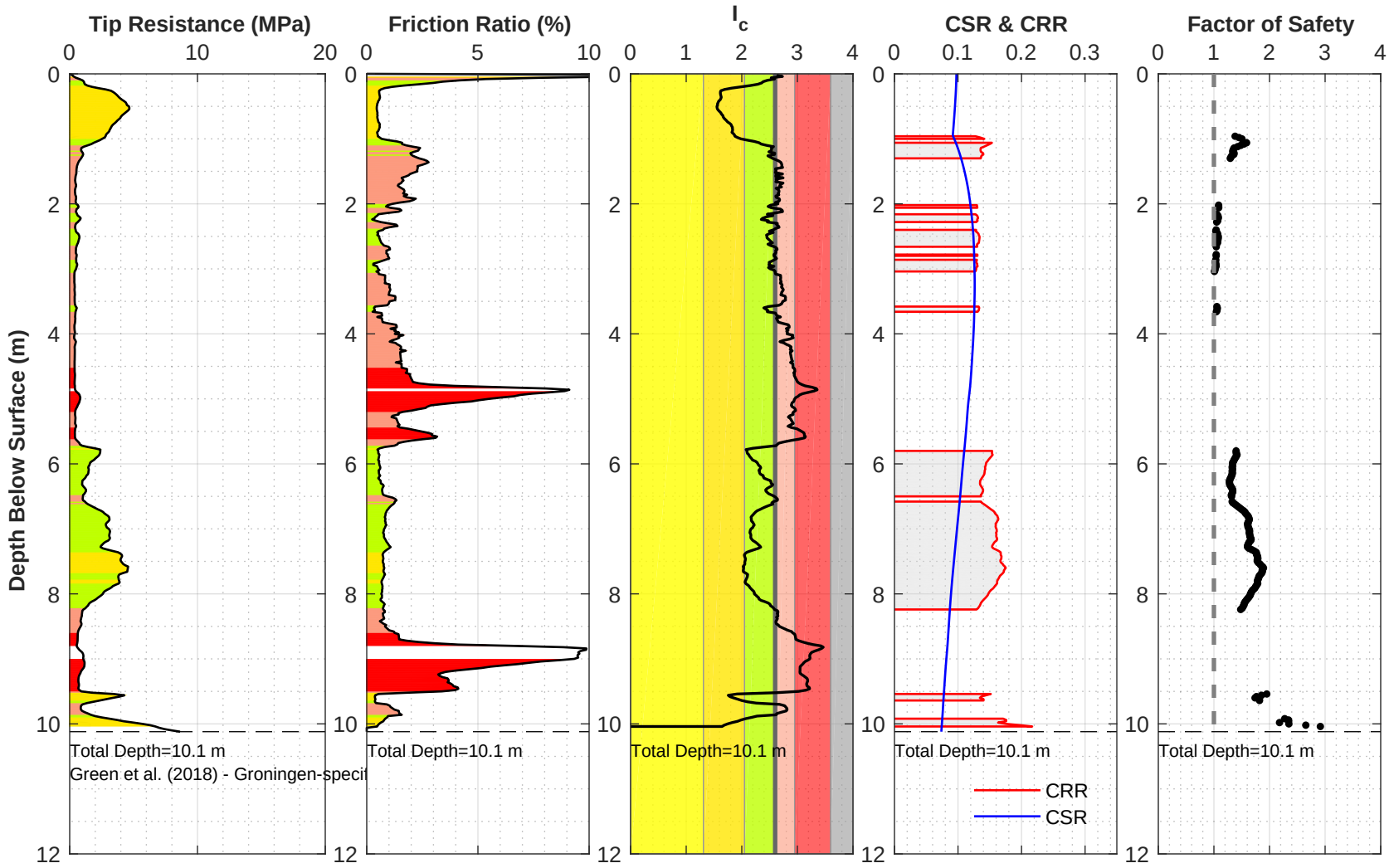

Location: 21225_286_coord
Surface EL: 1.5 m +/- (NAP)
Cone Diameter: 43.7 mm

Thin Layer Correction: NCEER (Youd et al. 2001)
Analysis Title: NC
Mw: 3.9 amax (g): 0.15

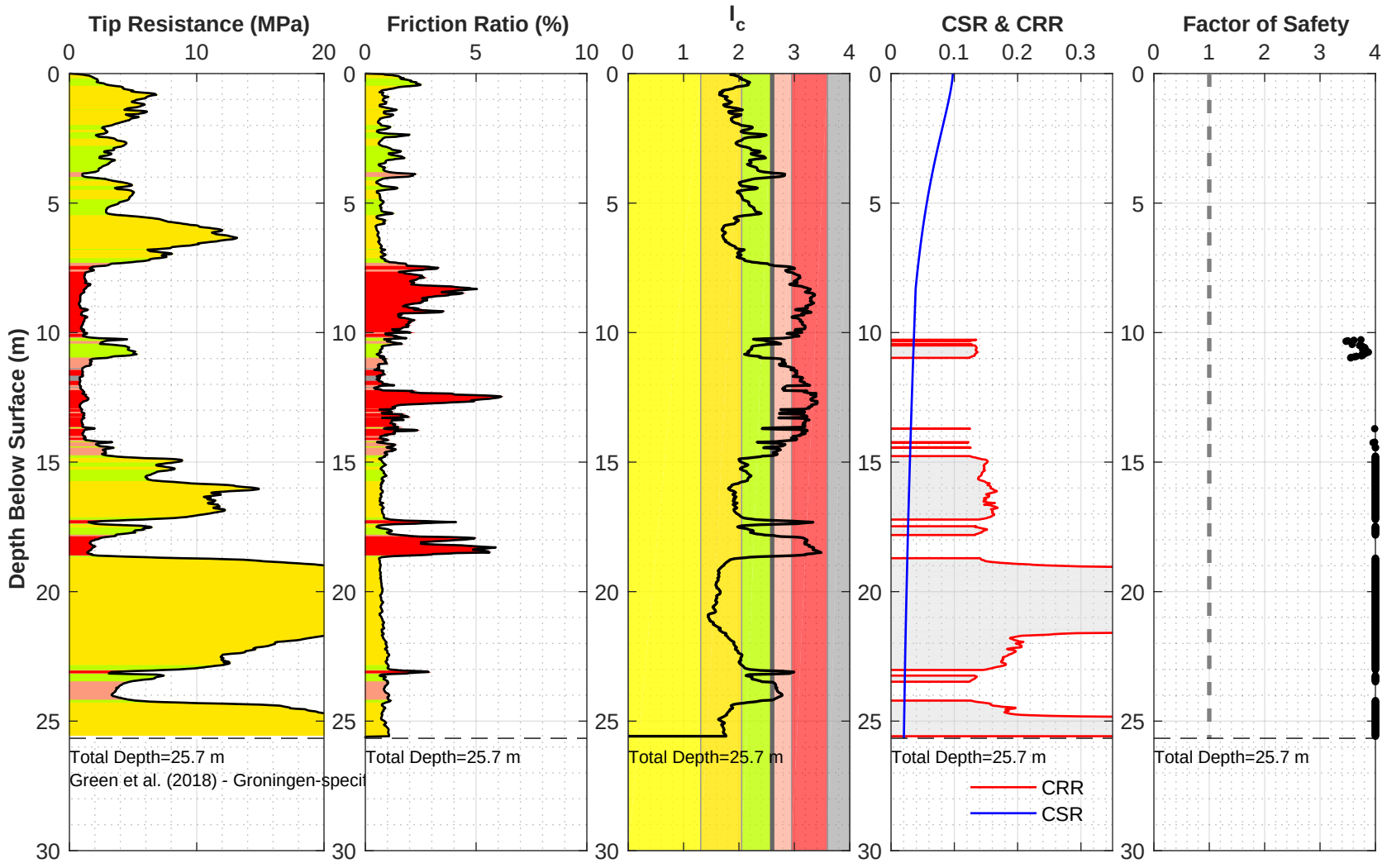

Location: 21225_287_coord
Surface EL: 8.8 m +/- (NAP)
Cone Diameter: 43.7 mm

Thin Layer Correction: NCEER (Youd et al. 2001)
Analysis Title: NC
Mw: 3.9 amax (g): 0.15

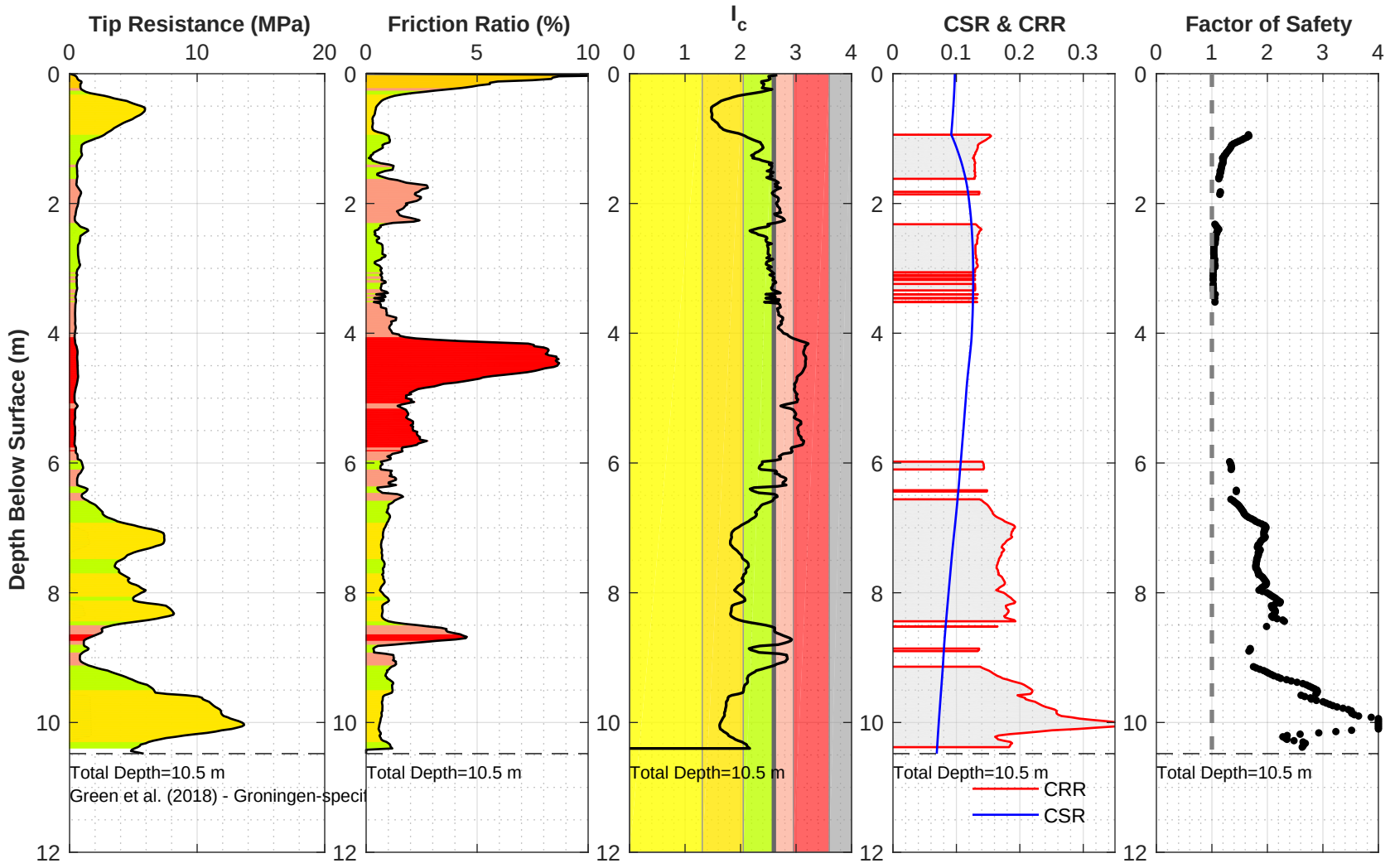

Location: 21225_288_coord
Surface EL: 1.4 m +/- (NAP)
Cone Diameter: 43.7 mm

Thin Layer Correction: NCEER (Youd et al. 2001)
Analysis Title: NC
Mw: 3.9 amax (g): 0.15

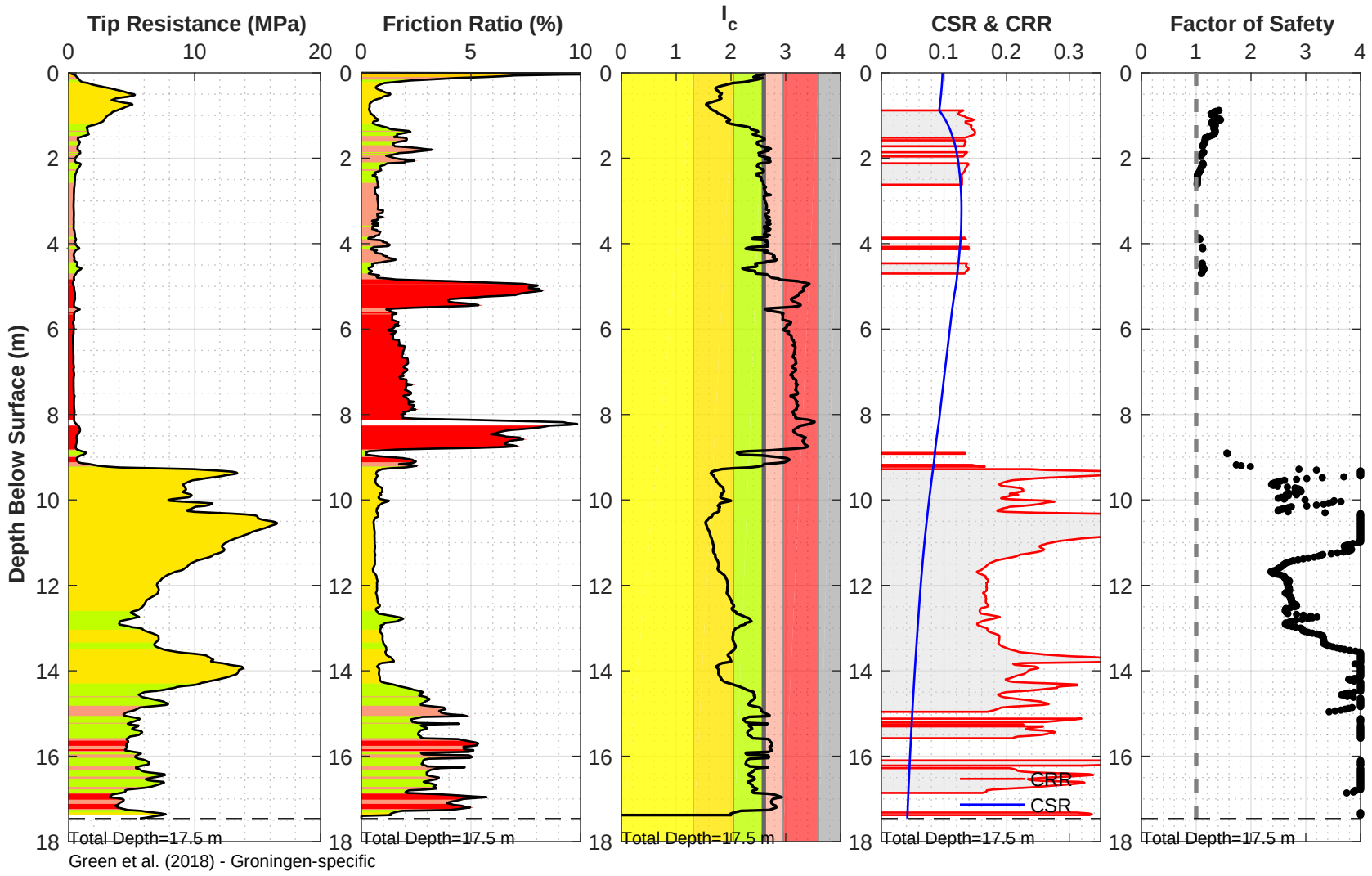

Green et al. (2018) - Groningen-specific

Location: 21225_289_coord
Surface EL: 1.4 m +/- (NAP)
Cone Diameter: 43.7 mm

Thin Layer Correction: NCEER (Youd et al. 2001)
Analysis Title: NC
Mw: 3.9 amax (g): 0.15

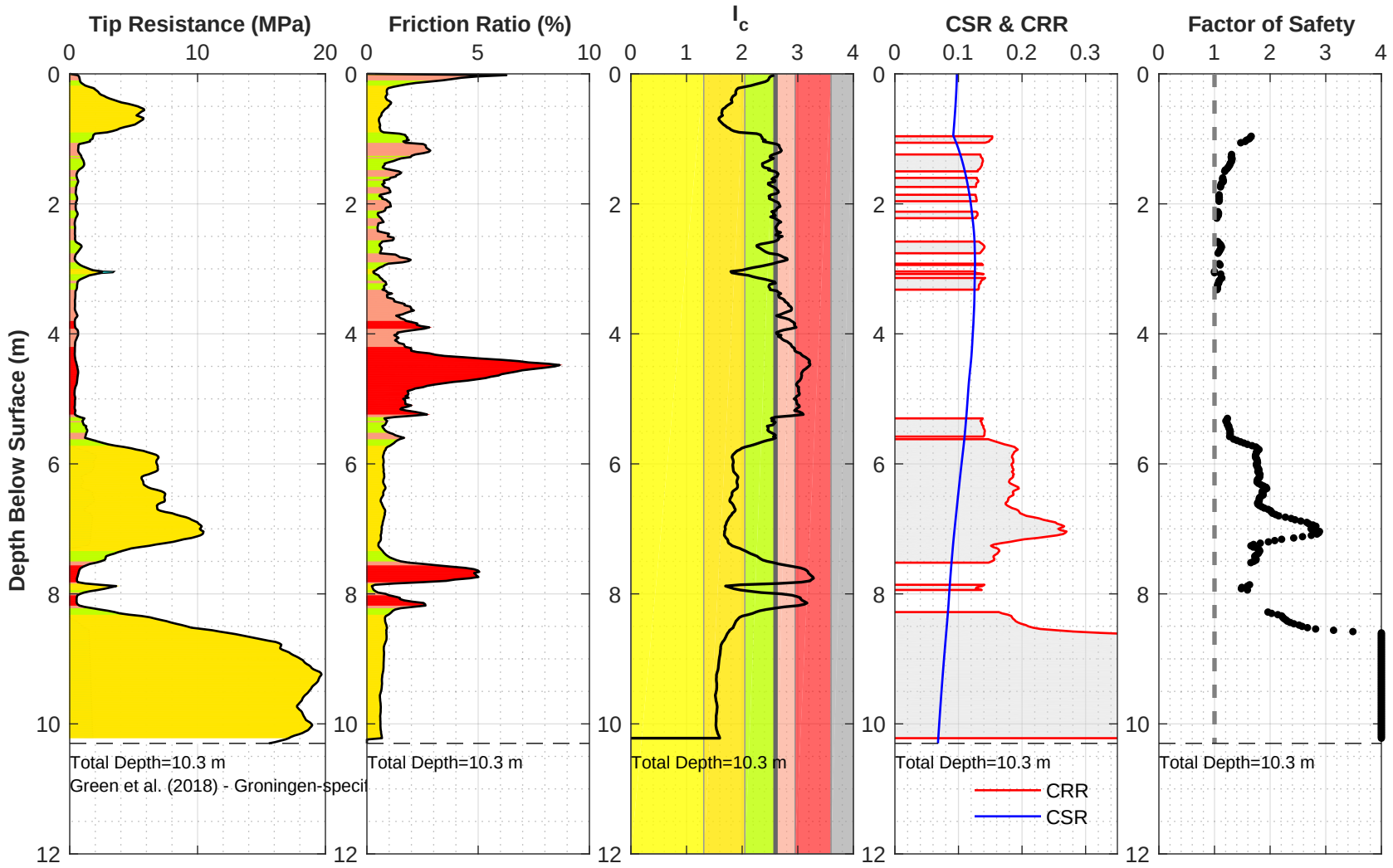

Location: 21225_290_coord
Surface EL: 1.5 m +/- (NAP)
Cone Diameter: 43.7 mm

Thin Layer Correction: NCEER (Youd et al. 2001)
Analysis Title: NC
Mw: 3.9 amax (g): 0.15

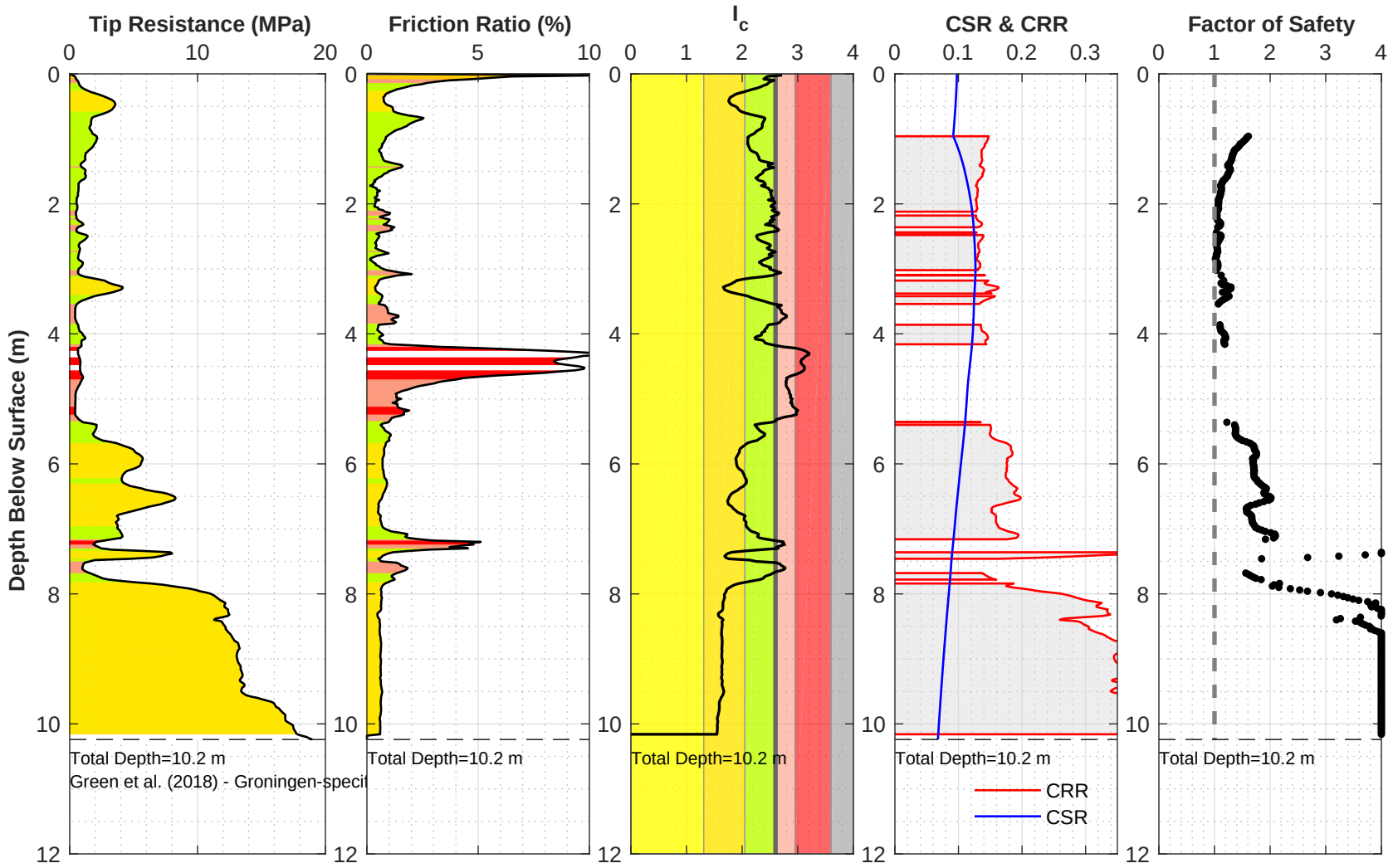

Location: 21225_291_coord
Surface EL: 1.5 m +/- (NAP)
Cone Diameter: 43.7 mm

Thin Layer Correction: NCEER (Youd et al. 2001)
Analysis Title: NC
Mw: 3.9 amax (g): 0.15

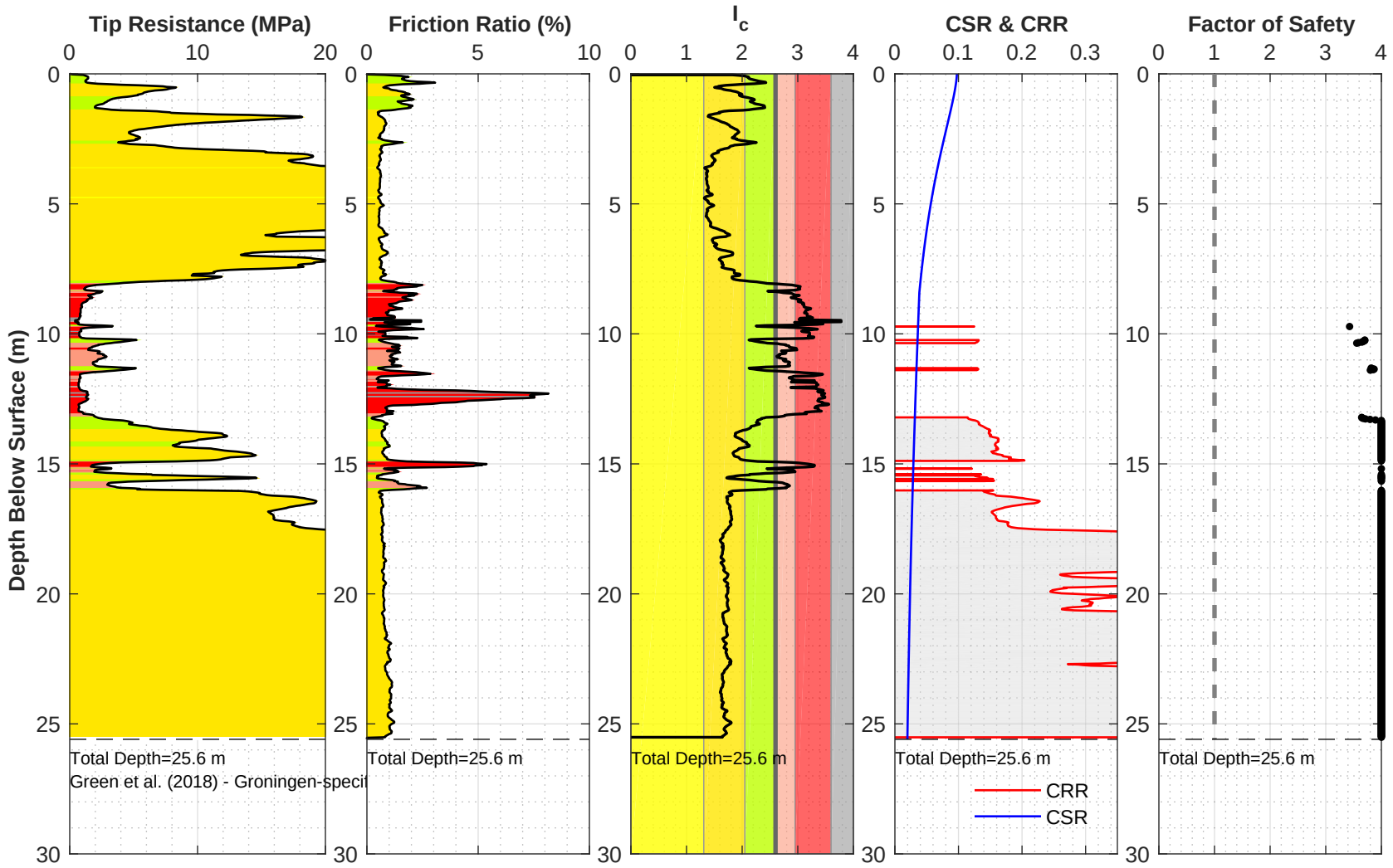

Location: 21225_292_coord
Surface EL: 8.9 m +/- (NAP)
Cone Diameter: 43.7 mm

Thin Layer Correction: NCEER (Youd et al. 2001)
Analysis Title: NC
Mw: 3.9 amax (g): 0.15

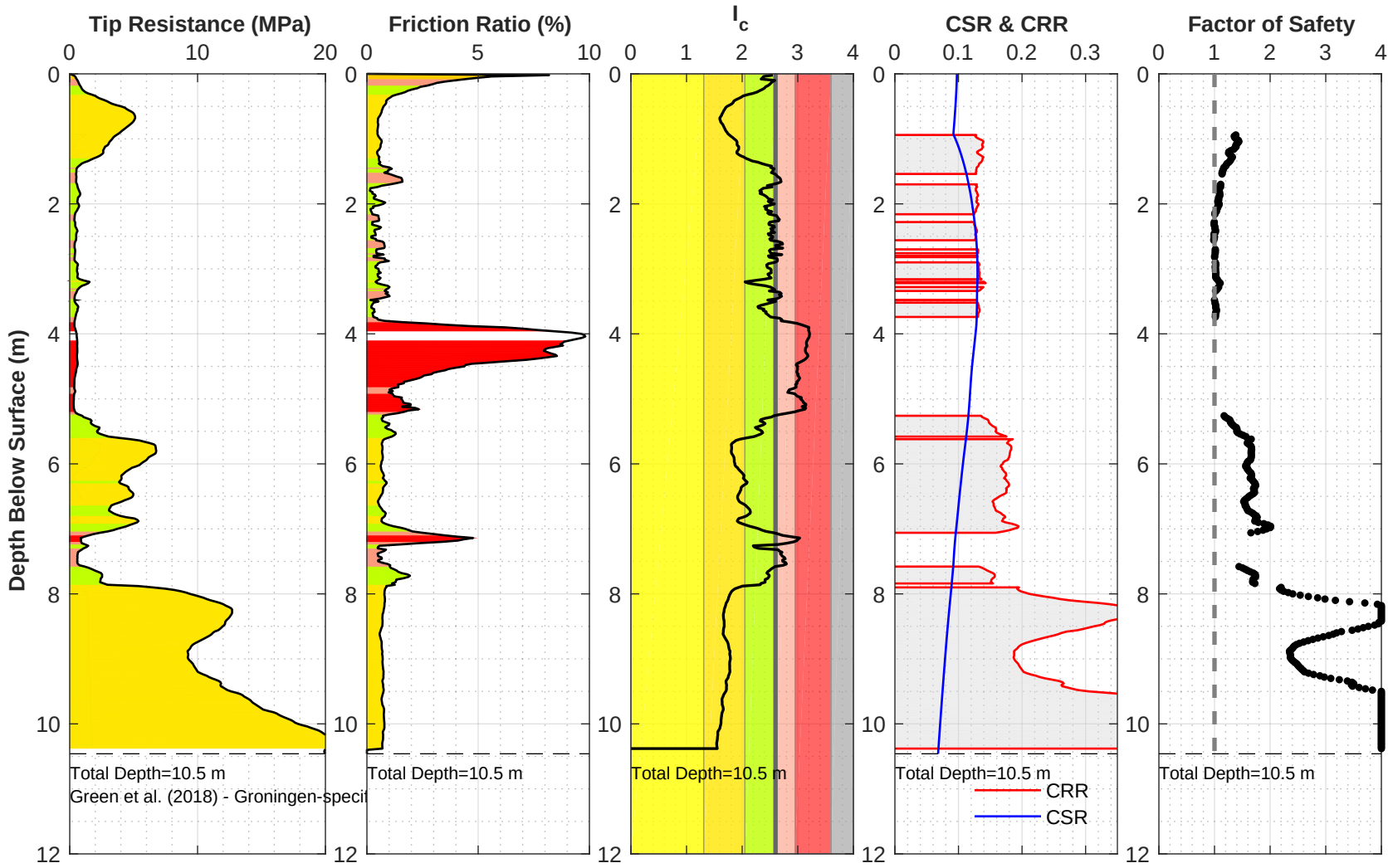

Location: 21225_293_coord
Surface EL: 1.4 m +/- (NAP)
Cone Diameter: 43.7 mm

Thin Layer Correction: NCEER (Youd et al. 2001)
Analysis Title: NC
Mw: 3.9 amax (g): 0.15

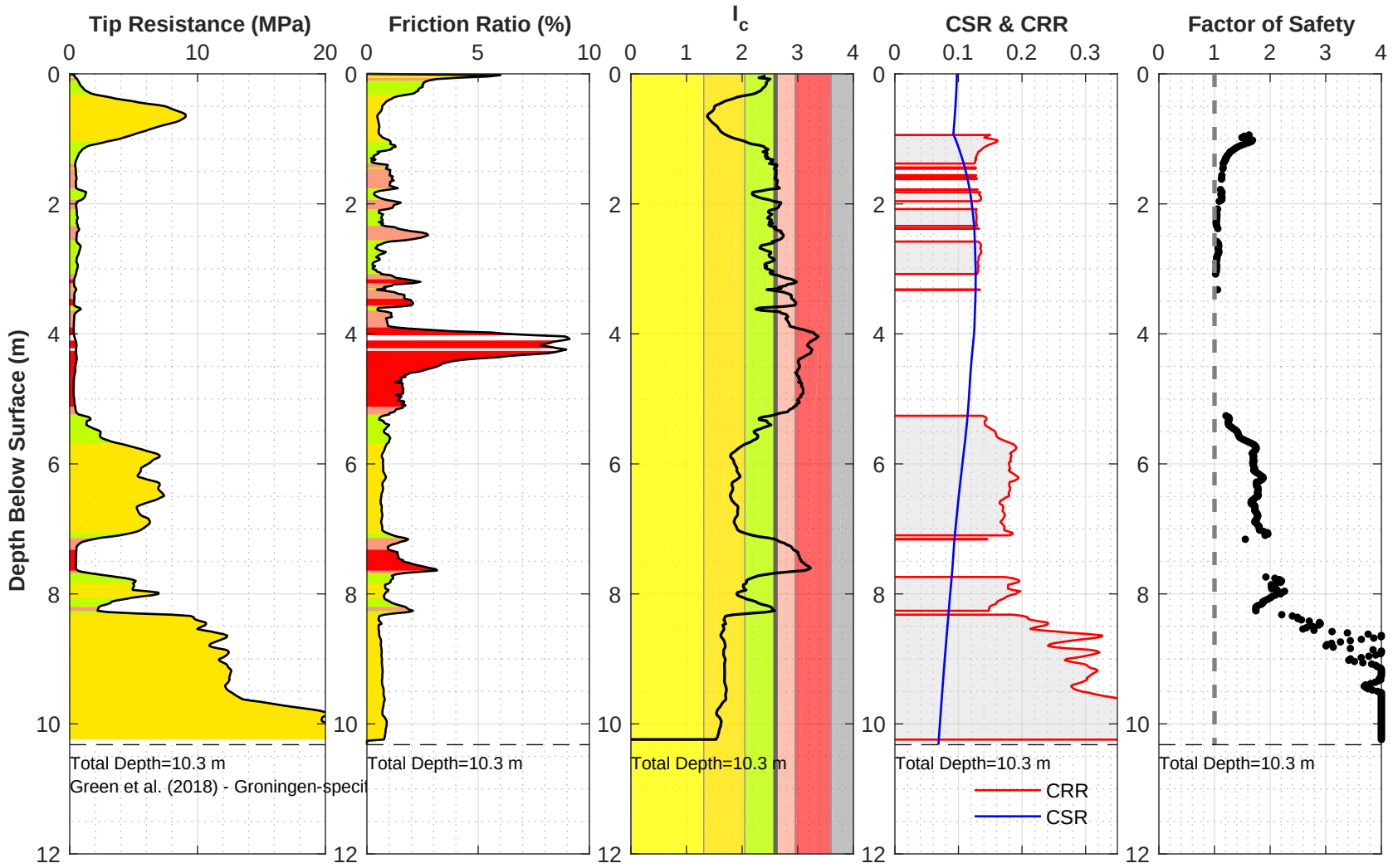

Location: 21225_294_coord
Surface EL: 1.4 m +/- (NAP)
Cone Diameter: 43.7 mm

Thin Layer Correction: NCEER (Youd et al. 2001)
Analysis Title: NC
Mw: 3.9 amax (g): 0.15

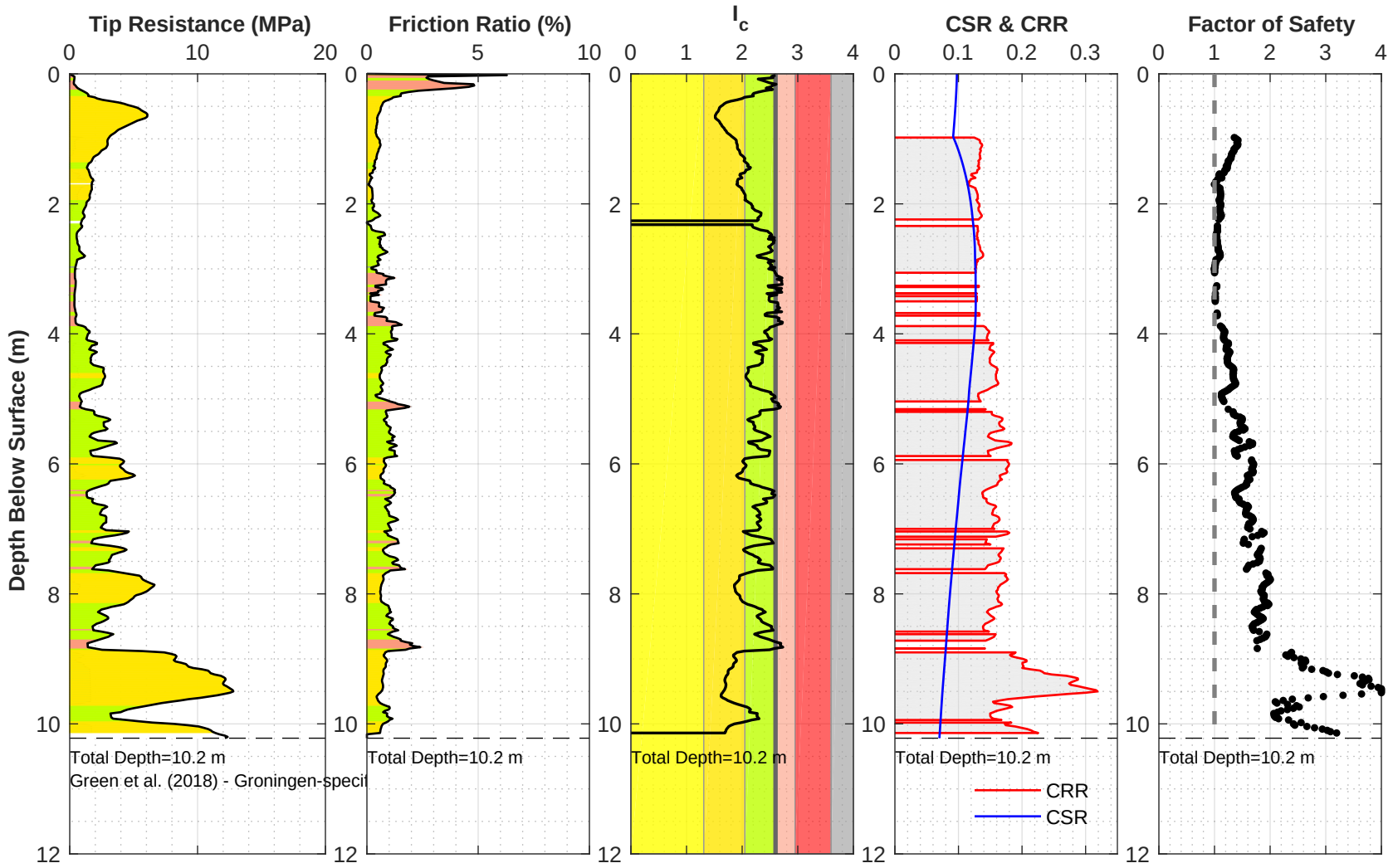

Location: 21225_295_coord
Surface EL: 1.5 m +/- (NAP)
Cone Diameter: 43.7 mm

Thin Layer Correction: NCEER (Youd et al. 2001)
Analysis Title: NC
Mw: 3.9 amax (g): 0.15

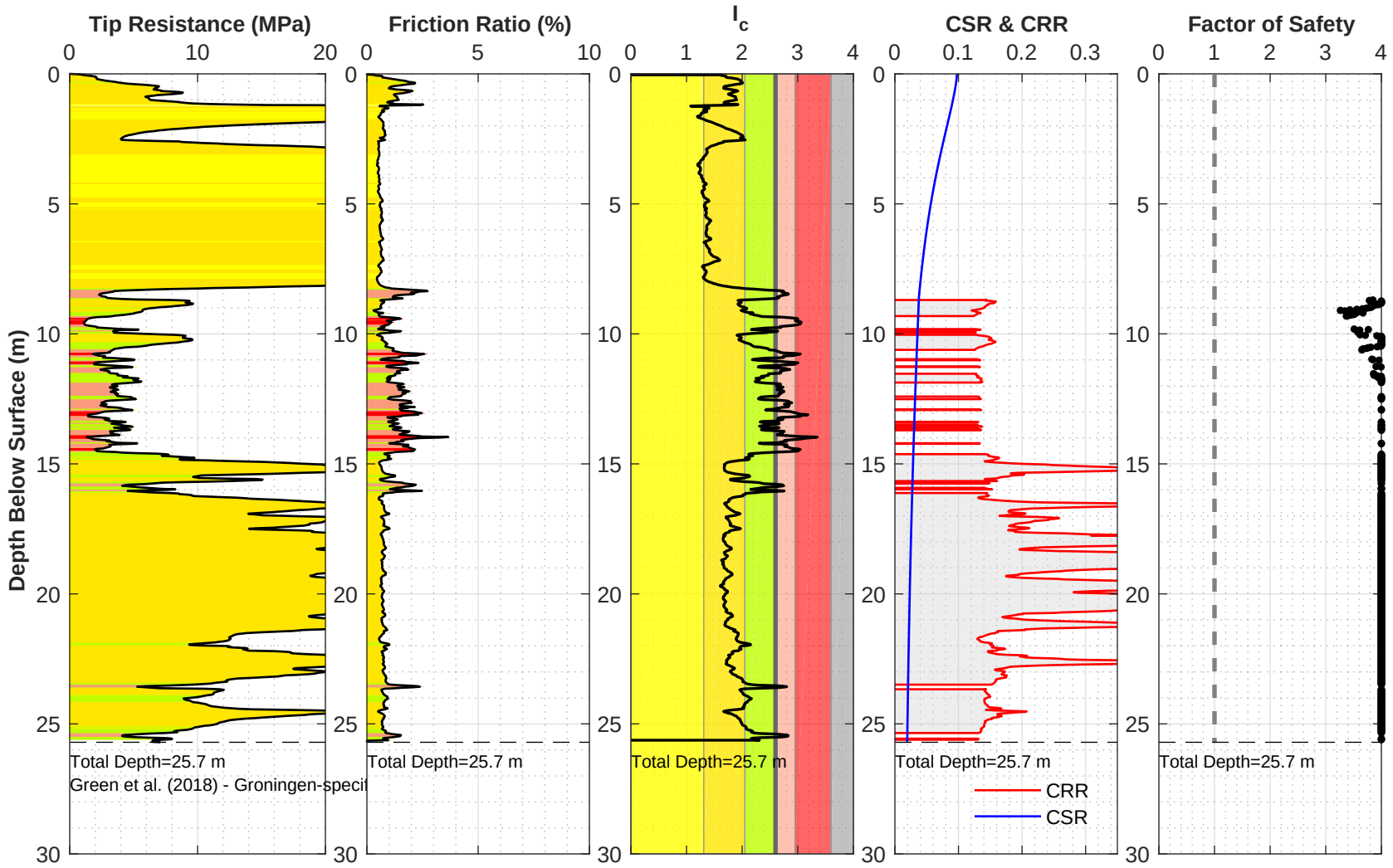

Location: 21225_296_coord
Surface EL: 9.1 m +/- (NAP)
Cone Diameter: 43.7 mm

Thin Layer Correction: NCEER (Youd et al. 2001)
Analysis Title: NC
Mw: 3.9 amax (g): 0.15

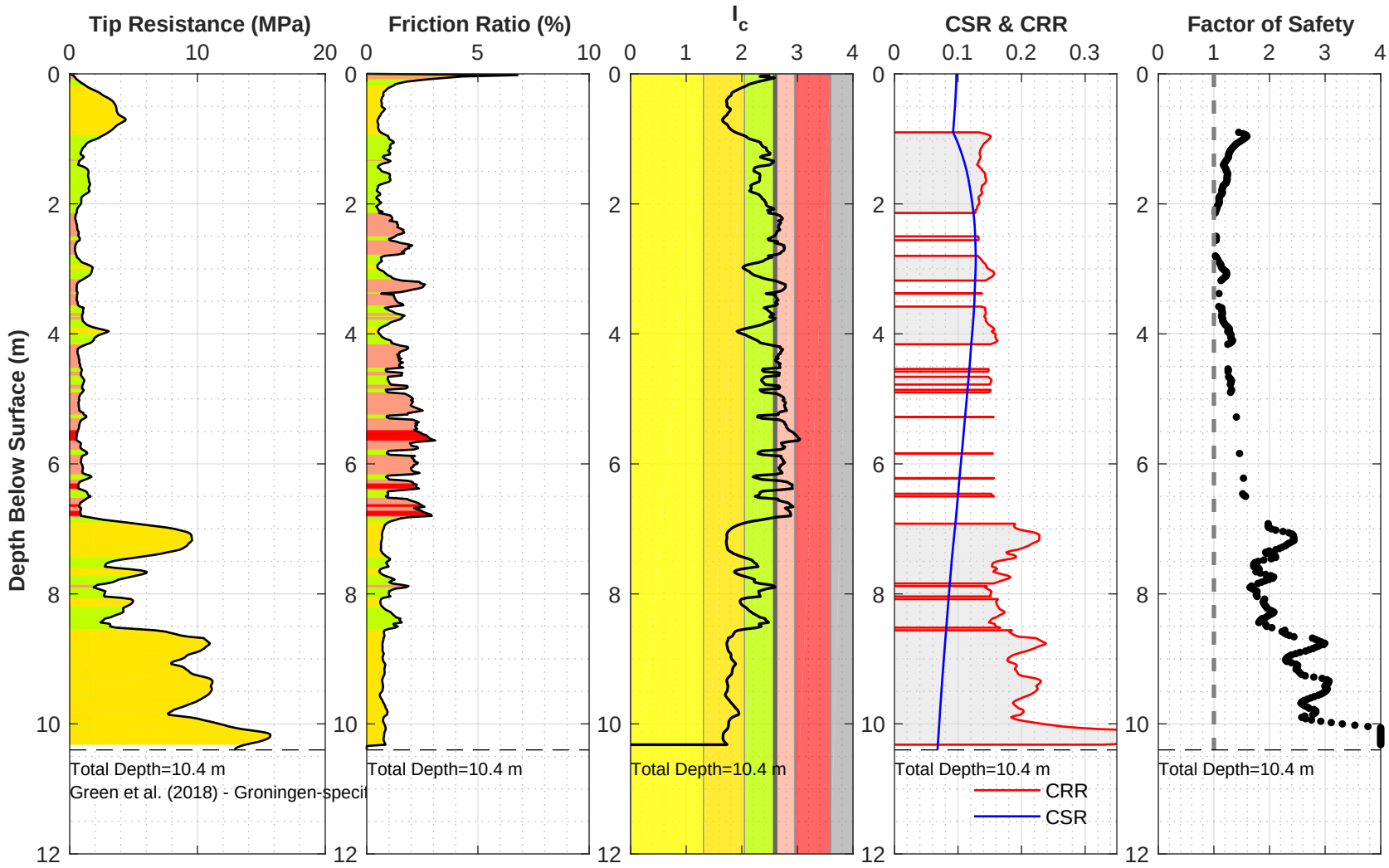

Location: 21225_297_coord
Surface EL: 1.4 m +/- (NAP)
Cone Diameter: 43.7 mm

Thin Layer Correction: NCEER (Youd et al. 2001)
Analysis Title: NC
Mw: 3.9 amax (g): 0.15

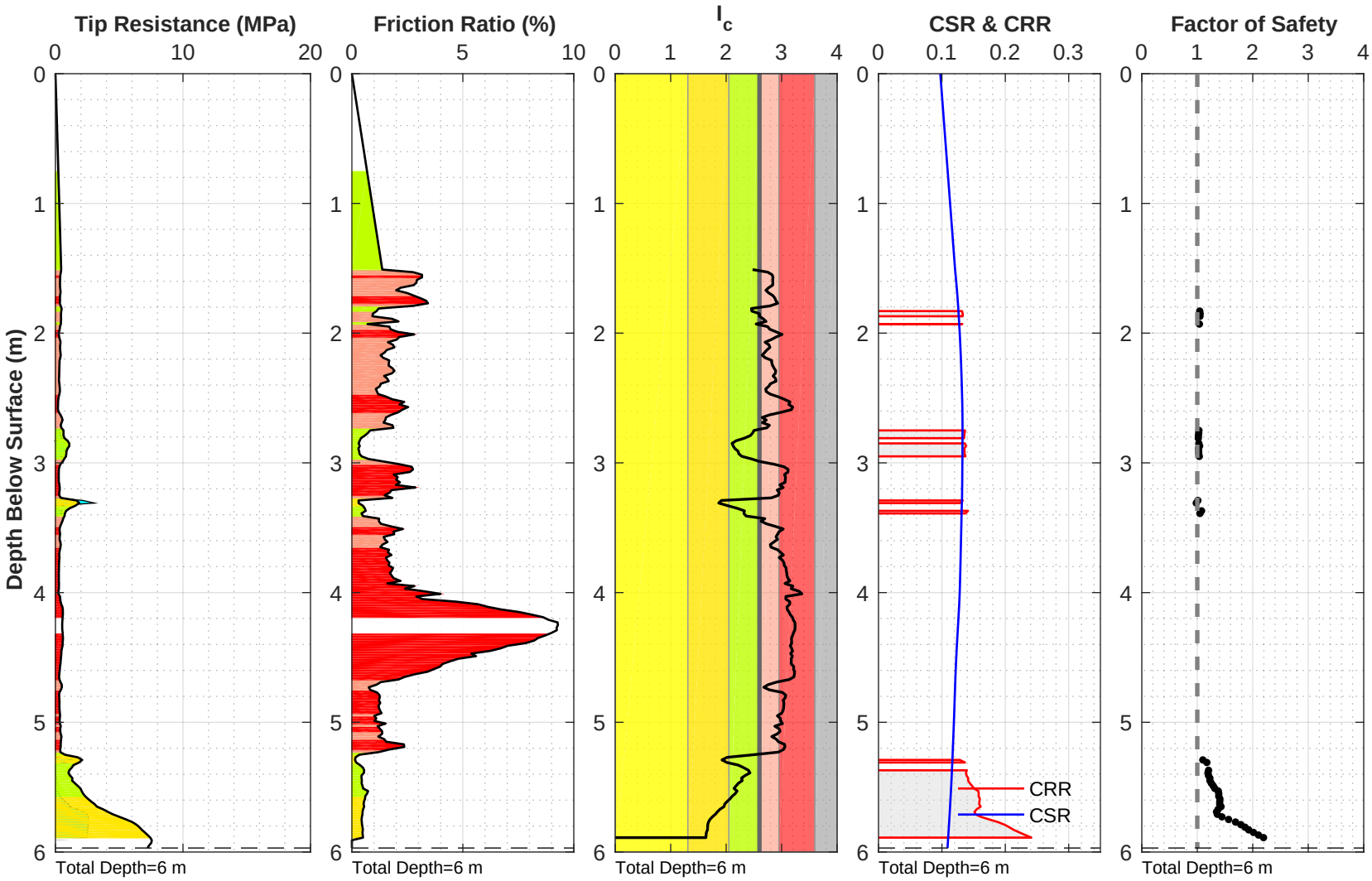

Green et al. (2018) - Groningen-specific

Location: S1-W48.1BIT
Surface EL: 1.2 m +/- (NAP)
Cone Diameter: 43.7 mm

Thin Layer Correction: NCEER (Youd et al. 2001)
Analysis Title: NC
Mw: 3.9 amax (g): 0.15

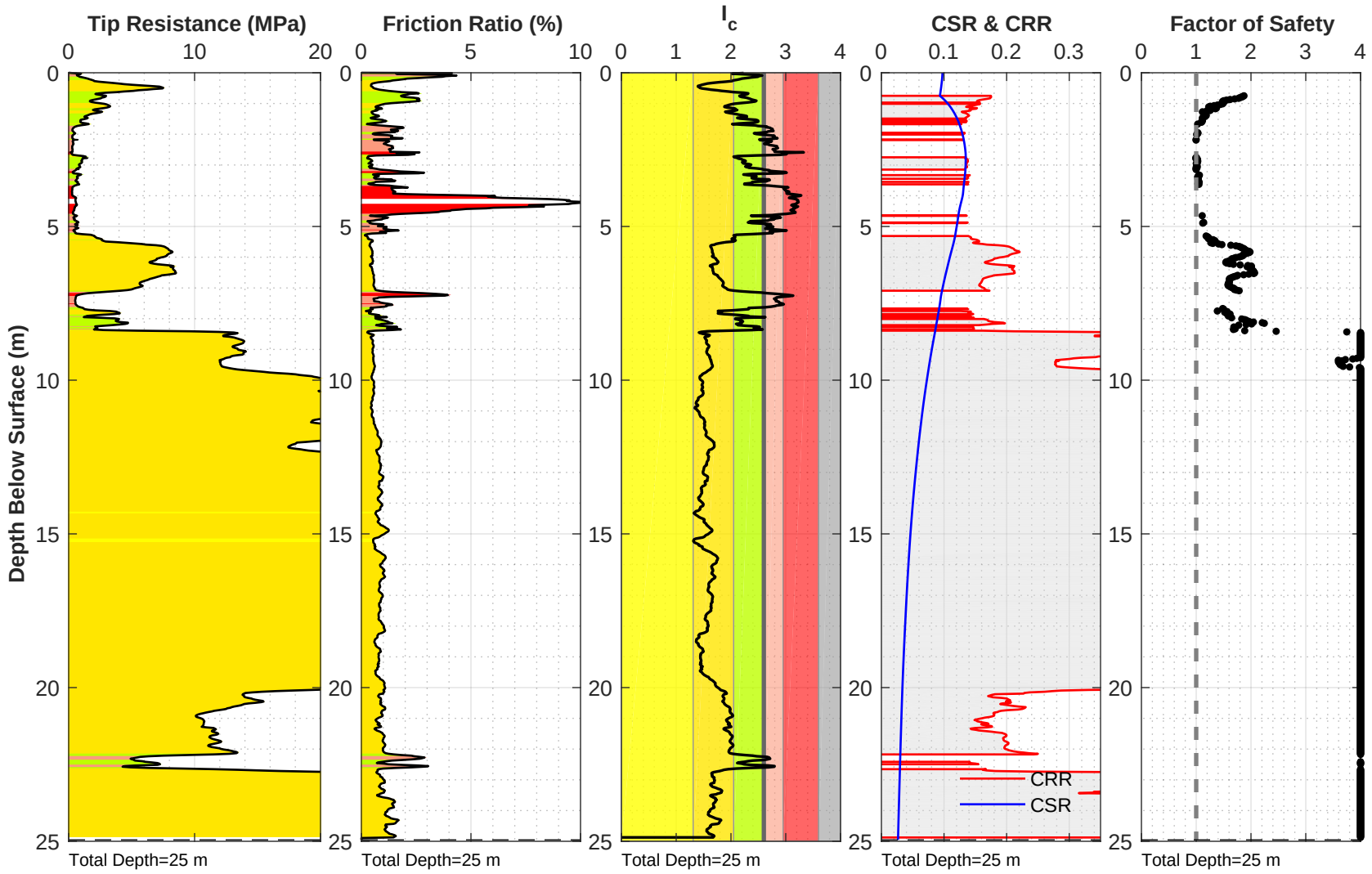

Green et al. (2018) - Groningen-specific
Location: S2-W48.1BIT
Surface EL: 1.3 m +/- (NAP)
Cone Diameter: 43.7 mm

Thin Layer Correction: NCEER (Youd et al. 2001)
Analysis Title: NC
Mw: 3.9 amax (g): 0.15

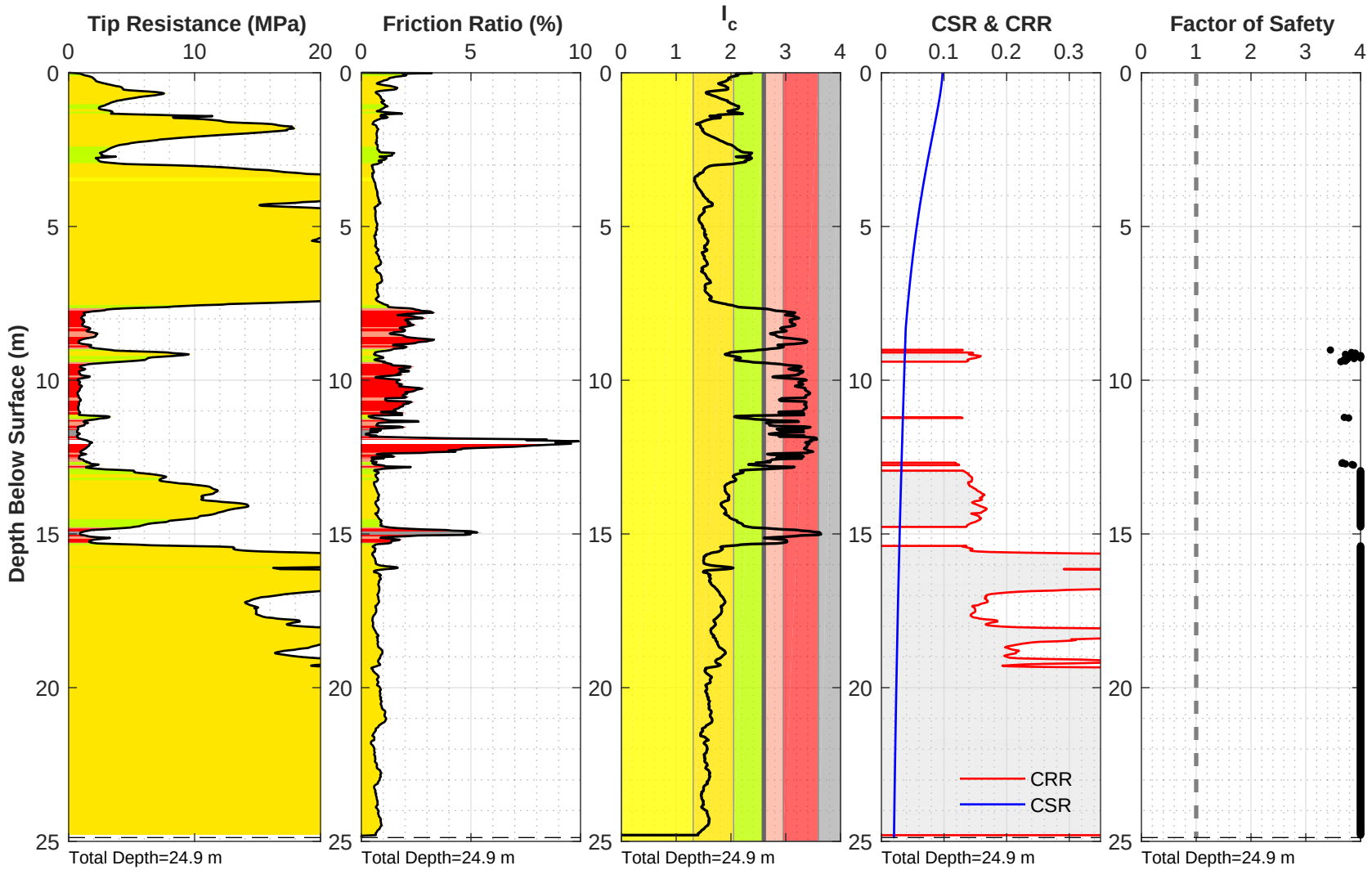

Green et al. (2018) - Groningen-specific

Location: S2-W48.1KR

Surface EL: 8.8 m +/- (NAP)

Cone Diameter: 43.7 mm

Thin Layer Correction: NCEER (Youd et al. 2001)

Analysis Title: NC

Mw: 3.9 amax (g): 0.15

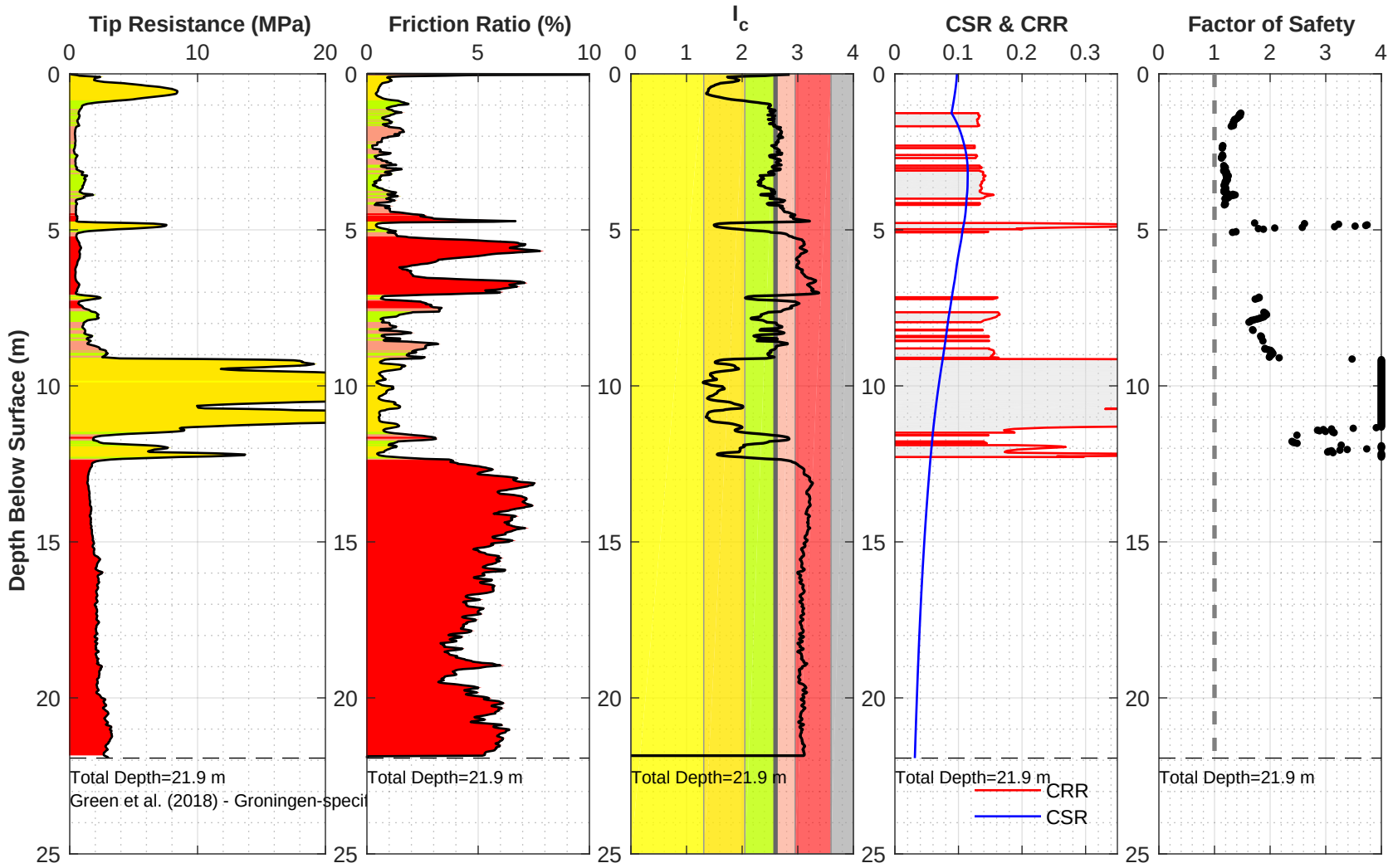

Location: 21225_234_coord
Surface EL: 1.8 m +/- (NAP)
Cone Diameter: 43.7 mm

Thin Layer Correction: NCEER (Youd et al. 2001)
Analysis Title: NC
Mw: 3.9 amax (g): 0.15

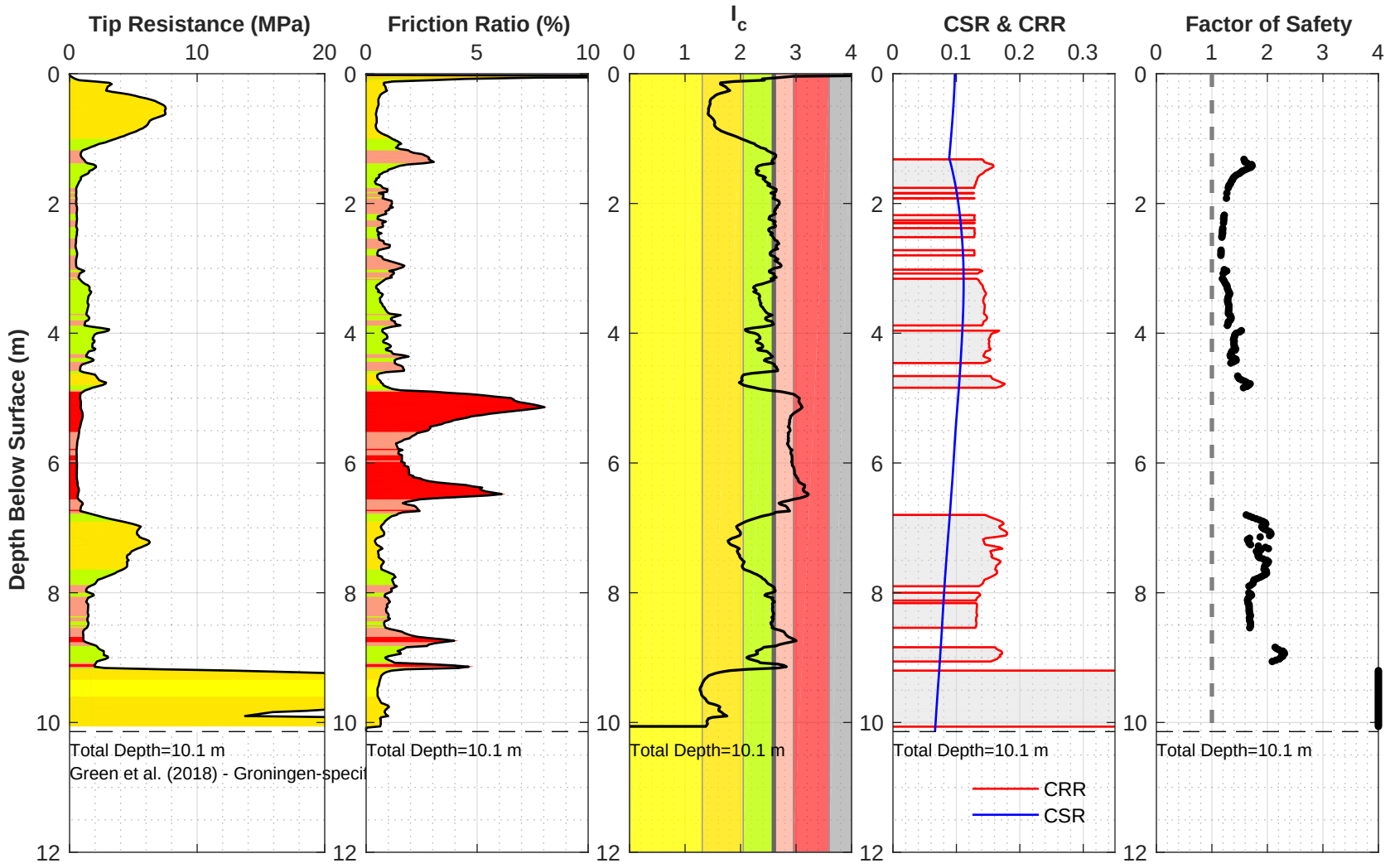

Location: 21225_235_coord
Surface EL: 1.8 m +/- (NAP)
Cone Diameter: 43.7 mm

Thin Layer Correction: NCEER (Youd et al. 2001)
Analysis Title: NC
Mw: 3.9 amax (g): 0.15

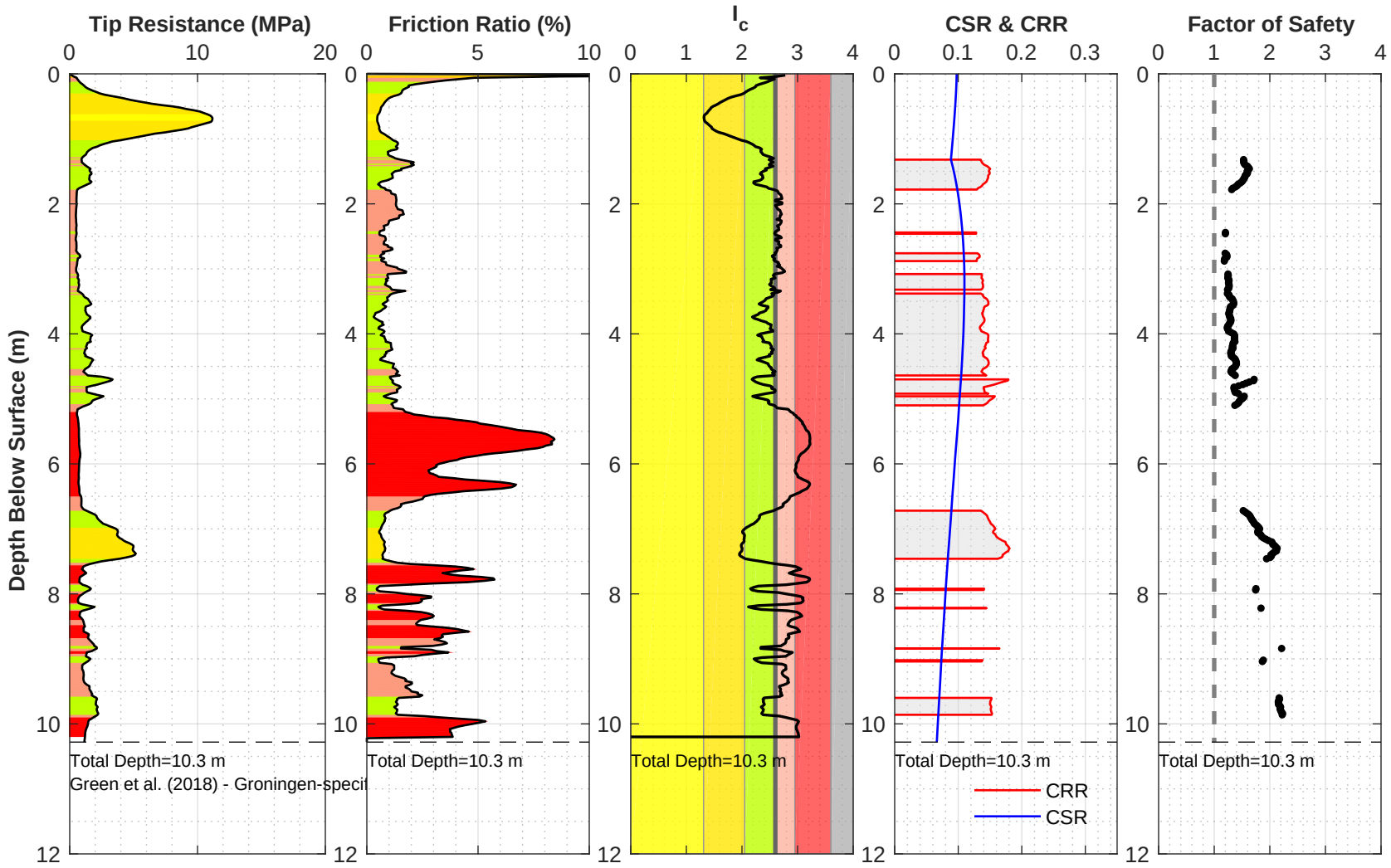

Location: 21225_236_coord
Surface EL: 1.8 m +/- (NAP)
Cone Diameter: 43.7 mm

Thin Layer Correction: NCEER (Youd et al. 2001)
Analysis Title: NC
Mw: 3.9 amax (g): 0.15

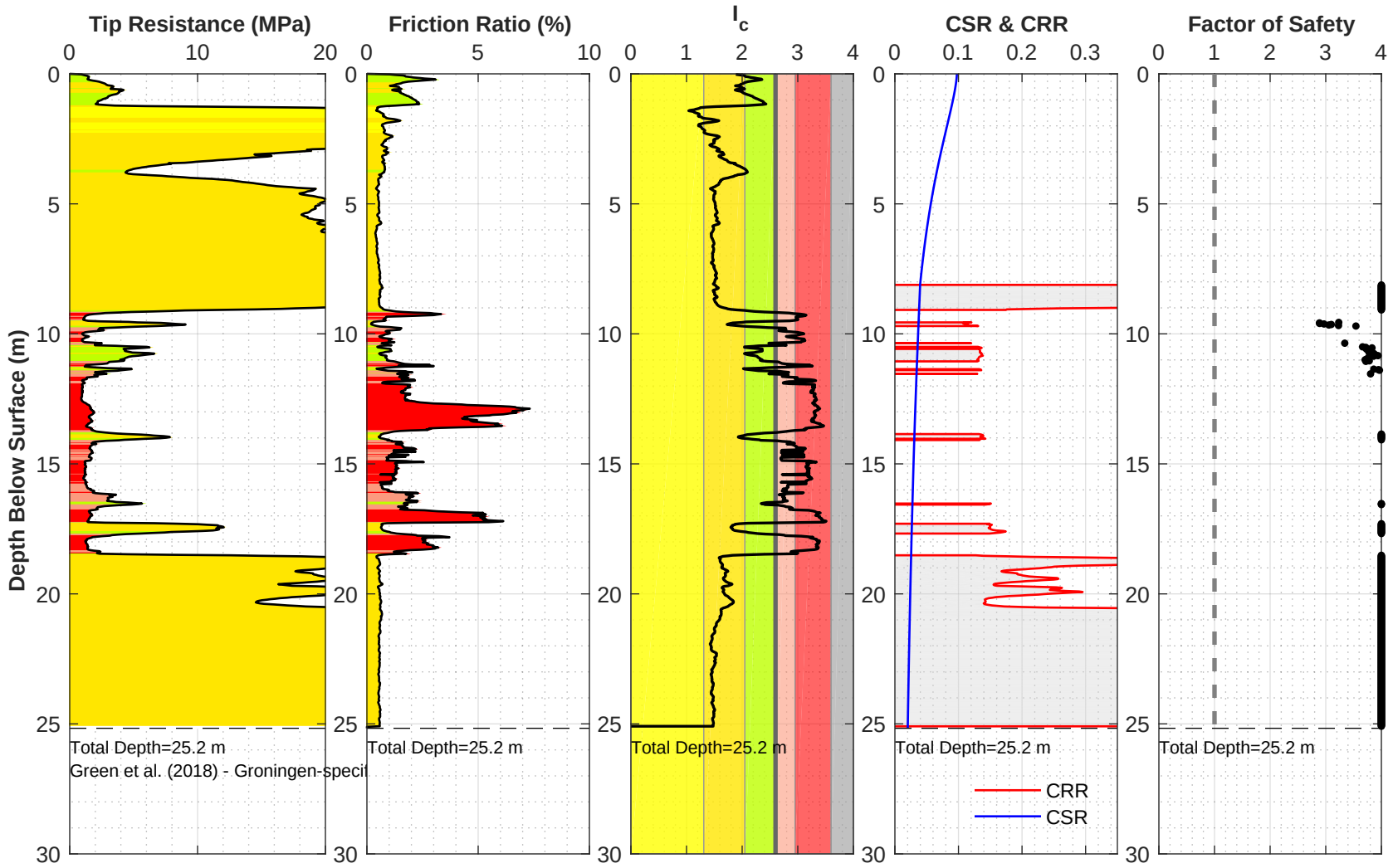

Location: 21225_237_coord
Surface EL: 8.6 m +/- (NAP)
Cone Diameter: 43.7 mm

Thin Layer Correction: NCEER (Youd et al. 2001)
Analysis Title: NC
Mw: 3.9 amax (g): 0.15

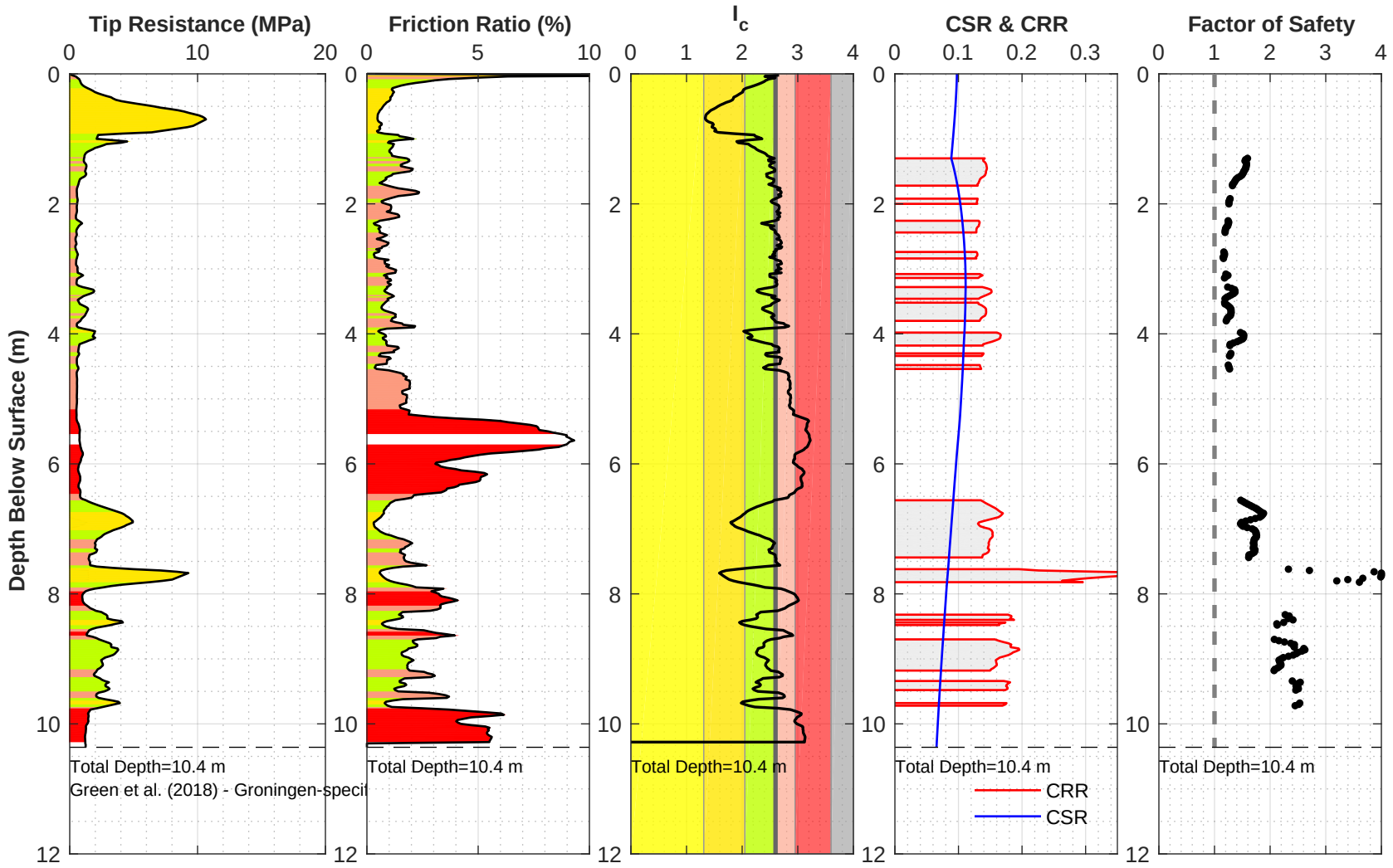

Location: 21225_238_coord
Surface EL: 1.8 m +/- (NAP)
Cone Diameter: 43.7 mm

Thin Layer Correction: NCEER (Youd et al. 2001)
Analysis Title: NC
Mw: 3.9 amax (g): 0.15

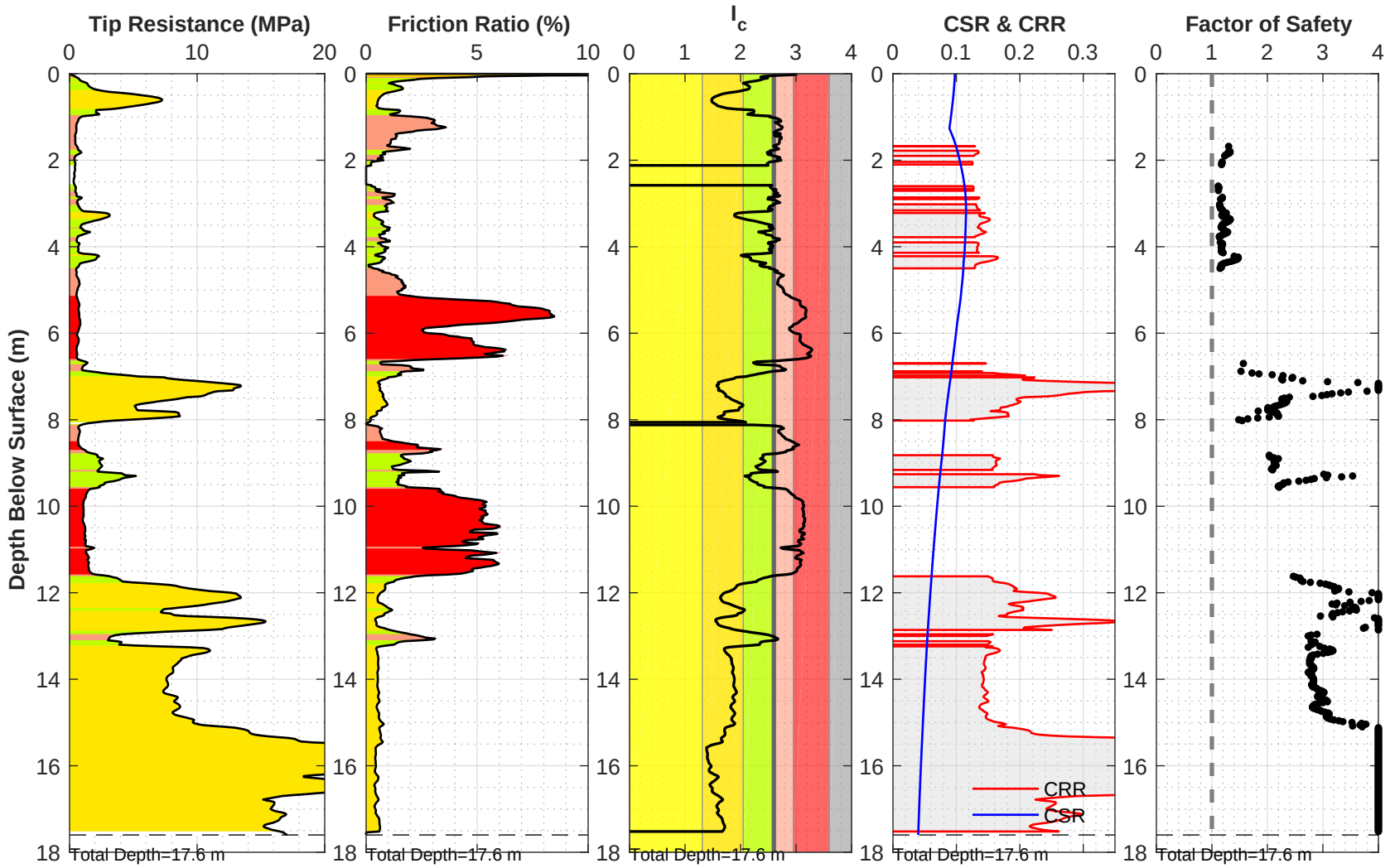

Green et al. (2018) - Groningen-specific

Location: 21225_239_coord
Surface EL: 1.8 m +/- (NAP)
Cone Diameter: 43.7 mm

Thin Layer Correction: NCEER (Youd et al. 2001)
Analysis Title: NC
Mw: 3.9 amax (g): 0.15

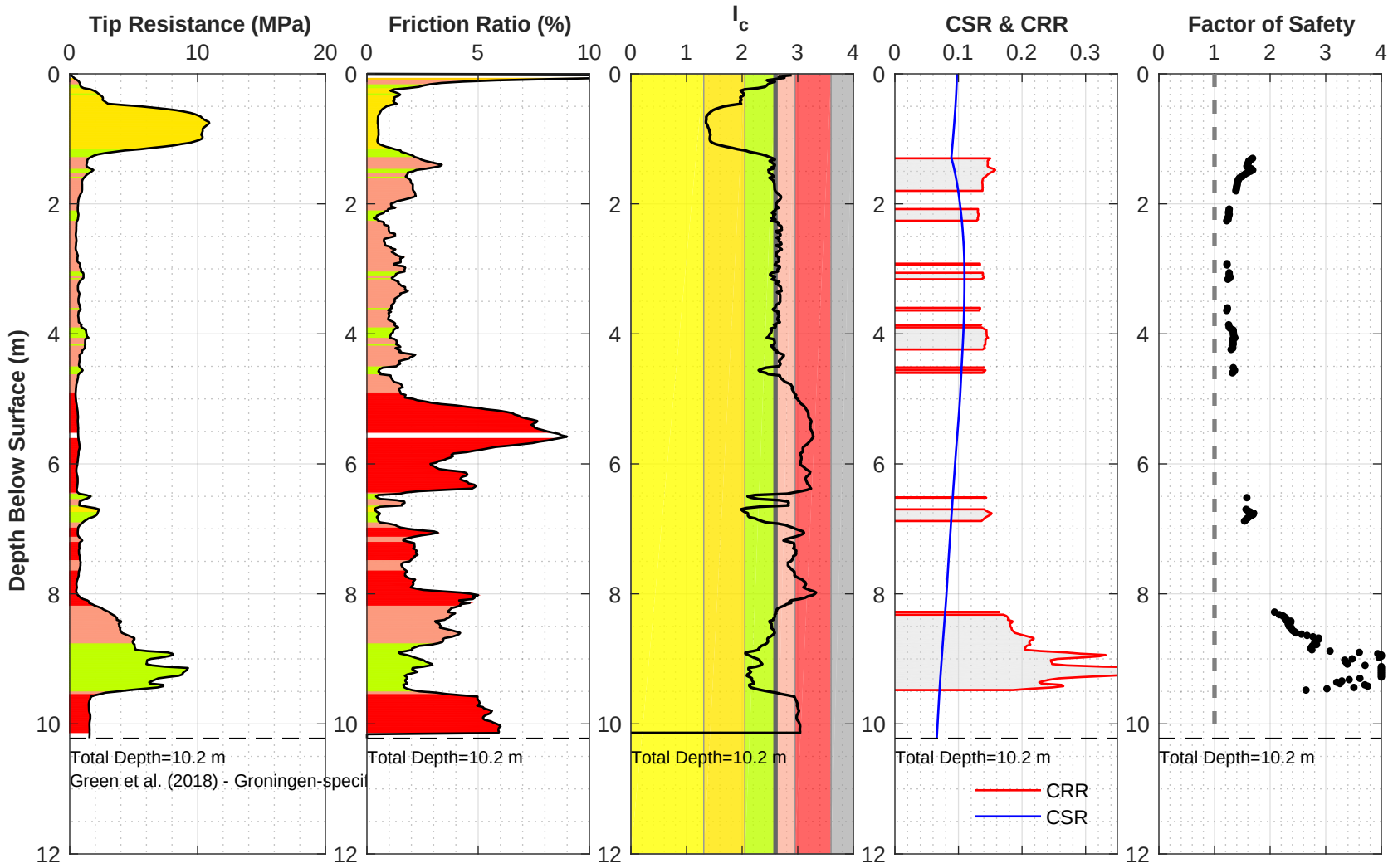

Location: 21225_240_coord
Surface EL: 1.8 m +/- (NAP)
Cone Diameter: 43.7 mm

Thin Layer Correction: NCEER (Youd et al. 2001)
Analysis Title: NC
Mw: 3.9 amax (g): 0.15

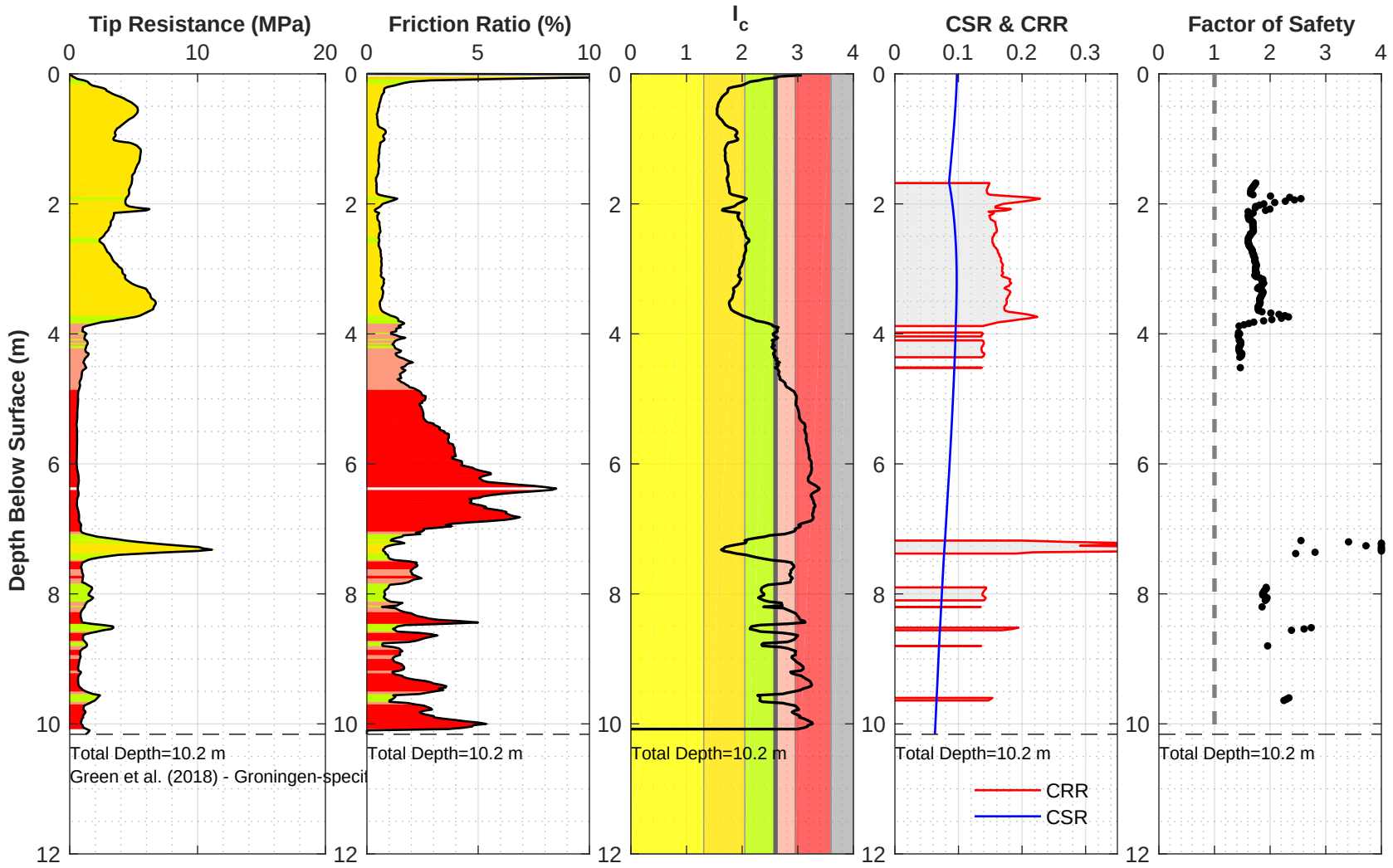

Location: 21225_241_coord
Surface EL: 2.2 m +/- (NAP)
Cone Diameter: 43.7 mm

Thin Layer Correction: NCEER (Youd et al. 2001)
Analysis Title: NC
Mw: 3.9 amax (g): 0.15

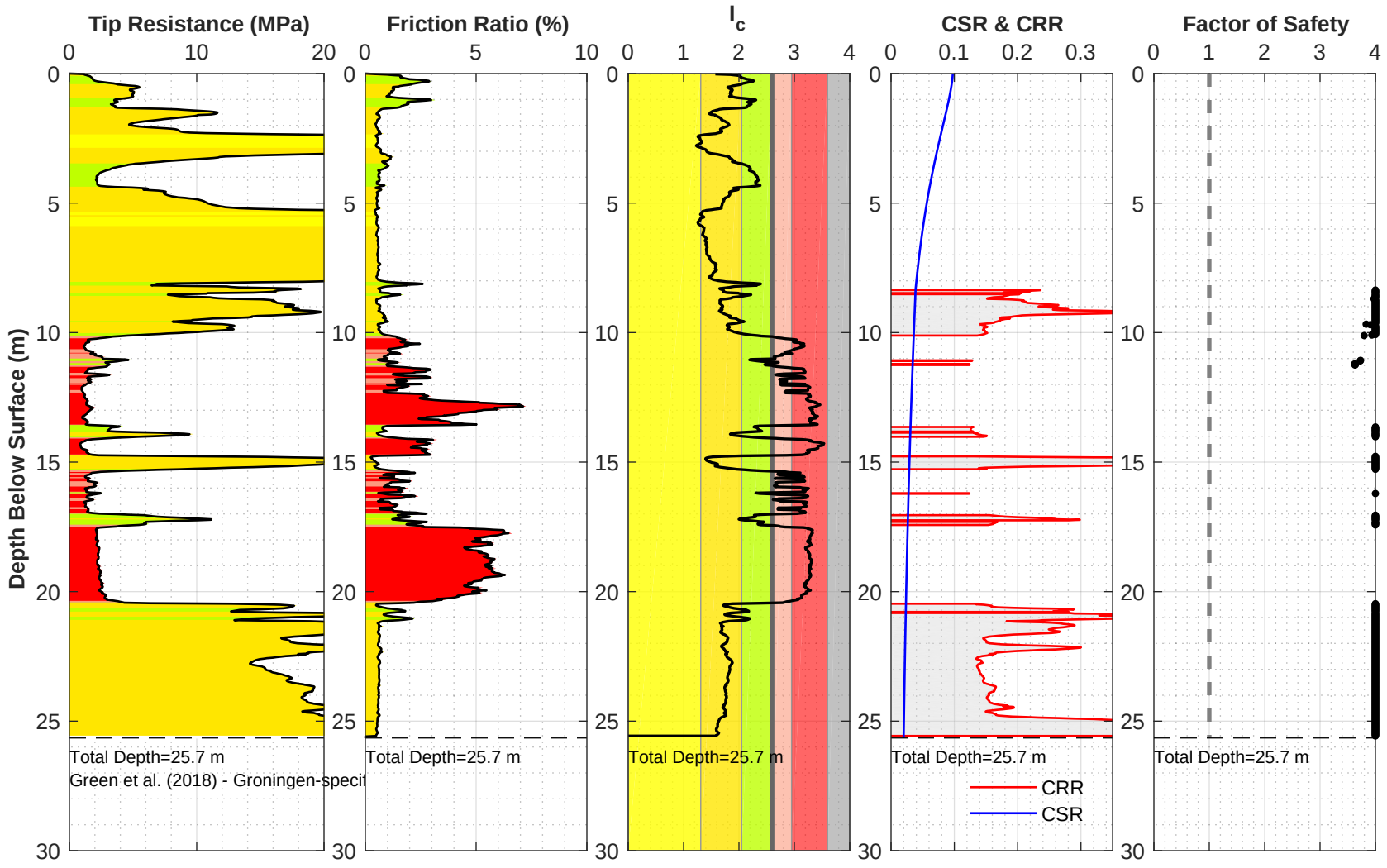

Location: 21225_242_coord
Surface EL: 8.8 m +/- (NAP)
Cone Diameter: 43.7 mm

Thin Layer Correction: NCEER (Youd et al. 2001)
Analysis Title: NC
Mw: 3.9 amax (g): 0.15

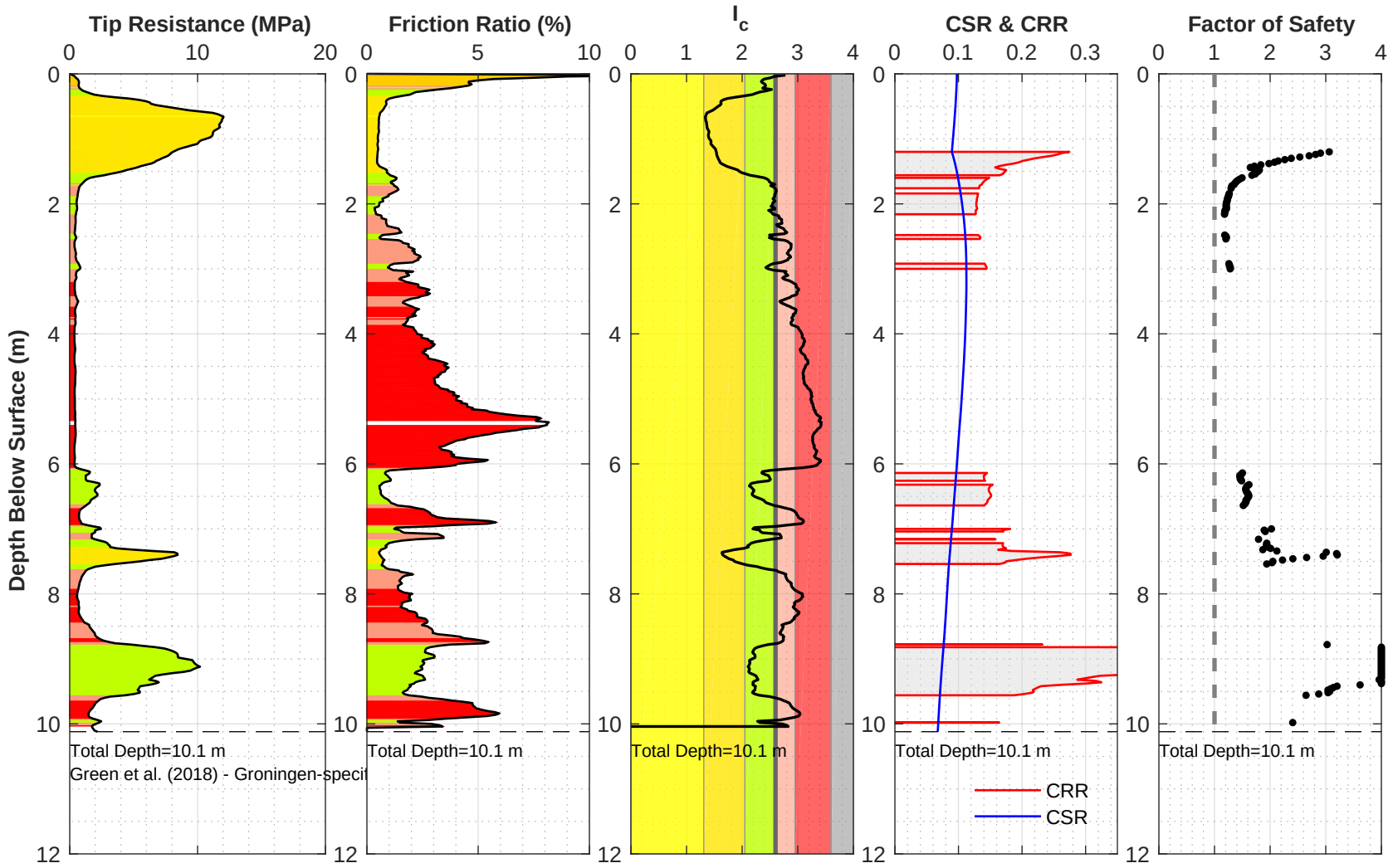

Location: 21225_243_coord
Surface EL: 1.7 m +/- (NAP)
Cone Diameter: 43.7 mm

Thin Layer Correction: NCEER (Youd et al. 2001)
Analysis Title: NC
Mw: 3.9 amax (g): 0.15

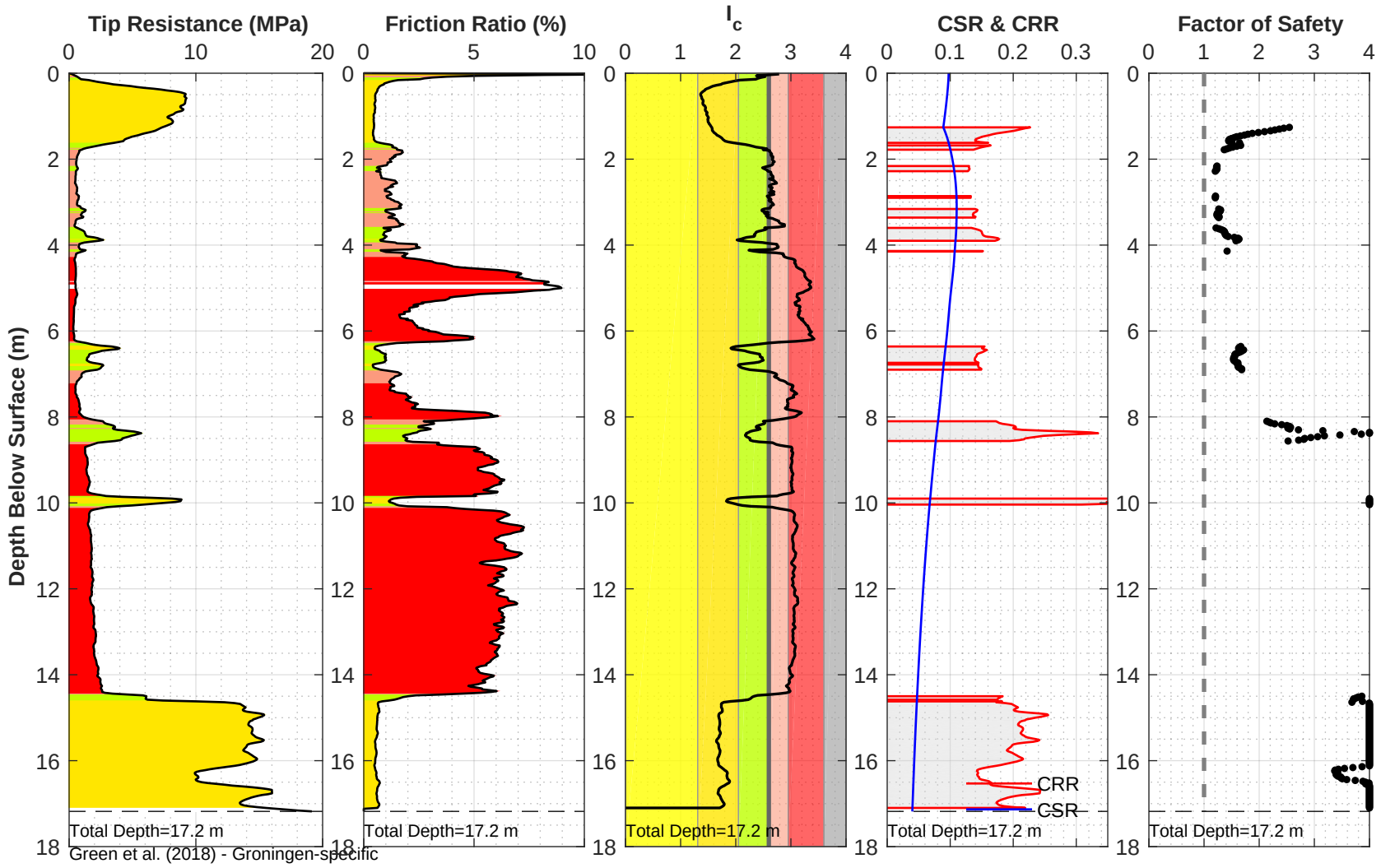

Location: 21225_244_coord
Surface EL: 1.8 m +/- (NAP)
Cone Diameter: 43.7 mm

Thin Layer Correction: NCEER (Youd et al. 2001)
Analysis Title: NC
Mw: 3.9 amax (g): 0.15

Ministerie van Infrastructuur en Milieu

> Retouradres Postbus 20904 2500 EX Den Haag

Waterschap Noorderzijlvest
T.a.v. De heer W.F. Brenkman
Postbus 18
9700 AA GRONINGEN

Bestuurskern
Dir. Algemeen Waterbeleid en Veiligheid
Afd. Waterveiligheid

Den Haag
Postbus 20904
2500 EX Den Haag

Contactpersoon
J. Poot
Senior Beleidsmedewerker

T 070-4567993
Koos.Poot@minienm.nl

Ons kenmerk
IENM/BSK-2017/172122

Uw kenmerk
Z/17/007036

Bijlage(n)
-

Datum 19 juli 2017
Betreft technische uitgangspunten voor belasting en sterkte van primaire keringen bij aardbevingen

Geachte heer Brenkman,

In uw brief van 22 juni 2017 verzoekt u mij, mede namens het waterschap Hunze en Aa's, in te stemmen met de in de memo "Eemshaven-Delfzijl - Uitgangspunten voor een aardbevingsbestendig ontwerp" vastgelegde technische uitgangspunten voor de belasting en sterkte van de primaire waterkering onder invloed van aardbevingen.

In mijn brief van 21 april 2016 heb ik ingestemd met de memo "Uitgangspunten voor een aardbevingsbestendig dijkontwerp" van Deltares van 15 april 2016. Op dat moment zou nog onderzoek plaatsvinden naar het al dan niet verweken van de ondergrond en de invloed daarvan op het versterken van de dijk. Als de verkregen inzichten daartoe aanleiding gaven, zouden de uitgangspunten worden aangevuld en/of aangescherpt.
In uw brief van 15 september 2016 heeft u mij geïnformeerd over de stand van zaken van de lopende onderzoeken naar de gevoeligheid van de ondergrond voor verweking.
Naar aanleiding van het uitgevoerde onderzoek adviseerden experts in november 2016 op een tweetrapsbenadering over te gaan:

1. Een globaal onderzoek van het gehele dijkvak om potentieel onvoldoende betrouwbare delen in beeld te krijgen.
2. Een geavanceerde analyse van de potentieel onvoldoende betrouwbare delen om te bepalen of deze wel of niet aan de veiligheidsnormen voldoen.

De uitvoering van deze aanpak is begeleid door een specialist op het gebied van risicoanalyse en het probabilistisch ontwerp van waterkeringen en gereviewd door een Amerikaanse specialist in het geotechnisch ontwerpen onder invloed van aardbevingen en een Nederlandse specialist op het vlak van het grondmechanisch ontwerp van dijken.
Het onderzoek en de analyses hebben geleid tot aanpassingen van de eerder opgestelde uitgangspunten. Met uw brief van 22 juni 2017 heeft u mij de geactualiseerde memo van 15 juni 2017 "Uitgangspunten voor een aardbevingsbestendig ontwerp" toegezonden.
Met de uitgangspunten in deze memo kan ik instemmen.

In de regeling "Veiligheid primaire waterkeringen 2017" is opgenomen dat bij de beoordeling van de veiligheid van de in Noord-Nederland gelegen waterkeringen

rekening gehouden dient te worden met de belasting door geïnduceerde aardbevingen. Deze beoordeling is een toets op maat. Daarbij kan gebruik gemaakt worden van de in de notitie van 15 juni 2017 opgenomen uitgangspunten.

De uitgangspunten voor een aardbevingsbestendig ontwerp zijn door intensief onderzoek en overleg door uw waterschap, de NAM, adviseurs en de Nationaal Coördinator Groningen tot stand gekomen. Ik heb veel waardering voor de wijze waarop deze partijen, ondanks de verschillende achtergronden, er in geslaagd zijn een gedeeld antwoord op dit, voor Nederland nieuwe vraagstuk, te vinden.

De Nationaal Coördinator Groningen, Hans Alders, de projectdirecteur bij de NAM, Thijs Jurgens, en Harm Küpers, secretaris-directeur waterschap Hunze en Aa's, heb ik een afschrift van deze brief doen toekomen.

Met vriendelijke groet,

DIRECTEUR-GENERAAL RUIMTE EN WATER, (plv.)

drs. P.R. Heij

Bestuurskern
Dir. Algemeen Waterbeleid en Veiligheid
Afd. Waterveiligheid

Datum
19 juli 2017

Ons kenmerk
IENM/BSK-2017/172122

Memo

Aan
Walja Karten (Waterschap Noorderzijlvest)

Datum	Kenmerk	Aantal pagina's
15 juni 2017	1220173-040-GEO-0011	31

Van	Doorkiesnummer	E-mail
Arjan Venmans	+31(0)88335 7263	arjan.venmans@deltares.nl

Onderwerp
Eemshaven-Delfzijl - Uitgangspunten voor een aardbevingsbestendig ontwerp

---

1 Inleiding

Vanwege de aardbevingen in Groningen heeft waterschap Noorderzijlvest een versnelde verbetering ingezet van de zeedijk tussen Eemshaven en Delfzijl. De reguliere toets- en ontwerpvoorschriften houden geen rekening met aardbevingen. Daarom heeft het waterschap in 2014 een onderzoeks- en afwegingstraject gestart, in samenwerking met Deltares. Het doel is om te komen tot een vastgestelde set van te hanteren uitgangspunten voor een sober en doelmatig aardbevingsbestendig ontwerp. Een dergelijk ontwerp biedt voldoende veiligheid tegen overstroming, maar is niet onnodig conservatief. De uitgangspunten worden vastgesteld door het Rijk, als kadersteller en toezichthouder. Daarmee geeft het Rijk duidelijkheid en zekerheid aan het waterschap als keringbeheerder en aan de NAM als financier van de meerkosten voor aardbevingsbestendigheid. Het in 2014 gestarte traject heeft in oktober 2016 geleid tot een eerste beoordelings- en ontwerpprotocol voor de zeedijk, inclusief een onderliggend uitgangspuntendocument. Naar aanleiding van de aanbevelingen van een panel van internationale experts in november 2016 (bijlage A) is eind 2016 aan dit traject een tweede spoor toegevoegd bestaande uit dynamische gekoppelde effectieve spanningsanalyses, uitgevoerd door Fugro. Hiervoor is in de periode tussen eind 2016 en maart 2017 een nieuwe beoordelings- en ontwerpmethode ontwikkeld, die bestaat uit twee stappen:

1 Een screening langs de hele zeedijk naar de gevoeligheid voor verweking van de grondslag onder de dijk, op basis van de Liquifaction Potential Index (LPI, Iwasaki et al., 1978).
2 Berekening van de kruindaling in de profielen die volgens de LPI screening maatgevend zijn, op basis van dynamische gekoppelde effectieve spanningsanalyses.

In het oorspronkelijke protocol en uitgangspuntendocument van oktober 2016 was screening nog geen aparte stap.

Jongejan et al. (2017) beschrijft de de procedure voor semi-probabilistisch ontwerp met dynamische gekoppelde effectieve spanningsanalyses (bijlage D).

Tijdens het traject heeft het waterschap diverse nationale en internationale deskundigen geraadpleegd:

- Expertise netwerk Waterkeren (ENW): schriftelijke raadpleging betreffende versie 2 van dit uitgangspuntenmemo, maart 2015.
- Expert workshop seismisch ontwerp: experts Boulanger, Chacko, Finn, Yoshida, juli 2015.
- Expert workshop terugkeertijd aardbevingsbelasting: experts Vrouwenvelder, Jongejan, Kok, Vrijling, Calle, december 2015.
- Tweede expert workshop terugkeertijd aardbevingsbelasting: experts Vrouwenvelder, Jongejan, Kok, Vrijling, Calle, december 2015.
- Expert workshop karakterisering van de verwekingsgevoeligheid: experts Towhata, Green, Kramer, mei 2016.
- Expert workshop seismisch ontwerp: experts Kramer, Green, Chacko, Towhata, november 2016, bijlage A.
- Review van LPI screening, dynamische gekoppelde effectieve spanningsberekeningen en code calibration van deze berekeningen door prof. Kramer, bijlage B.
- Review van code calibration van dynamische gekoppelde effectieve spanningsberekeningen door dr. Calle, bijlage C.

Verder heeft het waterschap alle betrokken publieke partijen tussentijds geïnformeerd door middel van een drie keer geactualiseerde uitgangspuntennotitie voor zowel primaire als regionale keringen (Deltares, 2015). Elke versie is besproken tijdens door het waterschap georganiseerde informatiebijeenkomsten.

De uitgangspunten en het protocol voor een regulier ontwerp voor hoogwaterbelasting zijn al vastgelegd in het document “Ontwerpuitgangspunten Hoogwateropgave Dijkverbetering Eemshaven-Delfzijl” (Deltares, 2016a). In het voorliggende document worden alleen de extra uitgangspunten voor een aardbevingsbestendig ontwerp behandeld. De extra uitgangspunten worden beschreven in:

- Veiligheidsfilosofie en terugkeertijd: het rapport “Code calibration for coupled, effective stress FEM-assessments of the primary flood defenses at Eemshaven-Delfzijl” (Jongejan et al., 2017).
- De wijze waarop de weerstand tegen verweking van het zand wordt bepaald in de LPI screening: “LPI screening for the Eemshaven-Delfzijl levee” (Deltares, 2017).
- De wijze waarop de weerstand tegen verweking van het zand wordt bepaald in de dynamische gekoppelde effectieve spanningsanalyses: het rapport “Code calibration for coupled, effective stress FEM-assessments of the primary flood defenses at Eemshaven-Delfzijl” (Jongejan et al., 2017).
- Aardbevingsbelasting, effect van de aardbeving op de ondergrond en de waterkering: het rapport “Evaluation of dynamic stability using code calibrated design parameters, Eemshaven-Delfzijl levee, The Netherlands” (Fugro, 2017).
- Kruindalingscriterium: appendix I.2 van het protocol “Seismisch Dijkontwerp – Protocol voor Eemshaven-Delfzijl” (Deltares, 2016b).

In paragraaf 2 is het overzicht opgenomen van de voorgestelde ontwerpuitgangspunten waarvoor vaststelling wordt gevraagd. In paragraaf 3 worden de voorgestelde ontwerpuitgangspunten nader toegelicht. Daarbij wordt achtereenvolgens ingegaan op:

- De te hanteren aardbevingsbelasting als functie van de terugkeertijd.
- Het te berekenen effect van de aardbeving op de ondergrond en de waterkering.
- De te hanteren veiligheidsfilosofie, waaruit ook de terugkeertijd voor de aardbevingsbelasting volgt.
- De wijze waarop de weerstand tegen verweking van het zand wordt gekarakteriseerd in de LPI screening en in de dynamische gekoppelde effectieve spanningsanalyses.

2 Overzicht voorgestelde ontwerpuitgangspunten

Kansverdeling aardbevingsbelasting

1 De door NAM geproduceerde en door KNMI gevalideerde resultaten uit de PSHA versie 2 “op maat” worden gebruikt voor het dijkontwerp, met als grondslag het GMPE v2 model met specifieke keuze voor M_{max} (M_{max}=5,0) en logic-tree gewichten (0; 0,5; 0,5).

Effect van aardbevingsbelasting op ondergrond en waterkering

2 De responsberekening bestaat uit twee stappen:
   1 Van een diepte van 350 m tot bovenkant Peelo formatie: 1D berekening met de *Total Stress, Equivalent Linear* rekenmethode.
   2 Van bovenkant Peelo formatie tot maaiveld: 2D berekening met dynamische gekoppelde effectieve spanningsanalyses.

3 De voor waterveiligheid relevante vervormingen tijdens en na de aardbeving worden bepaald met dynamische gekoppelde effectieve spanningsberekeningen.

Veiligheidsfilosofie

4 Het aardbevingsbestendig ontwerp vindt plaats op basis van een semi-probabilistische procedure. Door middel van rekenwaarden voor sterkte en belasting(en) wordt ervoor gezorgd dat de faalkans beneden de normwaarde (een op basis van de norm bepaalde toelaatbare waarde) blijft. Daarbij wordt rekening gehouden met de onwaarschijnlijkheid dat extreme waarden voor sterkte en belasting(en) tegelijk zullen voorkomen. Daarop aansluitend dient een dominante aardbevingsbelasting (met hoge terugkeertijd) te worden gecombineerd met een niet-dominante hydraulische belasting (met minder hoge terugkeertijd) en omgekeerd. Daarnaast moet ook het klassieke geval met alleen maatgevend hoogwater worden beschouwd. Bij elke te onderscheiden belastingcombinatie moet de kering voldoen aan de eis.

5 De invloedsfactor voor een dominante aardbevingsbelasting is 0,9. De invloedsfactor voor een dominante hydraulische belasting is 0,7.

6 Het faalkansbudget voor macrostabiliteit wordt verhoogd van 4 naar 24 %. Het faalkansbudget voor piping wordt dienovereenkomstig verlaagd van 24 naar 4 %.

7 Bij aardbevingen wordt het lengte-effect in rekening gebracht zoals beschreven in Jongejan et al. (2017). De parameters waarmee het lengte-effect wordt beschreven zijn a = 0,033 en b = 200 m.

8 Na significante vervormingen van de dijk als gevolg van een aardbevingsbelasting wordt gedurende de hersteltijd een voorwaardelijke kans van 1/10 op overstroming aangenomen.

9 Een voorwaardelijke overstromingskans van 1/10 leidt op grond van representatieve overslagberekeningen gedurende een hersteltijd van 3 maanden tot een maximaal toelaatbare kruindaling van 3 m.

10 Jongejan et al. (2017) beschrijft de procedure voor semi-probabilistisch ontwerp en de daarin toe te passen partiële veiligheidsfactoren voor alle van belang zijnde stochastische variabelen.

Weerstand tegen verweking in de LPI screening en in de dynamische gekoppelde effectieve spanningsanalyses

11 Een CPT datapunt wordt als zand geclassificeerd als de *soil type behaviour index* I_c volgens (Robertson & Wride, 1998) kleiner of gelijk is aan 2,6.

12 Rond discrete overgangszones zand/klei wordt over 0,2 m de conuswaarde in de zandlaag gecorrigeerd.

13 De weerstand tegen verweking wordt berekend op basis van:
- correlaties met sonderingen volgens Boulanger & Idriss (2014) in afzettingen die bestaan uit zand, al dan niet afgewisseld met relatief dikke kleilagen, waarin de I_c waarde kleiner is dan 2,05.
- cyclische laboratoriumproeven op ongeroerde monsters in afzettingen die bestaan uit een afwisseling van relatief dunne zand- en kleilaagjes, waarin de de I_c waarden tussen 2,05 en 2,6 liggen (afzettingen van het *Tfsc* type).

14 In de screening wordt de LPI bepaald op basis van alle data punten in de sondering met I_c kleiner dan of gelijk aan 2,6. Appendix G van Jongejan (2017) beschrijft de bepaling van de representatieve waarde van de conusweerstand en de weerstand tegen verweking voor de dynamische gekoppelde effectieve spanningsanalyses.

15 Op de genormaliseerde conusweerstand wordt een *fines* toeslag toegepast om te corrigeren voor het gunstige effect van het gehalte fijne fractie volgens Boulanger and Idriss (2014), met $CFC = 0$.

16 De magnitude scaling factor wordt bepaald volgens Boulanger and Idriss (2014).

17 De correctiefactor voor de verticale spanning K_σ en de correctiefactor voor statische schuifspanning K_α voor zand in taluds worden bepaald volgens Boulanger & Idriss (2014). In de LPI screening op basis van de sonderingen aan de zeezijde van de dijk wordt gerekend met $K_\alpha = 1$.

18 Voor de correctiefactor voor de leeftijd van de afzettingen K_{DR} wordt voor de relatief jonge holocene afzettingen een waarde 1 aangehouden, voor het pleistocene zand een waarde van 1,3.

3 Toelichting voorgestelde ontwerpuitgangspunten

3.1 Aardbevingsbelasting

De te hanteren aardbevingsbelasting heeft een overheersende invloed op het aardbevingsbestendig ontwerp van waterkeringen en andere objecten.

De kansverdeling wordt afgeleid uit een zogenaamde *Probabilistic Seismic Hazard Analysis* (PSHA). Hierna wordt kort beschreven voor welke PSHA versies door KNMI en NAM al resultaten zijn geleverd en welke specifieke vervolgontwikkeling heeft plaatsgevonden voor Eemshaven-Delfzijl.

Van 16 tot en met 18 juli 2015 heeft het waterschap vijf gerenommeerde internationale experts geconsulteerd op het gebied van *Geotechnical Earthquake Engineering*. De voornaamste aanbeveling van die kant was om in dialoog met NAM en KNMI te komen tot een PSHA “op maat” voor de waterkeringen. “Op maat” wil zeggen dat uit de PSHA aardbevingssignalen op diepte worden bepaald, bij de juiste terugkeertijd. Met deze aardbevingssignalen kan vervolgens weer de seismische respons van de dijk worden bepaald. Met hulp van dergelijke responsberekeningen worden piekversnellingen aan maaiveld begrensd door de beperkte sterkte van bovenste grondlagen. Daardoor resulteert minder aardbevingsbelasting op de waterkering die boven op deze grondlagen ligt.

PSHA versie 0 van KNMI. Tot en met juli 2015 is voor de waterkeringen gewerkt met de resultaten van een PSHA versie 0. Deze versie 0 is in 2013 opgezet door KNMI, voor NEN, in samenwerking met NAM (KNMI, 2013). Versie 0 is opgezet voor de in februari 2015 uitgekomen Nationale Praktijkrichtlijn (NPR) van de NEN (NEN, 2015). Deze NPR is alleen van toepassing op gebouwen. Versie 0 levert voor elke locatie een kansverdeling op voor de piekversnelling aan het maaiveld (*Peak Ground Acceleration,* PGA). In versie 0 is een maximum magnitude van 5 aangenomen en een gemiddeld jaarlijks aantal significante bevingen van 40. In maart 2015 is voor het dijkontwerp al voorzichtig geanticipeerd op ontwikkelingen in volgende PSHA versies, door te kiezen voor 27 significante aardbevingen per jaar.

PSHA versie 1 van KNMI. Oktober 2015 heeft KNMI versie 1 openbaar gemaakt (KNMI, 2015). Versie 1 is gebruikt voor een update van de NEN-NPR kaart, die in december 2015 is uitgebracht. Het gebruikte seismologisch model is weer opgezet in samenwerking met NAM. Ook in versie 1 is door KNMI een maximum magnitude van 5 aangenomen, in combinatie met een significant aantal jaarlijkse aardbevingen van 22,7. Direct vanaf de beschikbaarheid is versie 1 binnen het lopende referentieontwerp in gebruik genomen voor de seismische responsberekeningen van de dijk Eemshaven-Delfzijl. Gebruik van dergelijke responsberekeningen is aanbevolen door de internationale experts. Daartoe worden in Groningen gemeten aardbevingssignalen geschaald naar rato van de ontwerpwaarden aan het maaiveld, nadat deze signalen eerst op de meetlocatie naar diepte zijn vertaald.

PSHA versie 2 van NAM. Begin november 2015 heeft NAM de resultaten van PSHA versie 2 aan de minister van EZ opgeleverd, waarna halfjaarlijks updates zullen volgen (NAM, 2015). De PSHA is opgezet voor gebouwen en levert alleen informatie voor een terugkeertijd van 475 jaar. In versie 2 wordt voor het eerst onderscheid gemaakt tussen de versnellingen op

diepte en de daarmee locatie-specifiek bepaalde versnellingen aan maaiveld, rekening houdend met lokale grondcondities.

PSHA versie 2 "op maat" voor Eemshaven-Delfzijl. Op 7 december 2015 heeft NAM de PSHA "op maat" voor Eemshaven-Delfzijl opgeleverd (Bommer & Bourne, 2015), zoals aanbevolen door de experts. In aansluiting op de KNMI keuze voor versie 1 is daarbij een maximum magnitude van 5 gehanteerd. Ten opzichte van versie 1 levert deze analyse voor het eerst direct informatie op diepte, waaruit de benodigde aardbevingssignalen op diepte kunnen worden afgeleid. Dat maakt de met versie 2 bepaalde signalen beter geschikt voor een seismische responsberekening op de door de experts aanbevolen methode dan de met versie 1 bepaalde signalen.

De voor het ontwerp gebruikte versie PSHA versie 2 "op maat" heeft als grondslag het GMPE v2 model met specifieke keuze voor M_{max} (M_{max}=5,0) en logic-tree gewichten (0; 0,5; 0,5). Dit uitgangspunt sluit aan bij de meest actuele (internationale) kennis.

Voorgesteld uitgangspunt voor primaire keringen:

1 De door NAM geproduceerde en door KNMI gevalideerde resultaten uit de PSHA versie 2 "op maat" worden gebruikt voor het dijkontwerp, met als grondslag het GMPE v2 model met specifieke keuze voor M_{max} (M_{max}=5,0) en logic-tree gewichten (0; 0,5; 0,5).

3.2 Effect op ondergrond en waterkering

Macroinstabiliteit (hellinginstabiliteit en verlies van horizontaal evenwicht) en hoogteverlies worden beschouwd als de twee mechanismen met een verhoogde faalkans door aardbevingsbelasting. Als uitgangspunt voor het seismisch ontwerp gelden de methoden en modellen die door de internationale experts zijn geaccordeerd of aanbevolen. Daarom is vanaf september 2015 een overstap gemaakt naar seismische responsberekeningen op basis van versnellingssignalen op diepte, in plaats van direct gebruik van piekversnellingen aan maaiveld.

Hierna volgt voor de te hanteren methoden en modellen een samenvatting van de relevante uitgangspunten.

Seismische responsberekening. De responsberekening bestaat uit twee stappen:

1 Van een diepte van 350 m tot bovenkant Peelo formatie: 1D berekening met de *Total Stress, Equivalent Linear* rekenmethode. *Total Stress* wil zeggen dat het constitutieve model niet zelf de generatie van waterspanningen voorspelt (in tegenstelling tot *Effective Stress*).
2 Van bovenkant Peelo formatie tot maaiveld: 2D berekening met dynamische gekoppelde effectieve spanningsanalyses.

Het gebruik van de *Total Stress, Equivalent Linear* rekenmethode is in overeenstemming met de aanbevelingen van de expertgroepen:

- Expertbijeenkomst juli 2015: het versnellingssignaal ter plaatse van het dijklichaam en het cyclisch schuifspanningsverloop over de diepte dient te worden bepaald met 1D *Total Stress* responsberekeningen

- Expertbijeenkomst 12 en 13 mei 2016: een verwekingsanalyse volgens Boulanger & Idriss (2014) moet om consistentieredenen worden gecombineerd met een schuifspannings-verloop dat is bepaald met de *equivalent linear* methode.

De *equivalent linear* methode behelst een analyse in het frequentiedomein. Dit geeft de mogelijkheid om zowel van basis naar maaiveld te rekenen (convolutie), als ook andersom (deconvolutie). De niet-lineaire stijfheid en demping als functie van schuifrek worden op benaderende wijze in rekening gebracht door iteratieve aanpassing van de waarde die geldt voor de hele berekening. Vanwege deze aanpak zal deze software in het algemeen echter te veel demping introduceren bij hogere frequenties in combinatie met schuifrekniveaus vanaf 0,4 %. In die gevallen is voor het berekenen van de versnelling in principe een *Nonlinear* analyse in het tijdsdomein nodig.

Een alternatieve *Nonlinear* analyse zou worden uitgevoerd het tijdsdomein (bijvoorbeeld met de Deepsoil software). Dit biedt de mogelijkheid om per tijdstap een andere waarde voor demping en stijfheid te gebruiken. De Deepsoil software gebruikt daarbij dezelfde materiaalkarakterisering als voor een analyse in het frequentiedomein. In een “nonlinear” berekening met Deepsoil is elke laag in feite een element waarbinnen de schuifrekken en schuifspanningen als constant worden beschouwd. De versnellingen worden berekend op de randen van de elementen. De elementafmetingen moeten. handmatig worden beperkt om de beweging van schuifgolven te kunnen volgen, zoals beschreven in de Deepsoil handleiding (Hashash, 2015).

Bij verkennende berekeningen met de specifieke frequentieinhoud van de aardbevingssignalen voor Eemshaven-Delfzijl (Deltares, 2016c) bleek de equivalent linear methode echter altijd het meest conservatief, ook bij schuifrekniveaus boven 0,4 %. Daarom is gebruik van de *equivalent linear* methode in dit geval voldoende voor zowel de bepaling van het schuifspanningsverloop als ook voor de bepaling van de versnellingen van het dijklichaam.

Volgens NPR 9998 moeten in de responsberekening als belasting minimaal zeven verschillende aardbevingssignalen worden aangebracht. Overeenkomstig het review advies van prof. Kramer zijn elf verschillende aardbevingssignalen toegepast.

Jongejan et al. (2017) geeft de partiële factor die moet worden toegepast op de signalen aan de basis van de 2D modellen.

Vervormingsberekening tijdens en na de aardbeving. Conform het advies uit de expert workshop van november 2016 (bijlage A) wordt de kruindaling berekend met dynamische gekoppelde effectieve spanningsberekeningen.

Voorgestelde uitgangspunten voor primaire keringen:

2 De responsberekening bestaat uit twee stappen:
   1 Van een diepte van 350 m tot bovenkant Peelo formatie: 1D berekening met de *Total Stress, Equivalent Linear* rekenmethode.
   2 Van bovenkant Peelo formatie tot maaiveld: 2D berekening met dynamische gekoppelde effectieve spanningsanalyses.
3 De voor waterveiligheid significante vervormingen tijdens en na de aardbeving worden bepaald met dynamische gekoppelde effectieve spanningsberekeningen.

3.3 Veiligheidsfilosofie

De binnen een semi-probabilistisch ontwerp te hanteren terugkeertijd voor de aardbevingsbelasting volgt uit de faalkanseis voor een bepaald mechanisme in een doorsnede, in combinatie met een zogenaamde invloedsfactor voor de aardbevingsbelasting. De faalkanseis in de doorsnede is weer afhankelijk van de norm, de faalkansbegroting en het in rekening te brengen lengte-effect. Door middel van een reststerkte-aanname kan ten slotte rekening worden gehouden met de kans op overstroming gedurende de herstelperiode. Hierna wordt kort toegelicht wat deze begrippen en parameters betekenen en welke uitgangspunten op dat gebied worden voorgesteld. De uitgangspunten zijn eerst bijgesteld en daarna vastgesteld in overleg met een nationale expertgroep die is bijeengekomen op 9 december 2015 en op 17 februari 2016. De veiligheidsfilosofie wordt nader beschreven en onderbouwd in Jongejan et al. (2017).

Vooraf wordt hier al gemeld dat toepassing van de voorgestelde uitgangspunten voor macrostabiliteit (afschuiven) op traject 6_7 resulteert in een terugkeertijd van ongeveer 2300 jaar en op traject 6_6 in een terugkeertijd van ongeveer 1100 (Jongejan et al., 2017, paragraaf 8.1).

Mechanismen. Een aardbeving kan hoogteverlies en andere schade (losgeraakte bekleding, scheuren) veroorzaken. Daarbij is het van belang dat zich onder invloed van de cyclische aardbevingsbelasting in losgepakt zand tijdelijk een grote verwekingsgraad kan opbouwen, door wateroverspanning. Volledig verweekt zand gedraagt zich als drijfzand. Hoogteverlies en schade worden dus zowel veroorzaakt door macro-instabiliteit (taludinstabiliteit en verlies van horizontaal evenwicht) als door eerst wegpersen en daarna compacteren van verweekt zand. De gebeurtenissen kunnen gelijktijdig voorkomen, maar dat hoeft niet. Grote afschuiving en kruindaling zal vooral ontstaan wanneer ondiepe losgepakte zandlagen door de cyclische belasting verweken, zonder dat er vervormingsbeperkende maatregelen zijn genomen.

Figuur 3.1 Macroinstabiliteit en kruindaling door aardbeving, onder invloed van verweking

Ontwerpstappen. Ter beoordeling van de aardbevingsbestendigheid moeten de volgende drie stappen worden doorlopen:

1 Bepaal de in rekening te brengen versnellingssignalen tussen 350 m diepte en bovenkant Peelo formatie met hulp van 1D *Equivalent Linear* responsberekeningen. Maak hierbij gebruik van gegeven versnellingssignalen aan de basis, afgeleid uit PSHA versie 2 “op maat” (zie paragraaf 3.1).
2 Bereken de versnellingssignalen tussen de bovenkant van de Peelo formatie en het dijklichaam uit 2D dynamische gekoppelde effectieve spanningsanalyses.
3 Bepaal het benodigde ontwerp om te voldoen aan de eis aan de kruindaling van de dijk tijdens en direct na de aardbeving. Dit dient te gebeuren met dynamische gekoppelde effectieve spanningsanalyses onder invloed van de versnellingssignalen. De ontwerpmaatregelen kunnen bestaan uit (een combinatie van) extra berm, drainage, stabiliteitsscherm en verbetering van losgepakt zand.

Semi-probabilistisch ontwerp. Het voorgeschreven ontwerpinstrumentarium 2014 (OI2014) gaat uit van een semi-probabilistisch ontwerp per mechanisme en doorsnede. Door middel van rekenwaarden voor sterkte en belasting(en) wordt er voor gezorgd dat de faalkans beneden de normwaarde blijft. Daarbij wordt rekening gehouden met de onwaarschijnlijkheid dat extreme waarden voor sterkte en belasting(en) tegelijk zullen voorkomen. Daarop aansluitend dient een dominante aardbevingsbelasting (met hoge terugkeertijd) te worden gecombineerd met een niet-dominante hydraulische belasting (met minder hoge terugkeertijd) en omgekeerd (CUR, 1997). Daarnaast moet ook het klassieke geval met alleen maatgevend hoogwater worden beschouwd. Vervolgens wordt ontworpen op het meest ongunstige geval binnen deze drie belastinggevallen. Voor de niet-dominante hydraulische belasting wordt het 1-jaars maximum aangehouden, op basis van het advies uit de expertbijeenkomst van 9 december 2015. De drie te beschouwen gevallen worden getoond in Figuur 3.2.

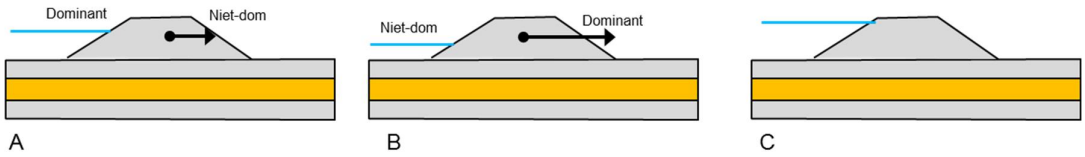

Figuur 3.2 Schematische weergave van de semi-probabilistisch te toetsen belastinggevallen: In geval A is de hydraulische belasting dominant, in geval B is de aardbevingsbelasting dominant en in geval C is er alleen sprake van een maatgevend hoogwater.

Invloedsfactor. Voor het bepalen van de terugkeertijd voor een dominante en niet-dominante belasting is een waarde nodig voor de zogenaamde invloedsfactor $\alpha_{belasting}$ (CUR, 1997; ISO, 2013). Deze factor geeft aan hoe groot de invloed van de onzekerheid in de belasting is op de faalkans. Hoe groter de $\alpha_{belasting}$, hoe groter de terugkeertijd van de rekenwaarde voor de belasting. Volgens ISO is $\alpha_{belasting}$ = 0.7 een veilige waarde voor een dominante belasting en is $\alpha_{belasting}$ = $0.4 \cdot 0.7$ een veilige waarde voor de daarmee te combineren niet-dominante belasting. Door het ExpertiseNetwerk Waterkeren (ENW) wordt voor aardbevingsbelasting echter de hogere waarde α_{PGA} = 0.9 geadviseerd (ENW, 2014a). Dit is bevestigd door de probabilistische FORM analyses in Jongejan et al. (2017).

Norm. De norm op de waterkering legt wettelijk vast wat de maximaal toelaatbare kans is op verlies van de kerende functie voor een bepaald dijktraject. Hoe groter de norm, hoe groter de terugkeertijd van de rekenwaarde voor de belasting (en dus hoe kleiner de maximaal toelaatbare faalkans). Voor Eemshaven-Delfzijl is in het OI2014 versie 3 een maximaal toelaatbare faalkans (afkeurgrens) vastgelegd voor de faalkans per dijktraject. Deze afkeurgrens bedraagt 1/1000 per jaar voor dijktraject 6_6 en 1/3000 per jaar voor dijktraject 6_7.

Faalkansbudget. In het OI2014 is verder ook een “standaard” faalkansbegroting vastgelegd. Deze legt vast welk deel van de normwaarde beschikbaar is voor dat mechanisme. Hoe kleiner het budget, hoe groter de terugkeertijd van de rekenwaarde voor de belasting. Volgens de standaard begroting is het budget 4% voor macrostabiliteit en 24% voor ontoelaatbare overloop en golfoverslag. Het OI2014 staat het toe om de budgetverdeling voor een heel dijktraject aan te passen. In het geval van Eemshaven-Delfzijl heeft het waterschap er als uitgangspunt voor gekozen om het budget voor macrostabiliteit te verhogen tot 24 %, door middel van een lager budget voor piping (van 24 % naar 4 %). Zo wordt meer ruimte gegeven voor het mechanisme dat bij aardbevingen een verhoogde kans van optreden heeft.

Lengte-effect. Het OI2014 beschrijft hoe de faalkanseis per mechanisme moet worden doorvertaald van de trajectlengte naar de lengte van onafhankelijke doorsneden (lengte-effect). Het lengte-effect brengt tot uitdrukking dat de faalkans voor een lange dijk groter is dan de faalkans voor een korte dijk. Hoe groter het lengte-effect, hoe groter de terugkeertijd. In eerste instantie is op basis van het advies uit de expertbijeenkomst van 9 december 2015 ervoor gekozen om deze parameters niet aan te passen in het geval van een dominante aardbevingsbelasting. Nadere beschouwing van het lengte-effect (Jongejan et al., 2017) heeft geleid tot aanpassing van de parameters. De parameters waarmee het lengte-effect wordt beschreven zijn a = 0,033 en b = 200 m. Op traject 6_7 resulteert dit in een terugkeertijd van ongeveer 2300 jaar en op traject 6_6 in een terugkeertijd van ongeveer 1100 jaar.

Reststerkte. Als uitgangspunt voor het ontwerp van Eemshaven-Delfzijl is een reststerkte-aanname geïntroduceerd bij grote vervormingen door een dominante aardbeving. Dat is gedaan omdat grote vervormingen door een dominante aardbeving niet zullen samenvallen met extreem hoogwater. In analogie met de gangbare praktijk voor buitenwaartse instabiliteit (bij laag water) is de reststerkte uitgedrukt in een voorwaardelijke kans op overstroming na het optreden van schade. Hoe groter de voorwaardelijke kans, hoe groter de terugkeertijd. De voorwaardelijke kans is geschat op 1/10, overeenkomstig de waarde die in de Leidraad Ontwerpen Rivieren wordt aangehouden in het vergelijkbare geval van schade zonder hoogwater door extreme regenval (TAW, 1985; TAW, 1989). Dit wil zeggen dat de terugkeertijd waaronder geen grote vervormingen van de dijk mogen optreden tien keer kleiner wordt aangenomen dan de terugkeertijd waaronder geen overstroming mag optreden.

Stabiliteitscriterium. Er is geen expliciet criterium geformuleerd voor stabiliteit tijdens en direct na de aardbeving. Indien de stabiliteit niet voldoende is zal dit leiden tot grote vervormingen en grote kruindaling, en zal niet worden voldaan aan het kruindalingscriterium. Daarom is de enige toets die plaatsvindt, die van de kruindaling.

Kruindalingscriterium. Uit representatieve overslagberekeningen is gebleken dat bij de voorwaardelijke kans van 1/10 een kruindalingscriterium van 3 m kan worden gehanteerd, indien wordt uitgegaan van een hersteltijd van 3 maanden (Deltares, 2016b, appendix I.2).

Onzekerheid berekeningen. Jongejan et al. (2017) beschrijft de procedure voor semi-probabilistisch ontwerp en de daarin toe te passen partiële veiligheidsfactoren voor alle van belang zijnde stochastische variabelen.

Voorgestelde uitgangspunten voor primaire keringen:

4 Het aardbevingsbestendig ontwerp vindt plaats op basis van een semi-probabilistische procedure. Door middel van rekenwaarden voor sterkte en belasting(en) wordt ervoor gezorgd dat de faalkans beneden de normwaarde (een op basis van de norm bepaalde toelaatbare waarde) blijft. Daarbij wordt rekening gehouden met de onwaarschijnlijkheid dat extreme waarden voor sterkte en belasting(en) tegelijk zullen voorkomen. Daarop aansluitend dient een dominante aardbevingsbelasting (met hoge terugkeertijd) te worden gecombineerd met een niet-dominante hydraulische belasting (met minder hoge terugkeertijd) en omgekeerd. Daarnaast moet ook het klassieke geval met alleen maatgevend hoogwater worden beschouwd. Bij elke te onderscheiden belastingcombinatie moet de kering voldoen aan de eis.

5 De invloedsfactor voor een dominante aardbevingsbelasting is 0,9. De invloedsfactor voor een dominante hydraulische belasting is 0,7.

6 Het faalkansbudget voor macrostabiliteit wordt verhoogd van 4 naar 24 %. Het faalkansbudget voor piping wordt dienovereenkomstig verlaagd van 24 naar 4 %.

7 Bij aardbevingen wordt het lengte-effect in rekening gebracht zoals beschreven in Jongejan et al. (2017). De parameters waarmee het lengte-effect wordt beschreven zijn a = 0,033 en b = 200 m.

8 Na significante vervormingen van de dijk als gevolg van een aardbevingsbelasting wordt gedurende de hersteltijd een voorwaardelijke kans van 1/10 op overstroming aangenomen.

9 Een voorwaardelijke overstromingskans van 1/10 leidt op grond van representatieve overslagberekeningen gedurende een hersteltijd van 3 maanden tot een maximaal toelaatbare kruindaling van 3 m.

10 Jongejan et al. (2017) beschrijft de procedure voor semi-probabilistisch ontwerp en de daarin toe te passen partiële veiligheidsfactoren voor alle van belang zijnde stochastische variabelen.

3.4 Weerstand tegen verweking van het zand

Classificatie van zandlagen. De *soil type behaviour index* I_c volgens (Robertson & Wride, 1998) wordt gebruikt voor het bepalen van de grondsoort die aan een CPT meting is gekoppeld en voor correlaties met de *fines content*. De index wordt uit de conusweerstand en de wrijving berekend. Voor I_c waarden kleiner dan 2,05 mag schoon zand worden verondersteld. Bij I_c waarden tussen 2,05 en 3 is waarschijnlijk sprake van zand/klei overgangen. Deze afzettingen blijken ook lage genormaliseerde conusweerstanden te hebben.

De correlatie tussen de klei fractie (percentage klei lagen) en de gemeten conusweerstand en *soil type behaviour index* I_c voor de Groningse gelaagde afzettingen is nader onderzocht om een grenswaarde vast te stellen tussen zand en klei (Deltares, 2016c). Uit de analyse blijkt dat

er een redelijk duidelijke correlatie bestaat tussen I_c en de klei fractie. Ook blijkt dat een I_c boven de 3 wijst op een pure kleilaag. Dit wijkt af van de waarde van 2,6 die in de meeste literatuur hiervoor wordt genoemd.

Correcties voor zand/klei overgangen en gelaagde afzettingen. Op de overgangen tussen zand en klei wordt de in zand gemeten conusweerstand beïnvloed door de kleilaag aan bovenzijde en onderzijde. De dikte van dergelijke overgangszones is maximaal 0,2 m (Deltares, 2016c). Om deze reden wordt een correctie op de conusweerstand toegepast.

In de LPI screening kan de dunne laag correctie op twee wijzen worden toegepast:

- Volgens de aanbevelingen van NCEER (1997) en Moss et al. (2006). De correctie wordt toegepast op alle potentieel als zand aangemerkte datapunten (met I_c waarden kleiner dan 2,6).
- Door in de eerste en laatste 0,2 m van de zandlaag een conusweerstand en een wrijvingsgetal te hanteren die overeenkomen met het gemiddelde van de volgende/vorige 0,2 m. De correctie wordt toegepast op alle potentieel als zand aangemerkte datapunten in overgangszones (met I_c waarden tussen 2,05 en 2,6).

Uit vergelijking van de gecorrigeerde conusweerstanden zijn geen significante verschillen gebleken die de LPI screening significant beinvloeden.

In de bepaling van de weerstand tegen verweking in de dynamische gekoppelde effectieve spanningsanalyses wordt de dunne laag correctie toegepast volgens de aanbevelingen van NCEER (1997) en Moss et al. (2006).

Voor afzettingen van het *Tfsc* type, met regelmatige afwisseling van dunne zand en kleilaagjes, wordt de sterkte onder cyclische belasting niet afgeleid uit de conusweerstand maar uit laboratoriumproeven (Jongejan et al., 2017, appendix D).

Veiligheidsfactor tegen volledige verweking. Door de cyclische aardbevingsbelasting kan tijdelijke verweking ontstaan in losgepakte zandlagen. Verweekt zand gedraagt zich als drijfzand, dat het gewicht van de dijk niet meer kan dragen. De weerstand tegen verweking van het zand wordt bepaald:

- Uit de conusweerstand gemeten in sonderingen in afzettingen die bestaan uit zand of uit afwisselingen van zand met relatief dikke kleilagen, volgens Boulanger & Idriss (2014). Dit model is internationaal gangbaar. Het model is empirisch en gebaseerd op ervaringen met tektonische aardbevingen van verschillende magnitudes.
- Uit cyclische laboratoriumproeven op ongeroerde monsters uit afzettingen die bestaan uit een afwisseling van relatief dunne zand- en kleilaagjes, de zogenaamde gelamineerde wadzand afzettingen.

Representatieve waarde van de genormaliseerde conusweerstand. In de screening wordt de LPI bepaald op basis van alle data punten in de sondering met I_c kleiner dan 2,6.

De bepaling van de representatieve waarde van de conusweerstand en de weerstand tegen verweking voor de dynamische gekoppelde effectieve spanningsanalyses gebeurt volgens Jongejan et al. (2017), appendix G.

***Fines* toeslag**. De *fines* toeslag volgens Boulanger and Idriss (2014) wordt toegepast op de conusweerstand, met *CFC* = 0.

Magnitude Scaling Factor. De magnitude scaling factor volgens Boulanger and Idriss (2014) wordt gebruikt.

Correctiefactoren voor de verticale spanning K_σ en statische schuifspanning K_α. De factor K_σ brengt in rekening dat de verwekingsgevoeligheid toeneemt bij een hogere effectieve verticale spanning, en dezelfde relatieve schuifspanningsamplitude CSR. De factor K_σ wordt bepaald volgens (Idriss & Boulanger, 2014).

De correctiefactor voor de statische schuifspanning K_α brengt het effect van de statische schuifspanning op de verwekingsgevoeligheid in rekening. Deze parameter is van belang voor zand in taluds. De LPI screening wordt uitgevoerd op basis van de sonderingen aan de zeezijde van de dijk, waarbij een horizontaal maaiveld wordt verondersteld (α=0). Om deze reden wordt een waarde K_α =1 gehanteerd.

Correctiefactor voor de leeftijd van de afzettingen K_{DR}. De gegevens in de database van Idriss & Boulanger hebben grotendeels betrekking op holoceen zand en jonge zandaanvullingen. Het is aannemelijk dat de bepaling van de $CRR_{7.5}$ vooral wordt bepaald door opgebracht zand met een leeftijd van minder dan 200 jaar. De leeftijd van het pleistocene Boxtel zand is 20.000 jaar en de leeftijd van het pleistocene Peelo zand is 425.000 jaar. De grotere weerstand tegen verweken bij dergelijke hoge leeftijden is in diverse onderzoeken aangetoond, maar is (nog) niet in normen of leidraden opgenomen. De relaties tussen leeftijd en relatieve verwekingsweerstand volgens (Arango & Migues, 1996), (Hayati & Andrus, 2009) en (Green, Maurer, Bradley, Wotherspoon, & Cubrinovski, 2013) zijn vergeleken in (Deltares, 2016c). De relaties volgens (Hayati & Andrus, 2009) en (Green, Maurer, Bradley, Wotherspoon, & Cubrinovski, 2013) zijn vrijwel aan elkaar gelijk. Indien de Green & Maurer functie wordt verschoven zodat de K_{DR} waarde bij een leeftijd van 200 jaar gelijk wordt aan 1, is de waarde bij een leeftijd van 20.000 jaar gelijk aan 1,3.

Voor de relatief jonge holocene afzettingen wordt dient K_{DR}=1 aangehouden.

Voorgestelde uitgangspunten voor primaire keringen:

11 Een CPT datapunt wordt als zand geclassificeerd als de *soil type behaviour index* I_c volgens (Robertson & Wride, 1998) kleiner of gelijk is aan 2,6.

12 Rond discrete overgangszones zand/klei wordt over 0,2 m de conuswaarde in de zandlaag gecorrigeerd.

13 De weerstand tegen verweking wordt berekend op basis van:
- correlaties met sonderingen volgens Boulanger & Idriss (2014) in afzettingen die bestaan uit zand, al dan niet afgewisseld met relatief dikke kleilagen, waarin de I_c waarde kleiner is dan 2,05.
- cyclische laboratoriumproeven op ongeroerde monsters in afzettingen die bestaan uit een afwisseling van relatief dunne zand- en kleilaagjes, waarin de de I_c waarden tussen 2,05 en 2,6 liggen (afzettingen van het *Tfsc* type).

14 In de screening wordt de LPI bepaald op basis van alle data punten in de sondering met Ic kleiner dan of gelijk aan 2,6. Appendix G van Jongejan (2017) beschrijft de bepaling van de representatieve waarde van de conusweerstand en de weerstand tegen verweking voor de dynamische gekoppelde effectieve spanningsanalyses.

15 Op de genormaliseerde conusweerstand wordt een *fines* toeslag toegepast om te corrigeren voor het gunstige effect van het gehalte fijne fractie volgens Boulanger and Idriss (2014), met $CFC = 0$.

16 De magnitude scaling factor wordt bepaald volgens Boulanger and Idriss (2014).

17 De correctiefactor voor de verticale spanning K_σ en de correctiefactor voor statische schuifspanning K_α voor zand in taluds worden bepaald volgens Boulanger & Idriss (2014). In de LPI screening op basis van de sonderingen aan de zeezijde van de dijk wordt gerekend met $K_\alpha = 1$.

18 Voor de correctiefactor voor de leeftijd van de afzettingen K_{DR} wordt voor de relatief jonge holocene afzettingen een waarde 1 aangehouden, voor het pleistocene zand een waarde van 1,3.

4 Referenties

Arango, I., & Migues, R. (1996). *Investigation of the seismic liquefaction of old sand deposits.* Rep. on Research, Bechtel Corporation, National Science Foundation Grant No. CMS-94-16169.

Bommer, J., & Bourne, S. (2015). *Seismic Hazard Analysis for the Eemshaven-Delfzijl Sea Levee, a report prepared for NAM.*

Boulanger, R., & Idriss, I. (2014). *CPT and SPT based liquefaction triggering procedures.*

CUR. (1997). *Kansen in de Civiele Techniek, deel 1.* CUR.

Deltares. (2015e). *Aardbevingsbestendige waterkeringen, Opties voor een haalbaar en betaalbaar ontwerp, versie 3.* Deltares rapport nr. 1220173-002-GEO-0001-v3.

Deltares. (2016a). *Ontwerpuitgangspunten Hoogwaterbelasting Dijkversterking Eemshaven-Delfzijl.* Deltares rapport 1220173-005-GEO-0016.

Deltares. (2016b). *Seismisch Dijkontwerp, protocol voor Eemshaven-Delfzijl.* Deltares rapport nr. 1220173-024-GEO-0001.

Deltares. (2016c). *Vak 7 (km 30) - RT6500 - Comparison 1D and 2D analyses.* Deltares report 1220173-000-GEO-0014.

Deltares (2017). *LPI screening for the Eemshaven-Delfzijl levee*. Deltares report no. 1220173-024-GEO-0067, version 3.

ENW. (2014a, december 8). *Advies aardbevingsbestendige zeedijk Eemshaven – Delfzijl*. Kenmerk ENW-14-15. Retrieved from http://www.enwinfo.nl/images/pdf/adviezen-2014/ENW-14-15-Advies-WaterschapNoorderzijlvest-aardbevingsbestendige-zeedijk-Eemshaven-Delfzijl.pdf

Fugro (2017). *Evaluation of dynamic stability using code calibrated design parameters, Eemshaven-Delfzijl levee, The Netherlands*. 1 March 2017, contract no. 1016-0459-000, version 00.

Green, R. A., Maurer, B. W., Bradley, B. A., Wotherspoon, L., & Cubrinovski, M. (2013). *Implications from liquefaction observations in New Zealand for interpreting paleoliquefaction data in the central eastern United States.* U.S. Geological Society Final Technical Report Award No. G12AP20002.

Hashash, Y. M. (2015). *Deepsoil, Nonlinear and Equivalent Linear Seismic Site Response of One-Dimensional Soil Columns, version 6.1.* University of Illinois.

Hayati, H., & Andrus, R. (2009). *Updated Liquefaction Resistance Correction Factors for Aged Sands*. J. Geotech. Geoenviron. Eng., 135(11): 1683-1692.

ISO. (2013). *General principles on reliability for structures, stage 40.20.*

Iwasaki, T., Tatsuoka, F., Tokida, K., and Yasuda, S. (1978). *A practical method for assessing soil liquefaction potential based on case studies at various sites in Japan*. Proc., 2nd Int. Conf. on Microzonation, San Francisco, pp. 885−896.

Jongejan R.B., Chacko J., Giannakou A., Drosos V., Tasiopoulou P. (2017). *Code calibration for coupled, effective stress FEM-assessments of the primary flood defenses at Eemshaven-Delfzijl*. 28 February 2017.

KNMI. (2013). *Report on the expected PGV and PGA values for induced eartquakes in the Groningen area.*

KNMI. (2015, Oktober). *Probabilistic Seismic Hazard Analysis for Induced Earthquakes in Groningen; Update 2015.*

Maurer, B., Green, R., Cubrinovski, M., & Bradley, B. (2014). *Assessment of aging correction factors for liquefaction resistance at sites of recurrent liquefaction.* Tenth U.S. National Conference on Earthquake Engineering Frontiers of Earthquake Engineering.

Moss, R.E.S, Seed, R.B., Kayen, R.E., Stewart, J.P., Der Kiureghian, A. (2006). *CPT-Based Probabilistic Assessment of Seismic Soil Liquefaction Initiation*. Report no. 2005/15, Pacific Earthquake Engineering Research Center, Richmond CA.

NAM. (2015). *Hazard and Risk Assessment for Induced Seismicity in Groningen, Interim Update November 2015.*

NCEER (1997). *Proceedings of the NCEER Workshop on Evaluation of Liquefaction Resistance of Soils*.Technical Report No. NCEER-87-0022.

NEN. (2015). *NPR9998 - Beoordeling van de constructieve veiligheid van een gebouw bij nieuwbouw, verbouw en afkeuren - Grondslagen voor aardbevingsbelastingen: Geïnduceerde aardbevingen.*

Robertson, P., & Wride, C. (1998). *Evaluating cyclic liquefaction potential using the cone penetration test*. Canadian Geotechnical Journal, vol. 35, 442 - 459.

TAW. (1985). *Leidraad voor het ontwerpen van rivierdijken. Deel 1 – Bovenrivierengebied.*

TAW. (1989). *Leidraad voor het ontwerpen van rivierdijken. Deel 2 – Benedenrivierengebied.*

Kopie aan

Bert de Wolff (Waterschap Noorderzijlvest), Geeralt van den Ham (Deltares)

A Expert workshop seismisch ontwerp: expert advies

Schiphol, 17-18 november 2016

December 3, 2016

Ms. Edith van Dijk
Principal Project Manager
Shell Global Solutions International BV

Dear Ms. Van Dijk:

This report describes the recommendations of the liquefaction expert panel engaged to review proposed protocols for evaluating the seismic stability of levees between Eemshaven and Delfzijl (E-D) in the Groningen region of the Netherlands. The recommendations are based on our reviews of documents provided to us in advance of the 17-18 November 2016 workshop, discussions held at the workshop, and discussions among the panel members following the workshop. We appreciated the clear presentations and frank discussions among the workshop participants, as they helped us to better understand the protocols that were being proposed. This understanding has allowed us to make some clear comments on the proposed protocols and to recommend a path forward.

This document provides a review and general comments on alternative approaches to evaluate the seismic stability of the E-D levee, and a recommended path forward. It does not present detailed or specific comments on the various documents we reviewed; such comments, if desired, can be compiled in a separate report.

Background
The process for evaluation of the stability of levees between Eemshaven and Delfzijl has been underway for some time. A great deal of subsurface exploration has taken place and has defined the major soil units within, underlying, and adjacent to the levees. The subsurface investigation has included extensive field and laboratory testing, and specialized laboratory testing of some of the unusual soils encountered in the investigations.

The levees are underlain by five main geologic formations. The Naaldwijk Formation extends from the original ground surface to depths of about 15 m, and consists of young, tidal and flood plain deposits including thinly interlayered loose to dense fine sands and soft to stiff silts and clays. The Naaldwijk Formation is underlain by the Nieuwkoop Formation, which consists of 0.5 m to 5 m thick layers of peat. The Naaldwijk and Nieuwkoop Formations are of Holocene age, and are underlain by Pleistocene sediments. The Boxtel Formation, comprised primarily of fine sands and silts, underlies the Naaldwijk and Nieuwkoop Formations. The Boxtel Formation is several to tens of meters thick at Eemshaven and generally less than 5 m thick and laterally discontinuous at Delfzijl. At Eemshaven, the Boxtel Formation is underlain by 3-5 m of fine to coarse sand with marine shells and shell fragments known as the Eem Formation. The Boxtel and Eem Formations are underlain all along the levee alignment by the Peelo Formation, a thick fluvio-glacial clay with some sand characterized by high penetration resistance. From the standpoint of seismic stability, the loose and soft Naaldwijk and Nieuwkoop soils are of primary concern, and particular attention is required for characterization of the interlayered Naaldwijk soils.

The levee sections vary at different locations. Near Eemshaven (km 37-38.7) the levees feature an old clay core on the landside. A short section (km 29-29.5) near Delfzijl is comprised of only sand. The great majority of the E-D levee, however, has a clay core on the outboard seaside of the levee. Many portions of the levees along the entire length from Eemshaven to Delfzijl contain loose, saturated sand that may be susceptible to liquefaction. The continuity of these sand layers is not always clear between individual explorations. Relatively thin, discontinuous pockets generally do not result in large, liquefaction-induced deformations, so the focus should be on sand layers of significant lateral continuity.

Subsurface investigations consisted of extensive cone penetration test (CPTu) soundings with various geophysical testing including shear wave velocity measurement, and gamma-gamma testing. A large number of borings were advanced with different types of sampling attempted; continuous sampling was performed in 74 Ackermann borings. Undisturbed samples were taken for consolidation, (static and cyclic) triaxial, and cyclic simple shear testing. Disturbed materials were tested for grain size characteristics, Atterberg limits, density, and water content. A recent investigation focused on collecting larger-diameter piston samples and Begeman samples of the interlayered Naaldwijk soils. These samples were then used for cyclic testing to help characterize the liquefaction resistance of these soils. An additional campaign of gel-push sampling was completed, but laboratory test results on these samples are not yet available.

Deltares Protocol

Deltares proposed a protocol for evaluating levee stability and the design of remedial measures, with the protocol based on a few different simplified models. The protocol involved: (a) performing one-dimensional site response analyses of different levee profiles (crest, landside, seaside) with PSHA-based ground motions to obtain cyclic stress ratios, (b) characterizing the cyclic resistance from the volumes of CPT data available for a given unit over stretches of levee, (c) using the maximum cyclic stress ratios of the three locations considered and a characteristic cyclic resistance to compute factors of safety against triggering of liquefaction, (d) using the lowest computed factors of safety to estimate pore pressure ratios – typically assuming pore pressure ratios of 1.0 for soils with factors of safety less than or equal to 1.0 and estimating excess pore pressure ratios in soils that did not liquefy from a laboratory test-based relationship, and (e) using the effective stresses corresponding to the computed pore pressure ratios to perform levee stability and settlement analyses. The stability analyses were to be performed using a displacement-compatible pseudo-static acceleration obtained by means of Newmark rigid sliding block analyses. The simplified models were incorporated in a framework that was described as being “semi-probabilistic.” The expert panel had comments on a number of components of the protocol, which were expressed verbally at the workshop and are repeated herein:

1. The use of the CPT for estimation of the liquefaction resistance of the soils along the E-D levee is considered appropriate for primarily sand layers of recognizable thickness. However, the in-situ characterization of the interlayered tidal deposits and the older Pleistocene deposits is challenging, regardless of the technique used. In particular the CPT resistance of thin layers that are not easily detected may not provide representative cyclic resistance values of these thin layers. Note that undisturbed sampling and laboratory testing of these deposits provides information on the liquefaction response of these soils, but there are also limitations with that approach (e.g., sample disturbance, load path, etc.). Nevertheless, the laboratory data represents the behavior of the Groningen soils themselves rather than empiricism imported from elsewhere under different geologic and tectonic conditions; the laboratory test results should be carefully compared with empirical case history-based results to estimate

liquefaction resistance. The laboratory tests performed to date show that for most interlayered materials, the direct use of the CPT penetration resistance in these deposits is conservative (i.e., use of penetration resistance with no corrections applied for layering to estimate liquefaction triggering resistance and post-liquefaction shear strength, and ignoring effects of mixing, during large deformations appears to be conservative). By contrast, the CPT tip resistances in the primarily sand layers typically show higher cyclic resistance than the laboratory test results.

2. Interpretations described as being “conservative” were introduced at different stages of the protocol. For example, a thin-layer correction factor of 1.8 is recommended, even though the best estimate value appears to be on the order of 3.0-3.5; the 33rd percentile CPT resistance of a volume of data which may include transitions from clay to sand in excessively thin layers is used for sand layers; treating the entire thickness of the interlayered materials as a single layer; ignoring fines corrections on the tip resistances of sand sub-layers within the interlayered deposits; and treating the lowest factor of safety over the height of a particular soil layer as being representative of the entire layer. The basis for, and degree of, the conservatisms were not described/quantified, so it is impossible to determine the probability associated with each. There was no indication of a consistent approach for making the conservative interpretations, and thus the degree of conservatism in each must be considered to be both unknown and inconsistent.
3. The conservative interpretations were applied to components of the stability evaluation process that built upon each other; thus, the results from the protocol will be affected by a compounding of conservatisms that will likely induce a conservative bias of unknown degree. This is inconsistent with a probabilistic (or semi-probabilistic) approach to evaluating the levee stability. The protocol would appear to estimate uncertainties about a biased mean or median estimate. In some cases the averaging of properties and strata, or ignoring where CPT data are representative, can result in misleading conclusions regarding the liquefaction resistance of the unit, and subsequently, the potential for liquefaction-induced deformations.
4. The relationship proposed to predict excess pore pressures from factor of safety is dated and very approximate. It is expected to provide, at best, a crude estimate of induced pore pressure for soils that do not liquefy. Other procedures that yield more accurate predictions of pore pressure are available.We believe it is more appropriate to use modern coupled-effective stress approaches for realistic evaluations of stability.
5. The sliding block analysis, in which a potentially unstable mass of soil is assumed to exhibit rigid-perfectly plastic behavior, is not applicable to stability evaluations involving significant amounts of liquefiable soil. The behavior of liquefiable soils subjected to cyclic loading is extremely complex and very different than that assumed in sliding block analyses; consequently displacement predictions based on that method are unreliable. The inability of the sliding block model to capture the complex mobilization of shearing resistance in liquefiable soils and its inability to model the actual mechanism(s) causing permanent deformations of the Groningen levees are significant factors. Given these limitations, the use of such a procedure to assess a critical yield acceleration is unreliable.
6. The proposed stability analyses are performed using effective stress strength parameters for both coarse- and fine-grained soils, and use estimated effective stresses at the end of shaking to compute shear strengths. This approach ignores the contributions of dilatancy to the shear strength of coarse-grained soils, and implies that drained strengths will be used for both coarse- and fine-grained soils. The effective stress at the end of shaking in coarse-grained soils is not the effective stress that would exist at failure – depending on their state, coarse-grained soils will tend to dilate (or

contract, if very loose) as they are sheared which will lead to changes in effective stress and shear strength as shearing progresses. Fine-grained soils have very low permeability, and would almost certainly be loaded under undrained conditions during and shortly after earthquake shaking. Since they are not heavily overconsolidated, the clays at the Groningen levee site would be expected to generate positive pore pressures that would cause their shear strength to be lower than the strength implied by drained loading. These pore pressures are most easily accounted for by using total stress (undrained) strengths in the short-term, total stress stability analyses.

On the basis of these comments, the expert panel judged the proposed Deltares protocol to be unsuitable for evaluation of the seismic stability of the levees, and for design of remedial measures. Some elements of the protocol could, after modification, be useful as part of a screening analysis to identify portions of the levee where liquefaction effects are likely to be more severe.

Fugro Effective Stress Analyses

Fugro reported on their interpretation of field and laboratory tests and presented the results of an extensive series of nonlinear, effective stress, finite difference analyses of two levee sections – one near Eemshaven and the other near Delfzijl. The field and laboratory test results were clearly presented and discussed. The interpretation of the test results appeared to be generally appropriate, although several comments are noted below. They described their numerical models of the two levee sections and the results of their analyses of the sections when subjected to different input motions developed from a PSHA and deterministic site response analyses.

1. Properly performed, nonlinear, effective stress analyses are suitable, and in fact preferred, for critical projects such as evaluation of the seismic stability of the Groningen levees. Effective stress analyses allow consideration of site-specific geometry/material behavior and interaction of modeled sites with specific ground motions. They also allow the identification of realistic deformation mechanisms without the constraints associated with many simplified methods of analysis. They require good site characterization and validated constitutive models – validation should be based on ability to represent material behavior at the element level, observed in high-quality laboratory tests, and also system level behavior of sites observed in well-documented field case histories and physical model tests. The levee response will likely be highly nonlinear and can be sensitive to constitutive model characteristics and numerical integration schemes. Multiple, redundant analyses should be performed for critical projects – using as a minimum different constitutive models and, where necessary, different numerical codes.
2. Dynamic effective stress analyses have developed to the point where they can provide useful indications of the performance of systems affected by liquefiable soils. However, they are very time-consuming and should therefore be performed only on levee sections at locations deemed to have significant potential for liquefaction-related damage.
3. With well-calibrated and validated constitutive models embedded in reliable numerical tools, dynamic effective stress analyses using multiple input motions can provide an indication of the range of expected levels of performance. They also allow evaluation of the sensitivity of response to various input parameters and modeling assumptions. It will be important, however, to recognize potential uncertainties in constitutive models and numerical analyses. For critical projects, parallel analyses should be performed using different constitutive models and different numerical tools. FLAC with UBCsand and PM4sand are good, but these analyses should be supplemented by parallel check

analyses using a different computational tool, e.g., OpenSees with PDMY model or FLIP with cocktail glass model.

4. The results of the Fugro numerical analyses included sensitivity analyses that help identify the most influential variables affecting levee crest settlement. They do not, however, address the uncertainty in crest settlement, which is necessary in order to properly characterize stability hazards given the requirements of limiting failure to a probability related to the high-water flooding probability. Procedures for estimating the distribution of crest settlement are required.

General Comments

A number of general comments came up during discussions during and following the workshop. These comments relate to the seismic stability evaluation, but relate to broader issues than the approaches pursued by Deltares and Fugro.

1. Performance standards should be explicitly identified, on a location-specific basis if necessary. Various documents have described performance requirements in terms of crest settlement (using values ranging from 0.10 m to 1.0 m) and in terms of allowable flooding probabilities. The standards should be stated in clear, unambiguous terms so that they are clearly understood by everyone performing and reviewing the levee stability evaluation. We understand that the performance criteria are to be expressed probabilistically, i.e., relative to the probability of flooding under high-water conditions. This type of criterion requires characterization of uncertainty in the seismic performance evaluation.
2. The impacts of repair methods on normal operation of levees and on performance during other extreme loading conditions must be considered when evaluating the need for, or selecting between alternative retrofits. For example, the use of an impermeable structural wall (e.g., a sheet pile wall) on the landside of the levee could cause the water level within the levee to rise during storm events and potentially reduce the stability of the levee under these conditions. Similarly, the use of anchors between parallel rows of bulkheads may increase the risk of piping. Preparedness for emergency situations (quick restoration) is also important.
3. Empirical relationships based on data from many soils under many different conditions can be very useful for estimating soil properties and their variation with in-situ conditions. However, they may not account for site-specific conditions in the way that laboratory tests on undisturbed samples from the site of interest can. Careful attention should be paid to the integration of site-specific data with data from empirical relationships to ensure that pertinent site-specific soil characteristics are properly accounted for.
4. While the use of probabilistic methods often provides guidance and improved decision making, this is only the case where the available data and geotechnical analyses are sufficiently developed to meaningfully capture the uncertainties and the full range of scenarios can be properly analyzed. For example, soil samples from the same site and the same depth may exhibit different behaviors during laboratory tests but we do not definitively know whether the differences are random, due to sample disturbance, heterogeneity of in-situ ground, etc. The results of probabilistic approaches should be checked by deterministic evaluations using reliable analytical models and reasonably conservative design parameters.

Recommendations

The Groningen levees span a considerable distance with variable soil conditions over their length. A great deal of effort has been expended in field and laboratory investigations of the properties of the soils that underlie the levees, and a great deal of effort will be required to

identify seismically vulnerable portions of the levee, and to design remedial measures for those portions. In the interests of both cost and time, it will be necessary to adopt an efficient approach to the seismic stability evaluation. We recommend that the seismic stability evaluation consist of two phases, a preliminary screening phase and a detailed analysis phase.

1. In the first phase, simplified procedures based on available CPT data should be used to estimate the potential liquefaction severity at each point where CPT data is available. The actual, best-estimate CPT data (rather than a percentile value from data aggregated over a large volume) should be used in these analyses. In addition to evaluations of factors of safety at each CPT location, we recommend that liquefaction severity be characterized using the Liquefaction Potential Index (LPI). Where the initially estimated liquefaction severity is significant, careful evaluation of the data should be conducted to confirm if the basic CPT data are representative of the resistance of the unit, whether detailed investigation is warranted for the vulnerable layers, or whether alternative sources such as laboratory test data should be used to evaluate liquefaction triggering.
2. If the Phase 1 analyses show a significant risk of liquefaction-related damage, a secondary phase involving detailed, nonlinear, effective stress analysis of levee sections that do not pass the preliminary screening should be initiated. In such cases, we recommend an approach based on two-dimensional, nonlinear, effective stress response analyses. Analyses should use multiple codes with multiple constitutive models to represent model uncertainty. Sensitivity analyses should be performed to identify important variables and compute uncertainty in crest settlement using simple methods such as point estimation, FOSM, or FORM – these ultimately would predict the distribution of crest settlement conditional upon a ground motion level (Sa [T], PGA, $PGA_{7.5}$, etc.).

The results of these analyses can be presented in the form of crest settlement fragility curves, which could then be convolved with PGA or PGA7.5 hazard curves to obtain crest settlement hazard curves – the design of remedial measures could then be based on allowable crest settlement for some design return period. The crest settlement hazard curve could also be interpreted in terms of the mean annual probability of exceeding various levels of crest settlement.

An immediate action that will expedite the implementation of the two-phase protocol includes performing a detailed, nonlinear, effective stress analysis parametric study of the two levee sections that were already analyzed, using motions scaled to increasing amplitudes. The results of this parametric study will help determine the threshold LPI value for intolerable levee deformations. The study should also help confirm the selection of LPI as a screening tool and guide the selection of threshold LPI values for triggering more sophisticated analyses.

Summary
We appreciate the opportunity to collect our thoughts and impressions and present them in the form of comments and recommendations that represent the consensus of the liquefaction expert panel. We believe that the phased approach described in this report provides a logical, methodical, and efficient path toward evaluation of seismic stability of the levees and toward design of any required improvements to them. We would be happy to answer any questions that you or others have about the comments and recommendations presented herein.

Sincerely,

Jacob Chacko
Russell A. Green
Steven L. Kramer
Ikuo Towhata

B Review letter prof. Kramer

STEVEN L. KRAMER, PH.D.
Consulting Engineer

5141 189th Avenue NE
Sammamish, WA 98074
(425) 836-4754

March 1, 2017

Dr. Mattijs de Mooij
Advisor
Nationaal Coördinator Groningen
Paterswoldseweg 1, 9726 BA
Groningen, Postbus 3006
9701 DA Groningen

Dear Dr. de Mooij,

I am writing to present my conclusions regarding the reports regarding seismic stability evaluations for the Eemshaven-Delfzijl levees that I have reviewed in draft form over the past several weeks. My reviews included the report on liquefaction potential index (LPI) screening analyses prepared by Deltares and the code calibration report prepared by Fugro. The code calibration report made use of two-dimensional, nonlinear dynamic analyses that I also reviewed.

I found the Deltares report on the LPI screening analyses to present the results of the screening analyses clearly and accurately. The analyses were based on soil conditions interpreted reasonably from the results of an extensive subsurface investigation program, and on ground motion hazards characterized by a state-of-the-art probabilistic seismic hazard analysis. I believe that the LPI screening analyses have identified the locations along the levee that are most likely to experience significant crest settlements, and have flagged those locations for more detailed analyses.

The detailed analyses used in the code calibration process described in the Fugro report included two-dimensional, nonlinear effective stress site response analyses performed using the finite difference code, FLAC. These analyses appear to have been performed with a high level of care and detail, and their results have been used to characterize the relationship between crest settlement and the various loading, material, and geometric parameters that affect it. The Fugro team also performed innovative analyses that helped characterize the behavior of the complex interlayered soils of Unit 8, which were critical to the evaluation of seismic stability.
I also reviewed and commented upon various aspects of the code calibration portion of the Fugro report. Reliability analyses and the requirements of the Dutch codes are beyond my area of technical expertise so my comments related primarily to the clarity and consistency of the descriptions of those analyses.

It has been a pleasure to work with you and the other professionals investigating the seismic stability of the Eemshaven-Delfzijl levees. I trust that this letter provides the information you require at this time. Please do not hesitate to contact me if you have any questions.

Sincerely,

Steven L. Kramer
Consulting Engineer

C Review letter dr. Calle

E.O.F Calle
Adviseur Waterveiligheid
Nesciohove 26
2726BH Zoetermeer
mob.: 0650202068

Zoetermeer, 3 Maart 2017.

Aan de heer drs. Mattijs de Mooij,
Adviseur, Nationaal Coördinator Groningen
Postbus 3006,
9701DA Groningen

Betr. Review Deltares Rapport

Geachte heer De Mooij,

Hiermee deel ik u de bevindingen mee van mijn review van het rapport:

Code calibration for coupled, effective stress FEM-assessments of the primary flood defenses at Eemshaven-Delfzijl

Auteurs: Ruben Jongejan (Jongejan RMC), Jacob Chacko (Fugro), Amalia Giannaku (Fugro) en Vasileos Drossos (Fugro).

Het rapport bevat componenten op het gebied van seismische technieken voor dammen (en dijken) en componenten op het gebied van de probabilistische veiligheidsfilosofie van dijken (waterkeringen) in Nederland. Bij de review heb ik me hoofdzakelijk gericht op de veiligheidsfilosofie en hieraan gerelateerde probabilistische betrouwbaarheidsanalyses. Dit omdat seismiek niet tot mijn expertise behoort en ook omdat seismische aspecten door internationaal erkende vakspecialisten werden (en deels al waren) gereviewd. Hierbij heb ik alleen gekeken naar de helderheid en consistentie van de beschrijvingen.

Het hoofdprobleem in het rapport betreft het optuigen van een methode voor het afleiden van aan te houden rekenwaarden van belasting- en sterkteparameters bij het ontwerpen van aardbevingsbestendige dijken, met behulp van de door Fugro ontwikkelde methode, gebaseerd op dynamische numerieke-analyses om de stabiliteit en kruindaling van aarden dammen tijdens en na aardbevingen te berekenen. Die ontwerpen moeten zodanig zijn dat dijken voldoen aan de in de Nederlandse wet vastgelegde veiligheidsnormen, in termen van nog net acceptabel kleine overstromingskansen (doorbraakkansen) in de zogenoemde normtrajecten van de primaire waterkeringen.

De reeks interpretatie/vertaal-slagen die hiervoor doorlopen moet worden, namelijk van "trajectkansen" → "toelaatbare bijdragen door de verschillende potentiële faalmechanismen" → "toelaatbare doorbraakkansen per faalmechanisme per dwarsdoorsnede" en, ten slotte, de vertaling van de laatste naar een rekenvoorschrift (karakteristieke waarden en partiële veiligheidsfactoren voor de rekenmodellen waarmee de veiligheid tegen een falen door een aardbeving wordt geverifieerd, is in het document helder beschreven.

De gekozen opzetten bij de vertaalslagen zijn conform geaccepteerde inzichten en uitgangspunten op het gebied van de probabilistische veiligheidsfilosofie voor de hoogwaterbescherming in Nederland, zoals beschreven in de Leidraad Grondslagen voor Waterveiligheid en andere leidraden van het ENW (Expertise Netwerk Waterveiligheid). Bij de vertaalslagen is gezocht naar optimale, maar nog wel voldoende veilige, aannamen om onnodig conservatisme in de beoogde ontwerpregels te vermijden. De aanpak is “State of the Art”.

Gegeven de tijdsdruk op het project zijn voor de review conceptversies van het rapport van 15 en 24 februari 2017 gebruikt. In deze conceptversies is via kantlijnopmerkingen en “track changes” commentaar gegeven. In de versie van 28 februari is dit commentaar verwerkt; dit is wat mij betreft akkoord.

Mocht u nog vragen hebben, dan zal ik die graag, voor zover dat binnen mijn bereik ligt, beantwoorden.

Met vriendelijke groet,

Ed Calle

D Rapport ‘Code calibration for coupled, effective stress FEM-assessments of the primary flood defenses at Eemshaven-Delfzijl’ (Jongejan et al., 2017)

Code calibration for coupled, effective stress FEM-assessments of the primary flood defenses at Eemshaven-Delfzijl

Final report

28 February 2017

Authors:
Ruben Jongejan (RMC)
Jacob Chacko (Fugro)
Amalia Giannakou (Fugro)
Vasileios Drosos (Fugro)
Panagiota Tasiopoulou (Fugro)

Table of contents

1 Introduction

This document concerns the derivation of design values for use with the assessment method developed by Fugro for the primary flood defenses at Eemshaven-Delfzijl (Fugro 2016a; Fugro 2016b). This method involves:

1. A fully coupled, dynamic, effective stress co-seismic analysis, in which displacements are calculated with dynamic FEM-calculations while excess pore pressures are being generated.
2. A static post-seismic analysis, in which residual displacements are calculated with the excess pore pressures and deformations at the end of shaking as a starting point.

This document presents the results of a code calibration study for the abovementioned numerical analyses. It also provides background information about the Dutch flood protection standards and code calibration studies in general. The code calibrated assessment procedure is summarized in chapter 8.

The code calibration assessment procedure has been developed for assessing the seismic stability of the Eemshaven-Delfzijl sea dikes. For other applications, such as for regional flood defenses, it is recommended to verify the applicability of the design values presented herein with probabilistic analyses.

2 Flood protection standards and code calibration

The Dutch flood protection standards are defined in terms of maximum allowable probabilities of flooding. The maximum allowable probabilities of flooding range from 1/100 per year to 1/100,000 per year. The Eemshaven-Delfzijl project covers parts of two different segments: segment 6-6 with a standard of 1/1,000 per year and segment 6-7 with a standard of 1/3,000 per year (Figure 1).

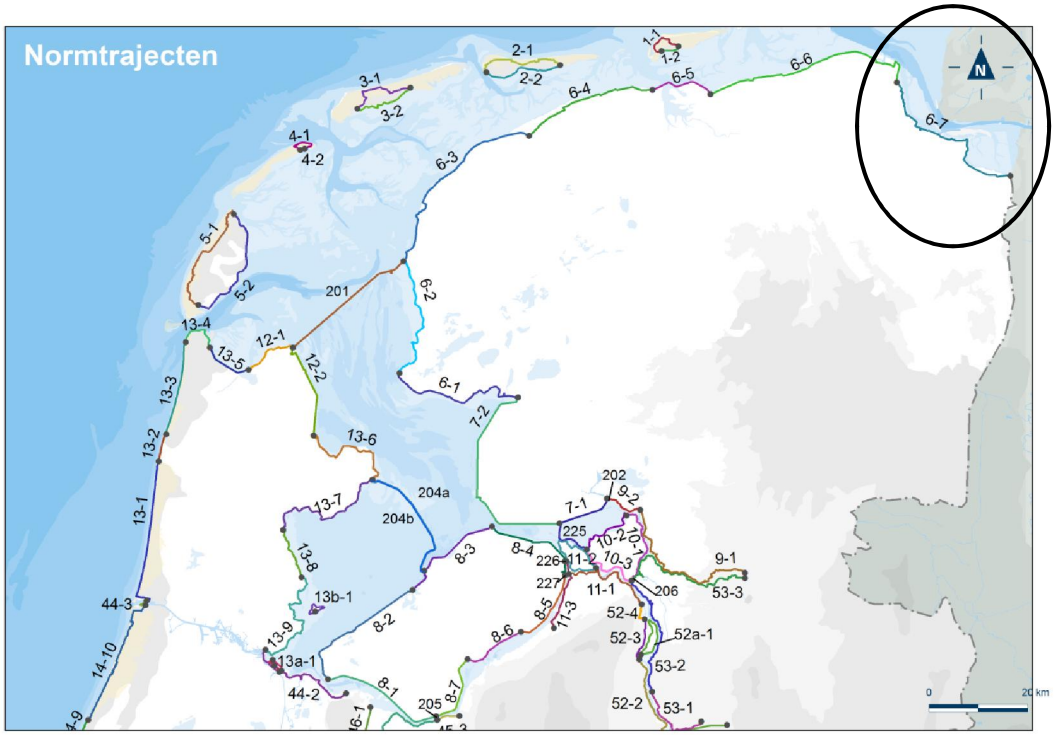

Figure 1. Overview of segments in the Flood Protection Act (in Dutch: Waterwet).

There are essentially two approaches for assessing whether a flood defense complies with a flood protection standard:

1. Probabilistic (using e.g. Monte Carlo, FORM)
2. Semi-probabilistic (design value or partial factor approach)

While the outcomes of probabilistic analyses can be compared directly to reliability requirements, most engineers are unfamiliar with probabilistic methods. Probabilistic analyses can also be prohibitively time consuming, which is the case for the model considered herein. A semi-probabilistic procedure is essentially an approximate procedure for evaluating whether a probability of flooding is smaller than required by law.

Probabilistic and semi-probabilistic safety assessments are closely related. Both rely on the same reliability requirements, the same limit state functions and the same probability distributions of stochastic variables. The only difference concerns the fact that a semi-probabilistic approach rests on a number of simplifications and approximations, giving it the appearance of a deterministic procedure.

In probabilistic safety assessments, analysts consider the probability that the ultimate limit state is exceeded, i.e. that load (S) exceeds resistance (R). The failure probability, P(S>R), should not exceed some maximum allowable or target probability of failure (P_T).

In semi-probabilistic assessments, analysts consider the difference between the design values of load (S_d) and strength (R_d): S_d should not exceed R_d. Design values are representative values such as 5^{th} or 95^{th} quantile values or 1/10.000 yr^{-1} water levels, factored with partial safety factors, see equations (1) and (2). Note that the

definitions from the Eurocode have been adopted here, similar terms may have different meanings in other codes.

$$S_d = S_{rep} \cdot \gamma_S \quad (1)$$

$$R_d = R_{rep} / \gamma_R \quad (2)$$

Where:

S_d	Design value of uncertain load variable
R_d	Design value of uncertain resistance variable
γ_S, γ_R	Partial factors

Design values, and hence (partial) safety factors, should be defined in such a manner that $S_d \leq R_d$ implies that the probability of failure meets the reliability requirement: $P(S>R) \leq P_T$. The relationship between probabilistic and semi-probability safety assessments is illustrated in Figure 2.

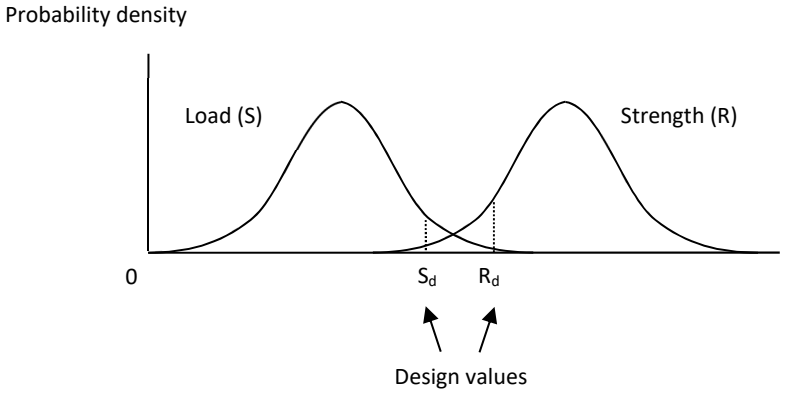

Fully probabilistic assessment: evaluate whether $P(R<S) \leq P_T$
Semi-probabilistic assessment: evaluate whether $S_d \leq R_d$

Figure 2. The probability density functions of load (S) and strength (R), and the design values of load and strength (S_d) and (R_d).

A close link between probabilistic and semi-probabilistic assessments can be achieved by equating the design values of the different stochastic variables to their design point values (see Figure 3 for a graphical representation):

$$X_d = F_X^{-1}(\Phi(-\alpha_X \cdot \beta_T)) \quad (3)$$

Where:

$F_X^{-1}(\cdot)$	Inverse of the cumulative distribution function of stochastic variable X
X_d	Design value of stochastic variable X
β_T	Target reliability index, which equals $\Phi(1-P_T)$
α_X	Influence coefficient for stochastic variable X

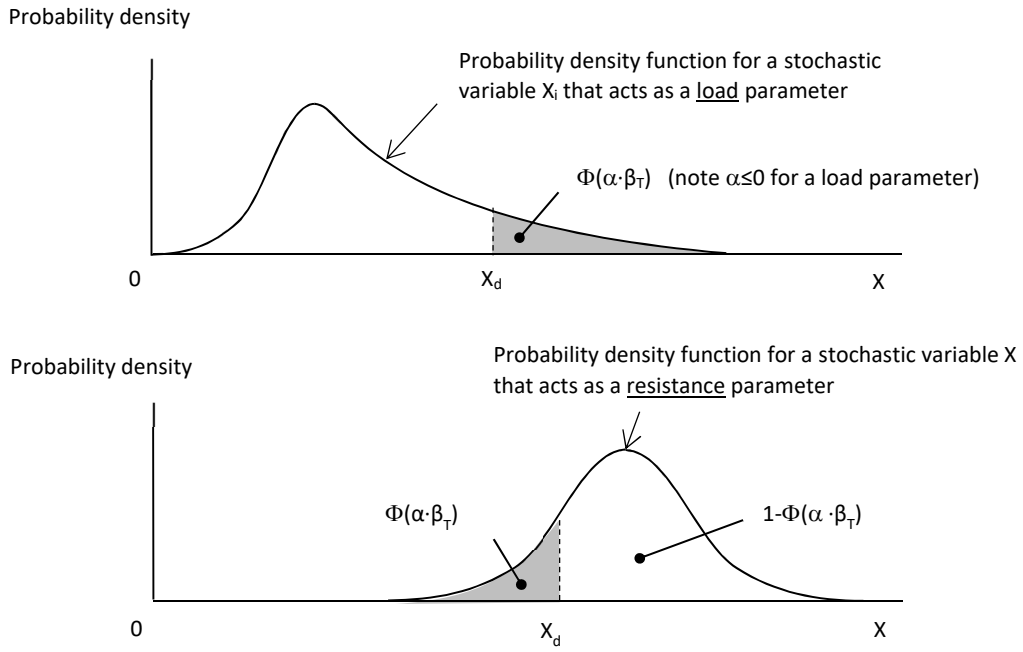

Figure 3. The design point values of stochastic load and resistance variables and their probabilities of exceedance.

For a normally distributed stochastic variable, equation (3) yields:

$$X_d = \mu_X - \alpha_X \cdot \beta_T \cdot \sigma_X \quad (4)$$

Where:

μ_X Mean value of the normally distributed variable X

σ_X Standard deviation of the normally distributed variable X

The above shows that a code calibration essentially revolves around:

1. the specification of appropriate target reliabilities and
2. the specification of appropriate influence coefficients.

NB1

In principle, there is no objection to extending the fully probabilistic PSHA to a fully probabilistic system-level reliability analysis. The reason for not doing so and opting for a semi-probabilistic approach is purely pragmatic.

NB2

The Dutch flood protection standards (2017 onwards) say nothing about the loads that primary flood defenses should be able to withstand. Without code calibration, appropriate design loads would remain unspecified. The same goes for resistance.

NB3

The terms “load” and “demand” are used as synonyms throughout this document. The same goes for “resistance” and “capacity”. While the terms “load” and “resistance” are commonly used in hydraulic engineering, the terms “demand” and “capacity” appear to be more common in earthquake engineering.

NB4

The fact that PSHAs are fully probabilistic and the fact that e.g. Boulanger & Idriss (2014) and Green et al. (2016) have characterized the uncertainties related to liquefaction triggering relationships by probability distributions shows that probabilistic concepts and techniques are already quite common in earthquake engineering. This has made it easier to relate earthquake models (for demand and capacity) to probabilistic standards.

3 Proposed code calibration procedure and action items

An overview of the steps taken to arrive at a calibrated semi-probabilistic assessment rule is given below.

Action item		Description	Objective
1	Characterize the uncertainties related to the input and output of the Fugro model (i.e. coupled, effective stress FEM)	1. Specify which variables should be treated as deterministic or stochastic 2. Specify distributions for the different stochastic variables 3. Describe the decay of spatial correlation for the different stochastic variables, or -as a first step- describe qualitatively what an (uncertain) realization of each individual stochastic variable could look like 4. Specify the meaning of the design values that are typically used in reliability analyses (e.g. the $CRR_{7,5,1atm}$-curve in B&I2014 rests on the 16% quantile value of an error term) On the basis of the results of the abovementioned steps, it will be possible to give an indication of the level of conservatism in the calculations presented by Fugro at the expert meeting and, hence, the direction of the outcomes of the code calibration exercise. This will be for useful decision making and/or for managing expectations.	Define the input of subsequent analyses Give an early impression of the level of conservatism in previous analyses
2	Derive (preliminary) estimates of design values from a probabilistic analysis using the simplified liquefaction procedure and the uncertainties specified by e.g. Green et al. (2016)	1. Specify the limit state function 2. Specify the uncertainties 3. Carry out a series of FORM analysis to “get a feel” for likely design point values. These can be used as input (starting point) for a FORM-analysis using the Fugro model (action item 3) and for informing the final choice of design values (action item 4). NB: Liquefaction triggering is a necessary but insufficient condition for failure of the Eemshaven-Delfzijl primary flood defense. This means that the limit state function considered here cannot be used as a basis for limit state design or safety assessments. This action item merely serves to put the results of more advanced analyses (action item 3) into perspective.	Get a feel for influence coefficients
3	FORM analysis using the Fugro model	1. Select start values for the first FORM iteration (design point estimate) 2. Compute partial derivatives 3. Normalize stochastic variables 4. Calculate estimate of the design point 5. Iterate (successive substitution)	Get a feel for influence coefficients
4	Revisit previous assumptions concerning the length effect	The cross sectional reliability requirement depends on (1) the flood protection standard, (2) the allowable contribution of slope instability to the probability of flooding, (3) a probability of flooding given severe earthquake damage and (4) a length effect factor. The length effect factor will be re-evaluated on the basis of (1) the results of the screening exercise and (2) a probabilistic analysis using the outcrossing method. The outcomes of the latter analysis depends on (1) the influence coefficients of the different stochastic variables and (2) their autocorrelation functions. This means there is a link with action items 1 to 3.	Define cross-sectional target reliabilities

5	Make an informed decision about design values	On the basis of the results of the abovementioned actions: decide on appropriate design values.	Establish design values on the basis of influence coefficients and target reliabilities (decision informed by results from action items above)

4 Action item 1: characterize uncertainties

The following stochastic variables were considered in the FORM-analyses with the FE-model:

1. The seismic demand at the base of the 2D numerical models (SA_{model_base}). The distribution of this stochastic variable rests on a convolution of the uncertainty related to the acceleration at the North Sea Upper Base and the uncertainty in the site response up to the base of the model.
2. The cyclic resistance ratio (CRR) of sand deposits
3. The cyclic resistance ratio of laminated deposits
4. The uncertainty related to residual strength ($\varepsilon_{Su/p'}$)
5. Model uncertainty (ε_M)

Two other important sources of uncertainty are:

1. The uncertainty related to stratification in the top 30 meters.
2. The uncertainty related to the characteristics of spectrally matched motions.

Each probabilistic analyses has been carried out for a given stratigraphy and a given motion. The uncertainty related to stratification can be dealt with by carrying out sensitivity analyses and (if needed) by combining the results of the assessments for the different stratifications with their probabilities (see ENW 2012). The same applies to the uncertainty related to motions, see section 4.7.

The five stochastic variables mentioned above are believed to be the most important ones in a probabilistic analysis for a given stratigraphy (top 30m) and a given motion. The fact that all other variables have been treated as deterministic is conservative within the present context. This is because this leads to a (slight) overestimation of the relative importance of the uncertainty related to the abovementioned stochastic variables, leading to more conservative design values for these variables.

4.1 Spectral acceleration (T=0.85s) at Top of Bedrock NSUB (SA_{NSUB})

The spectral period of 0.85 s has been selected as being representative of seismic demand in the FORM analyses with the FE model FE since:

a. it is near the fundamental period of the 1D soil column that extends from top of bedrock (at about -350 m depth) to the ground surface; and
b. it is near the fundamental period of the 2D numerical models.

The hazard curve of the spectral acceleration at the top of bedrock (NSUB) for a spectral period T=0.85s provided by KNMI has been approximated with a lognormal distribution (Figure 4 and Figure 5). Since the hazard curves at Eemshaven and Delfzijl locations are different, different lognormal distributions are used to approximate the hazard curves at top of bedrock for these locations.

Care was taken so that the fitted lognormal distribution is closest to the target curve around the design point. FORM analyses results indicate that the exceedance probability of the design point value of SA(0.85) is smaller than 1/1000 per year (i.e.: >1000 year return period). The difference of between the lognormal fit and the target curve at exceedance probabilities greater than 1/1000 per year (i.e. <1000 year return periods) does not influence results of the FORM-analysis.

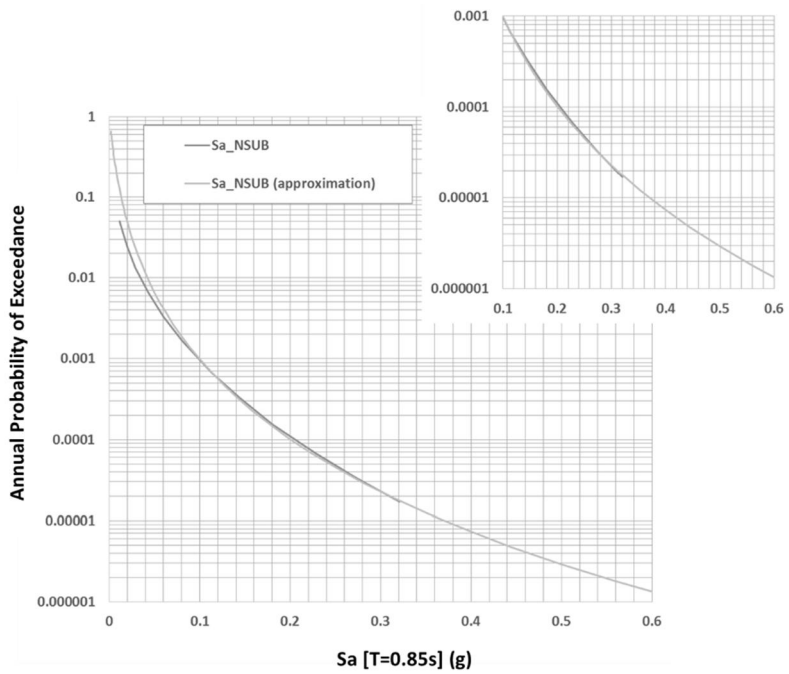

Figure 4. Spectral acceleration (T=0.85s) hazard curve at the top of bedrock at Eemshaven and approximation with a lognormal distribution [hazard curve provided by KNMI]. Lognormal distribution with $\mu_{ln(SA)}$ = -5.77 and $\sigma_{ln(SA)}$ = 1.12.

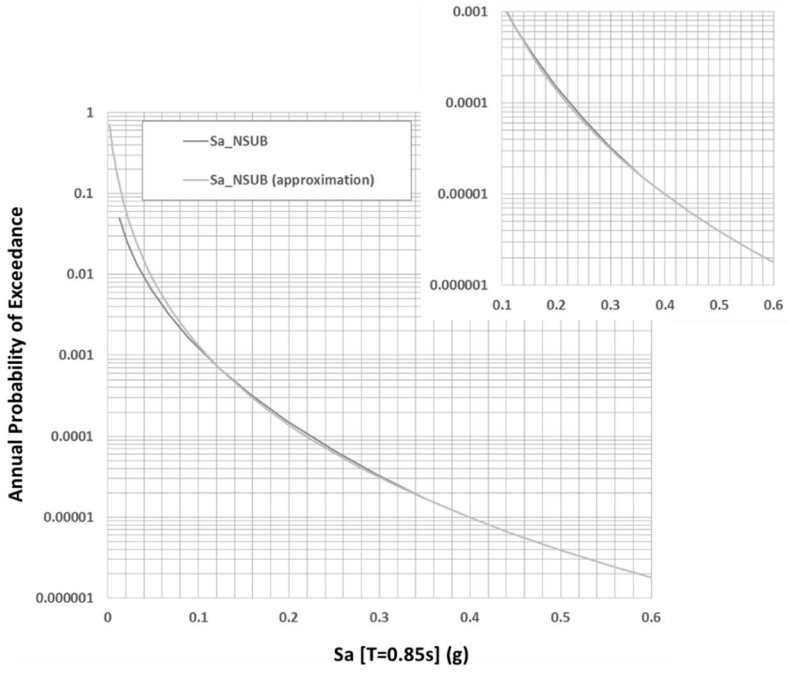

Figure 5. Spectral acceleration (T=0.85s) hazard curve at the top of bedrock at Delfzijl and approximation with a lognormal distribution [hazard curve provided by KNMI]. Lognormal distribution with $\mu_{ln(SA)}$ = -5.61 and $\sigma_{ln(SA)}$ = 1.10.

The mean and standard deviations of the lognormal distributions used to approximate the hazard curves at the top of bedrock are summarized in Table 1.

4.2 Spectral acceleration (T=0.85s) at Base of 2D Numerical Models (SA_{model_base})

The hazard curve of the spectral acceleration at base of the numerical model for a spectral period T=0.85s (i.e. NAP -30 m for Eemshaven and NAP-20m for Delfzijl, see Appendix C) is estimated following the procedure by Bazzurro and Cornell (2004) and Stewart et al. (2014) by a convolution of the hazard curve at top of bedrock (SA_{NSUB}) with the probability distribution of the site amplification factor described in Appendix C (Figure 6). Monte Carlo simulations were also performed for the convolution of the bedrock hazard curve and the site amplification probability distribution and similar results were obtained. The hazard curves of the spectral acceleration at the base of the numerical models (SA_{model_base}) for a spectral period T=0.85s was approximated with a lognormal distribution (Figure 7 and Figure 8). The mean and standard deviations of the lognormal distributions used to approximate the hazard curves at the base of the numerical models are summarized in Table 1.

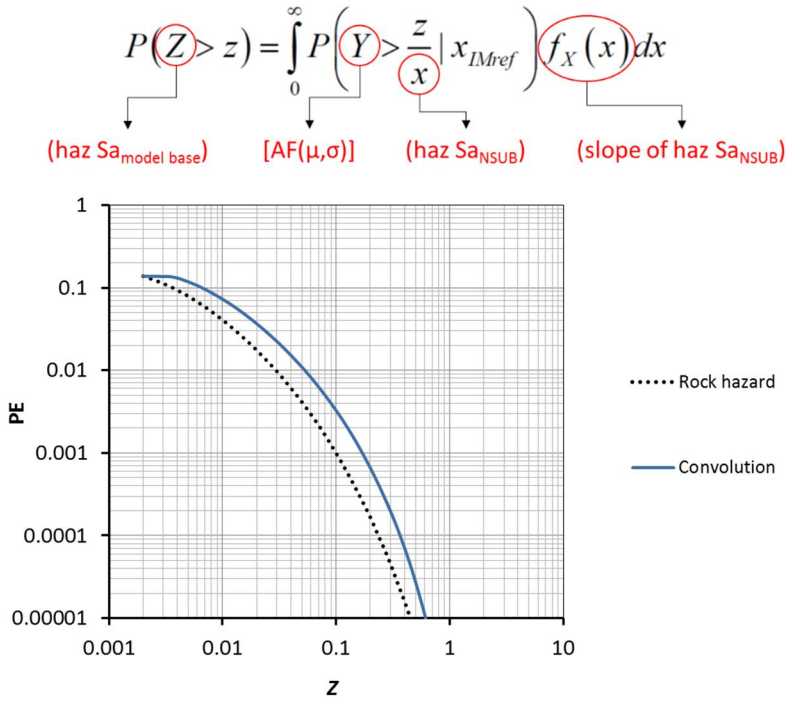

Figure 6. Example convolution results of rock hazard curve and probability distribution of site amplification factors (Stewart et al. 2014).

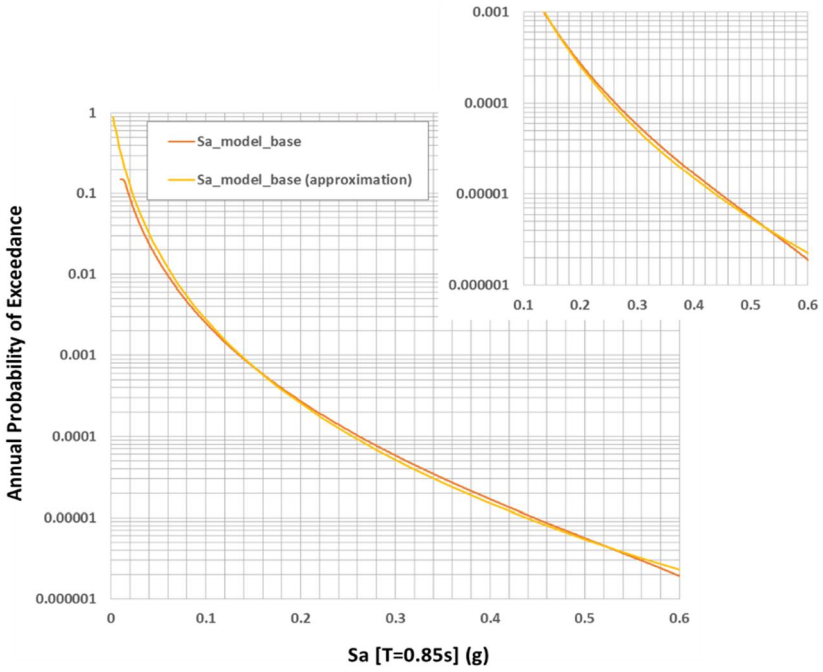

Figure 7. Convolved spectral acceleration (T=0.85s) hazard curve at the base of 2D model at Eemshaven and approximation with a lognormal distribution. Lognormal distribution with $\mu_{ln(SA)}$ = -5.05 and $\sigma_{ln(SA)}$ = 0.99.

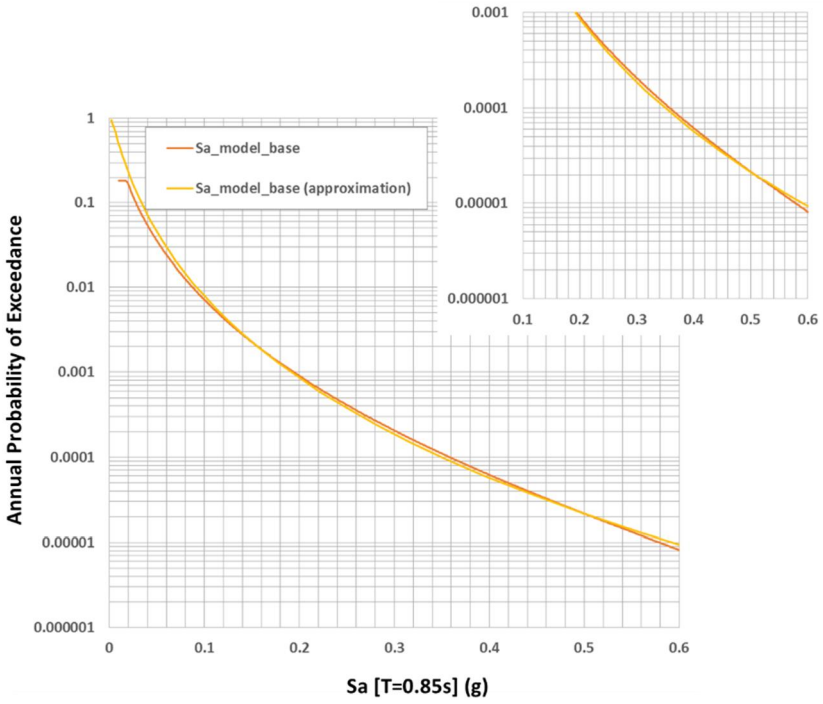

Figure 8. Convolved spectral acceleration (T=0.85s) hazard curve at the base of 2D model at Delfzijl and approximation with a lognormal distribution. Lognormal distribution with $\mu_{ln(SA)}$ = -4.62 and $\sigma_{ln(SA)}$ = 0.96.

4.3 $CRR_{M=7.5}$ in sand deposits

The probability distribution of the cyclic resistance at a reference magnitude M=7.5 (or 15 cycles) of sand layers with no clay laminations present at the Eemshaven area was estimated from the equation below proposed by Boulanger and Idriss (2014) using:

- the probability distribution of local q_{c1Ncs} values from CPT data that classified as Soil Behavior Type 6 per Robertson (1990) classification (Fugro 2016c). These q_{c1Ncs} values include thin layer correction and fines content correction (Fugro 2016c). In a uniform model, soil properties are assumed to be constant within an entire layer. This may lead to a significant overestimation of probabilities of failure when composite behavior is more accurately described by the spatial averages of individual data points (e.g. Vanmarcke 2011). A sensitivity study into such volume effects indicates that the use spatially distributed resistance values gives a result that is similar to the use of median resistance values in a uniform model, see Appendix G for further details. This is why the median of local q_{c1Ncs} values was selected for use with the Boulanger and Idriss (2014) relationship between q_{c1Ncs} and CRR.
- the model uncertainty term $\varepsilon_{\ln(R)}$ proposed by Boulanger and Idriss (2014) has a normal distribution with a mean value of 0 and a standard deviation of 0.2:

$$CRR_{M=7.5,\sigma'_v=1atm} = \exp\left(\frac{q_{c1Ncs}}{113} + \left(\frac{q_{c1Ncs}}{1000}\right)^2 - \left(\frac{q_{c1Ncs}}{140}\right)^3 + \left(\frac{q_{c1Ncs}}{137}\right)^4 - 2.60 + \varepsilon_{\ln(R)}\right)$$

On the basis of the above, a probability distribution of the $CRR_{M=7.5}$ has been derived, using the local median q_{c1Ncs} value and the $CRR_{M=7.5}$ curve of Boulanger and Idriss (2014).

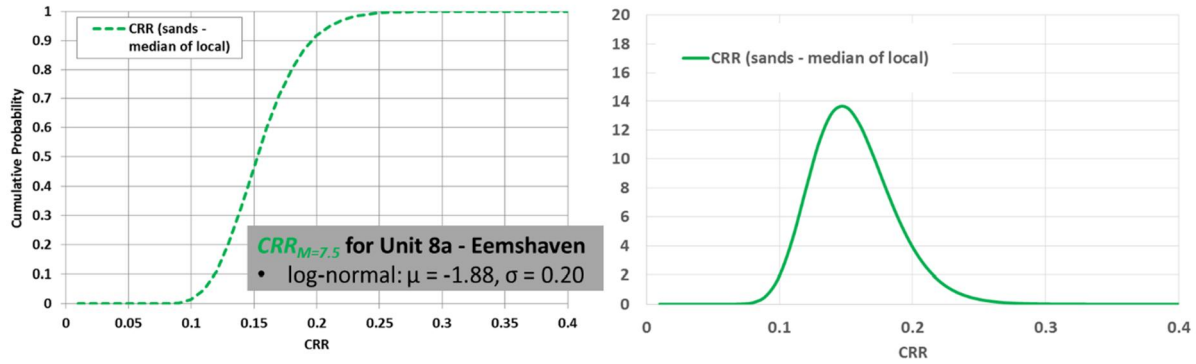

Figure 9. Probability distribution (left) and probability density function (right) of $CRR_{M=7.5}$ for sands at Eemshaven based on the median of local q_{c1Ncs} values.

4.4 $CRR_{M=5.0}$ in laminated deposits

The liquefaction triggering resistance from CPT measurements in laminated deposits appears to underestimate the triggering resistance of these deposits when compared to results from cyclic laboratory tests on laminated "undisturbed" samples (Fugro 2016c). This is most likely due to the significant influence of the clay layers on the CPT tip resistance measured within the thin "sandwiched" sand layers whose thickness is less than 10 to 20 cm.

Interpreted advanced cyclic laboratory tests on "undisturbed" laminated samples and numerical simulation results were used to develop a probability distribution of the cyclic resistance of laminated deposits at the Delfzijl side of the levee for locations were Unit 8 is present for use in FORM analyses as discussed in detail in Appendix D.

Cyclic resistance was defined at a reference magnitude M=5.0 (or 4 cycles) using the Boulanger and Idriss (2014) Magnitude Scaling Factor. It is noted that CRR for layered sands defined at 4 cycles (or for M=5.0) is used only as a reference to identify which triggering curve is used in the numerical analyses, since in the

constitutive models used in the numerical evaluations to simulate sand behavior, the complete liquefaction triggering curve is used rather than one value.

The probability distributions of the $CRR_{M=5}$ for laminated deposits after accounting for volume effects (spatial averaging, see Appendix G) are shown in Figure 10. Note: the means and standard deviations in Figure 10 concern the natural logarithms of the CRRs.

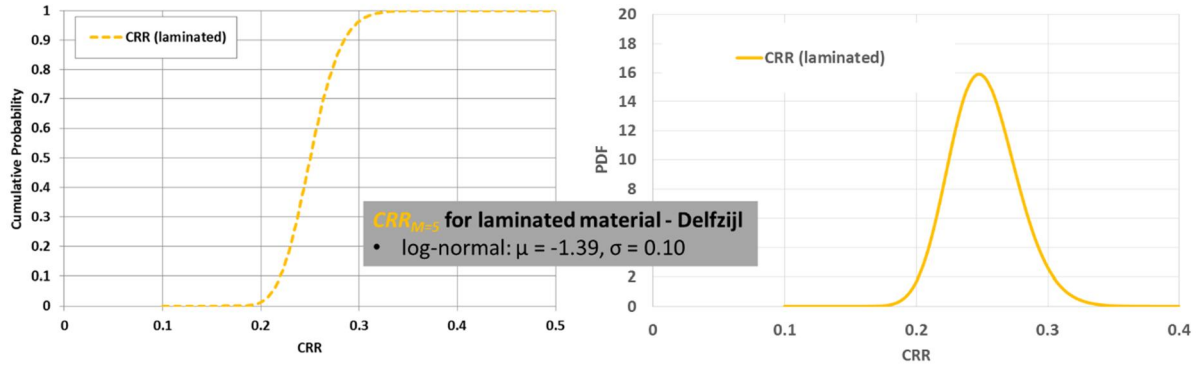

Figure 10. Probability distribution (left) and probability density function (right) of $CRR_{M=5}$ for laminated deposits at Delfzijl before and after accounting for volume effects.

The probability distribution of the CRR for laminated deposits shown above has been specified for a different magnitude than the non-laminated wadzand deposits encountered at Eemshaven. For the non-laminated wadzand deposits encountered at Eemshaven, the Boulanger and Idriss (2014) empirical correlation of $CRR_{M=7.5}$ (defined as CRR at 15 cycles) with q_{c1Ncs} was used for the estimation of liquefaction triggering resistance. For the laminated sand and clay layers within the wadzand deposits interpreted lab results were used to estimate liquefaction triggering resistance at 4 cycles ($CRR_{M=5.0}$), which is the estimated equivalent number of cycles for an M=5 earthquake (the primary contributor to the ground motion hazard for the return periods of interest) using the Boulanger and Idriss (2014) Magnitude Scaling Factor.

4.5 Uncertainty related to residual strength ($\varepsilon_{Su/p'}$)

Post-earthquake stability analyses were performed by assigning residual strength (i.e. defined as the ratio of residual undrained shear strength and in situ initial vertical effective stress, S_r/σ_{vc}') for areas where the maximum excess pore pressure during shaking exceeded a specified threshold indicative of liquefaction. The following distributions were considered:

- mean residual strength and standard deviation as proposed by Kramer and Wang (2015), which is about 0.37 for the range of conditions applicable (green lines in Figure 11 below). This is considered to be the preferred basis for probabilistic analyses since it includes an empirically based uncertainty term, without bias. The proposed relationship for mean residual strength by Kramer and Wang (2015) is a function of normalized SPT blowcounts (N_{160}). We have used Idriss and Boulanger (2008) correlation to convert N_{160} to q_{c1Ncs}. In order to account for the uncertainty in the conversion factor we have also considered a higher value for the standard deviation of 0.45 (red lines in Figure 11 below). We note that FORM analyses were performed considering both standard deviation values and results were found to be largely similar.
- residual strength proposed by Idriss and Boulanger (2008) assuming void redistribution effects are significant. A clear definition of the uncertainty in residual strength estimates is not available. An estimate of the uncertainty on residual shear strength was developed assuming that the proposed curve represents median values (despite a likely safe bias) and using engineering judgment to develop an estimate of the standard deviation on the assumed median residual strength curve. More details are provided in Appendix E. This residual strength distribution has been used to evaluate the sensitivity of the calculated FORM influence coefficients to different assumptions concerning residual strength.

A comparison of the two residual strength distributions considered is shown in Figure 11.

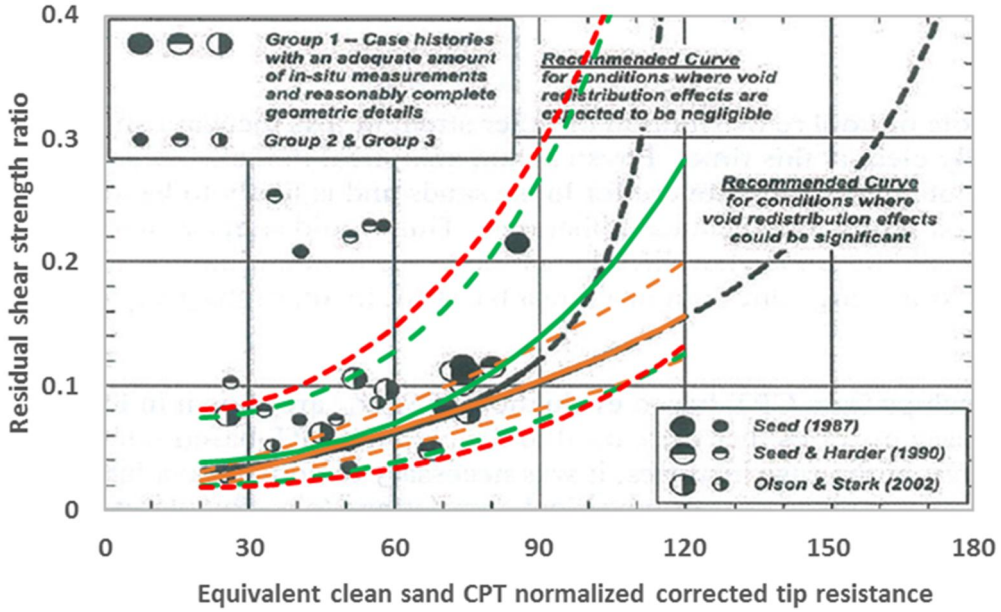

Figure 11. Uncertainty related to residual strength (95%-confidence interval) based on Kramer and Wang (2015) using the standard deviation proposed by the authors (green dashed curves) and an increased standard deviation of 0.45 (red dashed curves) to account for uncertainty in the conversion from $(N1)_{60}$ to q_{c1Ncs} , and Idriss and Boulanger (2008) assuming void redistribution and engineering judgment for the estimation of standard deviation (orange curves).

4.6 Model Uncertainty (ε_M)

This term accounts for the potential difference between numerical model prediction and observed levee response. The expert panel (2016) has recommended a comparison of constitutive models and their implementations for informing choices concerning model uncertainty. Various sensitivity studies have shown that the differences between the computed crest settlements with two different constitutive models (UBCsand and PM4sand) are relatively small (Fugro 2016a). A comparison of computed settlements with different computer codes (i.e. different implementations of these constitutive models) could not be carried out because of time constraints. In view of this the model uncertainty has conservatively been assumed to be considerable, even though the differences between different computer codes are expected to be significantly smaller than those between different constitutive models. A detailed discussion on the characterization of model uncertainty is included in Appendix F.

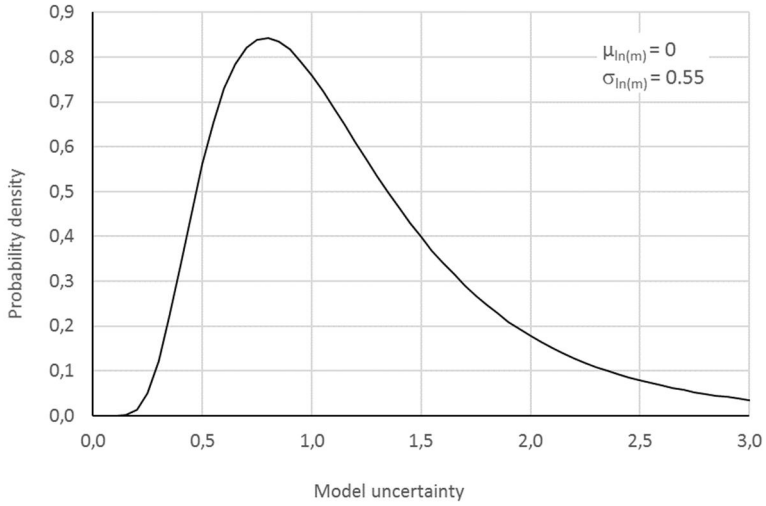

Figure 12. Model uncertainty.

4.7 Uncertainties related to motion characteristics

Ground motion characteristics mainly relate to amplitude, frequency content, and duration, but also to other characteristics of the ground motion that have to do with the details of the ground motion time history such as phasing, presence of velocity pulses that may create larger slope displacements, etc. The FE analyses have been conducted using motions that have been matched to a target spectral shape. Sensitivity analyses have been conducted to assess the variations in response for 7 different, two component motions (Fugro 2016a).

The effect of the uncertainties related to the characteristics of ground motion can be handled via scenarios. In that case, failure probabilities are first calculated for a set of motions and then combined, see Appendix H. For deriving design values for an assessment for an individual ground motion, FORM-analyses have been conducted using a single motion with a duration $D_{5\text{-}75}$ that is greater than the expected durations for 3000-6000 year return period ground motions in Groningen. Sensitivity analyses were also conducted with a shorter duration motion because the spectral acceleration at the design point has a significantly longer return period. In Groningen, duration and spectral acceleration are inversely correlated (Bommer et al. 2015). Longer return periods are associated with higher spectral accelerations and smaller duration motions.

4.8 Overview of stochastic variables

An overview of the stochastic variables, their distributions, autocorrelations and representative values is given in Table 1.

Table 1. Overview of stochastic variables.

Variable	Unit	Distribution type	Distribution parameters*	Mean (m) and standard deviation (sd)*	Motivation	Spatial correlation (also see section 7.4)
Spectral acceleration (T=0.85s) at NSUB (SA_{NSUB})**	g	Lognormal	Eemshaven μ = -5.77 σ = 1.12 Delfzijl μ = -5.61 σ = 1.10	Eemshaven m = 0.0058 g sd = 0.0092 g Delfzijl m = 0.0067 g sd = 0.0103 g	From KNMI hazard curves for Groningen	Strongly correlated over distances of several km
Spectral acceleration (T=0.85s) at base of model (SA_{model_base})	g	Lognormal	Eemshaven μ = -5.05 σ = 0.99 Delfzijl μ = -4.62 σ = 0.96	Eemshaven m = 0.0105 g sd = 0.0135 g Delfzijl m = 0.0156 g sd = 0.0135 g	Convolution of amplification factor distribution at base of 2D FE model and hazard curve at NSUB following Stewart et al (2014) procedure. The estimation of the amplification factor at base of FE models is described in Appendix C.	Strongly correlated over distances of several km
$CRR_{M=7.5}$ in sand deposits	-	Lognormal	μ = -1.88 σ = 0.20 (distribution of point values in the regional data set: μ = -1.80 σ = 0.30)	m = 0.16 sd = 0.03 (distribution of point values in the regional data set: m = 0.17 sd = 0.05)	Volume effects have been accounted for to obtain a distribution from a local data set of q_{c1Ncs}-values that can be used in a uniform model. For further details, , see Appendix G. The distribution of point values rests on a convolution of the model uncertainty term in the CRR-relationship by Boulanger & Idriss (2014), with μ = 0 and σ = 0.2, and the distribution of q_{c1Ncs} values in sand from a regional data set. This distribution has only been used for sensitivity analyses.	Strongly correlated over distances of several km for a given geological unit. Motivation: The $CRR_{M=7.5}$-values are derived from an empirical relationship that rests on back-calculations of historic events. Length effects are reflected in the individual historic observations. The above means that the uncertainty related to $CRR_{M=7.5}$ could be thought of as a model uncertainty which is typically assumed to be strongly spatially correlated.
$CRR_{M=5.0}$ in laminated deposits (from lab data)	-	Lognormal	μ = -1.39 σ = 0.10 (without spatial averaging: μ = -1.40 σ = 0.20)	m = 0.25 sd = 0.03 (without spatial averaging: m = 0.25 sd = 0.05)	Based on regressions of lab test results and numerical simulations (see Appendix D). Volume effects have been accounted for. For a discussion on volume effects, see Appendix G.	ρ_0 = 0 - 0.5 k = 100-150m (+ sensitivity analyses) A correlation distance (k) that is in line with the value used for material properties in slope stability analyses in the Netherlands seems justified. The variance is largely related to the variations in clay content (void ratio). For a given void ratio, the resistances are spatially correlated. A review of CPT-

Variable	Unit	Distribution type	Distribution parameters*	Mean (m) and standard deviation (sd)*	Motivation	Spatial correlation (also see section 7.4)
						data indicate that similar clay contents extend over distances of tens to hundreds of meters. A lower limit of the autocorrelation function (ρ_0) greater than zero seems reasonable because there is also an element of (spatially correlated) knowledge uncertainty related to the $CRR_{M=5.0}$ in layered deposits.
$\varepsilon_{Su/p'}$ (uncertainty related to Su/p' given median value of q_{c1Ncs})	-	Lognormal	$\mu = 0$ $\sigma = 0.45$ $\mu = 0$ $\sigma = 0.15$	m = 1.11 sd =0.52 m = 1.01 sd = 0.15	Su/p' from Kramer and Wang (2015). $Su/p' = f(q_{c1Ncs,50\%}) \cdot \varepsilon_{Su/p'}$ With $f(q_{c1Ncs,50\%})$ from Idriss & Boulanger (2008) with void ratio distribution. For further details, see Appendix E.	Strongly correlated over distances of several km (essentially model uncertainty)
Geometric parameters (crest height, width etc.)	m	Deterministic	-	-	Dimensions are well known	-
Model Uncertainty	-	Lognormal	$\mu = 0$ $\sigma = 0.55$	m = 1.16 sd = 0.69	Distribution based on engineering judgement, see Appendix F. The distribution corresponds to a probability of an error of at least a factor 2 of 10%.	Strongly correlated over distances of several km

* The values of μ and σ in this table are the means and standard deviations of the natural logarithms of the lognormally distributed variables. They are not the means and standard deviations of the lognormally distributed variables themselves, which have been indicated by m and sd respectively.

** This distribution will not play a role in the FORM-analyses. It is only mentioned here to be able to calculate the difference between the design value of the Spectral acceleration (T=0.85s) with and without a design value for the uncertainty in the response analysis.

5 Action item 2: FORM analyses using the simplified liquefaction procedure

The objective of this action item is to "get a feel" for the relative importance of the various uncertainties from probabilistic analyses with the simplified liquefaction procedure. The usefulness of this action item rests on the premise that the relative importance of stochastic variables that determine liquefaction triggering is broadly similar within a simplified liquefaction triggering analysis (the basis of the screening method) and more advanced FEM deformation analyses. The results presented below have been used for selecting the start values for the FORM-analyses with the FEM model, to reduce the required number of iterations. They have also been used for quality assurance, to make it easier to spot errors.

5.1 Limit state function

The simplified liquefaction procedure involves an evaluation of a "factor of safety" (FS_{liq}) against liquefaction (see Idriss & Boulanger 2008; Boulanger & Idriss 2014; Green et al. 2016). Note that FS_{liq} is a stochastic variable and not a partial factor.

$$FS_{liq} = CRR_{7,5,1atm} / CSR_{7,5,1atm} \quad (5)$$

$$CSR_{7,5,1atm} = 0{,}65 \cdot \sigma_v/\sigma'_v \cdot PGA/g \cdot r_d \cdot 1/MSF \cdot 1/ K_\sigma \quad (6)$$

$$CSR_{7,5,1atm} = c \cdot PGA \quad (7)$$

$$CRR_{7,5,1atm} = \exp[q_{c1Ncs}/113 + (q_{c1Ncs}/1000)^2 - (q_{c1Ncs}/140)^3 + (q_{c1Ncs}/137)^4 - C_o + \varepsilon_{ln(CRR)}] \quad (8)$$

Since $FS_{liq}<1$ implies liquefaction, the limit state function for liquefaction triggering can be written as follows:

$$Z = 1 - CRR_{7,5,1atm} / CSR_{7,5,1atm} \quad (9)$$

or (similar to Boulanger & Idriss 2014):

$$Z=\ln(CRR_{7,5,1atm}) - \ln(CSR_{7,5,1atm}) \quad (10)$$

or:

$$Z=\ln(CRR_{7,5,1atm}) - \ln(c \cdot PGA) \quad (11)$$

Where:

$CRR_{7,5,1atm}$	Cyclic resistance ratio (-)
$CSR_{7,5,1atm}$	Cyclic stress ratio (-)
PGA	Peak ground acceleration at the surface of the soil profile (m/s^2)
g	Gravitational acceleration (m/s^2)
σ_v	Total effective stress (kPa)
σ'_v	Effective vertical stress (kPa)
r_d	Depth reduction factor (-)
$\varepsilon_{ln(CRR)}$	Uncertainty term
MSF	Magnitude scaling factor (-)
K_σ	Overburden correction factor (-)
c	Constant (-)
q_{c1Ncs}	Equivalent, normalized cone resistance for clean sand (-)
C_0	Constant (-)

A PSHA has been carried out to estimate the seismic hazard at the top of North Sea Upper Base (NSUB) at a depth of about 350m by KNMI. For the estimation of PGA at the ground surface, amplification factors or functions (AF) have been estimated as a function of the spectral acceleration at NSUB by Bommer et al. (2015).

For every location and period, the parameter values of the following equation can be found in "V2_Site Response Zonations_date.xlsx":

$$\ln(AF) = f_1 + f_2 (PGA_{NSUB} + f_3) / f_3 + u \cdot \sigma_{lnAF} \quad (12)$$

Where:

AF Amplification factor (-)

f_1, f_2, f_3 Constants (-)

PGA_{NSUB} Peak ground acceleration at North Sea Upper Base (g)

u Standard normal variable (-)

σ_{lnAF} Standard deviation of the natural logarithm of the uncertainty related to the amplification function (-)

5.2 Input of probabilistic analyses

An overview of the stochastic variables and their distributions is given in Table 2.

Table 2. Overview of stochastic variables.

Variable	Unit	Distribution type	Distribution parameters	Mean (m) and standard deviation (sd)*	Motivation
PGA	g	Lognormal	μ = -3.95 σ = 0.61	m = 0.0232 g sd = 0.0156 g	The PGA hazard curve was estimated following the procedure by Bazzurro and Cornell (2004) and Stewart et al. (2014) by a convolution of the hazard curve at top of bedrock (PGA_{NSUB}) with the probability distribution of the site amplification factor by Bommer et al (2015) for Eemshaven (i.e. zone number 1035). Monte Carlo simulations were also performed for the convolution of the bedrock hazard curve and the site amplification probability distribution and similar results were obtained. The hazard curve of PGA at the ground surface was approximated with a lognormal distribution.
$CRR_{M=7.5}$ in sand deposits	-	Lognormal	μ = -1.88 σ = 0.20	m = 0.16 sd = 0.03	Based on a convolution of the model uncertainty term in the CRR-relationship by Boulanger & Idriss (2014), with μ = 0 and σ = 0.2, and the median of local q_{c1Ncs}-values in sand, see Appendix G for further details.

5.3 Results of FORM-analyses

The squared influence coefficients per stochastic variable are shown in Figure 13 below. The influence coefficients are identical for different values of the constant c (see equation (7)), and thus the same for different (target) reliabilities. For more information about FORM, see Appendix A.

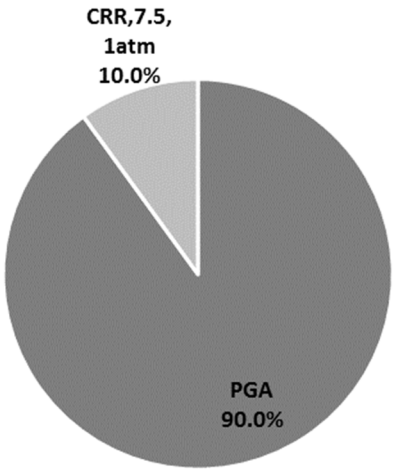

Figure 13. FORM-results for a simplified liquefaction triggering analysis.

For a range of c-values (see equation (7)) that seem reasonable for Eemshaven, the calculated reliability indices range from about 2.2 to 3.2.

5.4 Discussion

The results shown above are in line with:

1. the fact that the return period of the earthquake load is widely regarded as an all-important parameter,
2. the fact that a widely used “deterministic” triggering relationship corresponds to merely a 16%-quantile for model uncertainty (Boulanger & Idriss 2014).

6 Action item 3: FORM analyses using the 2D effective stress model

The objective of this action item is to "get a feel" for the relative importance of the various uncertainties from probabilistic analyses with the Fugro model. For more information about FORM, see Appendix A.

6.1 Limit state function

The limit state function is:

$$Z = c_{crit} - m \cdot C \quad (13)$$

Where

c_{crit} Critical crest settlement (m); c_{crit} = 3 m
C Computed crest settlement (m)
m Model uncertainty factor (-)

Crest settlements are calculated with dynamic effective stress FEM-analyses. For further details on the calculation procedure, the reader is referred to the guideline prepared by Fugro (2016b).

6.2 Input of probabilistic analyses

For an overview of the stochastic variables and their distributions, the reader is referred to Table 1 in chapter 4. The stratigraphies for the Eemshaven and Delfzijl levees that have been considered in FORM-analyses are given in Figure 14 and Figure 15 below. Conservative stratigraphies have deliberately been selected to minimize the gap between reliability indices close to target reliability indices. Additional stratigraphies have been considered in Fugro (2016a) as a part of sensitivity analyses.

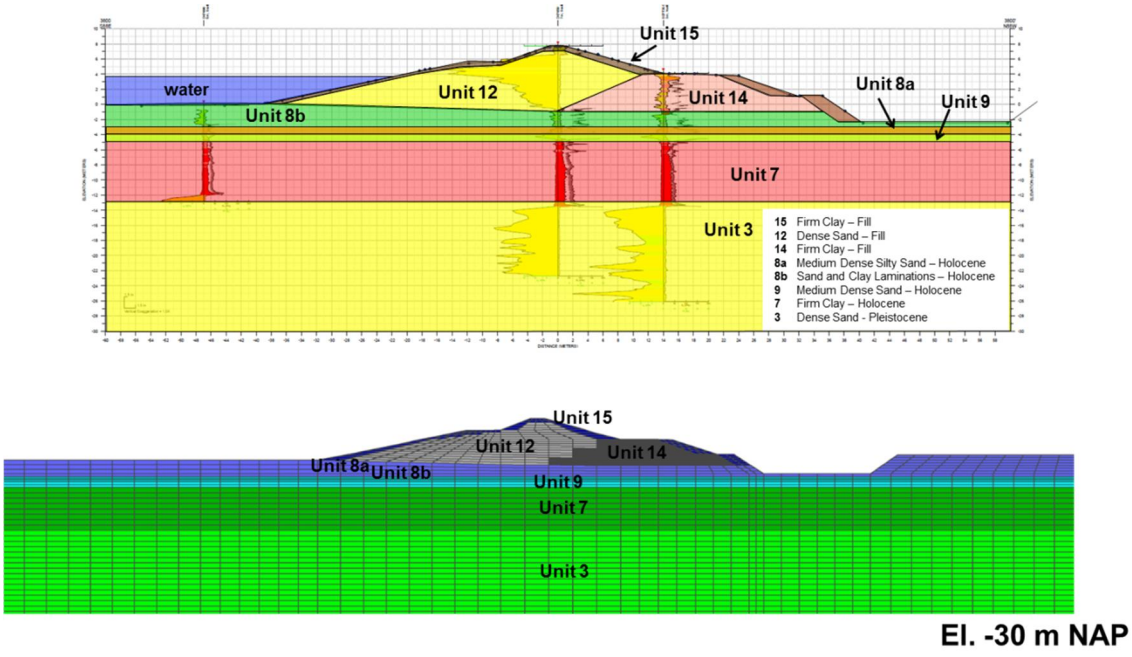

Figure 14. The stratigraphy for the Eemshaven cross-section considered in the FORM-analysis.

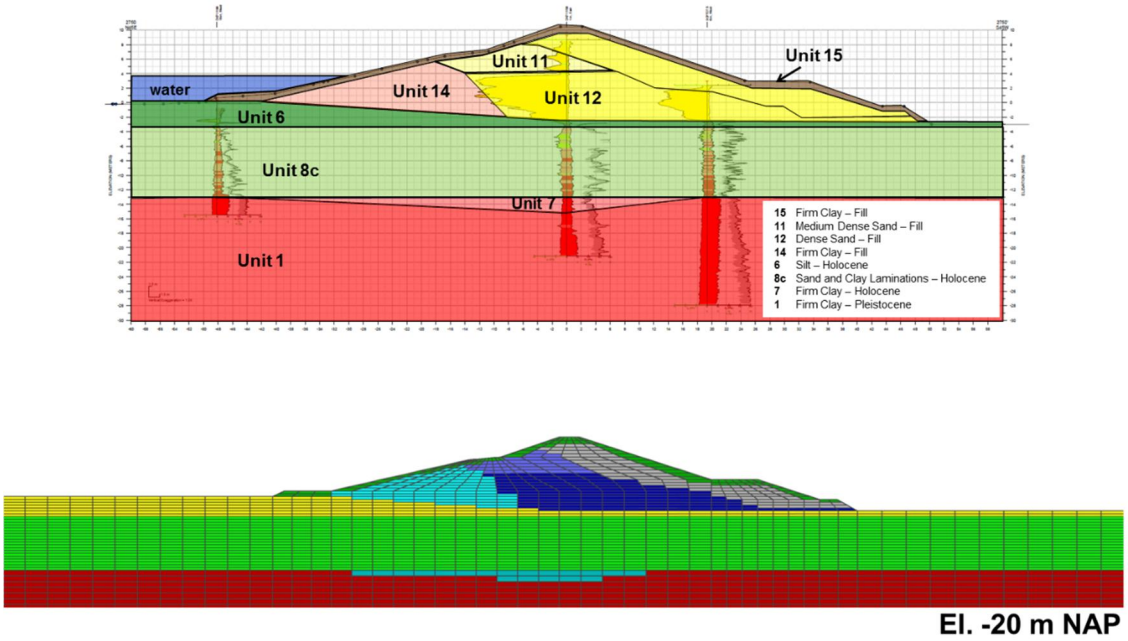

Figure 15. The stratigraphy for the Delfzijl cross-section considered in the FORM-analysis.

6.3 Results of FORM-analyses

The results of the FORM analyses using the 2D FEM results are presented in this section. The following cases were examined:

Base case

A. Eemshaven cross-section; Su/p' according to Kramer & Wang (2015); ground motion 4; using the median of local q_{c1Ncs}-values.
B. Delfzijl cross-section; Su/p' according to Kramer & Wang (2015); ground motion 4; using the median of local q_{c1Ncs}-values.

Sensitivity analyses

1. Eemshaven cross-section; Su/p' according to Kramer & Wang (2015); ground motion 6; using the median of local q_{c1Ncs}-values.
2. Delfzijl cross-section; Su/p' according to Kramer & Wang (2015); ground motion 6; using the median of local q_{c1Ncs}-values.
3. Eemshaven cross-section; Su/p' according to Idriss & Boulanger (2008); ground motion 4; using a regional data set of q_{c1Ncs}-values without spatial averaging.
4. Delfzijl cross-section; Su/p' according to Idriss & Boulanger (2008); ground motion 4; using a regional data set of q_{c1Ncs}-values without spatial averaging.

All FORM-analyses have been performed using a response surface. For both base cases, the design point (crest settlement and partial derivatives) has been verified using targeted FE-analyses (usually a set of 9 FE-analyses). The same applies to sensitivity analyses no. 3 and 4. For sensitivity analyses no. 1 and 2, only the crest settlement in the design point has been verified with a single, targeted FE-analysis.

The squared influence coefficients per stochastic variable are shown in Figure 16 to Figure 18 below for the cases examined. The calculated reliability indices are also shown on the figure for every case.

For a detailed overview of the results of the FORM-analyses, the reader is referred to Appendix I.

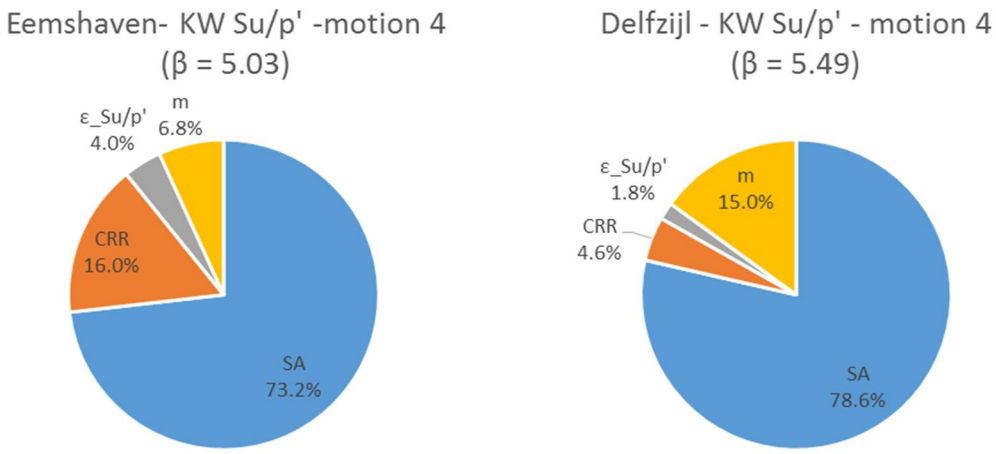

Figure 16. Base case A (left) and B (right): squared influence coefficients and reliability indices from FORM-analyses with the 2D FE model with Su/p' according to Kramer & Wang (2015) and the median of local qc1Ncs-values, for ground motion 4.

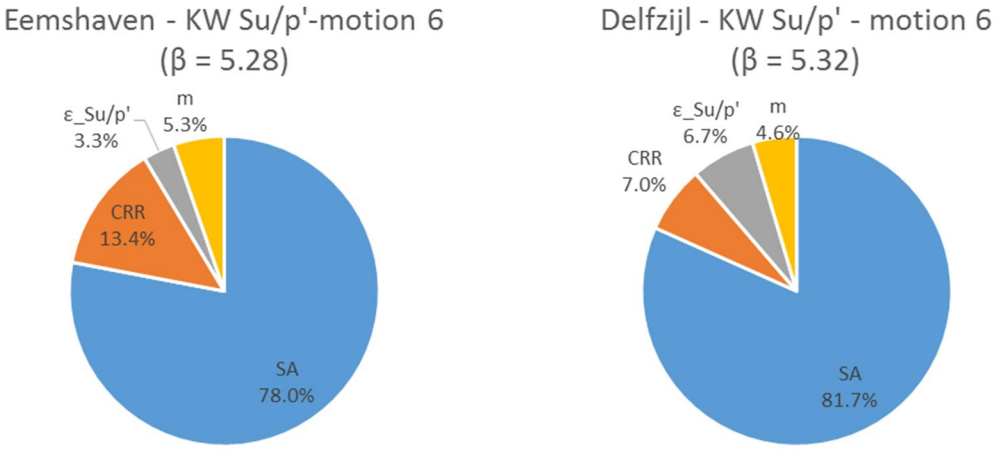

Figure 17. Sensitivity analyses 1 (left) and 2 (right): squared influence coefficients and reliability indices from FORM-analyses with the 2D FE model with Su/p' according to Kramer & Wang (2015) and the median of local qc1Ncs-values, for ground motion 6.

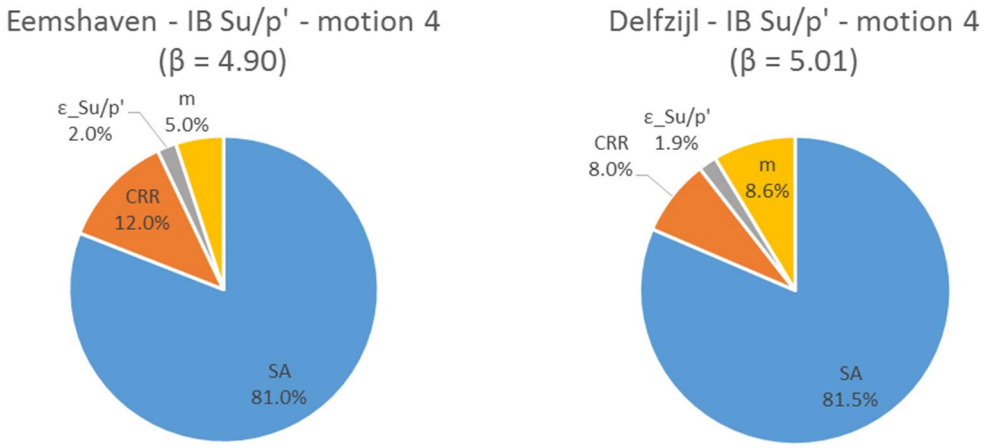

Figure 18. Sensitivity analyses 3 (left) and 4 (right): squared influence coefficients and reliability indices from FORM-analyses with the 2D FE model with Su/p' according to Idriss & Boulanger (2008), using a regional data set of q_{c1Ncs}-values without spatial averaging, for ground motion 4.

6.4 Discussion

The calculated influence coefficients for Eemshaven and Delfzijl appear broadly similar. The uncertainty related to the spectral acceleration is relatively important. This is in line with the results of the FORM-analyses for liquefaction triggering with the simplified liquefaction procedure (see chapter 5). It is also in line with the observation that the return period of the seismic action is widely considered to be an all-important parameter.

The calculated reliability indices are high, even though conservative assumptions have been made concerning stratigraphy: a reliability index of 5 corresponds to a probability of failure of about 1/3.500.000 per year ($2{,}9.10^{-7}$ per year). The calculated reliability indices are significantly greater than the ones calculated for liquefaction triggering in chapter 5. This is consistent with the fact that the FORM-analysis in chapter 5 concerns the probability that $FSl_{iq}<1$ somewhere. This is not the same as actual failure.

Analyses were conducted for two different residual strength distributions. As was to be expected on the basis of the similarities between the relationships presented in Figure 11 for lower values of q_{cN1cs}, the calculated reliability indices and influence coefficients are broadly similar.

A sensitivity analysis with a shorter duration motion shows a higher reliability index. The influence coefficient of ground motion is somewhat reduced.

The calculated influence coefficients are broadly similar across all cases.

7 Action item 4: Revisiting the length effect

7.1 Introduction: cross-sectional and system-level reliability assessments

The Dutch flood protection standards are defined in terms of maximum allowable probabilities of flooding. These standards are system-level reliability requirements: they apply to segments of about 5 to over 40 kilometers in length. The probability of flooding is the probability that a segment fails somewhere, for whatever reason, leading to the flooding of the hinterland (Figure 19).

A **segment** can be decomposed into sections. **Sections** are defined here as continuous lengths in which load and resistance properties are statistically homogeneous. The term "**uniform length**" is used here to refer to a length in which the spatial variability of demand and capacity along the dike can be ignored when evaluating a limit state function.[1] A reliability analysis for a uniform length is commonly referred to as a cross-sectional analysis. Segments may consist of numerous sections, and sections of numerous uniform lengths, see also Figure 20.

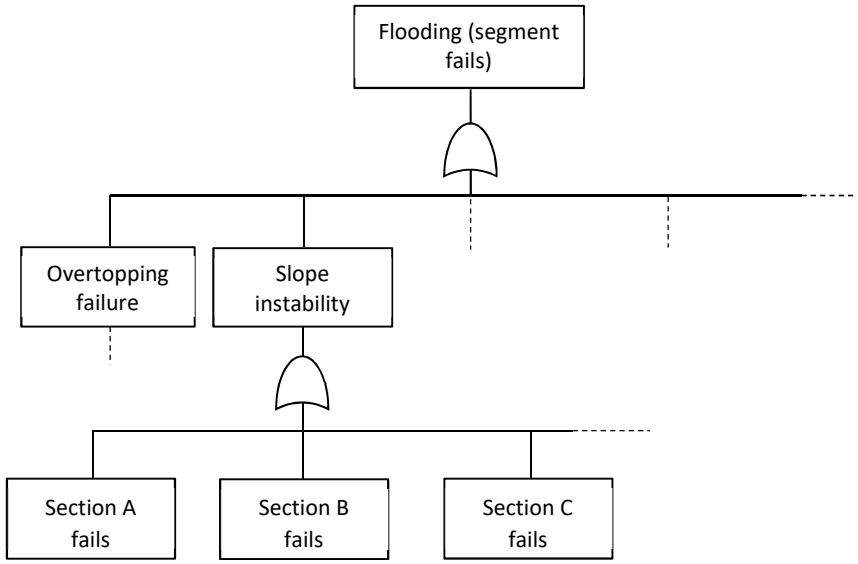

Figure 19. Fault tree for a segment.

Note that different terms and definitions are sometimes used for similar concepts. For instance, the USACE (2013): I-5) says: "A levee reach is defined for the purpose of risk analysis as a continuous length of levee exhibiting homogeneity of construction, geotechnical conditions, hydrologic and hydraulic loading conditions, consequences of failure, and possibly other features relevant to performance and risk". The main differences with a "section", as defined above, concerns the fact that only features related to performance are considered here and that a "section" could also be a dune or a structure. Jongejan & Maaskant (2015) used the term "cross-section" instead of "uniform length". Kwak et al. (forthcoming) use the term "reach" for "section" and "segment" for "uniform length".

[1] Demand and capacity may concern point values or spatial averages, depending on the limit state function.

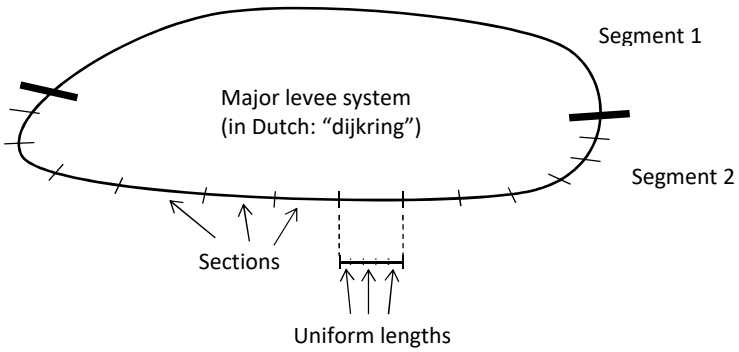

Figure 20. Major levee system, segments, sections and cross-sections.

The failure probability for a uniform length, $P(F_i)$, is the probability that the limit state function is smaller than zero in a 2-dimensional or cross-sectional analysis:

$$P(F_i) = P(Z_i<0) \quad (14)$$

Where
Z_i Limit state function of uniform length i (i=1..n); $Z_i<0$ indicates failure

A segment can be thought of as a series system consisting of numerous uniform lengths (grouped into sections). A segment's failure probability, $P(F_{system})$, follows from[2]:

$$P(F_{system}) = P(Z_1<0 \cup Z_2<0 \cup \ldots \cup Z_n<0) \quad (15)$$

The failure probability of a series system lies between the following bounds:

$$P(F_{system}) = \max(P(Z_i)<0) \quad \text{Lower bound (perfectly correlated limit state functions)} \quad (16)$$

$$P(F_{system}) = 1 - \Pi_{i=1\ldots n}(1 - P(Z_i<0)) \quad \text{Upper bound (independent limit state functions)} \quad (17)$$

For sufficiently small failure probabilities, the upper bound can be approximated by:

$$P(F_{system}) \approx \Sigma(P(Z_i<0)) \quad (18)$$

When the limit state functions of the different uniform lengths are strongly correlated, the system failure probability tends to the lower bound. When the limit state functions are weakly correlated, the system failure probability tends to the upper bound. The difference between expressions (16) and (17) is also strongly influenced by variations in cross-sectional failure probabilities. A single weak spot may strongly influence a series-system reliability, regardless of spatial correlations.

The system failure probability for a particular failure mechanism can be calculated on the basis of:
1. cross-sectional failure probabilities (identical throughout each section),
2. the effect of spatial correlations within each section and
3. the correlations between sections.

This is illustrated by Figure 21. Note that uniform lengths could be treated like sections when calculating a segment's failure probability. A distinction is made here because the homogeneity within sections allows for the use of relatively efficient computational techniques to calculate the failure probability of a section. A section is essentially a series system of uniform lengths, i.e. a system of correlated components. It can also be modelled as a series system of independent equivalent lengths. These independent equivalent lengths depend on the correlations between uniform lengths. With such an independent equivalent length, the failure

[2] For reasons of simplicity, only a single failure mechanism is considered here.

probability for a single uniform length can be scaled directly to the failure probability of an entire section (see e.g. Vrouwenvelder 2006).

Consider a series system (segment) that consists of two components (sections)

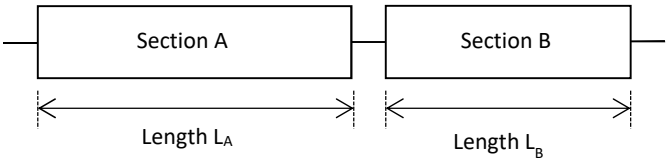

1. Calculate cross-sectional failure probabilities
(example for section A only)

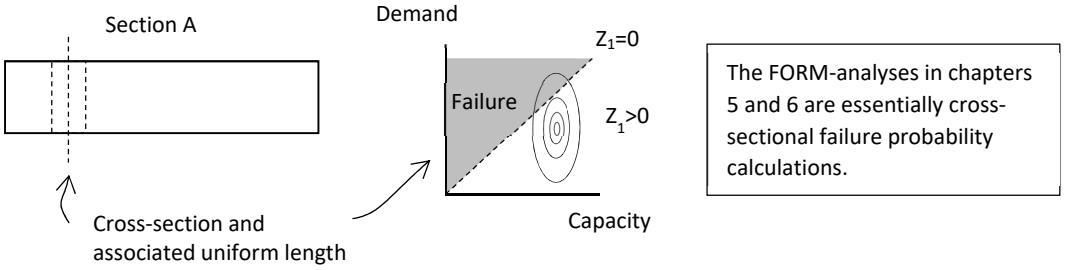

The FORM-analyses in chapters 5 and 6 are essentially cross-sectional failure probability calculations.

2. Calculate each section's failure probability, based on spatial correlations and cross-sectional reliabilities

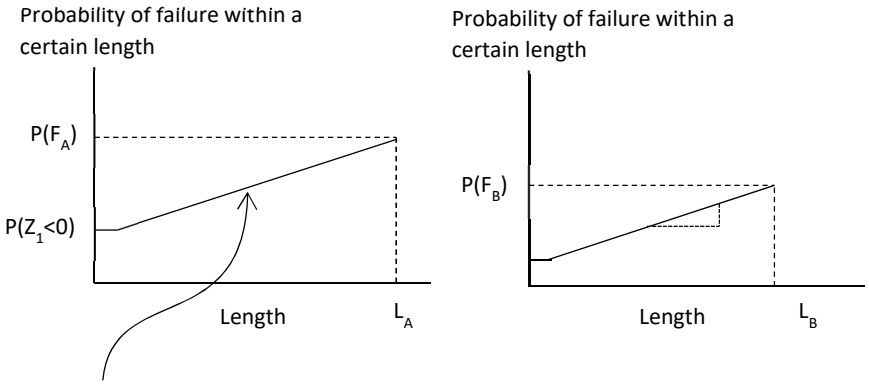

The steepness of this line depends on the (spatial) autocorrelation function of the limit state function Z_1

3. Combine the sections, taking their correlations and varying reliabilities into account

$P(F_{system}) = P(F_A \cup F_B) = P(Z_A<0 \cup Z_B<0)$

No correlation ($\rho_{Z_AZ_B}= 0$)

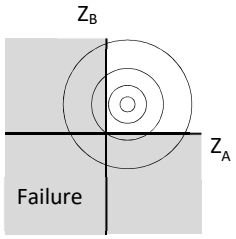

$P(Z_A<0 \cup Z_B<0) \approx P(Z_A<0) + P(Z_B<0)$

Strong correlation ($\rho_{Z_AZ_B} \approx 1$)

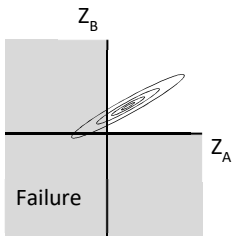

$P(Z_A<0 \cup Z_B<0) \approx \max(P(Z_A<0) , P(Z_B<0))$

Figure 21. Schematic overview of a system reliability analysis.

When engineers evaluate the reliability of e.g. a dike section using a semi-probabilistic or deterministic method, they carry out a 2-dimensional analysis. To be able to evaluate an individual cross-section without having to carry out a full system-level reliability analysis, the system-level reliability requirement has to be transformed into a cross-sectional reliability requirement.

7.2 The length effect and cross-sectional target reliabilities

When the limit state functions of different uniform lengths are not perfectly correlated, the system failure probability increases with the number of uniform lengths (Figure 22). This means that the system failure probability increases with length. This phenomenon is called the length effect.

The above can be understood as follows. When capacity is uncertain *and* spatially variable, it is uncertain (1) which spot is actually the weakest and (2) how weak this weakest spot actually is. This also explains why people that inspect levees during high waters do not stand still: the probability that they observe a sign of weakness increases with every step they take. Note that the spatial variability of demand can also lead to a length effect: the probability of observing a particular seismic demand *somewhere* in Groningen is higher than the probability that it is observed *at any specific location* in Groningen.

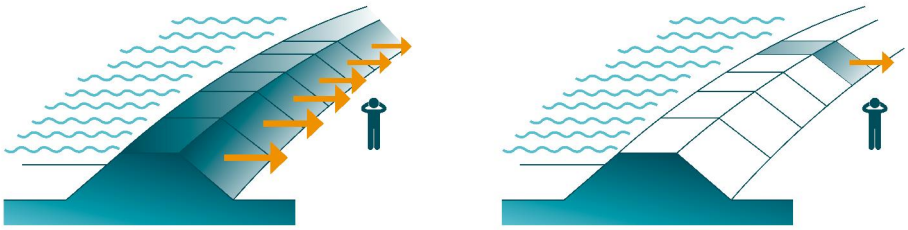

Figure 22. The length effect: the greater the number of uniform lengths that could fail independently, the greater the probability of flooding.

The Dutch flood protection standards are defined in terms of maximum allowable probabilities of flooding per segment ("dijktraject"). Cross-sectional target reliabilities for evaluating the probability of severe earthquake damage can be derived from these standards with the following expression:

$$P_T = P_{max} \cdot f / P_{F|D} / N \quad (19)$$

with:

$$N = a \cdot L / b \quad (20)$$

Where

P_T	Cross-sectional target failure probability for a seismic stability assessment (per year)
P_{max}	Maximum allowable probability of flooding (per year)
f	Maximum allowable contribution of instability to the probability of flooding (-)
$P_{F\|D}$	Probability of flooding given severe earthquake damage, defined as a crest settlement ≥3m (-)
N	Length effect factor for severe earthquake damage (-)
L	Length of segment (m)
a	Fraction of the total length of the segment that dominates the probability of failure of the segment for the failure mechanism under consideration (-)
b	Independent equivalent lengths within the abovementioned part of the segment (m)

The parameters a and b model a segment that consists of different sections with different characteristics in a simplified, equivalent manner, as shown in Figure 23. The failure probability of a segment is usually determined by a relatively short distance over which the probabilities of failure are relatively high, which is expressed by the a-value. Note that failure probabilities are usually plotted on a log-scale because they easily vary of orders

of magnitude; combining failure probabilities of e.g. 1/1000 and 1/100.000 gives a system failure probability close to 1/1000. Within the "critical length" (i.e. "a · L"), the effect of decay of spatial correlation can be modelled by means of "independent equivalent lengths". This is reflected by the b-value.

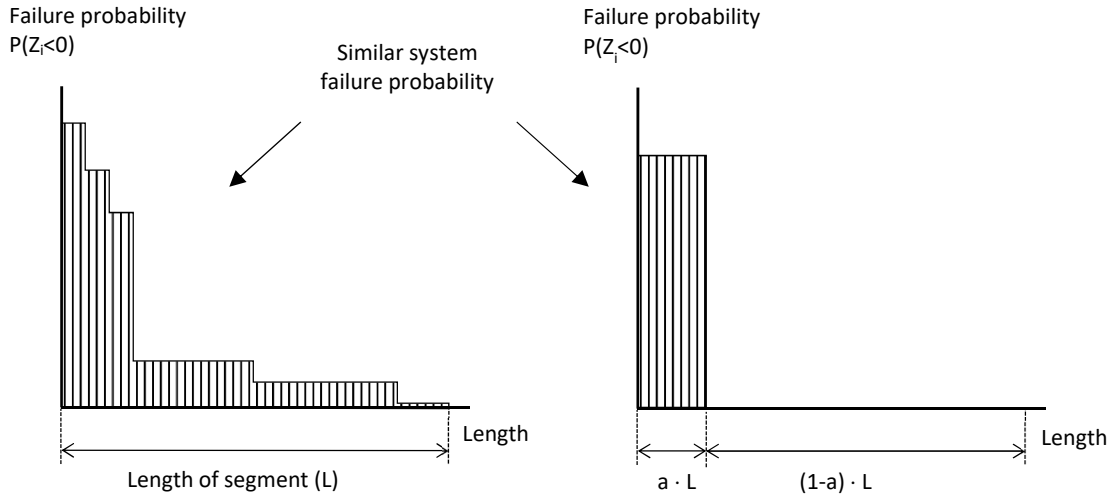

Figure 23. A simplified, equivalent way of describing a segment's reliability (the widths of the bars are independent equivalent lengths, or b-values).

The parameter values that have been assumed so far are shown in Table 3, together with the resulting target reliabilities.

Table 3. From standard of protection to cross-sectional target reliabilities for seismic stability assessments. Original values.

Variable	**Unit**	**Segment**	
		6_6 (includes Eemshaven)	**6_7 (includes Delfzijl)**
P_{max}	**per year**	**1/1,000**	**1/3,000**
f	-	0.24	0.24
$P_{F\|D}$	-	0.1	0.1
$P_{T,segment}$	**per year**	**0.0024**	**0.0008**
L	m	46100	38600
a	-	0.033	0.033
b	m	50	50
N	-	31.4	26.5
P_T	**Per year**	**7.64E-05**	**3.02E-05**
β_T	**-**	**3.79**	**4.01**

The values of parameters a and b in Table 3 were selected at a meeting held in December 2015. Back then, it was proposed to hold on to the values that are more commonly used in slope stability assessments in the Netherlands, i.e. a=0.033 (=1/30) and b=50m.[3] This was expected to be somewhat conservative, but little was known at the time about the seismic stability of the Eemshaven-Delfzijl levees. It was therefore proposed to revisit the length effect when the results of the first seismic stability assessments would come available (Figure 24). This action item could be viewed as a follow-up on the abovementioned proposal. It draws upon the results of the LPI-screening (Deltares 2017) and the FORM-analyses presented in chapter Figure 24 to re-evaluate the length effect.

[3] The value a=0.033 stems from an old study for the Alblasserwaard (one of the Dutch major levee systems) in which 10% of the levee system was found to be sensitive to slope instability. This value of 10% was divided in 3 following discussions over the effects of spatial correlations. The value has found its way into Dutch guidelines and is now widely used in slope stability assessments. The background of b=50m will be discussed in section 7.4. It rests on probabilistic analyses and is in line with the lengths of slope failures.

Aanwezig: Ton Vrouwenvelder (TNO), Ruben Jongejan (RMC), Matthijs Kok (TUD/HKV), Han Vrijling (Horvat), Ed Calle (Deltares), Marcel Visschedijk (Deltares, namens Noorderzijlvest), Bert de Wolff (namens Noorderzijlvest), Sjoerd de Wit (NAM), Geeralt van den Ham (notulist), Vincent Mures (NCG), Ate Wijnstra (Noorderzijlvest)

(page 1)

Met welk lengte-effect moet worden gerekend voor macrostabiliteit en hoogte, bij het bepalen van de maximaal toelaatbare faalkans in een doorsnede?

De correlatielengte voor aardbevingsbelasting is kleiner dan voor waterstandsbelasting en de invloedsfactor van de aardbevingsbelasting groter (0.9). Gegeven bovenstaande wordt voorgesteld om bij macrostabiliteit vast te houden aan de vertaling van eis per traject naar eis per doorsnede voor de situatie zonder aardbeving (conform OI2014, met a=0.033 en b=50 m). Dit lijkt enigszins conservatief, maar de gegevens ontbreken voor een betere inschatting en verwacht wordt dat het effect gering zal zijn.

(page 3)

- Voorgesteld wordt een nieuwe sessie te plannen zodra ontwerpprotocol D-E klaar is, met nieuwe verdeling pga (versie 2) en daarop gebaseerde nieuwe $\alpha_{aardbeving}$. Ook als de eerste ontwerpervaringen zijn opgedaan, is het verstandig om nog een keer samen te komen omdat dan de consequenties van keuzes beter bekend zullen zijn.

(page 7)

Figure 24. Quotes from the minutes of the meeting of December 2015 on the length effect (in Dutch).

7.3 Characterizing the length effect: the parameter a

The parameter a is defined as the fraction of the total length of the segment that dominates the probability of failure of a segment for the failure mechanism under consideration. Based on an LPI-screening for 11.5 km, 3 to 5 profiles have been selected for a detailed assessment to be able to give conclusions concerning the reliability of the entire stretch (Deltares 2017). These profiles are representative for a combined length of several hundred meters. Because of e.g. variations in stratigraphy, these four profiles are also unlikely to have identical failure probabilities. Considering this, there seems to be no obvious reason to move away from a=0.033.

7.4 Characterizing the length effect: the parameter b

7.4.1 Theory

The following theory forms the basis of the b=50m mentioned in section 7.2 that underlies the cross-sectional reliability requirements for slope stability assessments in the Netherlands (Calle & Barends 1990; Vrouwenvelder & Calle 2003). A levee could be thought of as a series system of statistically homogenous lengths. The failure probability of such a statistically homogeneous length L_{hom} can be approximated by (see e.g. Jongejan 2012 for a derivation):

$$P(F_{Lhom}) = 1-(1-P(F_{cross})) \cdot \exp(- L_{hom} /(2\pi) * \text{sqrt}(-d^2\rho_Z(0)/d\Delta^2) \cdot \exp(-\beta_{cross}^2/2)) \quad (21)$$

Where:
$P(F_{Lhom})$ Failure probability of a statistically homogeneous length (per year)
$P(F_{cross})$ Cross-sectional probability of failure (per year)
β_{cross} Cross-sectional reliability index (-)

The statistically homogenous length (L_{hom}) could be thought of, approximately, as a series system of independent, characteristics lengths (b):

$$b = P(F_{cross}) \cdot 2\pi / \text{sqrt}(-d^2\rho_Z(0)/d\Delta^2) \cdot \exp(\beta_{cross}^2/2) \quad (22)$$

which may be approximated as follows if β_{cross}, is positive and not very small, e.g. $\beta_{cross}>2$ (Vrouwenvelder 2006):

$$b = \mathrm{sqrt}(2\pi) / (\mathrm{sqrt}(-d^2\rho_Z(0)/d\Delta^2) \cdot \beta_{cross}) \quad (23)$$

The autocorrelation function of the limit state function can be approximated by the weighted sum of the autocorrelation functions for capacity and demand, with their weights being the squared influence coefficients:

$$\rho_Z(\Delta) = \Sigma\alpha_X^2 \, \rho_X(\Delta) \quad (24)$$

Where

$\rho_Z(\Delta)$ Value of the autocorrelation function of the limit state function, evaluated at lag Δ (-)

$\rho_X(\Delta)$ Value of the autocorrelation function of stochastic variable X, evaluated at lag Δ (-)

The different stochastic variables have different autocorrelation functions. The type of autocorrelation function that is widely used in stability analyses in the Netherlands has the following function form (Van Balen et al. 2016):

$$\rho_X(\Delta) = (1-\rho_0) \cdot \exp(-(\Delta/k)^2) + \rho_0 \quad (25)$$

Where:

ρ_0 Lower bound of the autocorrelation function (-)

k Spatial correlation length parameter (m)

Δ Distance/lag (m)

Examples of autocorrelation functions are given in Figure 25. A lower limit of the autocorrelation function greater than zero implies that part of the uncertainty related to a variable is (spatially correlated) epistemic uncertainty.

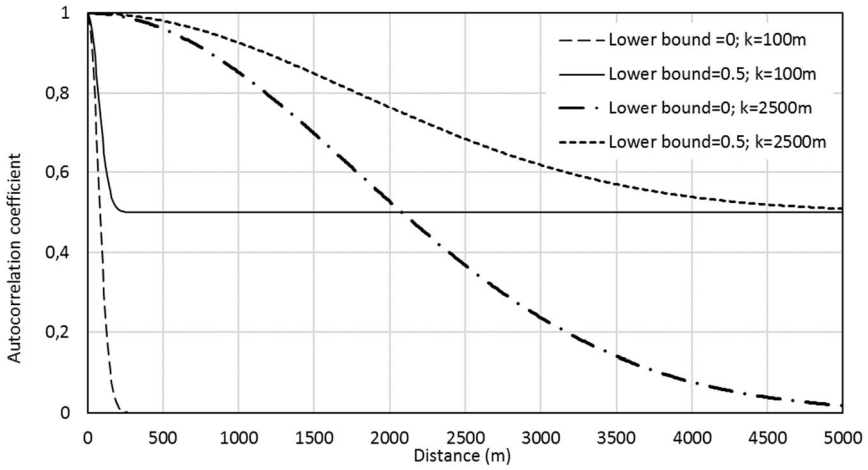

Figure 25. Examples of autocorrelation functions.

7.4.2 Sensitivity analyses

To inform a decision concerning the length effect, various sensitivity analyses have been performed. To simplify these analyses, the various stochastic variables from Table 1 have been grouped/combined into a stochastic variable that is strongly spatially correlated (named “demand” hereafter) and one that is not (named “capacity”). Treating the underlying variables separately does not change the results as long as each of these variables has the same autocorrelation function, see equation (24).

Not all variables are equally spatially variable. The ground motion, for instance, is strongly spatially correlated. The cyclic resistance ratio for layered deposits, on the other hand, is relatively weakly spatially correlated[4]. The influence coefficient from the FORM-analyses has been used as a reference for the influence coefficient of capacity, i.e. $\alpha_C^2 \approx 0.06$. The influence coefficient of capacity has also been increased to show the influence of e.g. treating the uncertainty related to $\varepsilon_{Su/p'}$ as equally spatially variable as the uncertainty related to the CRR in layered deposits (doing so would lead to $\alpha_C^2 \approx 0.08$; a higher value of 0.1 has been used instead). Similarly, it has been decreased ($\alpha_C^2 \approx 0.2$), which could be a reasonable approximation for cases without layered deposits. This is because the CRR for sand is based on an empirical relationship that rests on back-calculations of case histories (see also section 7.4.3). The influence coefficient for demand has been calculated by adding the squared influence coefficients of the remaining stochastic variables.

The results of the sensitivity analyses are shown in Table 4. The reported b-values stem from equation (22).

Table 4. Sensitivity analyses related to the length effect.

Case no.	β_{cross}	Capacity			Demand			b (m)
		α_C^2	$\rho_{0,C}$	k_C (m)	α_D^2	$\rho_{0,D}$	k_D (m)	
1	3	0,06	0,5	100	0,94	0	5000	310
2	4	0,06	0,5	100	0,94	0	5000	240
3	4	0,06	0,5	100	0,94	1	-	242
4	4	0,06	0,5	100	0,94	0	5000	240
5	4	0,06	0	150	0,94	0	5000	255
6	4	0,06	0,5	150	0,94	0	5000	357
7	4	0,1	0,5	100	0,9	0	5000	187
8	4	0,02	0,5	150	0,98	0	5000	600
9	4	0,5	0	100	0,5	1	-	59
10	4	0,5	0,5	100	0,5	1	-	84
11	4	0,5	0	150	0,5	1	-	89

Table 4 illustrates the following:

1. As shown by cases 1 and 2, the length effect increases with increasing reliability indices (as it should). A reliability index of 4 is close to the target reliability (slightly conservative). This is why this reliability index has been considered in the remaining case studies.
2. As shown by cases 2 and 3, the precise autocorrelation function for demand is largely irrelevant to the length effect, as long as this variable is much more strongly spatially correlated than capacity. The length effect is most strongly influenced by (1) the relative importance of the uncertainty related to capacity and (2) the autocorrelation function of capacity.
3. As shown by cases 3, 4 and 5, the length-effect depends on the autocorrelation function of the most weakly spatially correlated variables.
4. As shown by cases 6 and 7, the length effect increases (i.e. b decreases) when the relative importance of the uncertainty related to the spatially variable stochastic variables increases (i.e. α_C^2 increases, α_D^2 decreases).
5. As shown by cases 7 and 8, the length effect decreases (i.e. b increases) when the relative importance of the uncertainty related to the strongly spatially correlated stochastic variables increases (e.i. α_D^2 increases, α_C^2 decreases).
6. Cases 9 to 11 (bottom rows) show that the same procedure leads to b=50m-100m for inputs that are more common in slope stability assessments with a dominant hydraulic load (no earthquake). These analyses illustrate why b=50m is used as a basis for cross-sectional stability assessments in the WBI (the WBI is the instrument provided by the Minister for safety assessments).

The b-values in Table 4 for seismic stability are high compared to the b-value of 50m that underlies the Dutch technical guidelines for slope stability assessments (TAW 2001). This stems from the fact that the uncertainties related to strongly spatially variable stochastic variables are more important in seismic stability analyses than in high water stability analyses, making the limit state function fluctuate more slowly along the length of the dike.

[4] The CRR referred to here concerns a local average, see also Appendix G. Correlation distances for point values are considerably shorter.

7.4.3 Comparison with earthquake damage observations to embankments

Abstract
To verify whether the use of b-values of 200m to 350 m rather than 50m is justified for deriving cross-sectional reliability requirements for seismic stability assessments, the calculated b-values have been compared to damage observations from Japan and related academic research into spatial correlations. These comparisons show that embankment failures can indeed lead to significant damages that extend over hundreds of meters. The comparisons point to even higher b-values than those shown in Table 4. The conditions underlying the Japanese case histories and the conditions in Groningen differ markedly however. Hence, while the b-values in Table 4 still appear low in the light of damage observations, the use of higher values purely on the basis of damage observations is not considered prudent.

Interpreting independent, equivalent length as expected failure lengths
An independent equivalent length is often interpreted as the expected length of failures. This may not be correct, however, when the distributions of stochastic variables rest on back-analyses of case histories. Length effects are inherent to historical observations. When, for instance, liquefaction was not observed in a particular earthquake, it was not observed *anywhere* in the affected region. When distributions rest on back-calculations of case histories, the computed b-value should be interpreted as the length in which a levee is expected to fail somewhere (with a particular probability). In such cases, the computed b-value should be greater than the expected length of failures.

The distribution of the cyclic resistance ratio of sand deposits rests on an empirical relationship that originates from back-analyses of case histories. Hence, for Eemshaven, where sand deposits are critical, the computed b-value should be greater than the expected length of failures. This is different for Delfzijl. Here, laminated deposits are critical. The distribution of the cyclic resistance ratio of laminated deposits rests on laboratory tests, not back-analyses. Hence, at Delfzijl, the computed b-values should be interpretable as the expected lengths of slope failures.

The independent, equivalent length and damage observations
Sasaki and Tamura (2007) present an overview of earthquake damages to embankments in Japan from 1993 onwards (the original reports are in Japanese). Data from their publication has been summarized in Table 5 below.

The average damaged lengths in Table 5 have been calculated by dividing the total damaged lengths by the number of places where damages occurred. The severity of the damages associated with the total damaged lengths is often unclear. This is unfortunate since the length of damage depends on the (definition of the) damage state (see also Kwak et al. 2016). The average length of total collapse caused by liquefaction of the foundation in the Niigata-ken earthquake, which seems to be closest to the failure mechanism considered here, is 957 m. This clearly shows that liquefaction can lead to significant damage over considerable distances. Without accounting for the type/severity of damage, the average damaged lengths range from 317m to 1,732m.

Table 5. Overview of damages reported by Sasaki and Tamura (2007). Figures and quotes from Table 1 and Figure 2 in Sasaki and Tamura (2007).

Year	Earthquake	Severity of damage	Total damaged length (m)	No. of damaged stretches	Average damage length (m)
1993	Kushiro-oki (M=7.8)	Not clearly described ("liquefaction inside embankments, 3-d response of dike"); Kushiro river	10,100	28	361
		Not clearly described ("liquefaction inside embankments, 3-d response of dike"); Tokachi river	9,200	20	460
1993	Hokkaido Nansei-oki (M=7.8)	Not clearly described ("crest cave-in along diagonal slip plane")	6,600	18	367
1995	Hyogo-ken Nanbu (M=7.2)	Not clearly described ("separation into blocks, submerged into liquefied subsoil layer")	5,700	18	317
2000	Tottori-ken Seibu (M=7.3)	Not clearly described ("Bend of dike bottom, transverse cracks at a curvilinear part"	20,700	32	647
2003	Miyagi-ken Hokubu (M=6.4)	Not clearly described ("flow-like deformation")	Not available	66	Not available
2003	Tokachi-oki (M=8.0)	Not clearly described ("elongation of sluice gate length")	16,000	26	615
2004	Niigata-ken Chuetsu (M=6.8)	"Longitudinal cracks (shallower than H.W.L.)" 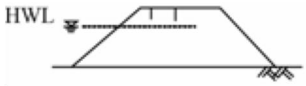	6,997	8	875
		"Longitudinal cracks (deeper than H.W.L.)" 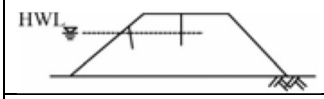	449	1	449
		"Transverse cracks (shallower than H.W.L.)" 	-	-	-
		"Transverse cracks (deeper than H.W.L.)" 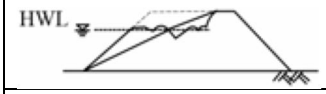	-	-	-
		"Slide of slope (failure of crest)" 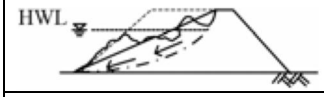	8,659	5	1,732
		"Total collapse of crest, no original shape remaining (liquefaction of foundation)" 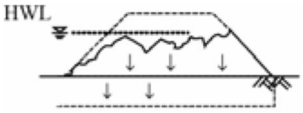	2,871	3	957

More details on the damages caused by the 1995 Hyogoken-Nanbu earthquake can be found in Matsuo (1996). According to Matsuo (1996), the Torishima dike along the Yodo-gawa was strongly impacted by the earthquake. A continuous crest settlements of 2-3 meters was observed over a distance of about 1.4 kilometers see Figure 26. This amount of crest settlement is broadly in line with the definition of the limit state considered here.

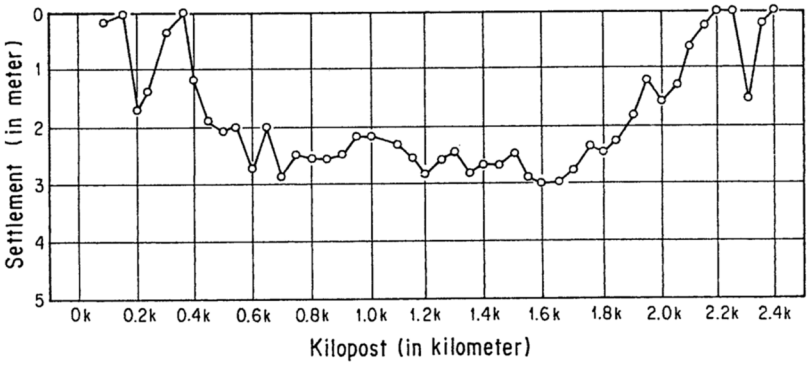

Fig. 1. Settlement of the Torishima Dike

Figure 26. Damages caused by the 1995 Hyogoken-Nanbu earthquake and a profile of observed crest settlement of the Torishima dike along the Yodo-gawa (from: Matsuo 1996).

The Japanese damage records indicate that liquefaction can lead to significant damage or collapse over lengths of a kilometer or more. It also appears that damages, irrespective of their severity, can easily extend over hundreds of meters. All average damage lengths in Table 5 far exceed 50m.

Damage observations and empirical autocorrelation functions

Observed damage lengths are influenced by the difference between capacity and demand: when design loads are strongly exceeded, damaged lengths are likely to much higher than when design loads are barely or not at all exceeded. To correct for this effect, back-analyses of the spatial pattern of damage states were performed by Kwak et al. (2016) *conditional on the seismic demands that led to these damages*. Two different fragility curves were used in these back-analyses, conditional on ground water level. Empirical autocorrelations functions of capacity were derived from the damages observed in the 2004 Niigata-ken Chuetsu earthquake and the 2007 Niigata-ken Chuetsu-oki earthquakes.

The squared exponential autocorrelation functions for capacity and demand from Kwak et al. (forthcoming) are considered here. Using the distribution of capacity and the distribution of demand *conditional on the M6.6 event*, α_C^2 is around 0.75. Results of sensitivity analyses with these autocorrelation functions are shown in Table 6.

Table 6. The calculated b-values for a M=6.4 earthquake using the empirical autocorrelation function developed by Kwak et al. (2016).

Case no.	β_{cross}	Capacity			Demand			b (m)
		α^2	ρ_0	k (m)	α^2	ρ_0	k (m)	
1	3	0,75	0	2765	0,25	0	8000	1869
2	4	0,75	0	2765	0,25	0	8000	1402

The results shown in Table 6 are in reasonable agreement with the damage reports from Table 4: the b-values are broadly in line with the average length of severe damage/collapse.

The empirical autocorrelation function of capacity developed by Kwak et al. (2016) is a property of the capacity the levee system for which it has been derived. The autocorrelation function of demand could be different from earthquake to earthquake. Using the (modified) autocorrelation function for capacity by Kwak et al. (2016), the b-values have been recalculated for several cases from Table 4. Results are shown in Table 7.

Table 7. Sensitivity analysis using an empirical autocorrelation function developed by Kwak et al. (2016).

Case no.	β_{cross}	Capacity			Demand			b (m)
		α^2	ρ_0	k (m)	α^2	ρ_0	k (m)	
1	4	0,08	0	2765	0,92	0	5000	1780
2	4	0,1	0	2765	0,9	0	5000	1780
3	4	0,02	0	2765	0,98	0	5000	1990

The b-values from Table 7 are significantly greater than the ones from Table 4. This could be because the results shown in Table 4 are conservative. It could also be, however, that the variations in the reliability of the Japanese levee systems were underestimated in the back analyses with the use of only two different fragility curves. The empirical autocorrelation function then describes the combined effect of:

1. changes in the reliability of cross-sections along the entire length of levee due (not fully accounted for by the two fragility curves) and
2. variations in material properties within homogenous lengths.

If so, the empirical autocorrelation function should be used in combination with a relatively high a-value in equation (20), i.e. a>0.033. After all, if the two fragility curves underestimate the variations in cross-sectional reliabilities, there could still be important variations within the "critical length" (= a · L). Note that a=0.033 in combination with the b-values from Table 4 (about 200-400m) leads to broadly similar cross-sectional reliability requirements to a=0.3 with the b-values from Table 7. Taking the empirical autocorrelation by Kwak et al. (forthcoming) in combination with a=0.033 would lead to target failure probabilities that are about a factor 10 greater. This would translate into a significant reduction of return periods (amongst other). Given that this research is relatively recent and has not been previously applied in projects, such a reduction in demand is not considered prudent for an assessment of a critical infrastructure like the Eemshaven-Delfzijl sea dike.

Discussion

While it is difficult to base a decision on a particular b-value purely on Japanese damage records, these records do suggest that embankment failures can extend over hundreds of meters. It also seems that b=200-350m is more realistic than b=50m.

It is important to note that the earthquakes covered by Sasaki and Tamura (2007), Matsuo (1996) and Kwak et al. (2016) had considerably greater magnitudes (M>6) than the maximum magnitude of around 5 expected in Groningen (NAM 2016). Also, soil conditions and levee designs differ in Groningen and Japan. This means that damage observations from Japan may not be entirely representative for Groningen. This is also why damage observations have been used to put the results of the "bottom-up" sensitivity analyses (Table 4) into perspective rather than the other way round.

7.4.4 Proposed b-value

Based on the results of the sensitivity analyses in Table 4 and the discussion above, a b-value of 200-350 m seems justified. The use of the lowest value from this range is proposed, i.e. b=200m. Should this still turn out to be too optimistic, the assumed 3 month repair time seems too pessimistic. This is because this month repair rests on the premise that earthquake damages may occur over several kilometers (Figure 24).

> Schade zal wellicht optreden over enkele km's. Noodreparatie kan ook bestaan uit alleen herstellen bekleding buitentalud. Groot deel dijk heeft kleikern aan buitenzijde. Een hersteltijd van 1 jaar wordt als lang beoordeeld: noodreparatie moet sneller kunnen. Een hersteltijd van 3 maanden is aannemelijker. (page 7)

Figure 27. Quotes from the minutes of the meeting of December 2015 on the length effect (in Dutch).

A repair time shorter than 3 months leads to a smaller probability of flooding in case of significant earthquake damage (i.e. $P_{F|D}$<1/10). Taken together, b=200m and $P_{F|D}$=1/10 seem to be a prudent basis for cross-sectional seismic stability assessments of the Eemshaven-Delfzijl sea dikes.

7.5 Updated cross-sectional target reliabilities

The following parameter values are proposed to characterize the length effect:

1. a = 0.033 (same as before)
2. b = 200m (before: 50m)

The impact of increasing the b-value from 50 to 200m leads to changes in the cross-sectional target reliabilities for segments 6-6 and 6-7, as shown in Table 8.

Table 8. Updated cross-sectional target reliabilities for assessing seismic stability.

Segment	Standard of protection (per year)	Cross-sectional target reliability for a=0.033 and b=50m (original, see Table 3)		Cross-sectional target reliability for a=0.033 and b=200m (proposed)	
		P_T	β_T	P_T	**β_T**
6_6 (includes Eemshaven)	1/1,000	7.64-05	3.79	2.79E-04	**3.45**
6_7 (includes Delfzijl)	1/3,000	3.02-05	4.01	1.09E-04	**3.70**

The changes in cross-sectional target reliabilities lead to a reduction of the return periods of the design values of the spectral accelerations at NSUB by about a factor 3, see also chapter 8. The changes also affect the design values of the other stochastic variables, albeit to a lesser extent. This is because their influence coefficients are relatively small.

8 Action item 5: Synthesis

8.1 From calculated FORM-influence coefficients and target reliabilities to design values

Design values have been derived on the basis of:

1. the influence coefficients obtained from FORM-analyses with the FE-model and
2. the target reliabilities from Table 8 in section 7.5, i.e. $\beta_T = 3.45$ (segment 6-6, Eemshaven) and $\beta_T = 3.70$ (segment 6-7, Delfzijl).

Table 9 and Table 10 show the cumulative probabilities of the design values that seem reasonable on the basis of the calculated FORM-influence coefficients and target reliabilities. As discussed in chapter 2, a design value can be split into a representative value and a partial factor (last two columns).

The design values in Table 9 and Table 10 all rest on influence coefficients that are greater than those obtained from FORM-analyses. The sum of squared influence coefficients on which the design values are based is an indicator of the amount of conservatism in the semi-probabilistic rule. For Eemshaven and Delfzijl, these sums are about 1.1. Recommended design values, based on Table 9 and Table 10, are shown in Table 11.

Table 9. From calculated influence coefficients and target reliability to design values. Results for the Eemshaven base case (segment 6-6).

Stochastic variable	Calculated		Possible basis for assessment					
	α^2	α	α^2	α	β_T	Cumulative probability	Representative value, quantile	Partial factor
Spectral acceleration at model base	0.732	-0.856	-	-	-	-	-	-
Spectral acceleration at NSUB	0.725	-0.851	0.81	-0.9	3.45	9.991E-01 per year	1056 year return period	1.0
Uncertainty in site response	0.007	-0.086	0.01	-0.1	3.45	0.635	50%	1.04
CRRM=7.5 in sand deposits	0.160	0.400	0.18	0.42	3.45	0.074	15%	1.09
Uncertainty related to residual strength*	0.040	0.200	0.04	0.21	3.45	0.234	50%	1.39
Model Uncertainty	0.068	0.261	0.08	0.28	3.45	0.167	50%	1.70
Total	1	-	1.12	-	-	-	-	-

** For residual strengths according to Kramer and Wang (2015).*

Table 10. From calculated influence coefficients and target reliability to design values. Results for the Delfzijl base case (segment 6-7).

Stochastic variable	Calculated		Possible basis for assessment					
	α^2	α	α^2	α	β_T	Cumulative probability	Representative value, quantile	Partial factor
Spectral acceleration at model base	0.786	-0.887	-	-	-	-	-	-
Spectral acceleration at NSUB	0.778	-0.882	0.81	-0.9	3.70	9.996E-01 per year	2290 year return period	-

Uncertainty in site response	0.008	-0.089	0.01	-0.1	3.70	0.644	50%	1.04
$CRR_{M=5.0}$ of laminated deposit	0.046	0.214	0.09	0.3	3.70	0.133	15%	1.01
Uncertainty related to residual strength*	0.018	0.134	0.03	0.16	3.70	0.277	50%	1.31
Model Uncertainty	0.150	0.387	0.17	0.41	3.70	0.070	50%	2.30
Total	1	-	1.10	-	-	-	-	-

** For residual strengths according to Kramer and Wang (2015).*

Recommended design values

The following design values are recommended for use with the Guideline for conducting dynamic effective stress analyses (Fugro 2016b).

Table 11. Recommended design values.

Stochastic variable	Representative value	Partial factor segment 6-6	Partial factor segment 6-7
Spectral acceleration at NSUB	Segment 6-6: 1100 year return period Segment 6-7: 2300 year return period	1.0	1.0
Uncertainty in site response	Median, i.e. time history amplitudes at model base, calculated on the basis of median properties ("best estimate")	1.05	1.05
CRR in sand deposits	16% quantile value of the $CRR_{M=7.5}$ from the probabilistic Boulanger & Idriss (2014) relationship for the median of local q_{c1Ncs}-values Put differently: the $CRR_{M=7.5}$ according to the "deterministic" relationship proposed by Boulanger & Idriss (2014) for the median of local q_{c1Ncs}-values.	1.10*	1.10
CRR in laminated deposits	16% quantile of the distribution of the spatial average at four cycles (regional data set)	1.0	1.0
Uncertainty related to residual strength in sand deposits **	Median, i.e. $(\varepsilon_{lnSu/p'})_{rep} = 1$	1.4 on $(S_{u/p'})_{rep}$, see equation (26)	1.4 on $(S_{u/p'})_{rep}$, see equation (26)
Uncertainty related to residual strength in laminated deposits **	Median, i.e. $(\varepsilon_{lnSu/p'})_{rep} = 1$	1.3 on $(S_{u/p'})_{rep}$, see equation (26)	1.3 on $(S_{u/p'})_{rep}$, see equation (26)
Model Uncertainty	Median, i.e. the computed crest settlement from an unbiased model	1.7	2.3

* *This is broadly equivalent to the use of a 25% quantile of qc1Ncs together with the deterministic Boulanger & Idriss (2014) relationship between qc1Ncs and CRR, which is more conservative than the 33% quantile proposed by Boulanger & Montgomery (2016) for cases like these where the dimensions of relevant deformations far exceed the sale of fluctuation.*

** *For residual strengths according to Kramer and Wang (2015).*

The design value of residual strength can be calculated using:

$$\left(\frac{Su}{p'}\right)_d = \frac{exp\left(-8.444 + 0.109\ (N_1)_{60} + 5.379\ p'^{0.1}\right)}{\gamma_{res}\ p'} \quad (26)$$

with γ_{res}=1.4 (sand deposit) or γ_{res}=1.3 (laminated deposit) and $(N_1)_{60}$ according to Idriss & Boulanger (2008):

$$(N_1)_{60} = 46 \cdot (0.478\ q_{c1N}^{0.264} - 1.063)^2 \quad (27)$$

where:

$(Su/p')_d$ Design value of normalized residual strength (-)
p' Initial effective vertical stress (atm)
$(N_1)_{60}$ Normalized SPT blow count (-), median value
q_{c1N} Normalized cone tip resistance (-)

8.2 Uncertainty related to motions

The following procedure is recommended for dealing with the uncertainty related to motions (see also Appendix H):

1. Select 11 independent motions with appropriate seismological characteristics (e.g. amplitude, frequency content and duration).
2. Compute crest settlements for each motion using the design values from Table 11.
3. Analyze the results: outliers should be understood.
4. The (subjective) probability that the crest settlement for a randomly selected motion exceeds the limit state should be less than 25%. If, for instance, all 11 motions are considered to be equally likely, the limit state should not be exceeded for more than 2 motions.

Note that it might be incorrect to treat the 11 motions as equally likely or to assume that the 11 selected motions span the entire set of possible motions. In some cases, it might be reasonable to assign low subjective probabilities to particular motions or to treat the 11 motions as members of a subset of relatively pessimistic motions.

8.3 Uncertainty related to stratigraphy

The uncertainty related to stratigraphy can be dealt with as follows:

1. consider a conservative, realistic stratigraphy,
2. carry out sensitivity analyses,
3. make an informed judgment.

A more rigorous procedure for dealing with uncertainty related to stratigraphy is given by ENW (2012). It is summarized in Appendix H (for motions, not stratigraphies). This procedure is laborious, however, since it involves a large number of evaluations of the limit state function.

8.4 Sea level (load combination)

The combination of a severe earthquake and an extremely high or low sea level is unlikely because water levels and earthquakes are uncorrelated and because both types of events have relatively short durations. Note that a higher water level on the sea side need not be conservative. It is recommended to use as a design sea level, whichever of the following is the most conservative:

1. the water level that is expected to be exceeded once a year (1 year return period) or
2. the low tide.

References

Van Balen, W. et al., 2016. *Hydra-Ring 2.0, Probabilistics toolbox for the WTI2017, Technical Reference Manual*, Deltares, report no. 1230088-DSC-0072.

Bazzurro & Cornell, 2004. Nonlinear Soil-Site Effects in Probabilistic Seismic-Hazard Analysis. *Bulletin of the Seismological Society of America*, 94(6), pp.2110–2123.

Bommer, J.J. et al., 2015. *Development of Version 2 GMPEs for Response Spectral Accelerations and Significant Durations from Induced Earthquakes in the Groningen Field* November 2. J. Van Elk & D. Doornhof, eds., NAM.

Boulanger, R.W. & Idriss, I.M., 2014. *CPT and SPT based liquefaction triggering procedures*, Report No. UCD/CGM-14/01, Center for Geotechnical Modeling, Department of Civil & Environmental Engineering, College of Engineering, University of California at Davis.

Boulanger, R.W. & Montgomery, J., 2016. Nonlinear deformation analyses of an embankment dam on a spatially variable liquefiable deposit. *Soil Dynamics and Earthquake Engineering*, 91, pp.222–233. Available at: http://linkinghub.elsevier.com/retrieve/pii/S026772611630104X.

Boulanger, R.W. & Montgomery, J., 2015. Nonlinear Deformation Analyses of an Embankment Dam on a Spatially Variable Liquefiable Deposit. In *6th International Conference on Earthquake Geotechnical Engineering*. Christchurch, New Zealand.

Calle, E.O.F., 2007. Statistiek bij Regionale Proevenverzamelingen deel 1. *Geotechniek*, July.

Calle, E.O.F., 2008. Statistiek bij Regionale Proevenverzamelingen deel 2. *Geotechniek*, Januari.

Calle, E.O.F. & Barends, F.B.J., 1990. *PROSTAB een computerprogramma voor probabilistische analyse van stabiliteit van taluds*, Grondmechanica Delft, CO-266484/32.

Deltares, 2017. *LPI screening for the Eemshaven-Delfzijl levee*, Deltares report no. 1220173-024-GEO-0067, version 3.

ENW, 2012. *Technisch Rapport Grondmechanisch Schematiseren bij Dijken*, Expertisenetwerk Waterveiligheid.

Expert Panel, 2016. *Expert Panel Report*, 2 December 2016. Letter addressed to E. van Dijk by Chacko, J. Green, R.A. Kramer, S.L. Towhata, I.

Fugro, 2016a. *Evaluation of dynamic stability Eemshaven-Delfzijl levee, The Netherlands*, Fugro, 2 December 2016, contract no. 1016-0459-000.

Fugro, 2016b. *Guidelines for dynamic effective stress finite element analyses Eemshaven-Delfzijl levee Groningen, the Netherlands*, Fugro, 10 August 2016, 1st issue, Contract No. 1016-0459-000.

Fugro, 2016c. *Interpretive report, Delfzijl / Eemshaven Levee Project in Groningen, the Netherlands, prepared for Nederlandse Aardolie Maatschappij B.V.* November.,

Green, R. et al., 2016. *Unbiased Cyclic Resistance Ratio Relationships for Evaluating Liquefaction Potential in Groningen*,

Idriss, I.M. & Boulanger, R.W., 2008. *Soil liquefaction during earthquakes*, EERI monograph MNO-12, Earthquake Engineering Research Institute.

Itasca, 2011. *Fast Lagrangian Analysis of Continua (FLAC2D)*, Version 6.0.

Jongejan, R.B., 2012. *Het lengte-effect in een statistisch homogeen vak*, Memorandum, 11 February 2012, Jongejan RMC.

Jongejan, R.B. & Maaskant, B., 2015. Quantifying Flood Risks in the Netherlands. *Risk Analysis*, 35(2), pp.252–264. Available at: http://doi.wiley.com/10.1111/risa.12285.

Kramer, S.L. & Wang, C.-H., 2015. Empirical Model for Estimation of the Residual Strength of Liquefied Soil. *Journal of Geotechnical and Geoenvironmental Engineering*, 141(9), p.4015038. Available at: http://ascelibrary.org/doi/10.1061/%28ASCE%29GT.1943-5606.0001317.

Kwak, D.Y. et al., Methods for Probabilistic Seismic Levee System Reliability Analysis. In *Georisk 2017*.

Kwak, D.Y. et al., 2016. Seismic Levee System Fragility Considering Spatial Correlation of Demands and Component Fragilities. *Earthquake Spectra*, 32(4), pp.2207–2228. Available at: http://earthquakespectra.org/doi/10.1193/083115EQS132M.

Matsuo, O., 1996. Damage to river dikes. *Soils and Foundations*, (Special issue, January 1996), pp.235–240.

Montgomery, J., 2015. *Issues in nonlinear deformation analysis of embankment dams affected by liquefaction*. University of California, Davis.

NAM, 2016. Toelichting resultaten Mmax-workshop.

Robertson, P.K., 1990. Soil classification using the cone penetration test. *Canadian Geotechnical Journal*, 27(1), pp.151–58.

Sasaki, Y. & Tamura, K., 2007. Failure mode of embankments due to recent earthquakes in Japan. In *4th International Conference on Earthquake Geotechnical Engineering, June 25028, 2007*. Thessaloniki, Greece: Paper No.1479.

Stewart, J., Afshari, K. & Hashash, Y.M., 2014. *Guidelines for Performing Hazard-Consistent One-Dimensional Ground Response Analysis for Ground Motion*, Pacific Earthquake Engineering Research Center.

TAW, 1989. *Leidraad voor het ontwerpen van rivierdijken deel 2 benedenrivierengebied*, Technische Adviescommissie voor de Waterkeringen.

TAW, 2001. *Technisch Rapport Waterkerende Grondconstructies; Geotechnische aspecten van dijken, dammen en boezemkaden*, Technische Adviescommissie voor de Waterkeringen.

USACE, 2013. *Engineering and design of I-Walls*, Washington, DC.

Vanmarcke, E., 2011. Risk of Limit-Equilibrium Failure of Long Earth Slopes: How It Depends on Length. In *Georisk 2011*. Reston, VA: American Society of Civil Engineers, pp. 1–24.

VanMarcke, E.., 1977. Reliability of Earth Slopes. *Journal of the Geotechnical Engineering Division*, 103(11), pp.1247–1265.

Vrouwenvelder, T., 2006. Spatial effects in reliability analysis of flood protection systems. In *Second IFED Forum*. Lake Louise, Canada.

Vrouwenvelder, T. & Calle, E., 2003. Measuring Spatial Correlation of Soil Properties. *Heron*, 48(4).

Appendix A First Order Reliability Method (FORM)

FORM is an efficient, approximate technique for computing probabilities of failure. In this appendix, a brief overview is given of the steps in a FORM analysis, together with an example.

FORM step by step
FORM is an iterative procedures that requires only few evaluations of a limit state function compared to e.g. Monte Carlo simulation. FORM calculation involves the following steps:

Step 1: Select start values
Select values for the stochastic variables for the evaluation of the limit state function (Z). Note: Z<0 implies failure, Z>0 implies the opposite.

Step 2: Calculate partial derivatives
Calculate the partial derivatives of the limit state function with respect to the different stochastic variables. This can be done by perturbing input values or by looking at the results of sensitivity analyses that have already been carried out.

Step 3: Transform all non-normally distributed variables to normally distributed variables.
This can be done on the basis of the following equations:

$$\sigma_{Xnorm,i} = \varphi\{ \Phi^{-1}(F_{X,i}(X_{i,0})) \} / f_{X,i}(X_{i,0}) \quad (28)$$

$$\mu_{Xnorm,i} = X_{i,0} - \Phi^{-1}(F_{X,i}(X_{i,0})) \cdot \sigma_{Xnorm,i} \quad (29)$$

Where:
$\sigma_{Xnorm,i}$ Standard deviation
$\mu_{Xnorm,i}$ Expected value
$\varphi(\cdot)$ Standard normal probability density function
$\Phi(\cdot)$ Standard normal distribution function
$F_{X,i}(X_{i,0})$ Cumulative distribution function of variable X_i, evaluated at $X_{i,0}$
$f_{X,i}(X_{i,0})$ Probability density function of variable X_i, evaluated at $X_{i,0}$

To check the end-result, the cumulative probabilities of $F_{X,i}(X_{i,0})$ and $\Phi(\sigma_{Xnorm,i}/\mu_{Xnorm,i})$ could be compared. These should be identical. The same should hold true for the probability densities.

Step 4: Calculate the standard deviation and expected value of the (normalized) limit state function
The standard deviation follows from:

$$\sigma_Z = (\Sigma (\partial Z/\partial X_i \cdot \sigma_{Xnorm,i})^2)^{1/2} \quad (30)$$

Where:
$\partial Z/\partial X_i$ Partial derivative of the limit state function with respect to stochastic variable X_i, evaluated at $X_{i,0}$.

The expected value follows from:

$$\mu_Z = Z(\underline{X_0}) + \Sigma\{\partial Z/\partial X_i \cdot (\mu_{Xnorm,i} - X_{i,0})\} \quad (31)$$

Where:
$\underline{X_0}$ Vector of the start values of all stochastic variables

Step 6: Calculate influence coefficients and reliability index
The influence coefficients follow from the product of the partial derivatives and the standard deviations from step 3.

$$\alpha_{Xi} = (\partial Z/\partial X_i \cdot \sigma_{Xnorm,i}) / \sigma_Z \quad (32)$$

The reliability index follows from:

$$\beta = \sigma_Z / \mu_Z \quad (33)$$

Step 6: Repeat steps 2-5, starting from the expected design point
The previous steps should be repeated until convergences is obtained. This can be done through successive substitution, i.e. by using the quantile values corresponding to the computed β and α-values as the start values for the next FORM iteration. The resulting reliability index is related to the probability of failure as follows:

$$P(F) = \Phi(-\beta) \quad (34)$$

The accuracy of a FORM computation can be checked by e.g. a Monte Carlo simulation. For a linear limit state function with independent, normally distributed variables, FORM yields the exact same result as MC or numerical integration.

Example
The following code could be run in e.g. Matlab or Octave. It concerns a simple, hypothetical limit state function with two lognormally distributed variables: demand and capacity. Note: the lognormally distributed variables are given here by the normal distributions of their natural logarithms. This is why normalization does not play a role here.

```
function [ Z ] = Z(x1,x2)

Z = exp(x2) - exp(x1);

endfunction
```

```
function [ ] = FORM(n)
% n = Number of FORM iterations, e.g. n=50 (increase until convergence is reached)

fun = "Z";      % here: Z = C - D

%% Distributions of stochastic variables
median_D    = 50;           % D = Demand
mu_lnD      = log(median_D);
sd_lnD      = 0.4;

median_C    = 200;        %C = Capacity
mu_lnC      = log(median_C);
sd_lnC      = 0.40;

%% Rename
mu1         = mu_lnD;
sd1         = sd_lnD;
mu2         = mu_lnC;
sd2         = sd_lnC;

%% Select start values for FORM iterations
x1(1)  = mu1;
x2(1)  = mu2;
```

```
%% Select parameter values for FORM iterations
r  = 0.8;            % relaxation factor: this factor helps to arrive at the design point in a more gentle manner
dx = 0.001;          % perturbation for computing partial derivatives

%% FORM iterations
for i = 2:n;
    dZ_dx1(i)     = ( feval( "Z", x1(i-1)+dx , x2(i-1) ) - feval( "Z", x1(i-1) , x2(i-1)) ) / dx;
    dZ_dx2(i)     = ( feval( "Z", x1(i-1) , x2(i-1)+dx ) - feval( "Z", x1(i-1) , x2(i-1)) ) / dx;

    mu_Z(i)  = feval(fun,x1(i-1),x2(i-1)) + ( dZ_dx1(i)*(mu1-x1(i-1)) + dZ_dx2(i)*(mu2-x2(i-1)) );

    sd_Z(i)   = sqrt( (dZ_dx1(i) * sd1)^2 + (dZ_dx2(i) * sd2)^2 );

    Beta(i)   = mu_Z(i)/sd_Z(i);

    a1(i)     = - dZ_dx1(i) * sd1 / sd_Z(i);
    a2(i)     = - dZ_dx2(i) * sd2 / sd_Z(i);

    x1d(i)    = mu1 + a1(i)*Beta(i)*sd1;
    x2d(i)    = mu2 + a2(i)*Beta(i)*sd2;

    x1(i)     = r*x1(i-1)+(1-r)*x1d(i);
    x2(i)     = r*x2(i-1)+(1-r)*x2d(i);
endfor

Beta   = Beta(n)
Pf     = normcdf(-Beta)

alpha_D = a1(n)
alpha_C = a2(n)


%% Check FORM results
% The limit state function should be equal to zero in the design point:
Z = feval( "Z", x1(n),x2(n))

% The probability of failure can also be computed using Monte Carlo simulation:
Pf_MC   = sum( exp(normrnd(mu1,sd1,1e7,1)) > exp(normrnd(mu2,sd2,1e7,1)) ) /1e7
```

In this case, FORM gives a failure probability of 0.0071. Monte Carlo gives practically the same result. The number of evaluations of the limit state function is several orders of magnitude smaller when using FORM, however.

For normalizing a Weibull distributed variable:

```
pdf_x = wblpdf( x, scale , shape );
cdf_x = wblcdf( x, scale , shape );

sd = normpdf( norminv( cdf_x ) ) / pdf_x;
mu = x - norminv( cdf_x ) * sd;
```

Indices have to be added to the x-values when this piece of code is placed within the FORM-loop shown above.

Appendix B Design point values

An overview of the **cumulative probabilities** of the design point values of capacity variables (α>0) is given below, together with the *exceedance probabilities* of demand variables (α<0), for a range of reliability indices.

α	**Reliability index β**								
	3	**3,2**	**3,4**	**3,6**	**3,8**	**4**	**4,2**	**4,4**	**4,6**
1,00	**1,35E-03**	**6,87E-04**	**3,37E-04**	**1,59E-04**	**7,23E-05**	**3,17E-05**	**1,33E-05**	**5,41E-06**	**2,11E-06**
0,95	**2,19E-03**	**1,18E-03**	**6,19E-04**	**3,13E-04**	**1,53E-04**	**7,23E-05**	**3,30E-05**	**1,46E-05**	**6,21E-06**
0,90	**3,47E-03**	**1,99E-03**	**1,11E-03**	**5,98E-04**	**3,13E-04**	**1,59E-04**	**7,84E-05**	**3,75E-05**	**1,74E-05**
0,85	**5,39E-03**	**3,26E-03**	**1,93E-03**	**1,11E-03**	**6,19E-04**	**3,37E-04**	**1,78E-04**	**9,20E-05**	**4,61E-05**
0,80	**8,20E-03**	**5,23E-03**	**3,26E-03**	**1,99E-03**	**1,18E-03**	**6,87E-04**	**3,90E-04**	**2,16E-04**	**1,17E-04**
0,75	**1,22E-02**	**8,20E-03**	**5,39E-03**	**3,47E-03**	**2,19E-03**	**1,35E-03**	**8,16E-04**	**4,83E-04**	**2,80E-04**
0,70	**1,79E-02**	**1,25E-02**	**8,66E-03**	**5,87E-03**	**3,91E-03**	**2,56E-03**	**1,64E-03**	**1,04E-03**	**6,41E-04**
0,65	**2,56E-02**	**1,88E-02**	**1,36E-02**	**9,64E-03**	**6,76E-03**	**4,66E-03**	**3,17E-03**	**2,12E-03**	**1,39E-03**
0,60	**3,59E-02**	**2,74E-02**	**2,07E-02**	**1,54E-02**	**1,13E-02**	**8,20E-03**	**5,87E-03**	**4,15E-03**	**2,89E-03**
0,55	**4,95E-02**	**3,92E-02**	**3,07E-02**	**2,39E-02**	**1,83E-02**	**1,39E-02**	**1,04E-02**	**7,76E-03**	**5,70E-03**
0,50	**6,68E-02**	**5,48E-02**	**4,46E-02**	**3,59E-02**	**2,87E-02**	**2,28E-02**	**1,79E-02**	**1,39E-02**	**1,07E-02**
0,45	**8,85E-02**	**7,49E-02**	**6,30E-02**	**5,26E-02**	**4,36E-02**	**3,59E-02**	**2,94E-02**	**2,39E-02**	**1,92E-02**
0,40	**1,15E-01**	**1,00E-01**	**8,69E-02**	**7,49E-02**	**6,43E-02**	**5,48E-02**	**4,65E-02**	**3,92E-02**	**3,29E-02**
0,35	**1,47E-01**	**1,31E-01**	**1,17E-01**	**1,04E-01**	**9,18E-02**	**8,08E-02**	**7,08E-02**	**6,18E-02**	**5,37E-02**
0,30	**1,84E-01**	**1,69E-01**	**1,54E-01**	**1,40E-01**	**1,27E-01**	**1,15E-01**	**1,04E-01**	**9,34E-02**	**8,38E-02**
0,25	**2,27E-01**	**2,12E-01**	**1,98E-01**	**1,84E-01**	**1,71E-01**	**1,59E-01**	**1,47E-01**	**1,36E-01**	**1,25E-01**
0,20	**2,74E-01**	**2,61E-01**	**2,48E-01**	**2,36E-01**	**2,24E-01**	**2,12E-01**	**2,00E-01**	**1,89E-01**	**1,79E-01**
0,15	**3,26E-01**	**3,16E-01**	**3,05E-01**	**2,95E-01**	**2,84E-01**	**2,74E-01**	**2,64E-01**	**2,55E-01**	**2,45E-01**
0,10	**3,82E-01**	**3,74E-01**	**3,67E-01**	**3,59E-01**	**3,52E-01**	**3,45E-01**	**3,37E-01**	**3,30E-01**	**3,23E-01**
0,05	**4,40E-01**	**4,36E-01**	**4,33E-01**	**4,29E-01**	**4,25E-01**	**4,21E-01**	**4,17E-01**	**4,13E-01**	**4,09E-01**
0,00	**5,00E-01**	**5,00E-01**	**5,00E-01**	**5,00E-01**	**5,00E-01**	**5,00E-01**	**5,00E-01**	**5,00E-01**	**5,00E-01**
-0,05	*4,40E-01*	*4,36E-01*	*4,33E-01*	*4,29E-01*	*4,25E-01*	*4,21E-01*	*4,17E-01*	*4,13E-01*	*4,09E-01*
-0,10	*3,82E-01*	*3,74E-01*	*3,67E-01*	*3,59E-01*	*3,52E-01*	*3,45E-01*	*3,37E-01*	*3,30E-01*	*3,23E-01*
-0,15	*3,26E-01*	*3,16E-01*	*3,05E-01*	*2,95E-01*	*2,84E-01*	*2,74E-01*	*2,64E-01*	*2,55E-01*	*2,45E-01*
-0,20	*2,74E-01*	*2,61E-01*	*2,48E-01*	*2,36E-01*	*2,24E-01*	*2,12E-01*	*2,00E-01*	*1,89E-01*	*1,79E-01*
-0,25	*2,27E-01*	*2,12E-01*	*1,98E-01*	*1,84E-01*	*1,71E-01*	*1,59E-01*	*1,47E-01*	*1,36E-01*	*1,25E-01*
-0,30	*1,84E-01*	*1,69E-01*	*1,54E-01*	*1,40E-01*	*1,27E-01*	*1,15E-01*	*1,04E-01*	*9,34E-02*	*8,38E-02*
-0,35	*1,47E-01*	*1,31E-01*	*1,17E-01*	*1,04E-01*	*9,18E-02*	*8,08E-02*	*7,08E-02*	*6,18E-02*	*5,37E-02*
-0,40	*1,15E-01*	*1,00E-01*	*8,69E-02*	*7,49E-02*	*6,43E-02*	*5,48E-02*	*4,65E-02*	*3,92E-02*	*3,29E-02*
-0,45	*8,85E-02*	*7,49E-02*	*6,30E-02*	*5,26E-02*	*4,36E-02*	*3,59E-02*	*2,94E-02*	*2,39E-02*	*1,92E-02*
-0,50	*6,68E-02*	*5,48E-02*	*4,46E-02*	*3,59E-02*	*2,87E-02*	*2,28E-02*	*1,79E-02*	*1,39E-02*	*1,07E-02*
-0,55	*4,95E-02*	*3,92E-02*	*3,07E-02*	*2,39E-02*	*1,83E-02*	*1,39E-02*	*1,04E-02*	*7,76E-03*	*5,70E-03*
-0,60	*3,59E-02*	*2,74E-02*	*2,07E-02*	*1,54E-02*	*1,13E-02*	*8,20E-03*	*5,87E-03*	*4,15E-03*	*2,89E-03*
-0,65	*2,56E-02*	*1,88E-02*	*1,36E-02*	*9,64E-03*	*6,76E-03*	*4,66E-03*	*3,17E-03*	*2,12E-03*	*1,39E-03*
-0,70	*1,79E-02*	*1,25E-02*	*8,66E-03*	*5,87E-03*	*3,91E-03*	*2,56E-03*	*1,64E-03*	*1,04E-03*	*6,41E-04*
-0,75	*1,22E-02*	*8,20E-03*	*5,39E-03*	*3,47E-03*	*2,19E-03*	*1,35E-03*	*8,16E-04*	*4,83E-04*	*2,80E-04*
-0,80	*8,20E-03*	*5,23E-03*	*3,26E-03*	*1,99E-03*	*1,18E-03*	*6,87E-04*	*3,90E-04*	*2,16E-04*	*1,17E-04*
-0,85	*5,39E-03*	*3,26E-03*	*1,93E-03*	*1,11E-03*	*6,19E-04*	*3,37E-04*	*1,78E-04*	*9,20E-05*	*4,61E-05*
-0,90	*3,47E-03*	*1,99E-03*	*1,11E-03*	*5,98E-04*	*3,13E-04*	*1,59E-04*	*7,84E-05*	*3,75E-05*	*1,74E-05*
-0,95	*2,19E-03*	*1,18E-03*	*6,19E-04*	*3,13E-04*	*1,53E-04*	*7,23E-05*	*3,30E-05*	*1,46E-05*	*6,21E-06*
-1,00	*1,35E-03*	*6,87E-04*	*3,37E-04*	*1,59E-04*	*7,23E-05*	*3,17E-05*	*1,33E-05*	*5,41E-06*	*2,11E-06*

Appendix C Uncertainty in site response analysis up to the model base

The following memo has been reviewed by J. Bommer and A. Rodriguez Marek.

To: **Julian Bommer and Adrian Rodriguez-Marek**

Copy: **Sjoerd de Wit, Jan Van Elk, Edith Van Dijk; NAM**

From: **Amalia Giannakou, Panagiotis Georgarakos and Jacob Chacko; Fugro**

Subject: Estimation of Amplification Factor from top of Bedrock to Base of 2D Finite Element Models of Eemshaven-Delfzijl Levee, Groningen, The Netherlands

---

Introduction and Background

Gas-extraction-induced earthquakes occur in the Groningen area. Consequently earthquake effects are to be considered in the levee reconstruction program for the Eemshaven-Delfzijl levee. In particular the presence of potentially liquefiable Holocene tidal deposits (i.e. the so-called "wadzand" deposits) underlying parts of the Eemshaven-Delfzijl levee have raised the issue of liquefaction-induced instability. Since the effect of liquefaction on structures and liquefaction-induced deformations cannot easily be assessed using simplified techniques, the dynamic stability of the levee at two locations was evaluated by Fugro using advanced numerical procedures. The 2D dynamic analyses were conducted using nonlinear, fully coupled, effective stress models (Fugro 2016). The 2D FE models extend from the top of levee to El. -30 m NAP at the Eemshaven area and to El. -20m NAP at the Delfzijl area (Figure 1). The results of the analyses were presented at the Liquefaction Expert Panel during the Workshop in Amsterdam (November 17th-18th 2016).

An effort is currently underway to:

- Characterize the uncertainties related to the input and output of the 2D FE dynamic analyses model (i.e. coupled, effective stress FEM)
- Perform FORM analysis using the 2D FE dynamic analyses model; and
- Make an informed decision about design values including length effects that contribute to the design return period.

For Step 1 above it is necessary to specify distributions for the different stochastic variables that affect the problem. The main stochastic variables associated with the seismic demand that is used as input in the 2D FE model include:

- the spectral acceleration at NSUB and
- the Amplification Factor from top of rock (NSUB) to the base of the 2D FE models (currently at El. -30 m and -20 m NAP).

Design spectra provided by KNMI were used to define the seismic demand at the top of NSUB for the design return period. For the estimation of the distribution of spectral acceleration values at top of NSUB, the seismic hazard curve for T=0.85sec at the top of NSUB is used. The seismic hazard curve is approximated with a logarithmic probability density function and this distribution is used in the FORM analyses.

In addition to the spectral acceleration at the top of bedrock (NSUB) the amplification of the ground motion from the top of bedrock to the base of the 2D FE models (i.e. NAP -30 m and -20 m) needs to also be considered. In the V2 Groningen report (Bommer et al 2015), only the Amplification Factor from top of rock to the ground surface is provided (Equations ES.15 and Es.16).

This project memorandum presents a methodology to derive estimates of amplification factor from top of rock (NSUB) to the base of the FE models (NAP -30 m and -20 m) following the procedure of Stewart et al (2014).

Proposed Approach

For the estimation of the amplification factor at the base of the 2D FE models we have followed the approach of Stewart et al (2014) for fitting ground response analysis results to a site amplification function.

1D equivalent linear site response analyses were performed at select locations along the levee to propagate the motion from the top of NSUB to the base of the 2D FE model. The deep shear wave velocity profiles provided by Professor Rodriguez-Marek in an email dated October 4th 2016 were used (Vs_profiles_levee_csv_mod_with corrected u0_20160902_GdL_ARM.xlsx).

Equivalent linear site response analyses were performed for different amplitudes of input motions. Results of the site response analyses were regressed using the following functional form:

$$\ln \overline{Y}(f) = f_1 + f_2 \ln\left(\frac{x_{IMref} + f_3}{f_3}\right)$$

and constraining f_3 to a value of 0.5, the same value used in Bommer et al (2015). Regression of the site response analyses results was performed to estimate f_1 and f_2 factors. For the estimation of f_1 (which represents weak-motion (linear) amplification) site response analyses were performed for an input PGA amplitude of 0.01g. The amplification factor at the base of the FE models was defined as the ratio of the outcrop motion at NAP -20 m (or -30m) to the outcrop motion at the top of NSUB.

Estimation of Amplification Factor from NSUB to Base of 2D FE Model

This section presents example results for the Delfzijl area using the approach described above. Site response analyses were performed at the Delfzijl side of the levee using 7 ground motions with 2 horizontal components matched to the normalized target spectrum at top of NSUB. Ground motions were scaled to PGA values of 0.01g, 0.1g, 0.16g, 0.2g, 0.3g 0.4g, and 0.5g to obtain amplification factors at multiple hazard levels. The estimated V_{s30} value below -20m NAP is 288 m/s. Figure 2 presents regression results of the amplification factor using $f_1 = 0.67$, $f_2 = -0.49$ and $f_3 = 0.5$.

Figure 2 presents the mean amplification factor between top of NSUB and El – 20 m. No site specific geotechnical data are available below NAP -20 m and the deep velocity profiles at the Delfzijl side (i.e. between NAP -20m to top of NSUB) are almost the same. Much of the site to site variability is thus expected to be related to the soils above NAP -20 meters. The minimum value of the standard deviation for site-to-site variability for amplification ratios between NSUB and the ground surface is constrained to 0.2 in Bommer et al (2015). When we compare the variation in amplification ratios between NSUB and the ground surface from 9 different profiles in the Delfzijl area, we estimate a standard deviation of 0.2, which is associated largely with variability above El. -20 meters. Therefore we propose to reduce the standard deviation for site-to-site variability in amplification ratios between top of NSUB and the base of the FE models to 0.1 (in natural log units).

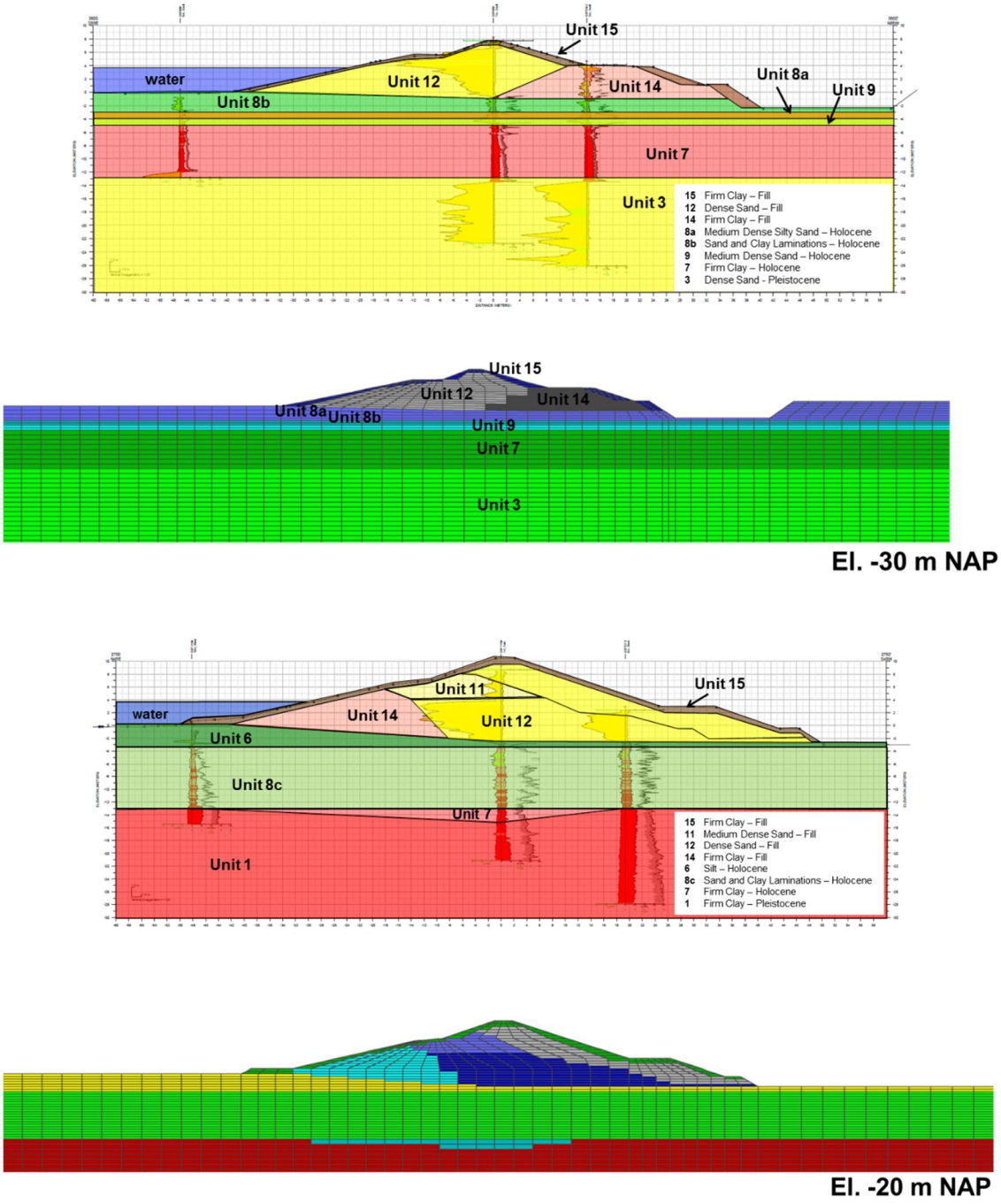

Figure 1. FE models at Eemshaven (upper illustration) and Delfzijl (lower illustration) side of the levee.

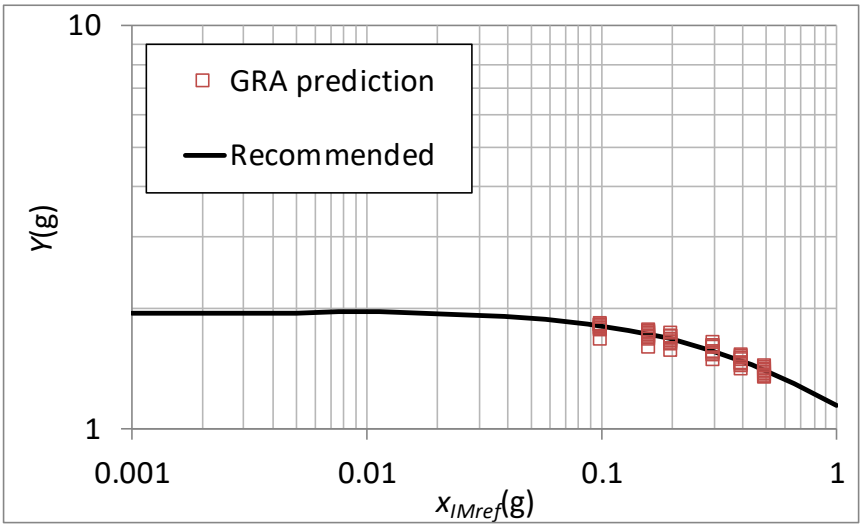

Figure 2. Mean amplification values for Sa (0.85 sec) from GRA and mean fit using equation above with f_3 fixed at 0.5.

The resulting equation for the mean amplification factor from top of NSUB to NAP-20 m is shown below:

$$\ln(AF) = 0.67 - 0.49\ln[(SaNU_B, g + 0.5)/0.5]$$

The proposed standard deviation of the amplification function is 0.1 (ln units).

References

Bommer, J.J., Dost B., Edwards B., Kruiver P.P., Meijers P., Ntinalexis M., Polidoro B., Rodriguez-Marek A. and Stafford P.J. (2015) "Development of Version 2 GMPEs for Response Spectral Accelerations and Significant Durations from Induced Earthquakes in the Groningen Field", Report Groningen Seismic Hazard and Risk Assessment Model.

Fugro (2016) "Evaluation of Dynamic Stability Eemshaven-Delfzijl Levee, the Netherlands", prepared for NAM, December 2016

Stewart J.P and Hashash, Y. M. A. (2014). "Guidelines for Performing Hazard-Consistent One-Dimensional Ground Response Analysis for Ground Motion Prediction," PEER Report 2014/16, October 2014.

Note: The coefficients for Eemshaven are f_1 = 0.37, f_2 = -0.32, f_3 = 0.5 and ϕ = 0.1.

Appendix D Cyclic Resistance of Laminated Deposits

The following memo has been prepared by Fugro on January 31st 2017 and has been revised on February 10th to address comments by Professor S. Kramer

INTRODUCTION AND BACKGROUND

Gas-extraction-induced earthquakes occur in the Groningen area. Consequently earthquake effects are to be considered in the levee reconstruction program for the Eemshaven-Delfzijl levee. In particular the presence of potentially liquefiable Holocene tidal deposits (i.e. the so-called "wadzand" deposits) underlying parts of the Eemshaven-Delfzijl levee have raised the issue of liquefaction-induced instability.

In order to estimate the liquefaction triggering resistance of these deposits empirical procedures based on measured CPT tip resistance were used (i.e. Boulanger and Idriss 2014) as well as a series of advanced cyclic laboratory tests on "undisturbed" samples (Fugro 2016a). As discussed in Fugro (2016b) although liquefaction triggering resistance from CPT measurements in uniform sand deposits compared reasonably well with cyclic laboratory test results on "undisturbed" samples from uniform sands (differences in results were mainly attributed to effects of sample disturbance resulting to loosening of samples tested in the lab), liquefaction triggering resistance from CPT measurements in laminated deposits appear to underestimate the triggering resistance of these deposits when compared to results from cyclic laboratory tests on laminated "undisturbed" samples. This is most likely due to the significant influence of the clay layers on the CPT tip resistance measured within the thin "sandwiched" sand layers whose thickness is less than 10 to 20 cm in thickness.

Laminated deposits are mostly present between km 27.2 to 28.5 (Section L) and around km 29.5 (Section K) at the Delfzijl side as well as around km 36.0 (Section D) at the Eemhaven side.

In order evaluate the cyclic resistance of laminated deposits the following were considered:

1. CDSS and CTX test results on laminated deposits. Five (5) CDSS and seven (7) CTX cyclic tests were performed on laminated "undisturbed" samples obtained with Piston and Begemann samplers (Fugro 2016a). Additionally, three (3) CDSS and seven (7) CTX were performed on laminated "undisturbed" samples (without static bias) obtained with the Gel Push sampler. The results of these additional tests have been interpreted and are plotted together with the interpreted lab results presented in Fugro 2016b.
2. Numerical simulations of cyclic response of laminated samples performed to evaluate the conversion factor between Cyclic Simple Shear and Cyclic Triaxial tests on laminated samples
3. Numerical simulations of the response of laminated samples under cyclic simple shear loading conditions to develop liquefaction triggering curves for samples with different percentages of clay laminations

This project memorandum presents interpreted laboratory test results on laminated samples and results of numerical evaluations of the cyclic behavior of laminated soils and provides recommendations for the cyclic resistance of laminated deposits.

EVALUATION OF LIQUEFACTION TRIGGERING FROM CYCLIC LABORATORY TESTS

A series of stress controlled Cyclic Direct Simple Shear (CDSS) and Cyclic Triaxial (CTX) tests was performed on "undisturbed" samples (i.e. obtained with Piston and Begemann samplers) from "wadzand" deposits (Fugro 2016a).

Five (5) CDSS tests were performed on samples that included clay laminations and seven (7) CTX tests were performed on laminated/stratified coarse- and fine-grained materials. Interpretations of these test results in the form of liquefaction triggering curves were presented in Fugro (2016b).

Fugro performed an additional site investigation campaign in October 2016 using the Gel Push sampler to collect high quality "undisturbed" samples from the tidal deposits at the same locations where Piston and Begemann samples were collected. Xrays and MSCL scanning was performed on select Gel Push Tubes. Review of Xray and MSCL results indicated less disturbance (i.e. higher quality samples) effects on Gel Push samples compared to Piston and Begemann samples.

Additional cyclic tests were performed on select Gel Push samples. Three (3) CDSS tests and seven (7) CTX tests were performed on laminated Gel Push samples. In addition, six (6) CDSS tests were performed on uniform sand samples. These additional cyclic test results on Gel Push samples together with Xray and MSCL scans of the Gel Push Tubes will be included in an Addendum to the Factual Report, currently under preparation.

A summary of the tests performed on uniform and laminated tidal deposits without bias is presented in Table 1. The reported void ratios on Table 1 are the initial void ratios of the overall sample consisting of either sand only (Unit 8a) or sand/clay laminations (Units 8b and 8c).

Table 1. Summary of Cyclic Tests on Laminated and Uniform Samples (no bias)

Unit	**Initial void ratio, e_0**	**Description**	**CPT classification zone - I_c**	**Tests**
8a	~ 0.62 – 0.76	mainly sand (non-laminated, not seen in Delfzijl)	CPT classification zone 6 (Robertson) I_c < ~2.05	CSS03 (B), CSS05 (B), CSS15R (P), CSS08 (GP), CSS22R (GP), CSS23(GP), CSS27(GP), CSS28(GP), CSS25(GP)
8b	~ 0.79 – 0.92 (lower end of the void ratio range for laminated deposits, primarily from Eemshaven boreholes)	laminated, with higher percentages of sands	CPT classification zone 5 (Robertson) ~2.05< I_c <~2.6	CSS13 (P), CSS17(P), CSS18 (P), CSS19 (GP), CSS20 (GP), CSS21 (GP) CTX06 (P), CTX07 (P), CTX08 (GP), CTX12 (GP)
8c	~ 0.99 – 1.25 (higher end of the void ratio range for laminated deposits, from Delfzijl boreholes)	laminated, with lower percentages of sands and higher percentages of clay	CPT classification zones 5 and 4 (Robertson) 5 : ~2.05< I_c <~2.6 4 : 2.6< I_c <2.95 (screened out in simplified method)	CTX01 (P), CTX02 (P), CTX03R (P), CTX17(GP), CTX10 (GP), CTX14 (GP), CTX16 (GP), CTX15 (GP)

Unit	Initial void ratio, e_0	Description	CPT classification zone - I_c	Tests
9a	~ 0.63 – 0.75	Grey or dark grey fine sand	CPT classification zone 6 (Robertson) I_c < ~2.05	CCS01 (P), CCS07R (P), CCS11 (P)
9b, 9c	~ 0.95, 1.18	Grey or dark grey fine sand with thin laminae of dark clay and silt.	CPT classification zones 5 and 4 (Robertson) 5 : ~2.05< I_c <~2.6 4 : 2.6< I_c <2.95	CTX04 (P), CTX05 (P)

Figure 1 presents the Cyclic Stress Ratio (CSR) as a function of the number of cycles to liquefaction from the CDSS and CTX tests performed on Piston, Begemann and Gel Push samples from tidal deposits without static bias. For the CDSS tests without bias, liquefaction was considered to have triggered at 3.0 percent Single Amplitude shear strain. For the CTX tests without bias liquefaction was considered to have triggered at 1.5-2 percent Single Amplitude axial strain. We note that the CSRs of the CTX tests on laminated samples plotted on Figure 1 have been multiplied by a factor of 0.8 to convert to equivalent cyclic simple shear loading conditions based on results of numerical simulations as discussed in the following section.

As discussed in Fugro (2016b) due to the variable nature of the inter-tidal deposits, it is near impossible to identify identical samples with the same void ratio (relative density or percentage clay layers) for cyclic testing at multiple cyclic stress ratios. Therefore, it was not possible to characterize laminated samples in terms of relative density since the direct measurement of minimum/maximum density is not possible on each variable sample. In order to provide a basis for identifying similar samples and to develop reasonable cyclic resistance versus number of cycles relationships, the initial sample void ratio was used as an indicator and is plotted next to each test on Figure 1. These void ratio values provide an indication of absence of thin fine-grained layers within the sample (corresponding to void ratios less than about 0.76, Unit 8a, from uniform samples collected from Eemshaven boreholes) or presence of thin fine grained layers within the sample (void ratios of about 0.85, Unit 8b, from laminated samples primarily collected from Eemshaven boreholes and void ratios higher than 1 from laminated samples primarily collected from Delfzijl boreholes). As shown on this figure the samples tested all have different void ratios.

On Figure 1 liquefaction triggering curves are shown for:

- Relatively Uniform sand, Unit 8a (solid black line) present at Eemshaven explorations (i.e km 38.5, 38.0, 37.5 and 37.2). This unit is practically absent from Delfzijl explorations (i.e. it could only be identified in about 2% of the total CPT penetration length performed at Delfzijl side). The dashed black line is the interpreted liquefaction triggering curve for Unit 8a in Fugro 2016b that was also used in the effective stress dynamic levee stability evaluations (Fugro, 2016c).
- Laminated sand and clay deposits with higher percentages of sands, Unit 8b, (solid blue line) present primarily at Eemshaven explorations and to a lesser degree at Delfzijl explorations (i.e. only 2 of the 12 laminated samples tested from Delfzijl explorations had initial void ratios less than 1). The dashed blue line is the interpreted liquefaction triggering curve for Unit 8b in Fugro 2016b that was also used in the effective stress dynamic levee stability evaluations (Fugro, 2016c).
- Laminated sand and clay deposits with lower percentages of sands, Unit 8c, (solid purple line) present at Delfzijl explorations (i.e. only 10 of the 12 samples tested from Delfzijl explorations had initial void ratios larger than 1)

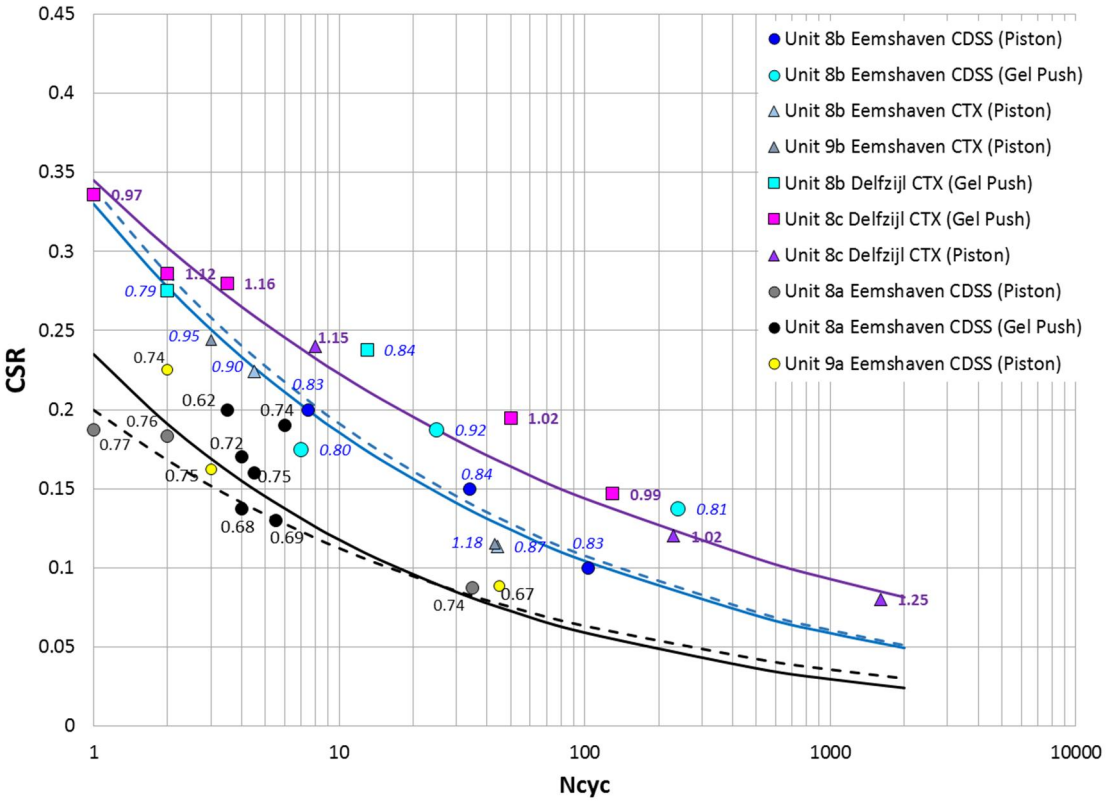

Figure 1. Liquefaction Triggering Resistance of Uniform (Unit 8a, Unit 9a) and Laminated Samples (Unit 8b, Unit 8c, Unit 9b) from Tidal Deposits (no static bias). The initial void ratio (before application of consolidation stress) is plotted next to each test.

NUMERICAL SIMULATIONS OF CYCLIC RESPONSE OF LAMINATED DEPOSITS

Evaluation of Conversion Factor from Cyclic Triaxial to Cyclic Simple Shear Loading

Two types of cyclic testing were used to assess the liquefaction triggering of the tidal deposits: i) CTX and ii) CDSS tests. Although CDSS tests provide more representative loading conditions, the small specimen height (i.e. 3 cm) in combination with the nature of the laminated deposits (i.e. clay lamination thicknesses on the order of 1-2 cm) necessitated the testing of taller specimens for the laminated samples. Therefore CTX tests were performed for most of the laminated samples although a number of CDSS tests were also performed on specimens with clay laminations.

In order to correlate the two cyclic testing types, Seed and Peacock (1971) recommended a conversion factor applied on the CSR_{TX} (i.e. cyclic stress ratio from triaxial testing) ranging from 0.6 to 0.7 for normally consolidated specimens based on data for clean sands. The recommended conversion factor depended on the value of the coefficient of earth pressure at rest, Ko.

For fine-grained samples, Donahue et al (2007) reported that:

- when studying the liquefaction susceptibility of a normally consolidated fine-grained soil deposit after the 1989 Loma Prieta earthquake, Boulanger et al. (1998) used a conversion factor of 0.7
- Sancio (2003) found a conversion factor of 0.85 when testing shallow, fine-grained soils from Adapazari with a PI < 12, at a mean effective stress of 100 kPa.

Donahue et al (2007) used a conversion factor of 0.84 based on results from CDSS and CTX tests on fine-grained samples reconstituted with the Slurry Deposition Method and tested at an effective confining pressure of 50 kPa.

In order to evaluate the conversion factor between CTX and CDSS tests on laminated deposits, numerical simulations were performed with the finite difference code FLAC2D (Itasca 2016).

As a first step, numerical simulations were performed to estimate the conversion factor between CTX and CDSS tests on a uniform sand sample (i.e. Unit 8a). PM4Sand constitutive model was used to model the cyclic behavior of a uniform sand sample under cyclic direct simple shear loading conditions. The model was calibrated to the liquefaction triggering curve for Unit 8a (black line) shown on Figure 1 (Fugro, 2016c).

Having simulated the CDSS test results on a uniform sand sample, numerical simulations of a uniform sand sample under cyclic plane strain compression loading conditions (Ko=1) were performed to approximate the CTX test. Figure 2 presents liquefaction triggering results from numerical simulations of a uniform sand sample under cyclic direct simple shear and plane strain compression (CPSC) loading conditions for different CSR. The resulting conversion factors range between 0.64 and 0.72 for a uniform sand sample which are in agreement with the range proposed by Seed and Peacock (1971) for uniform sands.

As a second step, numerical simulations were performed to estimate the conversion factor between CTX and CDSS tests on a laminated sample. First numerical simulations of test CTX07 (i.e. CSR=0.28, initial void ratio e0=0.9) on a laminated sample were performed. Figure 3 shows a photo of Sample CTX07, the X-ray section and the detailed 2D numerical model. The clay laminations were identified in the sample using the X-ray section, leading to the idealized numerical grid shown in the same Figure 3. The calibrated parameters for PM4Sand were used for the sand layers within the sample while the clay layers were modeled with a Mohr-Coulomb model. The deformed shape of the numerical model is compared with the cyclic triaxial sample on Figure 4, showing somewhat similar characteristics. Also, shown on Figure 5 is the development of cyclic strains versus cycles of loading. Both experiment and simulation suggest triggering (1.5% axial strain) at about 4 to 4.5 cycles. The cyclic responses are also compared in terms of stress-strain plots, and as stress paths. Again similar trends are noted in both experiment and simulation despite the idealization of the clay laminations and the differences in loading conditions (plane-strain versus triaxial).

Having simulated the cyclic behavior of a laminated sample under cyclic triaxial conditions reasonably, numerical simulations of the same laminated sample under cyclic simple shear conditions were performed. Figure 6 presents liquefaction triggering results from numerical simulations of a laminated sample under cyclic direct simple shear and plane strain compression loading conditions for different CSR. The resulting conversion factors range between 0.78 and 0.83 for a laminated sample which are higher than the conversion factors of uniform sand deposits, but in line with experimental findings on fine-grained samples discussed above.

Based on the above a conversion factor of 0.8 was applied on the CSRTX for the laminated samples.

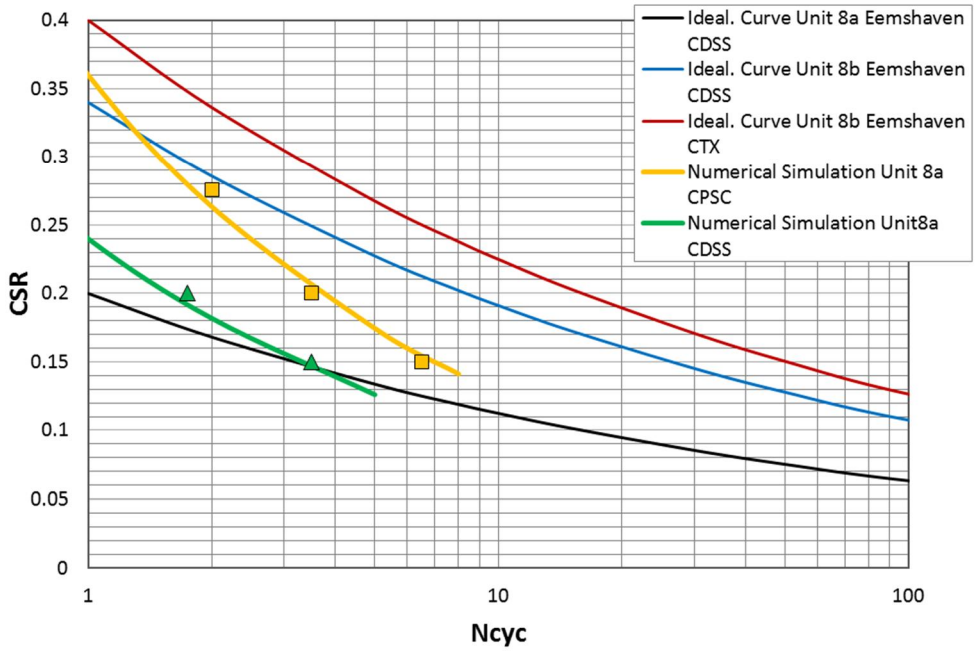

Figure 2. Liquefaction triggering curves obtained from numerical simulations of CDSS and CPSC loading conditions on uniform sand (Unit 8a).

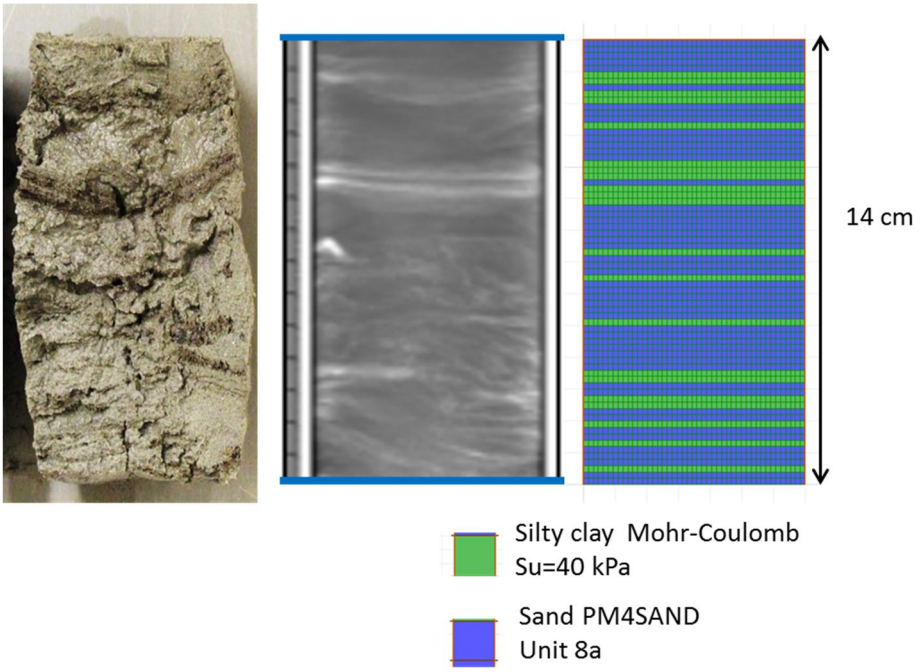

Figure 3. Photo, X-ray section and numerical model of laminated sample CTX07.

Figure 4. Photo (left) and deformed grid (right) of laminate sample CTX07 at the end of cyclic loading.

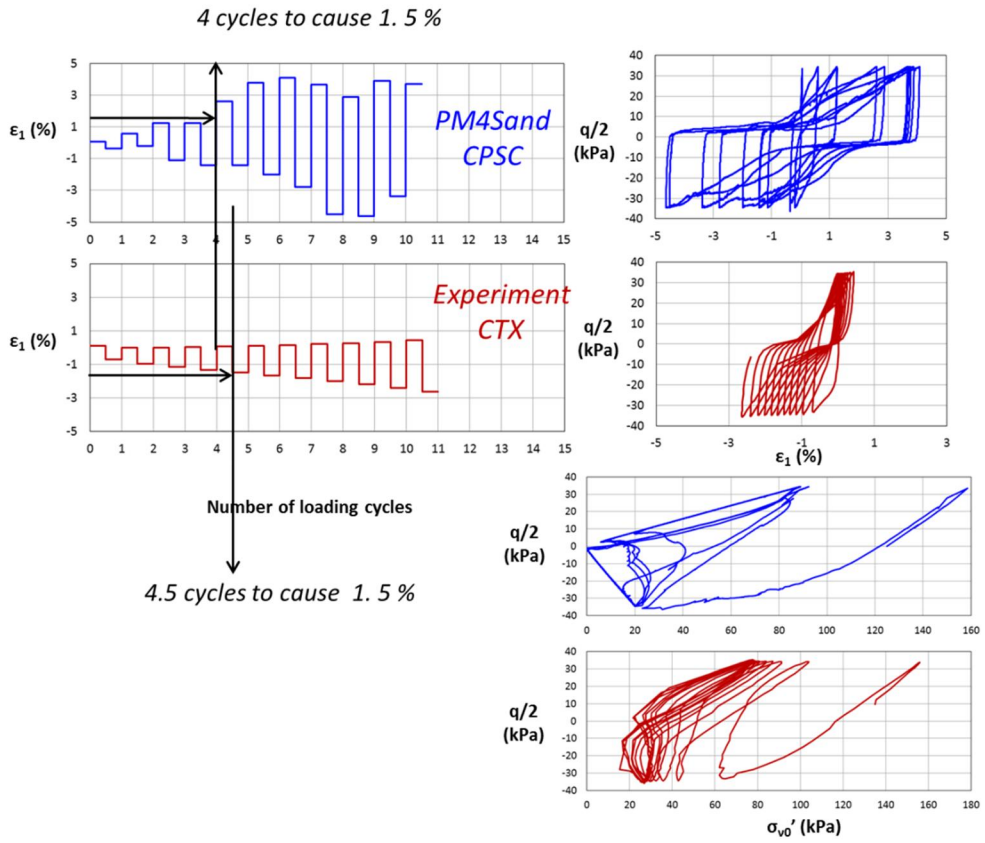

Figure 5. Comparison between numerical and experimental results for laminated sample CTX07.

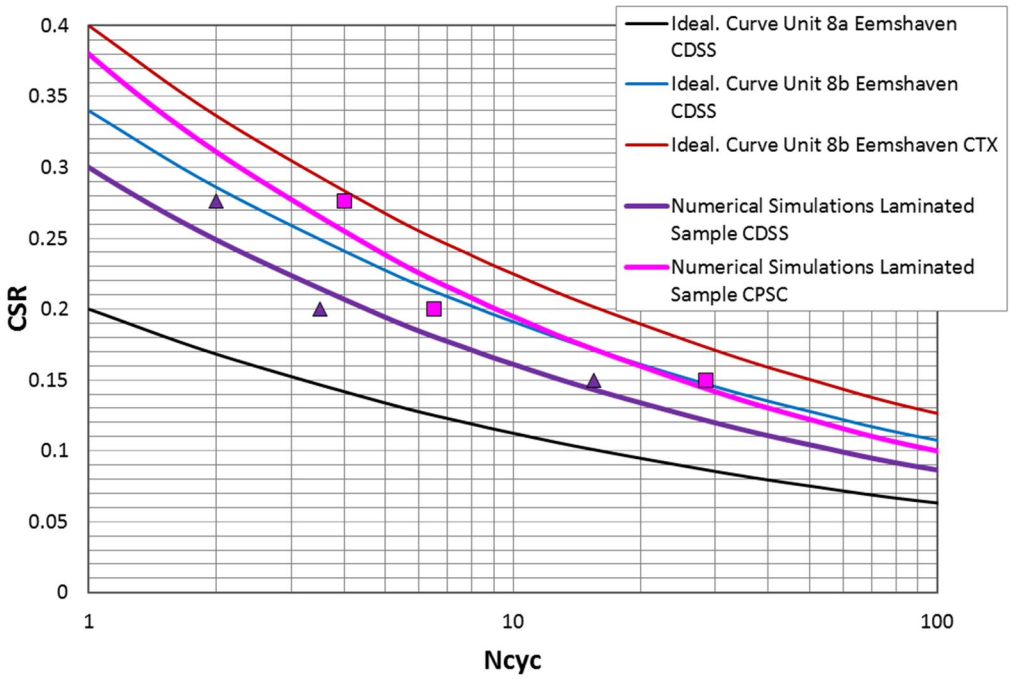

Figure 6. Liquefaction triggering curves obtained from numerical simulations of CDSS and CPSC loading conditions on laminated sample (shown on Figure 3).

Evaluation of Liquefaction Triggering

Numerical simulations of laminated samples under cyclic direct simple shear loading conditions were performed in order to develop estimates of liquefaction triggering resistance for different percentages of clay laminations within the sample.

First numerical simulations of test CDSS18 (i.e. CSR=0.2, initial void ratio e0=0.83) on a laminated sample were performed. Figure 7 shows a photograph of Sample CDSS18. Two clay sub-layers/laminations are identified in the sample. The calibrated parameters for PM4Sand and UBCSAND for Unit 8a were used for the sand layers within the sample while the clay layers were modeled with a Mohr-Coulomb model. Figure 8 presents a comparison between the laboratory test and numerical simulation test results. The percentage of clay laminations (CPL) within this sample was estimated to be on the order of 40% (defined as the total thickness of clay laminations within the sample divided by the sample height). Using the same configuration (CPL=40%), the numerical model was subjected to CSR=0.15 in an attempt to reproduce the test CDSS17 (e0=0.84). The comparison between numerical and experimental results for CDSS17 is shown on Figure 9.

Having simulated reasonably the CDSS test results on a laminated sample, parametric numerical simulations of CDSS tests on laminated samples with different percentages of clay laminations and different distributions of clay laminations within the sample were performed in order to evaluate the liquefaction triggering resistance of laminated sample. Simulations were performed at different CSR values. Analyses were performed using both PM4Sand and UBCSAND models (calibrated to Unit 8a triggering curves) to simulate the sand layer behavior.

Figure 10 presents results of numerical simulations of CDSS tests on laminated samples with clay lamination percentages (CLP) ranging from 10% to 60% (grey lines) plotted together with interpreted lab results shown on Figure 1. Different distributions of clay laminations within the sample were assumed in the numerical simulations of of CDSS tests (example schematizations shown on Figure 11a).

The numerical results shown on this figure are from analyses using UBCSand to model the sand layer behavior. As shown on Figure 10:

- numerical simulations of CDSS tests on laminated samples with CLP of 40% (i.e. higher sand percentage within the sample) produce results close to the liquefaction triggering curve from lab results for Unit 8b (blue line)
- numerical simulations of CDSS tests on laminated samples with CLP of 60% (i.e. lower percentages of sands and higher percentages of clay) produce results close to the liquefaction triggering curve from lab results for Unit 8c (purple line)
- results of numerical simulations show that even the presence of a small amount of clay laminations in the sample (i.e. CLP 10%) results in an increase of cyclic resistance compared to the uniform sand sample

It is also noted that results of parametric numerical analyses of different distributions of clay and sand layers within a sample for a given CLP (Figure 11a) indicate that the distribution of the clay layers within the sample does not significantly change the triggering resistance.

Figure 11b presents a comparison of the liquefaction triggering curves derived from numerical simulations of CDSS tests on laminated samples using PM4Sand and UBCSand to model the sand layers. As shown on Figure 11, the two models predict a similar trend.

The black line on Figures 11a and 11b correspond to the triggering resistance of a sand layer without clay laminations.

We note that as discussed in Fugro (2016c) numerical analyses results indicate that void redistribution effects, tend to be reduced as the thickness of sand layers decreases, or as the percentage of clay interlayers increases.

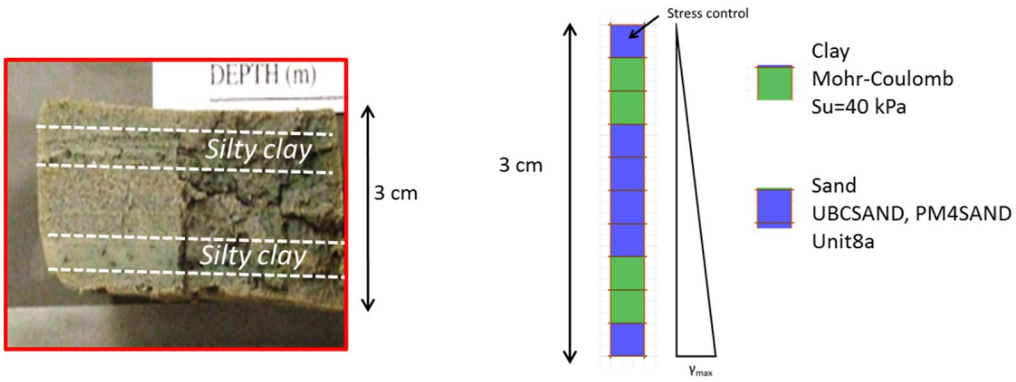

Figure 7. Photo and numerical model of laminated sample CDSS18.

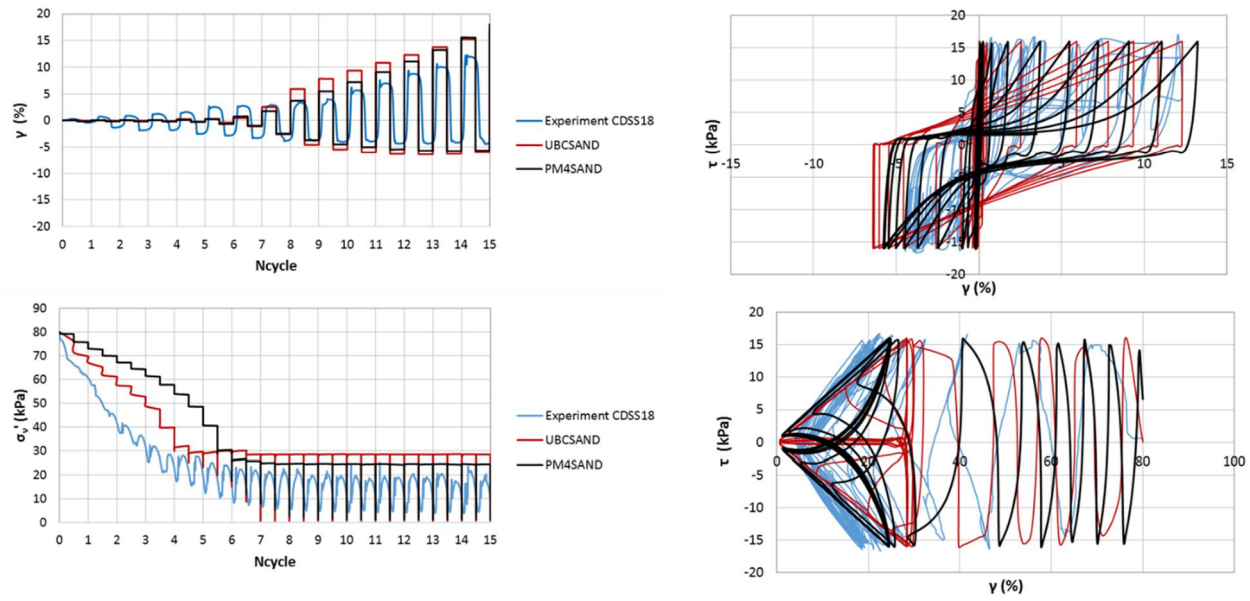

Figure 8. Comparison between numerical and experimental results for laminated sample CDSS18.

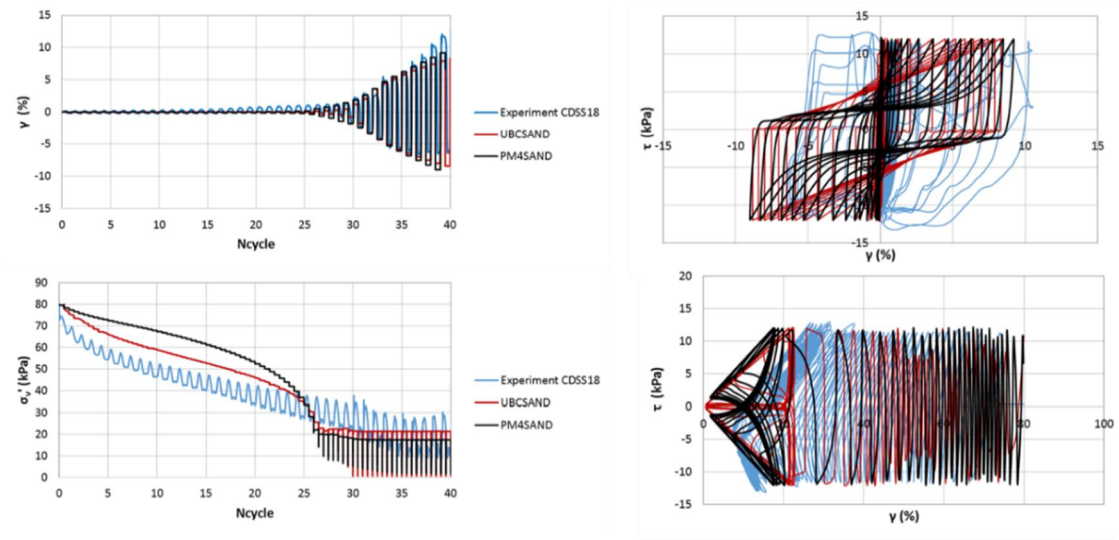

Figure 9. Comparison between numerical and experimental results for laminated sample CDSS17.

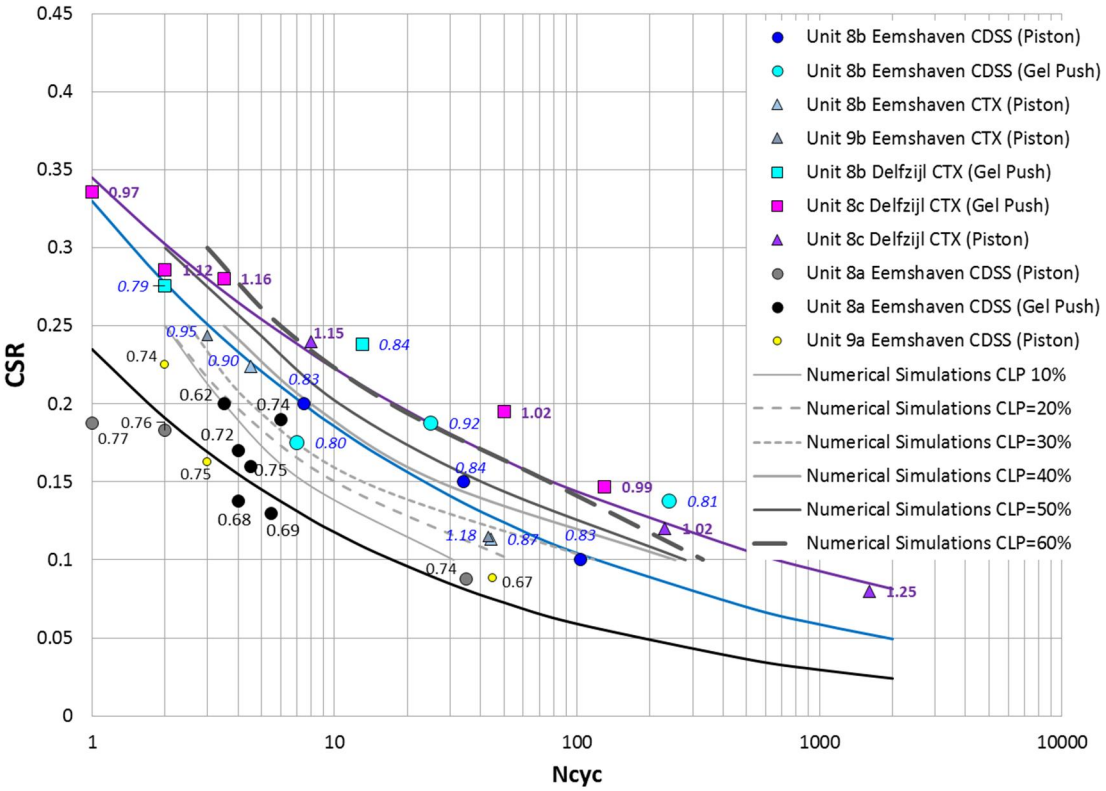

Figure 10. Liquefaction Triggering Resistance Curves from Numerical Simulations of CDSS tests on Laminated Samples with different clay lamination percentages.

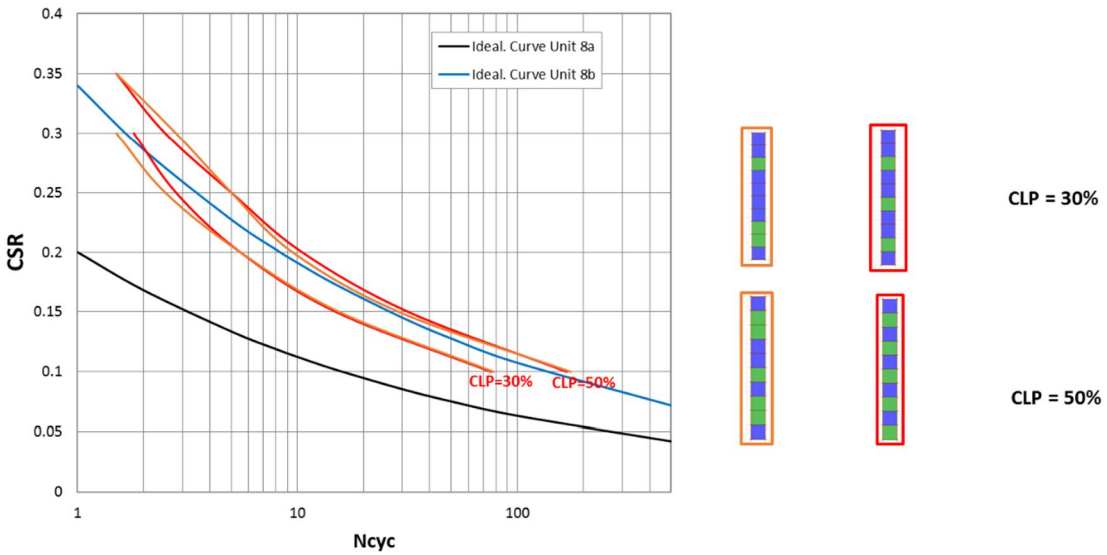

Figure 11a. Numerical simulation results for CLP 30% and 50% assuming different distributions of clay laminations within the sample.

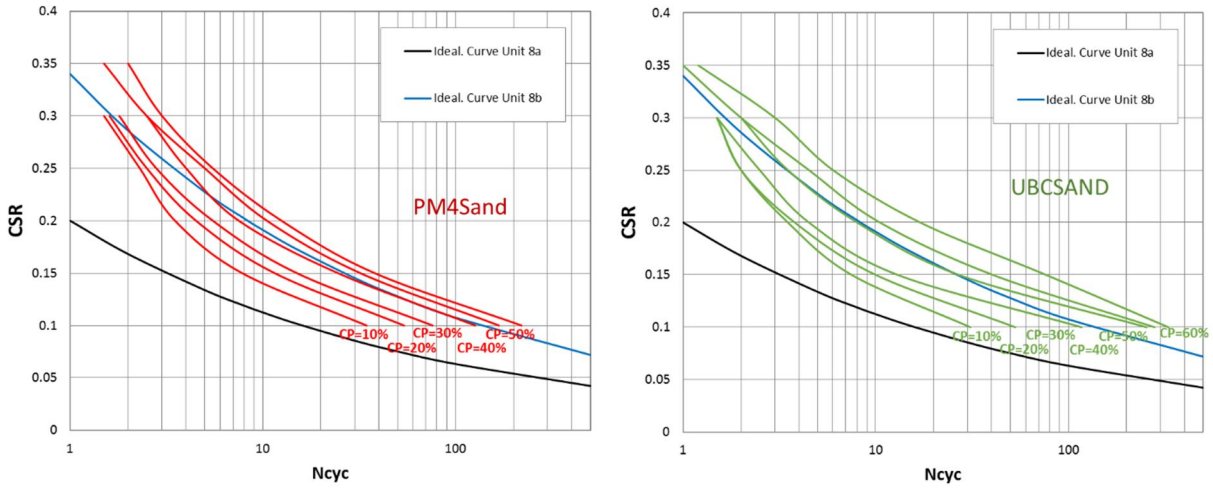

Figure 11b. Liquefaction Triggering Resistance Curves obtained from Numerical Simulations of CDSS tests on Laminated Samples with different clay lamination percentages (left: PM4Sand and right: UBCSAND).

PROPOSED CRR DISTRIBUTION FOR LAMINATED DEPOSITS

Interpreted laboratory test results and numerical simulations were used to develop a proposed distribution of the cyclic resistance (CRR) of laminated deposits at the Delfzijl side of the levee for locations were Unit 8 is present for use in FORM analyses. For these evaluations the number of cycles corresponding to a magnitude M 5 earthquake (i.e. N=4) was estimated using the MSF of Boulanger and Idriss (2014).

As discussed previously the cyclic test results were evaluated considering separate groups of materials including: Unit 8b – Laminated materials with a higher percentage of sands ($0.79 < e_o < 0.92$) and Unit 8c – Laminated materials with a lower percentage of sands ($0.99 < e_o < 1.25$). These laboratory test data were regressed to develop distributions of cyclic resistance for each group of samples. Figure 12 shows the regressions for Unit 8b samples including the mean and 90% confidence interval, while Figure 13 shows the regression for Unit 8c samples.

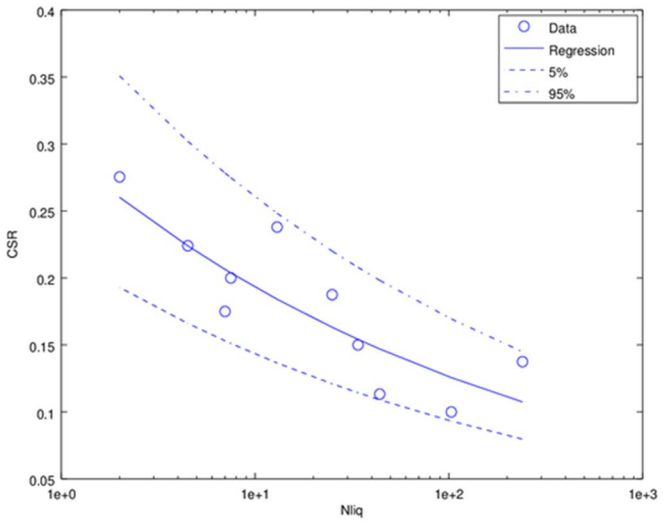

Figure 12. CRR for Unit 8b samples.

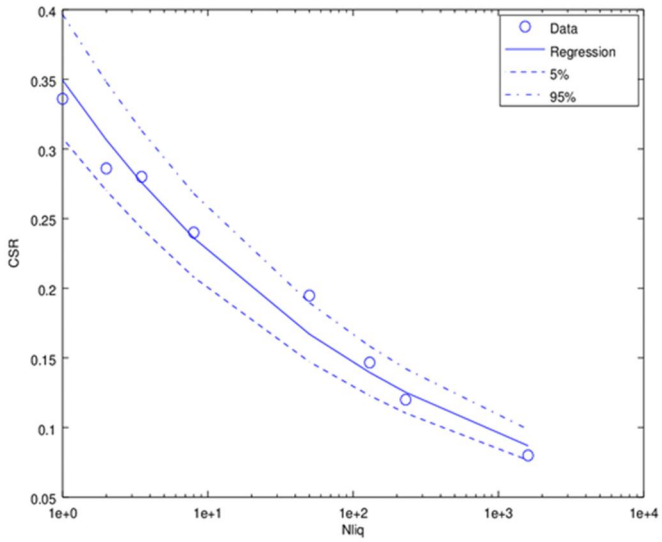

Figure 13. CRR for Unit 8c samples.

The CPT classification data also provide an indicator of the relevant content of sand within the laminated deposits. Qualitative assessments of the available CPT data suggest that in Delfzijl the laminated deposits are composed of about 50% of Unit 8b type material and 50% Unit 8c type material.

For these evaluations the number of cycles corresponding to a magnitude M 5 earthquake (i.e. N=4) was estimated using the MSF of Boulanger and Idriss (2014). Probability density functions corresponding to the cyclic resistance at 4 cycles were calculated for the Unit 8b and Unit 8c materials above and a combined distribution developed assuming equal weights to each of the two distributions. These probability density functions are shown on Figure 14.

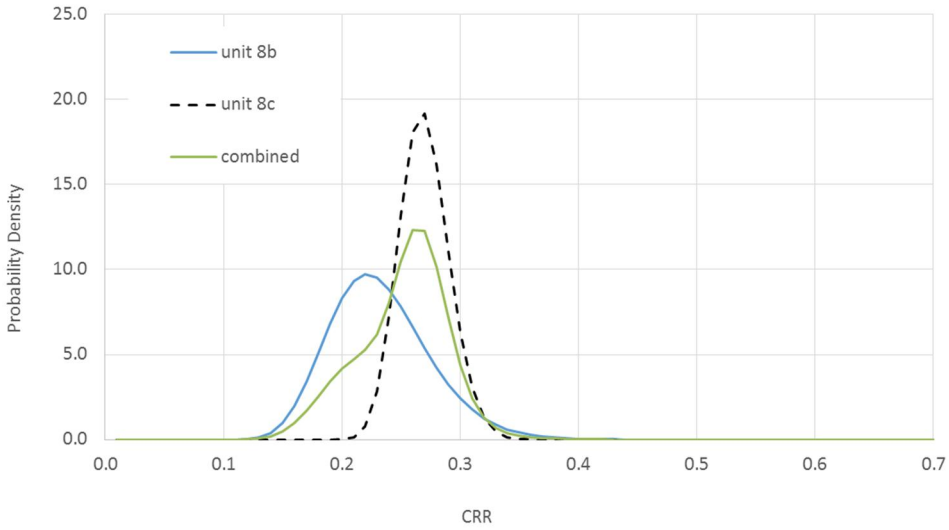

Figure 14. Probability Density Function for Unit 8b, 8c and combined.

The cumulative probability density of the combined distribution is shown relative to the lognormal fit of the distribution on Figure 15.

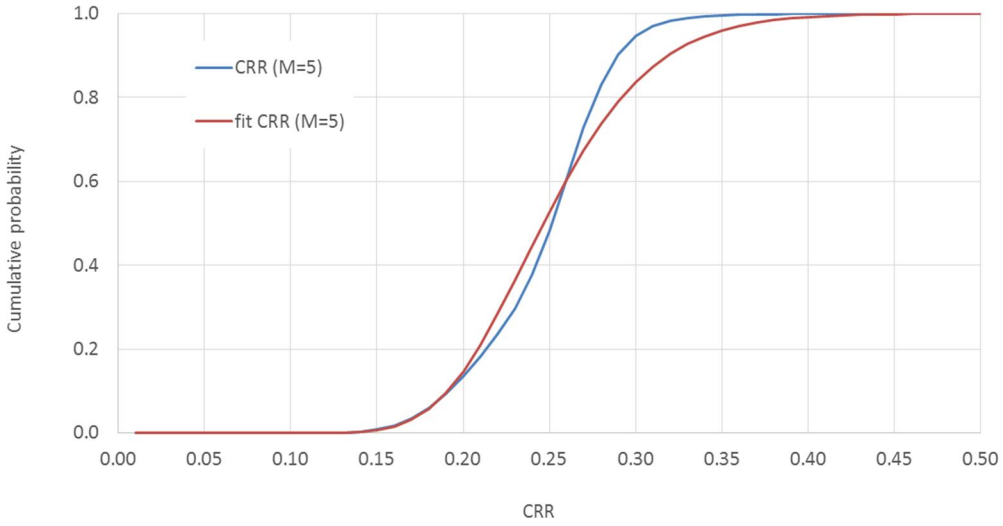

Figure 15. CRR for M=5, Delfzijl. Lognormal with μ= -1.4 and σ = 0.2.

The CRR distribution for the laminated materials is compared with the typical curves calculated from laboratory tests and numerical modeling on Figure 16. The following observations are made.

- Non-laminated sand layers (i.e. Robertson Zone 6) appear to be present in no more than 2% of the CPT data collected in Delfzijl. Estimated CRR for the laminated materials is interpreted to be mostly above the liquefaction triggering results of non-laminated sand layers (i.e. Unit 8a, black curve on Figure 16).
- A ~60% cumulative probability is assigned to liquefaction triggering results from laminated samples with initial void ratios larger than 1 as shown on Figure 16 (CLP 60%). These samples with lower percentages of sands and higher percentages of clay are considered representative of the Delfzijl conditions.
- The triggering curve used for laminated samples with initial void ratios of about 0.8 (i.e. Unt 8b in Fugro's numerical evaluations, blue curve on Figure 13) is derived primarily from CSS tests on samples from Eemshaven borehole 38.0 where a larger percentage of sand is present within the laminated deposits (CLP=40% based on numerical simulation results) compared to Delfzijl explorations based on both CPT data and borehole sample descriptions. Theses resistances are interpreted to have a 36% quantile value.
- A 10% cumulative probability corresponds to the triggering curve derived from numerical simulation results of CDSS tests on laminated samples with CLP 10% (grey curve on Figure 13) since even a small percentage of clay laminations leads to an increase of liquefaction triggering resistance as was shown from numerical simulation results. This percentage of clay laminations is considered to be low for the conditions encountered at Delfzijl explorations.
- An approximately 85% cumulative probability is assigned to the resistance level based on numerical simulations of CDSS tests on laminated samples with CLP=70%.

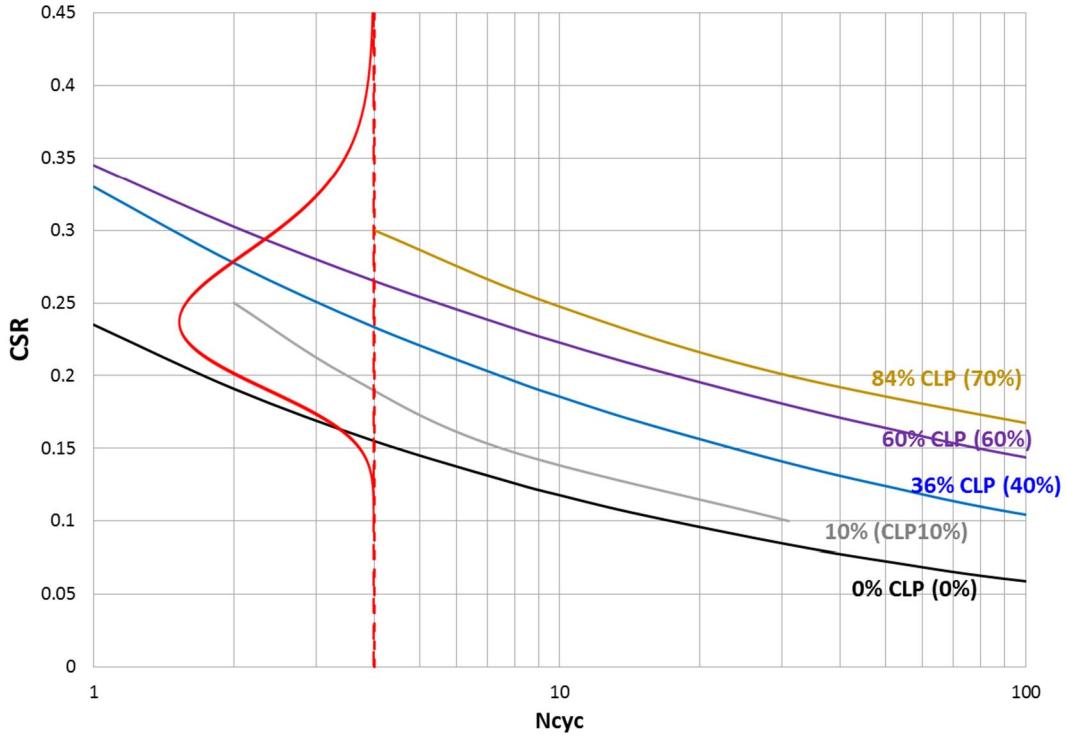

Figure 16. Quantile Values for the typical CRR curves.

REFERENCES

Boulanger R. W., Meyers M. W., Mejia L. H. & Idriss I. M. (1998) “Behavior of a fine-grained soil during the Loma Prieta earthquake,” Canadian Geotechnical Journal, Vol. 35, pp. 146-158.

Donahue J. L., Bray J. D., and Riemer M. F. (2007) The Liquefaction Susceptibility, Resistance, and Response of Silty and Clayey Soils, U.S.G.S. Award Number: 05HQGR0009, November

Fugro (2016a) Site investigation and Cyclic Laboratory Testing, Factual data report, Delfzijl / Eemshaven Levee Project in Groningen, the Netherlands, prepared for Nederlandse Aardolie Maatschappij B.V., November

Fugro (2016b) Interpretive report, Delfzijl / Eemshaven Levee Project in Groningen, the Netherlands, prepared for Nederlandse Aardolie Maatschappij B.V., November

Fugro (2016c) Evaluation of Dynamic Stability Eemshaven-Delfzijl Levee, the Netherlands, prepared for NAM, December 2016

Sancio, R. B., Bray, J. D., Riemer, M. F. and Durgunoglu, T. (2003) "An assessment of the liquefaction susceptibility of Adapazari silt," 2003 Pacific Conference on Earthquake Engineering, Christchurch, New Zealand.

Seed, H. B. and Peacock, W. H. (1971) “Test procedures for measuring soil liquefaction characteristics,” Journal of Soil Mechanics and Foundations Division, ASCE, Vol. 97, No 8, pp. 1099-1119.

Appendix E Residual strength

Documented cases have shown that post-earthquake stability may be critical even if stability is ensured during shaking (e.g. Lower San Fernando dam case history).

Sand Layers. As mentioned in Fugro (2016a) post earthquake stability analyses were performed by assigning residual strength (i.e. defined as the ratio of residual undrained shear strength and in situ initial vertical effective stress, S_r/σ_{vc}') as a function of q_{c1Ncs} as proposed by Idriss and Boulanger (2008) for areas where the maximum excess pore pressure during shaking exceeded a specified threshold indicative of liquefaction. Fugro (2016a) considered that void redistribution effects could be significant and used the lower of the two curves plotted in Figure 28.

Since both the Cyclic Resistance Ratio (i.e. CRR) to liquefaction triggering and residual strength are a function of q_{c1Ncs}, this means that in general when CRR increases then the residual strength ratio S_r/σ_{vc}' should also increase and vice versa.

Laminated deposits within Unit 8. As discussed in Fugro (2016a) the presence of clay interlayers does create permeability contrasts that theoretically would allow for the development of void redistribution. However, given the limited thickness of the individual sand layers, the volume of water that could migrate upwards is limited. Moreover, Unit 8 is typically characterized by an overall low hydraulic conductivity, likely due to the limited lateral continuity and thickness of the sand sub-layers. In the absence of the ability for water inflow, the potential for suppression of dilation will be limited, and shear resistance will likely increase as shear strains exceed 5 to 15 percent. Additionally, due to the relatively low percentage of sand sublayers within the unit and the limited thickness of the sand sublayers, even the occurrence of relatively large shear strains (10 or 20%) within the layers will likely not result in large horizontal deformations prior to the development of dilation-induced shear resistance. Parametric numerical evaluations performed in Fugro (2016a) also point to the mitigating effect of thin layers in laminated deposits on the potential for void redistribution.

Despite the above we have conservatively used the residual strength defined above for sand layers also for the laminated soils. Since the CRR for the laminated soils is defined from laboratory test data, the residual strength for the laminated soils was estimated through a back-calculated q_{c1Ncs}. The value was backcalculated from the CRR value used for the laminated deposits in the FE analyses using the Boulanger and Idriss (2014) relationship.

A clear definition of the uncertainty in residual strength estimates is not available. For the purpose of these evaluations we have assumed that the uncertainty increases as the CRR (or q_{c1Ncs}) increases based on the fact that the recommended relationship by Idriss and Boulanger (2008) is extrapolated for larger q_{c1Ncs} values (i.e. dashed black lines in Figure 28 below). We have used a lognormal distribution to model the uncertainty on CRR with $\mu=0$ and $\sigma=0.15$. Figure 28 shows the resulting 95% confidence interval of residual strength ratios using the uncertainty term described above. The uncertainty is intended to cover both the range of data used to develop the empirical relationship as well as factors such as possible effects of mixing during large deformations etc.

An alternative probability distribution for residual strength based on Kramer and Wang (2015) was also considered in the FORM analyses. The Kramer and Wang (2015) probability distribution for residual strength is based an empirical model consistent with steady-state concepts and behavior observed in laboratory tests and also calibrated on the basis of residual strengths back-calculated from flow-side case histories. The Kramer and Wang (2015) model predicts residual strengths as a function of normalized SPT blowcounts (N_{160}) and as a function of overburden stress. A comparison of the residual strength distributions considered in the FORM analyses is shown on Figure 28. Boulanger and Idriss (2008) relationship between N_{160} and q_{c1Ncs} was used to plot the residual strength proposed by Kramer and Wang (2015) as a function of normalized tip resistance. The residual strength curves plotted on Figure 28 from Kramer and Wang (2015) were derived for 1.5 atm overburden stress.

In order to account for the uncertainty on the conversion between N_{160} and q_{c1Ncs} the standard deviation considered in Kramer and Wang (2015) was increased from 0.37 (green curves) to 0.45 (red curves).

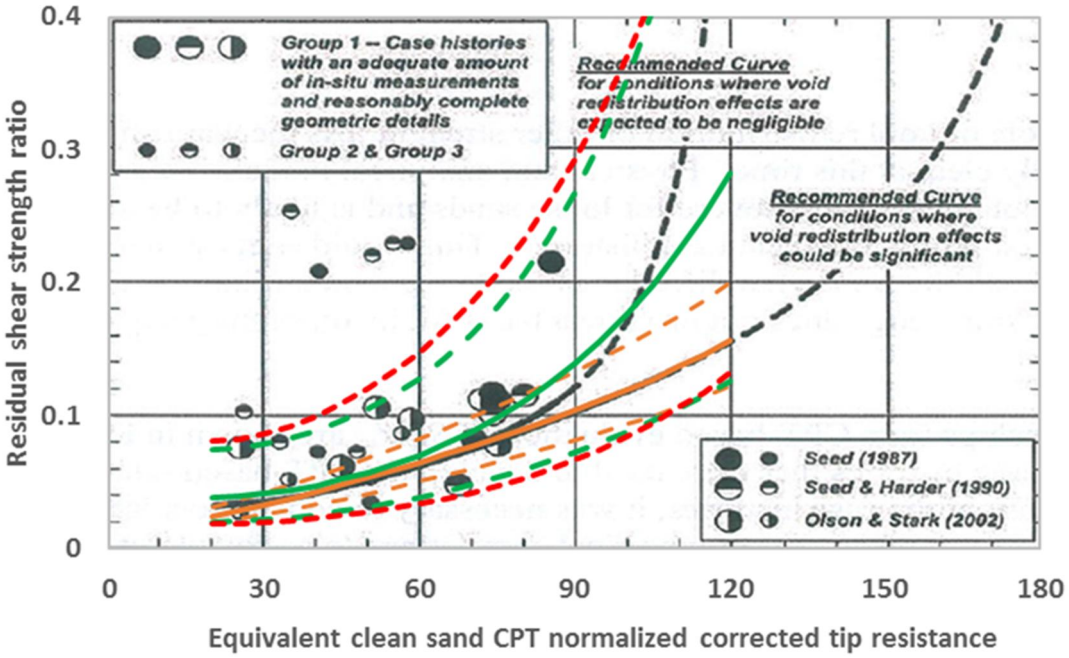

Figure 28. Uncertainty related to residual strength (95%-confidence interval) based on Kramer and Wang (2015) using the standard deviation proposed by the authors (green dashed curves) and an increased standard deviation of 0.45 (red dashed curves) to account for uncertainty in the conversion from $(N1)_{60}$ to q_{c1Ncs} , and Idriss and Boulanger (2008) assuming void redistribution and engineering judgment for the estimation of standard deviation (orange curves).

Appendix F Model uncertainty

Two dimensional, effective-stress, dynamic analyses were performed using the finite difference code FLAC (Itasca 2011). Two different constitutive models were used to model the effective stress behavior of coarse-grained layers to account for epistemic uncertainty: UBCSand, developed by Professor Peter Byrne and his team at the University of British Columbia; and PM4Sand developed by Professor Ross Boulanger and Dr Katerina Ziotopoulou at UC Davis. Both constitutive models were calibrated against site-specific cyclic laboratory tests in order to capture soil triggering and strain accumulation behavior for both level (no-bias) and sloping ground (with static-bias) conditions. The reasonable comparison between observed and simulated behavior suggests that the calibrated constitutive models can be tailored to adequately simulate cyclic soil behavior at the element level both in terms of liquefaction triggering and in terms of post-liquefaction shear strain accumulation (Fugro 2016a).

In order to validate the constitutive models used for the liquefiable sands (i.e. determine the degree to which a model is an accurate representation of the real world from the perspective of the intended uses of the model) and evaluate the predictability of the implemented constitutive model at a system level, numerical simulations of real-scale boundary-value problems, such as case histories and centrifuge experiments, were performed and numerical results were compared with recorded measurements in the field and in the centrifuge, respectively. The case studies (case histories or centrifuge tests) used for validation involved liquefaction induced displacements of slopes and embankments founded on liquefiable layers in order to validate the ability of the two models to predict liquefaction induced deformations (Fugro 2016a).

Several "deterministic" sensitivity analyses have been carried out with two different constitutive models. Differences between computed crest settlements with PM4sand and UBCsand were found to be smaller than a factor 1.3 for all motions considered, for a given stratigraphy and return period Figure 29. Differences of about a factor 1.1-1.2 were found for 10 different stratigraphies (for a given motion and return period) and for 2 different return periods (for a given motion and 2 different stratigraphies), see Figure 30 and Figure 31.

As indicated in the expert panel report from December 3rd 2016 (Expert Panel 2016), with well-calibrated and validated constitutive models embedded in reliable numerical tools, dynamic effective stress analyses using multiple input motions can provide an indication of the range of expected levels of performance. They also allow evaluation of the sensitivity of response to various input parameters and modeling assumptions. It is important, however, to recognize potential uncertainties in constitutive models and numerical analyses. For critical projects, parallel analyses would ideally be performed using different constitutive models and different numerical tools. As described above, in Fugro (2016a) the computer code FLAC was used with two different calibrated and validated constitutive models to simulate the behavior of liquefiable sands. Ideally these analyses should be supplemented by parallel check analyses using a different computational tool (e.g., OpenSees with PDMY model or FLIP with cocktail glass model). Due to time constraints additional analyses with a different computational software have not been performed. To account for this we have introduced a model uncertainty term in the limit state function.

Considering the results of the "deterministic" sensitivity analyses, a model uncertainty distribution with $\mu_{ln(m)}=0$ $\sigma_{ln(m)}=0.42$ would seem reasonable. However, considering the fact that sensitivity analyses have only been carried out with different constitutive models, but not with different software packages, a wider distribution has been assumed. We have assumed that the crest settlements estimated in Fugro (2016a) correspond to the mean value of observed settlements and that there is a 10% probability of exceedance of the predicted crest settlements by a factor of 2. The resulting model uncertainty function is a lognormal distribution with $\mu_{ln(m)}=0$ and $\sigma_{ln(m)}=0.55$ (Figure 32).

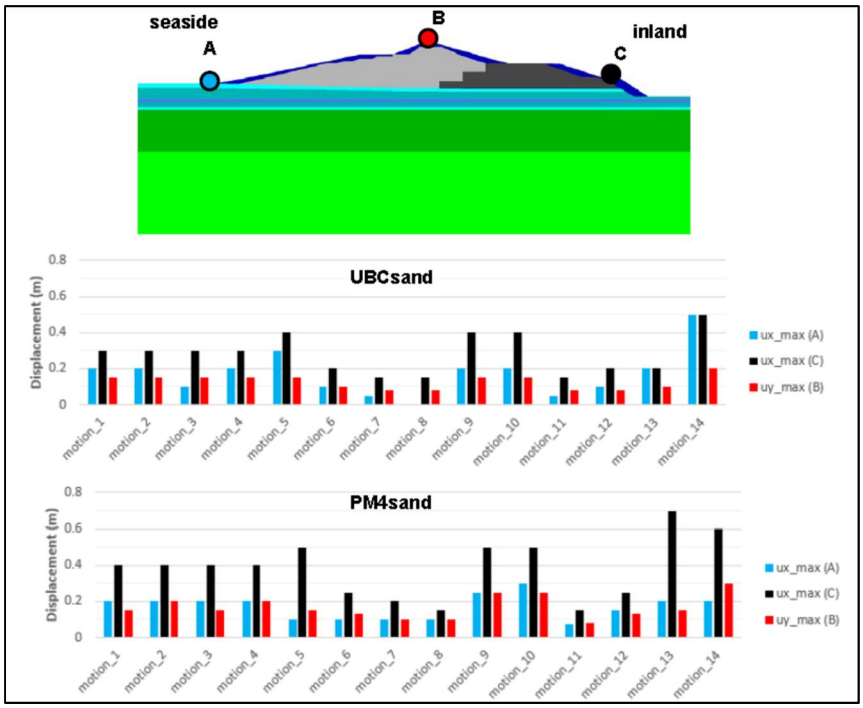

Figure 29. Calculated displacements with UBCsand and PM4sand for 14 different motions (Fugro 2016a: Figure 6-29b, page 42).

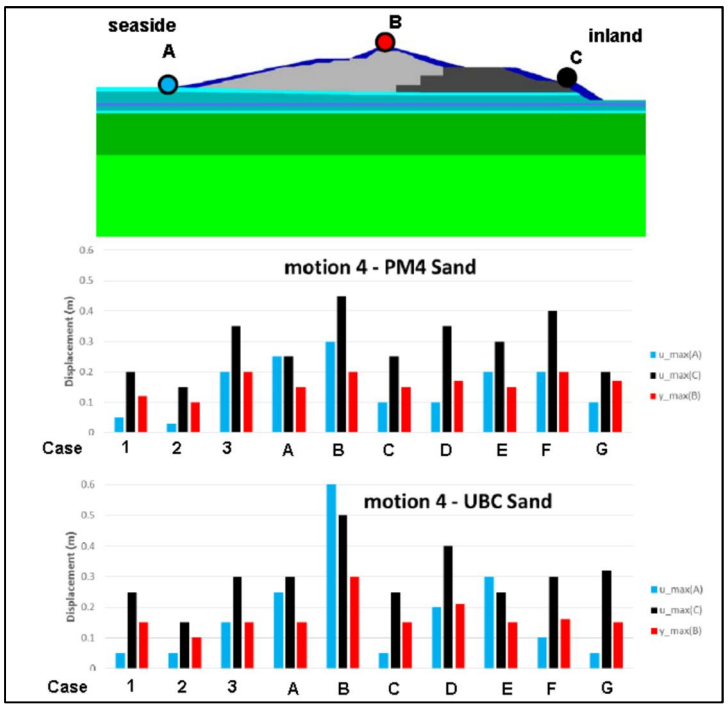

Figure 30. Calculated displacements with UBCsand and PM4sand for 10 different stratigraphies (Fugro 2016a: Figure 6-31b, page 45).

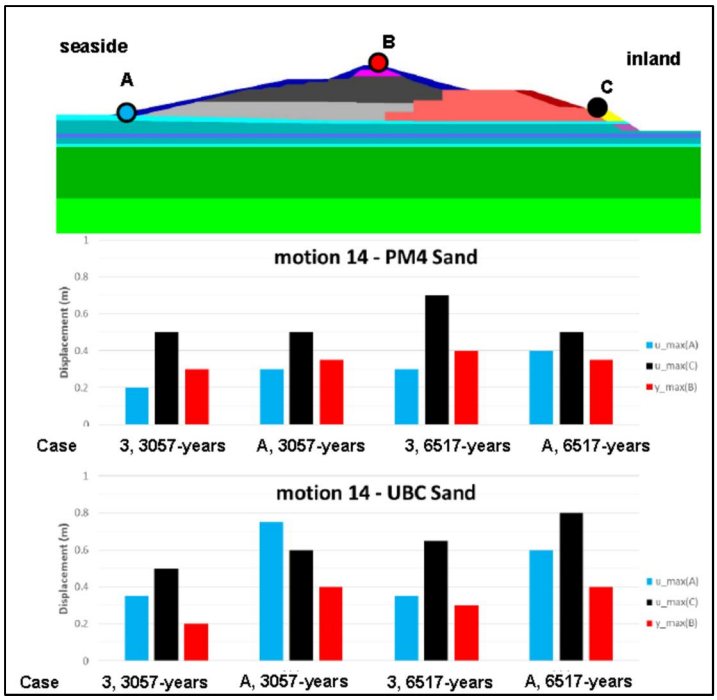

Figure 31. Calculated displacements with UBCsand and PM4sand for 2 different return periods, for 2 different stratigraphies (Fugro 2016a: Figure 6-32b, page 47).

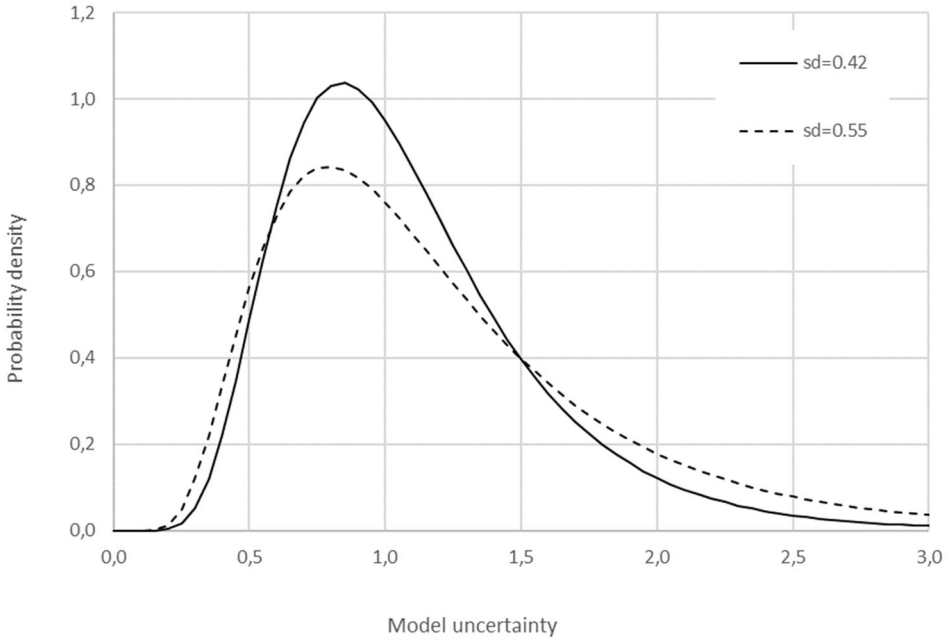

Figure 32. Model uncertainty: lognormal distributions for distribution parameters $\mu_{ln(X)}=0$ and $\sigma_{ln(X)}=0.42$, and $\mu_{ln(X)}=0$ and $\sigma_{ln(X)}=0.55$.

Appendix G Volume effects

Introduction

A laminated deposit consists of a series of alternating sand and clay layers. The resistance of the deposit to liquefaction depends on the composite behavior of these layers. Each lab test gives the resistance to liquefaction of a relatively small volume of laminated material.

Similarly, uniform sand deposits encountered at Eemshaven are characterized by a probability distribution of cyclic resistance based on q_{c1Ncs} values measured in uniform sands at Eemshaven (i.e. Unit 8a, see Fugro 2016c).

It is possible to fit numerous samples into the volume of Unit 8 that plays in a role in a seismic stability analysis. Layers of laminated material as well as sands without clay laminations of variable relative densities are treated as uniform in stability analyses (spatial variability within layers is not modelled explicitly). It is therefore important to specify the distribution that describes the uncertainty related to the composite behavior of such a larger volume of liquefiable material.

The uncertain resistance of such a larger volume (or the resistance of an "equivalent uniform layer") is denoted by CRR in this Appendix. The uncertain resistance of a small volume (sample size) is denoted by $\underline{CRR}$. The difference between the distributions of CRR and $\underline{CRR}$ is caused by the effects ("volume effects") of spatial variability.

Spatial variability could turn out to be favorable, when local weakness are compensated by strengths elsewhere. It could, however, also turn out to be unfavorable, when local weaknesses dominate composite behavior:

1. In case of (only) a "weakest link/series system"-effect, the standard deviation of CRR will be smaller than the standard deviation of $\underline{CRR}$. The mean value of CRR will also be smaller than the mean value of $\underline{CRR}$.
2. In case of (only) spatial averaging, the standard deviation of CRR will be smaller than the standard deviation of $\underline{CRR}$, while the expected values of both variables will be the same (their median values could be different).
3. In case of (only) a "strongest link/parallel system"-effect, the standard deviation of CRR will be smaller than the standard deviation of $\underline{CRR}$ but the mean value of CRR will be greater.

In normal slope stability analyses, some degree of spatial averaging of resistance properties over the slip plane is typically assumed (VanMarcke 1977; Calle & Barends 1990).

An approximate way of modelling the two types of spatial variability described above would be to model a layer as a composite of n x m x p smaller volumes with random/uncertain resistances, denoted by $\underline{CRR}_{i,j,k}$, with i=1..n and j=1..m and k=1..p. This is shown schematically in Figure below. Each element in Figure has a resistance that can be described by the same distribution, but that can be different for each element. Note that it seems reasonable to assume that correlation distances are much smaller in a vertical direction than in the horizontal plane.

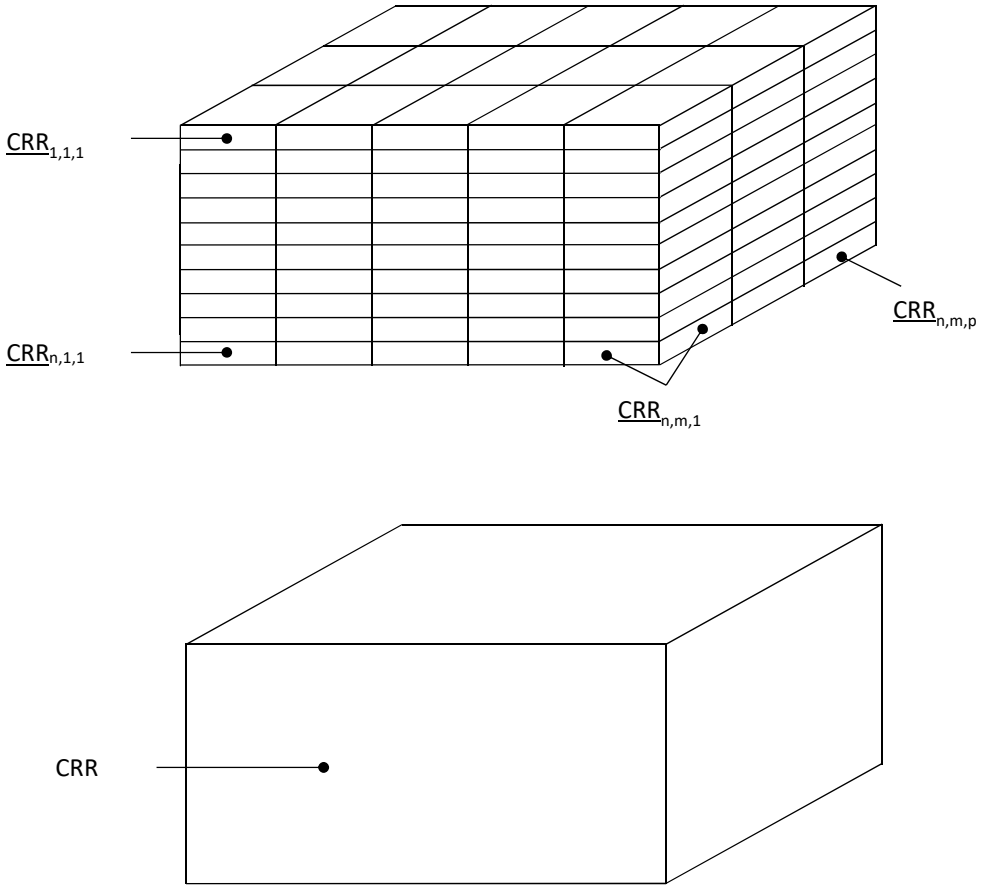

Figure 33. Illustration of a heterogeneous model and an equivalent uniform model.

The heterogeneous model shown in Figure 33 Figure merely serves an illustrative purpose. It would be too time-consuming to use it for deriving a distribution for CRR. Doing so could also easily yield a false sense of accuracy, since such an analysis would involve modelling assumptions that would themselves be highly uncertain (e.g. assumptions concerning the correlation structure).

Sensitivity analyses

It is possible to get insight into volume effects from simplified numerical simulations. This can be done by comparing the computed crest settlements for a cross-section with uniform properties across a sand layer and a similar cross-section in which the layer has spatially variable properties. The following analyses have been performed (Figure 34):

1. An analysis in which the CRR varies in both a horizontal and vertical direction with 2 random assignments of CRR-values.
2. An analysis in which the CRR within a layer only varies along the vertical (horizontal continuity).

It is stressed that these cases are highly schematic: they do not accurately reflect reality. The spatial variations have not been constructed with a random fields model, as done by Montgomery & Boulanger (Montgomery 2015; Boulanger & Montgomery 2015; Boulanger & Montgomery 2016). Rather, 5%, 50% and 95% quantile values from the CRR-distribution have been assigned randomly within the liquefiable layer.

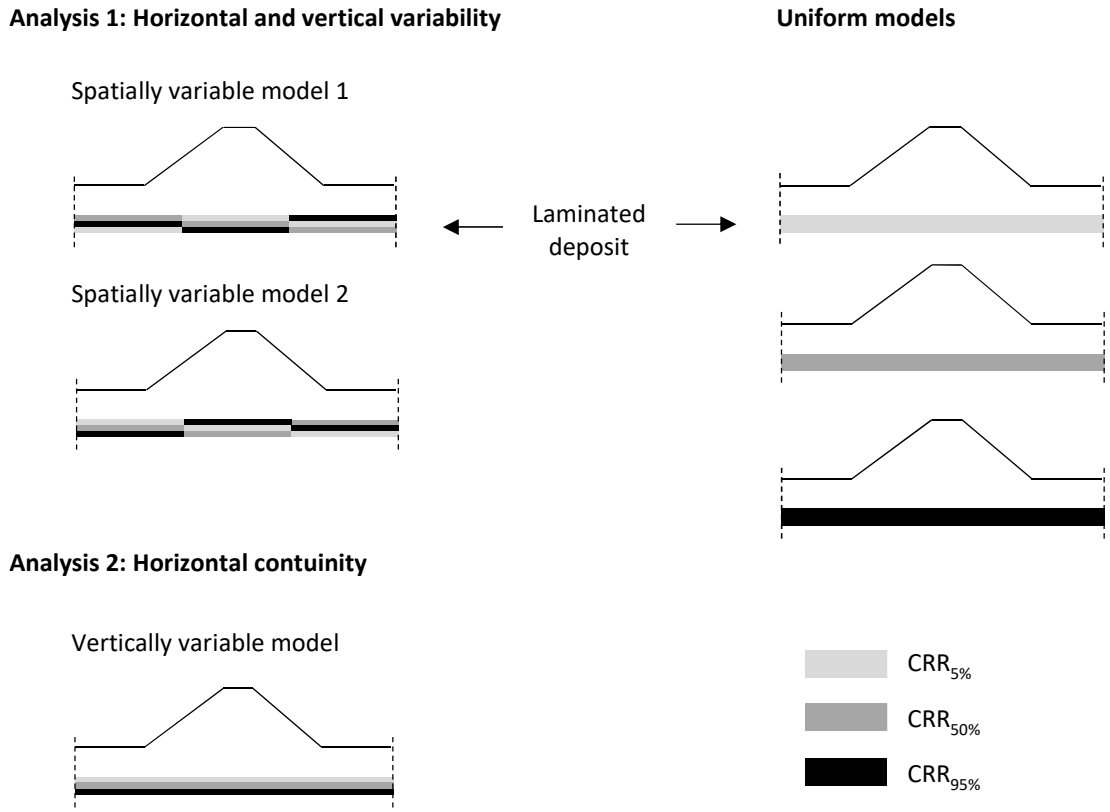

Figure 34. Sensitivity studies to get a feel for the effect of spatial variability within interlayered deposits.

Note that the effect of variability in the third dimension (perpendicular to this sheet of paper) cannot be dealt with in a 2D-model. It seems reasonable, however, to assume that variability in the third dimension reinforces the behavior observed in the 2D-senstivity analysis.

Numerical models simulating the idealized schematizations shown in Figure 34 were developed for the evaluation of volume effects. Analyses were performed with the finite difference code FLAC. The UBCSand constitutive model was used to simulate the sand behavior. The model parameters were calibrated to cyclic resistances corresponding to 5% (pink line, Figure 35), 50% (blue line, Figure 35) and 95% (cyan line, Figure 35) of the CRR-distribution for uniform sands encountered at Eemshaven since this distribution results in lower (less favorable) cyclic resistance values compared to the distribution used for laminated deposits.

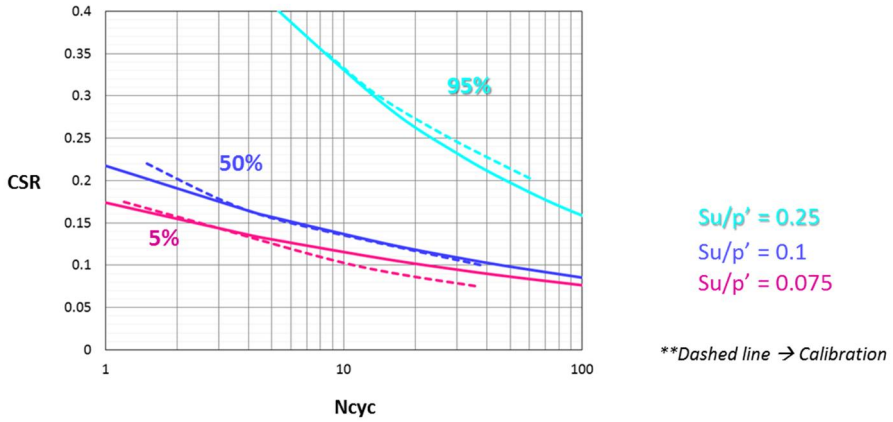

Figure 35. Calibrated constitutive model to different 5%, 50% and 95% percentiles of CRR for Eemshaven.

Analysis 1: Horizontal and vertical variability

The numerical models for the spatially variable case and the uniform case for Unit 8 are shown on Figure 36. Results of numerical evaluations of volume effects are shown in Figure 37 in the form of co-seismic and post-seismic crest settlements for the following cases:

- Model with spatial variability 1 in Unit 8 (upper-left illustration Figure 26)
- Model with spatial variability 2 in Unit 8 (mid-left illustration Figure 26)
- Uniform Unit 8 modeled with the 5% quantile value of CRR
- Uniform Unit 8 modeled with the 50% quantile value of CRR
- Uniform Unit 8 modeled with the 95% quantile value of CRR

As shown in Figure 37, the spatially variable Unit 8 properties result in decreased crest settlements compared to the cases where Unit 8 properties are uniformly modeled using 5% and 50% quantile CRR values. It is worth noting that the both models with spatial variability 1 and 2 give similar results.

Analysis 2: Horizontal continuity / Vertical Variability

The numerical model for the vertically variable case (where horizontal continuity is maintained) is shown in Figure 36 (bottom). As shown in the graph of Figure 37, the vertical variability in the properties of Unit 8 leads to crest settlements similar to the case where Unit 8 properties are uniformly modeled using 50% quantile CRR values.

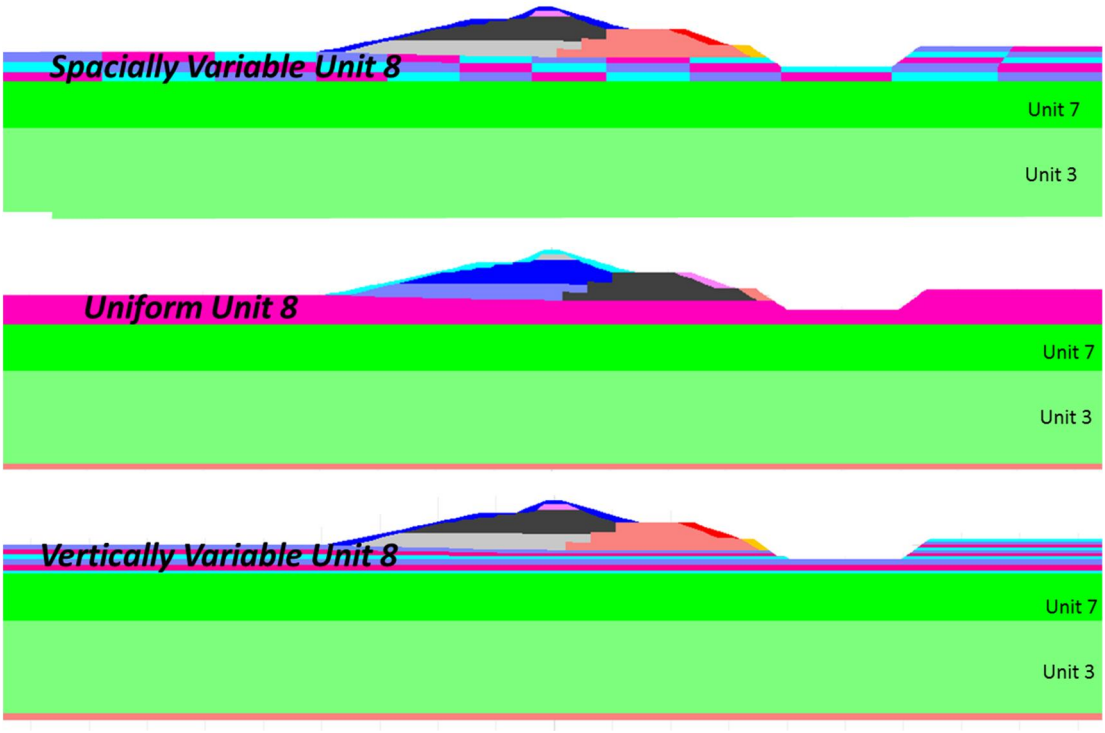

Figure 36. Numerical Models for Assessment of Spatial Variability of Unit 8.

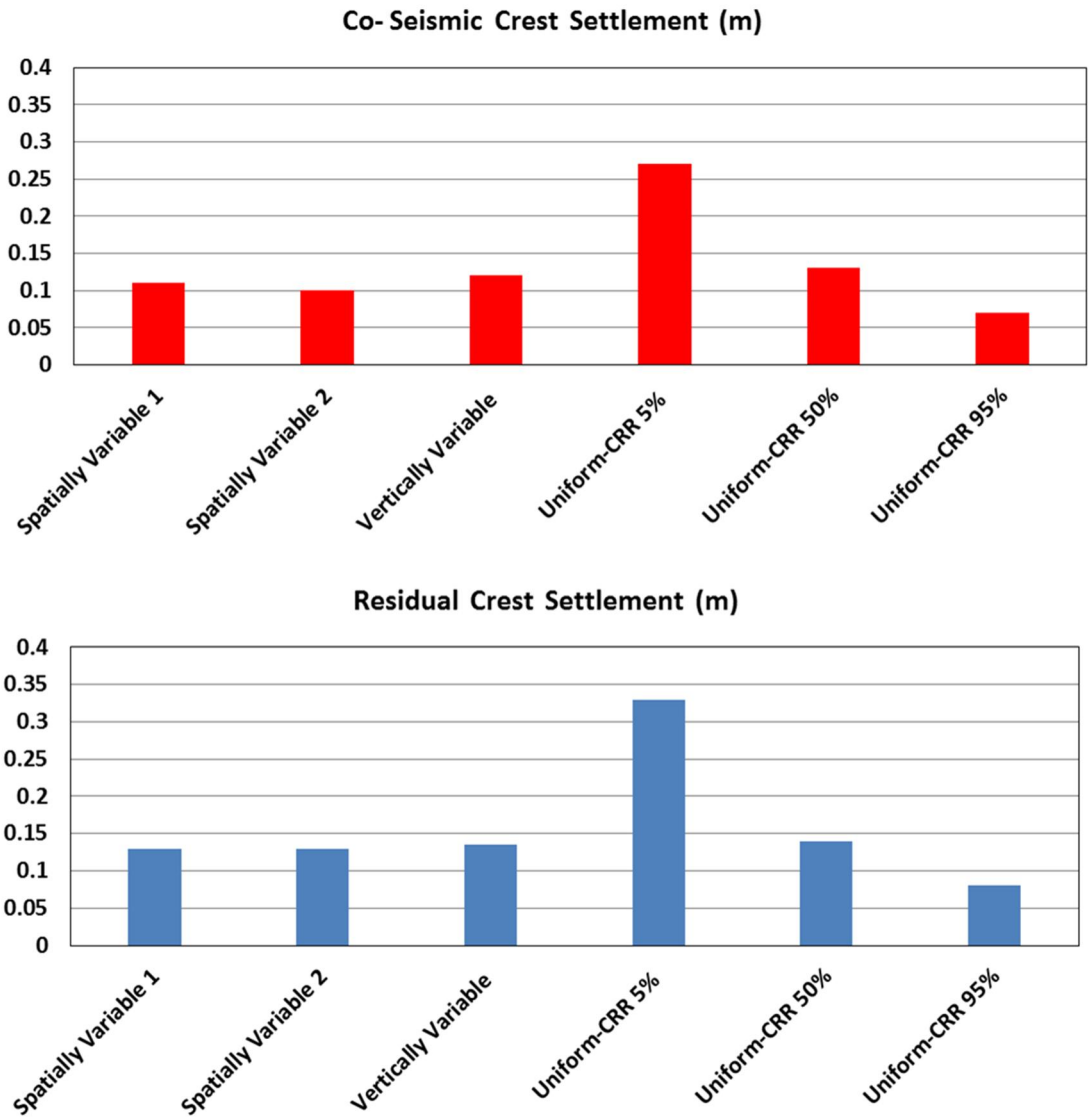

Figure 37. Estimated crest settlements using spatially variable and uniform properties for Unit 8.

Discussion

The results shown in Figure 37 indicate that spatially averaged CRR-values should be used in a uniform model to mimic the results of a model in which the spatial variability of CRR-values within deposits is modelled explicitly (a random fields model). This finding is in line with a comparison between numerical analyses using a random fields model and a uniform model performed for a dam by Boulanger & Montgomery (2016). In this case study, a random fields model with a coefficient of variation of $(N_1)_{60cs}$ of 0,4 and a scale of fluctuation in of 20 m horizontally and 1 m vertically was compared to a uniform model. The case study concerned large deformations, as is the case here. Boulanger & Montgomery (2016) recommend a 33rd percentile value for use in deterministic analyses (conservative) and a range of 30-70% in risk assessments.

The abovementioned sensitivity analyses and more detailed case study all assumed that the uncertainty related to the cyclic resistance ratio or $(N_1)_{60cs}$ can be attributed to fluctuations of point values relative to a spatial average or median value. In case of a regional data set, i.e. a data set that consists of measurements from various locations (or case histories), the local average or median can be uncertain as well. This part of the variance should not be treated as spatially variable in a cross-sectional reliability analysis. Considering this, the uncertainty related to a local average may be expressed as follows (after TAW 2001):

$$\sigma_X = \sigma_{\underline{X}} \cdot \{ (1-\omega) + \omega \cdot \Omega^2 \}^{1/2} \qquad (35)$$

Where:

σ_X Standard deviation of the spatial average of stochastic variable $\underline{X}$ (-)

ω Part of the total variance that can be attributed to fluctuations of point values relative to the local average (-)

Ω Variance reduction factor (-); $0 \leq \Omega \leq 1$

Recommended $CRR_{M=5.0}$-distribution for laminated deposits for use in a uniform model

Based on the results of the sensitivity analyses and the case study by Boulanger & Montgomery (2016), a variance reduction factor Ω of 0 seems reasonable. Note: the average of a lognormally distributed variable is higher than its median value. The difference is negligible however, for the distribution of the CRR for laminated deposits (a factor 1.02). This means that the distribution of the local average is almost identical to the distribution of the local median.

Since the $\underline{CRR}$-distribution for laminated deposits is based on a regional data set, i.e. samples taken at various locations, a value of ω of 0.75 is proposed here. This value in line with Dutch engineering practice for dealing with regional data sets in slope stability assessments (e.g. TAW 1989: page 90; TAW 2001: page 254), see also Calle (2007; 2008) for a statistical basis/interpretation.

The distributions of the point values and the local medians of the cyclic resistance ratio of a laminated deposit are given in Table 12. These distributions are shown in Figure 38.

Table 12. Distributions of cyclic resistance ratios for laminated deposits. Both distributions rest on a regional data set.

Variable	Symbol	Distribution type	Parameter values
Point value of CRR (unsuitable for use in a uniform model)	$\underline{CRR}$	Lognormal	$\mu_{ln(\underline{CRR})} = -1.4$ $\sigma_{ln(\underline{CRR})} = 0.2$
Local average of CRR	CRR	Lognormal	$\mu_{ln(CRR)} = -1.39$ $\sigma_{ln(CRR)} = 0.1$

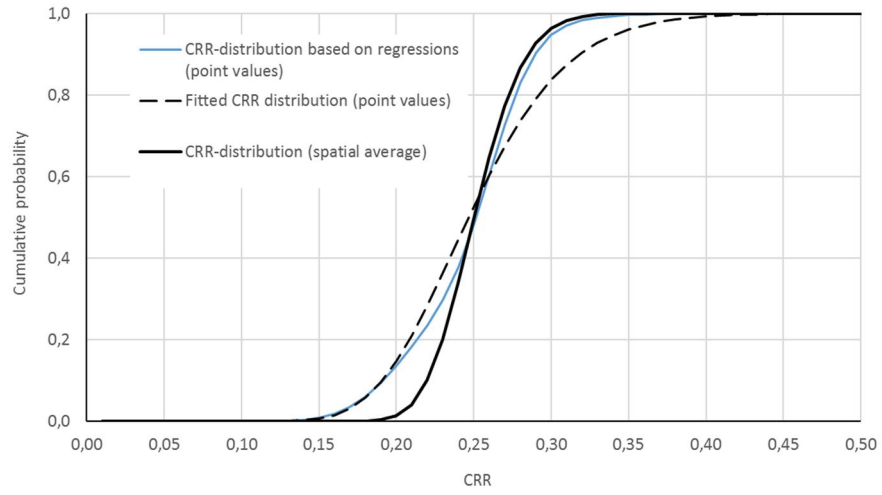

Figure 38. Cyclic resistance ratio for laminated deposits.

Recommended $CRR_{M=7.5}$-distribution for sand deposits for use in a uniform model

The distribution of point values of q_{c1Ncs} for any given layer rests a local CPT data, i.e. a local data set. Within a local data set, regional variations are small. This implies $\omega \approx 1$ in equation (35) (see also TAW 1989, TAW 2001). Based on the results of the sensitivity analyses and the case study by Boulanger & Montgomery (2016) (that all essentially rest on the assumption $\omega=1$), the use of the median of q_{c1Ncs} from the local data set is recommended (not the mean; the median could be about 10% smaller). This means that the distribution of $CRR_{M=7.5}$ for sand deposits for use in a uniform model follows directly from the median of local q_{c1Ncs}-values and the probabilistic relationship between the cyclic resistance ratio and q_{c1Ncs} of Boulanger and Idriss (2014).

The distributions of the point values and the local medians of the cyclic resistance ratio of a sand deposit are given in Table 13. These distributions are shown in Figure 39.

Table 13. Distributions of cyclic resistance ratios for sand deposits.

Stochastic variable	Symbol	Distribution type	Parameter values
Point value of CRR in the local data set (unsuitable for use in a uniform model)	$\underline{CRR}$	Lognormal	$\mu_{ln(\underline{CRR})} = -1.88$ $\sigma_{ln(\underline{CRR})} = 0.22$
Local median of CRR	CRR	Lognormal	$\mu_{ln(CRR)} = -1.88$ $\sigma_{ln(CRR)} = 0.20$
Point value of CRR in the regional data set (unsuitable for use in a uniform model; used in sensitivity analyses because the distribution is relatively wide)	$\underline{CRR}$	Lognormal	$\mu_{ln(\underline{CRR})} = -1.80$ $\sigma_{ln(\underline{CRR})} = 0.30$

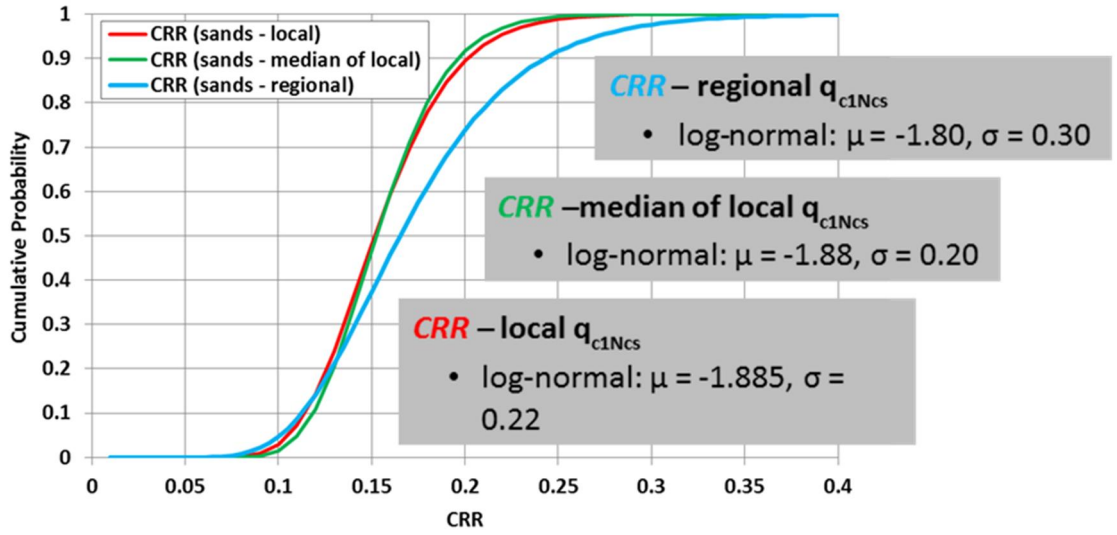

Figure 39. Cyclic resistance ratio for sand deposits.

The left-hand tail of the distribution for point values of q_{c1Ncs} is largely determined by the uncertainty in the Boulanger & Idriss (2014)-relationship, as shown by the FORM influence coefficients (Figure 40). This explains why the left-hand tails of the distributions for point values and the median of q_{c1Ncs} are rather similar. This means that the assumption of $\omega \approx 1$ in equation (35) hardy influences the results of FORM-analyses and semi-probabilistic assessments.

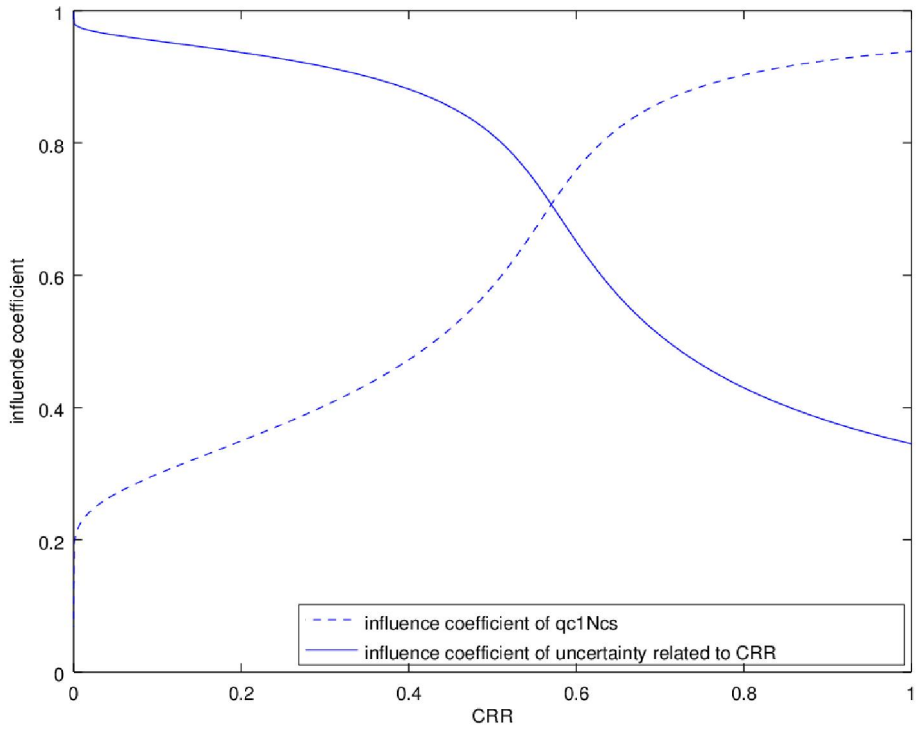

Figure 40. FORM-influence coefficients for the convolution of local point values of q_{c1Ncs} and the uncertainty in the Boulanger & Idriss (2014) relationship.

Appendix H Uncertainty related to motions

Computed displacements depend on the selected ground motion (spectrally matched to the target design spectrum). This is because matched motions have different characteristics such as duration and velocity pulses. This uncertainty cannot easily be modelled by continuous stochastic variables. This can be dealt with in a simpler manner by conditioning computed deformations and failure probabilities on motions, and to consider the subjective probabilities ("degrees of belief") associated with each motion. This is discussed below.

Theory
Consider a set of i=1..n motions that spans all possible motions. Probabilities of failure could be calculated for each given motion. The probability of failure then equals:

$$P(F) = \sum P(F|M_i) \cdot P(M_i) \quad (36)$$

Where:
P(F) Probability of failure (per year)
$P(F|M_i)$ Probability of failure given motion i (per year), i=1..n. A motion is thought of here as a "basic" time series that can be scaled to whatever spectral acceleration. This, however, is an oversimplification. When motions are matched to a particular spectrum, their durations are held constant, even though motions should have shorter durations for higher accelerations in the Groningen area. This is an important reason why the selection of "basic" motions should depend on the target design spectrum. This issue is discussed at the end of this section.
$P(M_i)$ Probability of motion i (-). Note that $\sum P(M_i)=1$. The motions M_i are mutually exclusive, collectively exhaustive.

In a probabilistic assessment, the failure probabilities for the different motions could be obtained from e.g. MC or FORM-analyses. These could then be combined with the probabilities assigned to each motion into a probability of failure, P(F). This failure probability could then be compared to the target failure probability, P_T.

In a semi-probabilistic assessment, the following procedure could be followed (in line with the procedure described in ENW 2012), i.e.:

1. For each motion:
    a. Vary the target reliability index (or target failure probability) and compute the associated design values, using a functional relationship between reliability indices and design values (see equation (3))
    b. Select the target reliability index for which a calculation with the design values from step 1a just leads to the critical crest settlement (limit state function equal to zero).
    c. Calculate the probability of failure associated with the reliability index from step 1b.
    d. Multiply the probability of failure from step c with the probability of the motion under consideration.
2. Take the sum of the results from step 1. This is an estimate of the probability of failure (see equation (36)).
3. Compare the estimate of the probability of failure from step 2 to the target failure probability.

The procedure described above is theoretically correct but impractical since it involves a large number of evaluations of the limit state function.

Pragmatic way forward
The number of evaluations could be strongly reduced if we were able to identify a motion M_d for which the following holds:

$$P(F) \leq P(F|M_d) \quad (37)$$

Obviously, taking the most conservative motion ($M_d = M_n$), would certainly satisfy the condition given by equation (37). This, however, would also be highly conservative.

To be able to define the design motion in probabilistic terms, we could order the motions on the basis of their conditional failure probabilities, with motion 1 having the smallest failure probability and motion n the highest, i.e.

$$P(F|M_i) \leq P(F|M_w) \qquad \text{with} \qquad i < w \tag{38}$$

The following procedure is suggested for dealing with the uncertainty related to motions:

1. Select independent motions with appropriate seismological characteristics, including duration.
2. Compute crest settlements for each motion (semi-probabilistically). This is an important step because it is difficult to predetermine which motion gives the greatest deformation.
3. Analyze the results: outliers should be understood.
4. A slightly conservative motion should be treated as representative, which could be interpreted as a motion an "exceedance probability" of 20% (see below).
   Note that it might be incorrect to treat the motions being considered as equally likely or to assume that the 11 selected motions span the entire set of possible motions. In some cases, it might be reasonable to assign low subjective probabilities to particular motions or to treat the set of motions as a subset of relatively pessimistic scenarios. This means that M_d need not be a conservative motion within the set of motions being considered.

Even when the differences between the failure probabilities for different motions are substantial, a motion with an "exceedance probability" in of 20% is still likely to be sufficiently conservative, even when the failure probabilities per motion differ substantially. To illustrate this, consider the following purely hypothetical examples.

Case 1
Consider 4 equally probable motions, each with a different (conditional) failure probability. The "overall" failure probability equals $1{,}875 \cdot P_0$ (Table 14). This is smaller than $P(F|M_3)$, which implies that motion 3 could be used as a basis for a simplified assessment. This is a motion with a cumulative probability of 75%, or an "exceedance probability" of 25%.

Table 14. Hypothetical case 1: four equally likely motions with associated failure probabilities that differ up to a factor 8.

Motion	$P(M_i)$	Cumulative probability	$P(F\|M_i)$	$P(M_i) \cdot P(F\|M_i)$
1	1/4	1/4	$1/2 \cdot P_0$	$1/8 \cdot P_0$
2	1/4	2/4	P_0	$1/4 \cdot P_0$
3	1/4	3/4	$\mathbf{2 \cdot P_0}$	$1/2 \cdot P_0$
4	1/4	1	$4 \cdot P_0$	P_0
Sum	1	-	-	$\mathbf{1{,}875 \cdot P_0}$

Case 2
Consider 11 equally probable motions, with (conditional) failure probabilities that increase exponentially. The smallest and highest failure probabilities differ by a factor 100. The "overall" failure probability equals $24{,}48 \cdot P_0$ (see Table 15). Here, the "design motion" has a cumulative probability of 8/11, or an "exceedance probability" of 27%.

Table 15. Hypothetical case 2: four equally likely motions with associated failure probabilities that differ up to a factor 100.

Motion	$P(M_i)$	Cumulative probability	$P(F\|M_i)$	$P(M_i) \cdot P(F\|M_i)$
1	1/11	1/11	$1{,}00 \cdot P_0$	$0{,}09 \cdot P_0$
2	1/11	2/11	$1{,}58 \cdot P_0$	$0{,}14 \cdot P_0$
3	1/11	3/11	$2{,}51 \cdot P_0$	$0{,}23 \cdot P_0$
4	1/11	4/11	$3{,}98 \cdot P_0$	$0{,}36 \cdot P_0$
5	1/11	5/11	$6{,}31 \cdot P_0$	$0{,}57 \cdot P_0$
6	1/11	6/11	$10{,}00 \cdot P_0$	$0{,}91 \cdot P_0$

7	1/11	7/11	15,85 · P_0	1,44 · P_0
8	1/11	8/11	**25,12** · P_0	2,28 · P_0
9	1/11	9/11	39,81 · P_0	3,62 · P_0
10	1/11	10/11	63,10 · P_0	5,74 · P_0
11	1/11	1	100,00 · P_0	9,09 · P_0
Sum				**24,48 · P_0**

The use of motions with a fixed duration in FORM-analyses

The same (scaled) motion (motion 4) has been used in the FORM-analyses. For the relatively low exceedance probability of the design point value of the spectral acceleration, a motion with a shorter duration than the duration of motion 4 would have been appropriate (e.g. 1.5 seconds rather than 4.2 seconds). The fact that duration has not been adjusted has led to overestimation of the probability of failure (conservatism). This, however, is largely irrelevant for our purposes. More important is that it has also led to overestimation of the relative importance of the uncertainty related to the spectral acceleration of the model base, i.e. overestimation of $\alpha_{SAmodel\_base}^2$ (and underestimation of the squared other influence coefficients). This is because it has "fattened the tail of the load distribution". When deciding on design values, this has to be kept in mind.

Figure 41 plots significant duration (D5-75) and cumulative absolute velocity (CAV) estimates of the 11 motions used for the design basis case for Eemshaven section presented in the LPI-screening report (Deltares 2017) versus post-seismic crest settlements. The estimated significant duration for a 3057-year return period event using Bommer et al. (2015) empirical correlation for Groningen is 3.8 seconds. For the FORM analysis, motion 4 was considered representative of the entire suite of 11 motions. Motion 6 was considered in a sensitivity analysis.

Figure 42 plots significant duration (D5-75) and cumulative absolute velocity (CAV) estimates of the 11 motions used for the design basis case for Delfzijl section presented in the LPI-screening report (Deltares 2017) versus post-seismic crest settlements. The estimated significant duration for a 6537-year return period event using Bommer et al (2015) empirical correlation for Groningen is 3.6 seconds. For the FORM analysis, motion 4 was considered representative of the entire suite of 11 motions. Motion 6 was considered in a sensitivity analysis.

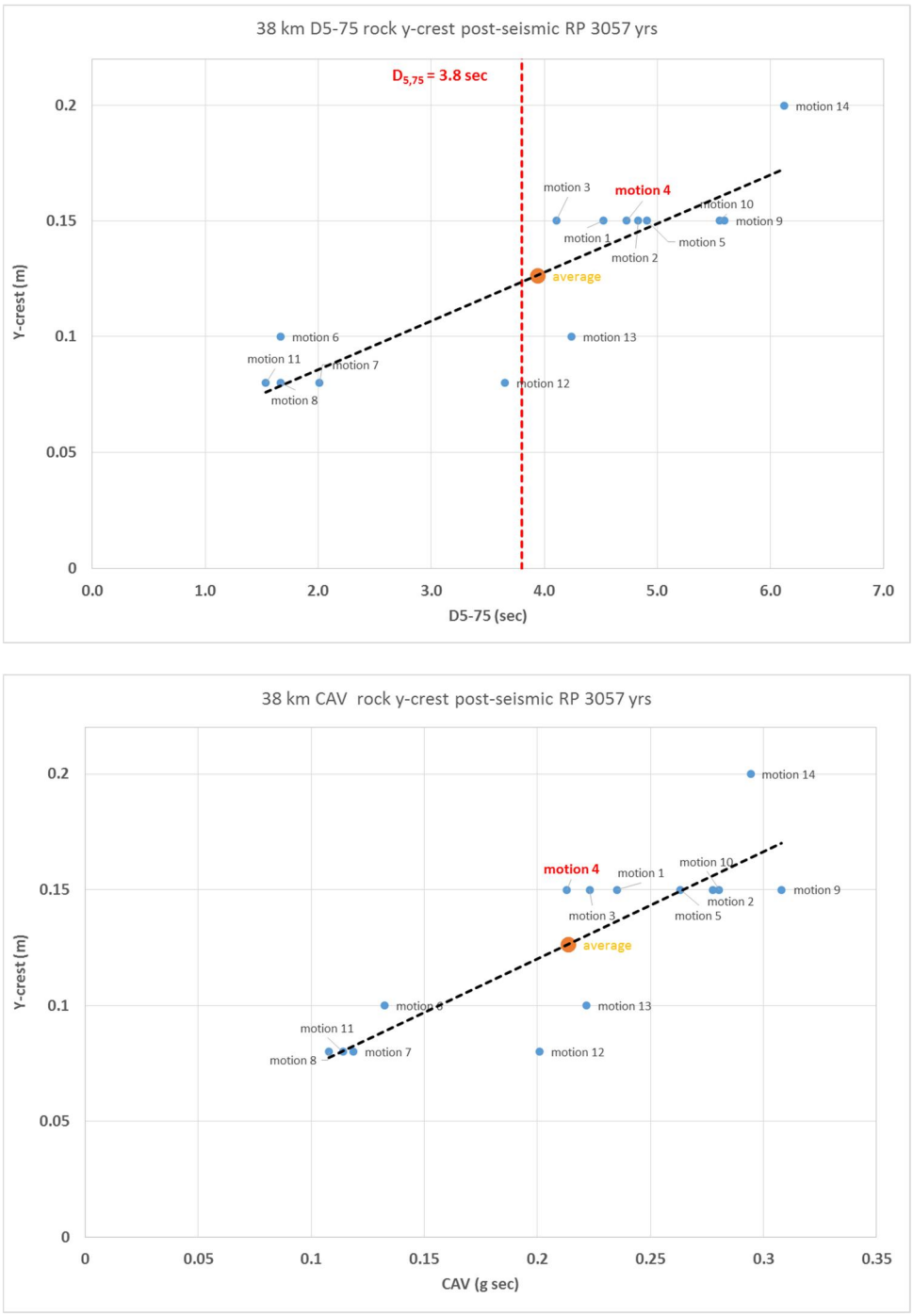

Figure 41. Range of crest settlements versus significant duration (upper illustration) and cumulative absolute velocity (lower illustration) from 14 different ground motions for Eemshaven Design Basis Case (Deltares 2017).

Figure 42. Range of crest settlements versus significant duration (upper illustration) and cumulative absolute velocity (lower illustration) from 14 different ground motions for Delfzijl Design Basis Case (Deltares 2017).

Appendix I Results of FORM-analyses for the 2D finite elements model

An overview of the results of the FORM-analyses are in the tables below. Prior to the FORM-iterations shown in these tables, at least 15 iterations were carried out.

Table 16. Results of FORM-analyses for Eemshaven profile using the median of local q_{c1Ncs} data [Base case A : Su/p' according to Kramer & Wang (2015); ground motion 4]

No.	Sa [g] ($=e^{x1}$)	CRR [-] ($=e^{x2}$)	εSu/p' [-] ($=e^{x3}$)	m [-] ($=e^{x4}$)	Z [m]	$\partial Z/\partial x_1$	$\partial Z/\partial x_2$	$\partial Z/\partial x_3$	$\partial Z/\partial x_4$	μ_Z	σ_Z	Beta	α_{x1}^2	α_{x2}^2	α_{x3}^2	α_{x4}^2	x_{1d}	x_{2d}	x_{3d}	x_{4d}
0	0.450	0.100	0.700	2.000	0.148	-5.310	10.677	3.540	-2.999	30.630	6.120	5.005	0.738	0.122	0.068	0.073	-0.794	-2.224	-0.586	0.742
1	0.450	0.102	0.669	2.020	0.137	-5.418	11.790	3.153	-3.011	31.418	6.252	5.025	0.736	0.142	0.052	0.070	-0.782	-2.254	-0.513	0.732
2	0.452	0.102	0.654	2.032	0.114	-5.484	12.409	3.016	-3.035	31.914	6.345	5.030	0.732	0.153	0.046	0.069	-0.790	-2.268	-0.484	0.728
3	0.452	0.102	0.646	2.039	0.093	-5.543	12.717	2.958	-3.057	32.280	6.417	5.030	0.731	0.157	0.043	0.069	-0.792	-2.274	-0.470	0.725
4	0.452	0.103	0.642	2.044	0.075	-5.589	12.885	2.934	-3.076	32.547	6.470	5.031	0.731	0.159	0.042	0.068	-0.791	-2.276	-0.462	0.724
5	0.453	0.103	0.640	2.048	0.061	-5.623	12.987	2.927	-3.091	32.743	6.508	5.031	0.732	0.159	0.041	0.068	-0.790	-2.277	-0.458	0.723
6	0.453	0.103	0.638	2.050	0.049	-5.649	13.056	2.927	-3.103	32.889	6.537	5.031	0.732	0.160	0.041	0.068	-0.790	-2.277	-0.456	0.722
7	0.453	0.103	0.637	2.052	0.040	-5.668	13.105	2.930	-3.113	33.000	6.560	5.031	0.732	0.160	0.040	0.068	-0.789	-2.277	-0.455	0.722
8	0.453	0.103	0.637	2.053	0.032	-5.683	13.142	2.934	-3.121	33.087	6.577	5.031	0.732	0.160	0.040	0.068	-0.789	-2.277	-0.454	0.722
9	0.453	0.103	0.636	2.055	0.026	-5.695	13.171	2.938	-3.128	33.155	6.590	5.031	0.732	0.160	0.040	0.068	-0.789	-2.277	-0.454	0.722
10	0.454	0.103	0.636	2.055	0.021	-5.704	13.193	2.941	-3.133	33.210	6.601	5.031	0.732	0.160	0.040	0.068	-0.789	-2.277	-0.454	0.722
11	0.454	0.103	0.636	2.056	0.017	-5.712	13.210	2.945	-3.137	33.253	6.610	5.031	0.732	0.160	0.040	0.068	-0.789	-2.277	-0.454	0.722
12	0.454	0.103	0.636	2.057	0.014	-5.718	13.224	2.947	-3.140	33.288	6.616	5.031	0.732	0.160	0.040	0.068	-0.789	-2.277	-0.454	0.722
13	0.454	0.103	0.636	2.057	0.011	-5.722	13.235	2.950	-3.143	33.316	6.622	5.031	0.732	0.160	0.040	0.068	-0.789	-2.277	-0.454	0.722

The design point has been verified using the FEM analysis. The final step of FORM analysis based on the response space results to a crest settlement of 1.45 m, the calculated crest settlement from FEM analysis is 1.50 m. A final FORM iteration using numerical analyses leads to similar influence factors (α_i^2), as shown in the table below.

No.	Sa [g] ($=e^{x1}$)	CRR [-] ($=e^{x2}$)	εSu/p' [-] ($=e^{x3}$)	m [-] ($=e^{x4}$)	Z [m]	$\partial Z/\partial x_1$	$\partial Z/\partial x_2$	$\partial Z/\partial x_3$	$\partial Z/\partial x_4$	α_{x1}^2	α_{x2}^2	α_{x3}^2	α_{x4}^2
final	0.454	0.103	0.636	2.057	-0.085	-6.171	13.371	3.085	-3.245	0.753	0.144	0.039	0.064

Table 17. Results of FORM-analyses for the Delfzijl profile with spatial averaging [Base case B : Su/p' according to Kramer and Wang (2015); ground motion 4]

No.	Sa [g] ($=e^{x1}$)	CRR [-] ($=e^{x2}$)	εSu/p' [-] ($=e^{x3}$)	m [-] ($=e^{x4}$)	Z [m]	$\partial Z/\partial x_1$	$\partial Z/\partial x_2$	$\partial Z/\partial x_3$	$\partial Z/\partial x_4$	μ_Z	σ_Z	Beta	α_{x1}^2	α_{x2}^2	α_{x3}^2	α_{x4}^2	x_{1d}	x_{2d}	x_{3d}	x_{4d}
0	1.100	0.220	0.700	3.000	-0.016	-4.160	9.747	1.325	-3.171	24.766	4.505	5.497	0.786	0.047	0.018	0.150	0.058	-1.509	-0.327	1.171
1	1.092	0.220	0.704	3.044	-0.012	-4.157	9.708	1.331	-3.168	24.748	4.502	5.497	0.786	0.047	0.018	0.150	0.059	-1.509	-0.329	1.170
2	1.086	0.220	0.707	3.079	-0.010	-4.155	9.680	1.336	-3.165	24.732	4.499	5.497	0.786	0.046	0.018	0.150	0.059	-1.508	-0.330	1.170
3	1.081	0.221	0.709	3.107	-0.008	-4.152	9.660	1.338	-3.163	24.716	4.496	5.498	0.786	0.046	0.018	0.150	0.059	-1.508	-0.331	1.170
4	1.077	0.221	0.711	3.129	-0.006	-4.150	9.645	1.340	-3.161	24.703	4.493	5.498	0.786	0.046	0.018	0.150	0.060	-1.508	-0.332	1.170
5	1.074	0.221	0.712	3.148	-0.005	-4.148	9.635	1.342	-3.160	24.692	4.491	5.498	0.786	0.046	0.018	0.150	0.060	-1.508	-0.333	1.170
6	1.071	0.221	0.713	3.162	-0.004	-4.147	9.627	1.342	-3.159	24.682	4.490	5.498	0.786	0.046	0.018	0.150	0.060	-1.508	-0.333	1.170
7	1.069	0.221	0.714	3.174	-0.003	-4.145	9.621	1.343	-3.158	24.675	4.488	5.498	0.786	0.046	0.018	0.150	0.060	-1.508	-0.333	1.170
8	1.068	0.221	0.715	3.184	-0.002	-4.144	9.617	1.343	-3.157	24.668	4.487	5.498	0.786	0.046	0.018	0.150	0.059	-1.508	-0.333	1.170
9	1.066	0.221	0.715	3.192	-0.002	-4.143	9.613	1.343	-3.157	24.663	4.486	5.498	0.786	0.046	0.018	0.150	0.059	-1.508	-0.333	1.170
10	1.065	0.221	0.715	3.198	-0.001	-4.143	9.611	1.343	-3.156	24.659	4.485	5.498	0.786	0.046	0.018	0.150	0.059	-1.508	-0.333	1.170
11	1.065	0.221	0.716	3.203	-0.001	-4.142	9.609	1.344	-3.156	24.656	4.485	5.498	0.786	0.046	0.018	0.150	0.059	-1.508	-0.334	1.170
12	1.064	0.221	0.716	3.207	-0.001	-4.142	9.607	1.344	-3.156	24.654	4.484	5.498	0.786	0.046	0.018	0.150	0.059	-1.508	-0.334	1.170
13	1.063	0.221	0.716	3.210	-0.001	-4.141	9.606	1.344	-3.156	24.652	4.484	5.498	0.786	0.046	0.018	0.150	0.059	-1.508	-0.334	1.170

The design point has been verified using the FEM analysis. The final step of FORM analysis based on the response space results to a crest settlement of 0.98 m, the calculated crest settlement from FEM analysis is 0.95 m. A final FORM iteration using numerical analyses leads to similar influence factors (α_i^2), as shown in the table below.

No.	Sa [g] ($=e^{x1}$)	CRR [-] ($=e^{x2}$)	εSu/p' [-] ($=e^{x3}$)	m [-] ($=e^{x4}$)	Z [m]	$\partial Z/\partial x_1$	$\partial Z/\partial x_2$	$\partial Z/\partial x_3$	$\partial Z/\partial x_4$	α_{x1}^2	α_{x2}^2	α_{x3}^2	α_{x4}^2
final	1.060	0.220	0.720	3.210	-0.049	-3.852	9.630	1.605	-3.207	0.750	0.051	0.029	0.171

Table 18. Results of FORM-analyses for the Eemshaven profile using the median of local q_{c1Ncs} data [Sensitivity case 1 : Su/p' according to Kramer & Wang (2015); motion 6]

No.	Sa [g] ($=e^{x1}$)	CRR [-] ($=e^{x2}$)	εSu/p' [-] ($=e^{x3}$)	m [-] ($=e^{x4}$)	Z [m]	$\partial Z/\partial x_1$	$\partial Z/\partial x_2$	$\partial Z/\partial x_3$	$\partial Z/\partial x_4$	μ_Z	σ_Z	Beta	α_{x1}^2	α_{x2}^2	α_{x3}^2	α_{x4}^2	x_{1d}	x_{2d}	x_{3d}	x_{4d}
0	0.634	0.104	0.663	2.071	0.054	-6.616	13.604	3.001	-3.098	39.162	7.418	5.279	0.780	0.135	0.033	0.053	-0.435	-2.267	-0.432	0.667
1	0.636	0.104	0.662	2.058	0.050	-6.623	13.620	3.002	-3.103	39.203	7.426	5.279	0.780	0.135	0.033	0.053	-0.436	-2.267	-0.432	0.667
2	0.637	0.104	0.660	2.047	0.046	-6.629	13.634	3.003	-3.107	39.240	7.433	5.279	0.780	0.135	0.033	0.053	-0.436	-2.267	-0.432	0.668
3	0.638	0.104	0.659	2.037	0.042	-6.634	13.647	3.004	-3.111	39.274	7.439	5.279	0.779	0.135	0.033	0.053	-0.436	-2.267	-0.432	0.668
4	0.639	0.104	0.658	2.028	0.038	-6.639	13.658	3.004	-3.115	39.304	7.445	5.280	0.779	0.135	0.033	0.053	-0.436	-2.267	-0.431	0.668
5	0.639	0.104	0.657	2.020	0.035	-6.643	13.668	3.006	-3.118	39.332	7.450	5.280	0.779	0.135	0.033	0.053	-0.436	-2.267	-0.431	0.668
6	0.640	0.104	0.657	2.013	0.032	-6.647	13.676	3.007	-3.121	39.357	7.454	5.280	0.779	0.135	0.033	0.053	-0.436	-2.267	-0.431	0.669
7	0.641	0.104	0.656	2.007	0.029	-6.651	13.684	3.008	-3.124	39.380	7.459	5.280	0.779	0.135	0.033	0.053	-0.436	-2.267	-0.431	0.669
8	0.641	0.104	0.655	2.001	0.027	-6.655	13.692	3.009	-3.127	39.402	7.463	5.280	0.779	0.135	0.033	0.053	-0.436	-2.267	-0.431	0.669
9	0.642	0.104	0.655	1.996	0.025	-6.658	13.698	3.010	-3.129	39.421	7.466	5.280	0.779	0.135	0.033	0.053	-0.436	-2.267	-0.431	0.669
10	0.642	0.104	0.654	1.992	0.023	-6.661	13.704	3.011	-3.131	39.439	7.470	5.280	0.779	0.135	0.033	0.053	-0.436	-2.267	-0.431	0.670
11	0.643	0.104	0.654	1.988	0.021	-6.663	13.710	3.011	-3.133	39.456	7.473	5.280	0.779	0.135	0.033	0.053	-0.436	-2.267	-0.431	0.670
12	0.643	0.104	0.653	1.985	0.019	-6.666	13.715	3.012	-3.135	39.471	7.476	5.280	0.779	0.135	0.033	0.053	-0.436	-2.267	-0.431	0.670
13	0.644	0.104	0.653	1.982	0.017	-6.668	13.720	3.013	-3.137	39.485	7.478	5.280	0.779	0.135	0.033	0.053	-0.436	-2.267	-0.431	0.670

The design point has been verified using the FEM analysis. The final step of FORM analysis based on the response space results to a crest settlement of 1.51 m, the calculated crest settlement from FEM analysis is 1.52 m.

Table 19. Results of FORM-analyses for the Delfzijl profile with spatial averaging [Sensitivity case 2 : Su/p' according to Kramer and Wang (2015); ground motion 6]

No.	Sa [g] ($=e^{x1}$)	CRR [-] ($=e^{x2}$)	εSu/p' [-] ($=e^{x3}$)	m [-] ($=e^{x4}$)	Z [m]	$\partial Z/\partial x_1$	$\partial Z/\partial x_2$	$\partial Z/\partial x_3$	$\partial Z/\partial x_4$	μ_Z	σ_Z	Beta	α_{x1}^2	α_{x2}^2	α_{x3}^2	α_{x4}^2	x_{1d}	x_{2d}	x_{3d}	x_{4d}
0	1.000	0.214	0.536	1.904	-0.181	-8.018	22.520	4.885	-3.346	45.268	8.517	5.315	0.817	0.070	0.067	0.047	-0.008	-1.541	-0.617	0.632
1	0.999	0.214	0.537	1.900	-0.147	-7.942	22.322	4.836	-3.310	44.835	8.436	5.315	0.817	0.070	0.067	0.047	-0.009	-1.541	-0.617	0.631
2	0.997	0.214	0.537	1.895	-0.119	-7.880	22.157	4.797	-3.280	44.482	8.370	5.315	0.817	0.070	0.067	0.046	-0.009	-1.541	-0.617	0.630
3	0.996	0.214	0.538	1.892	-0.097	-7.830	22.021	4.766	-3.257	44.195	8.316	5.314	0.817	0.070	0.067	0.046	-0.009	-1.541	-0.617	0.630
4	0.995	0.214	0.538	1.889	-0.078	-7.789	21.909	4.741	-3.237	43.961	8.273	5.314	0.817	0.070	0.066	0.046	-0.009	-1.541	-0.617	0.629
5	0.994	0.214	0.538	1.886	-0.063	-7.756	21.817	4.720	-3.222	43.771	8.237	5.314	0.817	0.070	0.066	0.046	-0.009	-1.541	-0.617	0.629
6	0.994	0.214	0.539	1.884	-0.051	-7.729	21.741	4.704	-3.209	43.617	8.208	5.314	0.817	0.070	0.066	0.046	-0.009	-1.541	-0.617	0.628
7	0.993	0.214	0.539	1.882	-0.042	-7.707	21.680	4.690	-3.199	43.491	8.185	5.314	0.817	0.070	0.066	0.046	-0.009	-1.541	-0.617	0.628
8	0.993	0.214	0.539	1.881	-0.034	-7.689	21.630	4.679	-3.191	43.389	8.166	5.314	0.817	0.070	0.066	0.046	-0.009	-1.541	-0.617	0.628
9	0.993	0.214	0.539	1.879	-0.027	-7.674	21.590	4.670	-3.184	43.307	8.150	5.314	0.817	0.070	0.066	0.046	-0.009	-1.541	-0.617	0.628
10	0.992	0.214	0.539	1.878	-0.022	-7.663	21.557	4.663	-3.178	43.239	8.137	5.314	0.817	0.070	0.066	0.046	-0.009	-1.541	-0.617	0.628
11	0.992	0.214	0.539	1.877	-0.018	-7.653	21.530	4.657	-3.174	43.185	8.127	5.314	0.817	0.070	0.067	0.046	-0.009	-1.541	-0.617	0.628
12	0.992	0.214	0.539	1.876	-0.015	-7.645	21.508	4.653	-3.170	43.141	8.119	5.314	0.817	0.070	0.067	0.046	-0.009	-1.541	-0.617	0.628
13	0.992	0.214	0.540	1.876	-0.012	-7.639	21.490	4.649	-3.167	43.105	8.112	5.314	0.817	0.070	0.067	0.046	-0.009	-1.541	-0.617	0.628

The design point has been verified using the FEM analysis. The final step of FORM analysis based on the response space results to a crest settlement of 1.60 m, the calculated crest settlement from FEM analysis is 1.70 m.

Table 20. Results of FORM-analyses for the Eemshaven profile without spatial averaging [Sensitivity case 3 : Su/p' according to Idriss and Boulanger 2008; ground motion 4]

No.	Sa [g] ($=e^{x1}$)	CRR [-] ($=e^{x2}$)	εSu/p' [-] ($=e^{x3}$)	m [-] ($=e^{x4}$)	Z [m]	$\partial Z/\partial x_1$	$\partial Z/\partial x_2$	$\partial Z/\partial x_3$	$\partial Z/\partial x_4$	μ_Z	σ_Z	Beta	α_{x1}^2	α_{x2}^2	α_{x3}^2	α_{x4}^2	x_{1d}	x_{2d}	x_{3d}	x_{4d}
0	0.500	0.100	0.900	2.000	-0.198	-7.376	9.128	7.361	-3.363	39.631	8.091	4.898	0.815	0.115	0.019	0.052	-0.673	-2.297	-0.100	0.616
1	0.502	0.100	0.901	1.969	-0.160	-7.267	9.024	7.284	-3.324	39.067	7.976	4.898	0.814	0.115	0.019	0.053	-0.676	-2.299	-0.101	0.617
2	0.503	0.100	0.902	1.946	-0.130	-7.182	8.936	7.222	-3.292	38.625	7.886	4.898	0.813	0.116	0.019	0.053	-0.678	-2.299	-0.101	0.618
3	0.504	0.100	0.902	1.927	-0.105	-7.116	8.863	7.172	-3.266	38.276	7.816	4.897	0.813	0.116	0.019	0.053	-0.680	-2.300	-0.101	0.619
4	0.505	0.100	0.902	1.913	-0.085	-7.064	8.803	7.131	-3.245	38.001	7.760	4.897	0.812	0.116	0.019	0.053	-0.681	-2.300	-0.101	0.619
5	0.505	0.100	0.903	1.902	-0.069	-7.023	8.755	7.098	-3.228	37.782	7.715	4.897	0.812	0.116	0.019	0.053	-0.681	-2.300	-0.101	0.620
6	0.505	0.100	0.903	1.893	-0.056	-6.991	8.716	7.071	-3.214	37.608	7.680	4.897	0.812	0.116	0.019	0.053	-0.681	-2.300	-0.101	0.620
7	0.505	0.100	0.903	1.886	-0.045	-6.965	8.685	7.049	-3.203	37.469	7.652	4.897	0.812	0.116	0.019	0.053	-0.682	-2.300	-0.101	0.620
8	0.505	0.100	0.903	1.881	-0.037	-6.944	8.660	7.031	-3.194	37.359	7.629	4.897	0.812	0.116	0.019	0.053	-0.682	-2.300	-0.102	0.620
9	0.505	0.100	0.903	1.876	-0.030	-6.928	8.639	7.016	-3.186	37.270	7.611	4.897	0.812	0.116	0.019	0.053	-0.682	-2.300	-0.102	0.620
10	0.506	0.100	0.903	1.873	-0.024	-6.914	8.623	7.004	-3.181	37.199	7.597	4.897	0.812	0.116	0.019	0.053	-0.682	-2.300	-0.102	0.620
11	0.506	0.100	0.903	1.870	-0.020	-6.904	8.610	6.994	-3.176	37.142	7.585	4.897	0.812	0.116	0.019	0.053	-0.682	-2.300	-0.102	0.620
12	0.506	0.100	0.903	1.868	-0.016	-6.895	8.599	6.986	-3.172	37.096	7.576	4.897	0.812	0.116	0.019	0.053	-0.682	-2.300	-0.102	0.620
13	0.506	0.100	0.903	1.866	-0.013	-6.888	8.591	6.980	-3.169	37.059	7.569	4.897	0.812	0.116	0.019	0.053	-0.682	-2.300	-0.102	0.620

The design point has been verified using the FEM analysis. The final step of FORM analysis based on the response space results to a crest settlement of 1.62 m, while the calculated crest settlement from FEM analysis is 1.60 m. A final FORM iteration using numerical analysis results concludes to similar influence factors (α_i^2) as shown in the table below.

No.	Sa [g] ($=e^{x1}$)	CRR [-] ($=e^{x2}$)	εSu/p' [-] ($=e^{x3}$)	m [-] ($=e^{x4}$)	Z [m]	$\partial Z/\partial x_1$	$\partial Z/\partial x_2$	$\partial Z/\partial x_3$	$\partial Z/\partial x_4$	α_{x1}^2	α_{x2}^2	α_{x3}^2	α_{x4}^2
final	0.506	0.100	0.900	1.870	0.008	-6.545	8.415	5.610	-3.147	0.806	0.122	0.014	0.058

Table 21. Results of FORM-analyses for the Delfzijl profile without spatial averaging [Sensitivity case 4 : Su/p' according to Idriss and Boulanger 2008; ground motion 4]

No.	Sa [g] ($=e^{x1}$)	CRR [-] ($=e^{x2}$)	εSu/p' [-] ($=e^{x3}$)	m [-] ($=e^{x4}$)	Z [m]	$\partial Z/\partial x_1$	$\partial Z/\partial x_2$	$\partial Z/\partial x_3$	$\partial Z/\partial x_4$	μ_Z	σ_Z	Beta	α_{x1}^2	α_{x2}^2	α_{x3}^2	α_{x4}^2	x_{1d}	x_{2d}	x_{3d}	x_{4d}
0	0.800	0.190	0.900	2.300	-0.145	-5.843	8.997	5.367	-3.393	31.285	6.232	5.020	0.810	0.083	0.017	0.090	-0.282	-1.690	-0.097	0.827
1	0.791	0.189	0.901	2.297	-0.127	-5.847	8.933	5.447	-3.374	31.264	6.230	5.019	0.812	0.082	0.017	0.089	-0.279	-1.688	-0.099	0.822
2	0.784	0.188	0.902	2.293	-0.110	-5.842	8.881	5.497	-3.355	31.211	6.221	5.017	0.813	0.082	0.018	0.088	-0.277	-1.687	-0.100	0.819
3	0.778	0.188	0.903	2.288	-0.094	-5.833	8.837	5.528	-3.338	31.142	6.208	5.016	0.814	0.081	0.018	0.087	-0.276	-1.686	-0.101	0.816
4	0.774	0.187	0.903	2.282	-0.079	-5.822	8.801	5.546	-3.322	31.067	6.194	5.016	0.814	0.081	0.018	0.087	-0.275	-1.685	-0.101	0.814
5	0.771	0.187	0.903	2.277	-0.067	-5.810	8.771	5.557	-3.309	30.993	6.180	5.015	0.815	0.081	0.018	0.087	-0.275	-1.685	-0.101	0.812
6	0.769	0.186	0.903	2.272	-0.056	-5.798	8.746	5.562	-3.297	30.924	6.167	5.015	0.815	0.080	0.018	0.086	-0.274	-1.684	-0.102	0.811
7	0.767	0.186	0.903	2.268	-0.047	-5.787	8.725	5.565	-3.287	30.861	6.154	5.014	0.815	0.080	0.018	0.086	-0.274	-1.684	-0.102	0.810
8	0.766	0.186	0.903	2.264	-0.039	-5.777	8.708	5.565	-3.279	30.805	6.144	5.014	0.815	0.080	0.018	0.086	-0.274	-1.684	-0.102	0.809
9	0.765	0.186	0.903	2.261	-0.032	-5.769	8.694	5.565	-3.272	30.756	6.134	5.014	0.815	0.080	0.019	0.086	-0.274	-1.684	-0.102	0.809
10	0.764	0.186	0.903	2.258	-0.027	-5.761	8.683	5.564	-3.266	30.714	6.126	5.014	0.815	0.080	0.019	0.086	-0.274	-1.684	-0.102	0.809
11	0.763	0.186	0.903	2.255	-0.022	-5.755	8.674	5.562	-3.261	30.678	6.119	5.014	0.815	0.080	0.019	0.086	-0.275	-1.684	-0.103	0.808
12	0.762	0.186	0.903	2.253	-0.019	-5.749	8.666	5.561	-3.257	30.648	6.113	5.014	0.815	0.080	0.019	0.086	-0.275	-1.684	-0.103	0.808
13	0.762	0.186	0.903	2.251	-0.015	-5.744	8.660	5.560	-3.253	30.622	6.108	5.013	0.815	0.080	0.019	0.086	-0.275	-1.684	-0.103	0.808

The design point has been verified using the FEM analysis. The final step of FORM analysis based on the response space results to a crest settlement of 1.34 m, while the calculated crest settlement from FEM analysis is 1.30 m. A final FORM iteration using numerical analysis results concludes to similar influence factors (α_i^2) as shown in the table below.

No.	Sa [g] ($=e^{x1}$)	CRR [-] ($=e^{x2}$)	εSu/p' [-] ($=e^{x3}$)	m [-] ($=e^{x4}$)	Z [m]	$\partial Z/\partial x_1$	$\partial Z/\partial x_2$	$\partial Z/\partial x_3$	$\partial Z/\partial x_4$	α_{x1}^2	α_{x2}^2	α_{x3}^2	α_{x4}^2
final	0.762	0.186	0.903	2.250	0.075	-5.625	7.875	5.625	-3.076	0.828	0.070	0.020	0.081

Appendix J Sensitivity analyses on design sea water level

In Fugro (2016c) dynamic levee stability evaluations the water table level for earthquake loading (i.e. corresponding to a 1-year flood event) was used in the analyses together with the application of earthquake loading. The water level corresponding to the 1-year flood event is at El. +3.75m NAP at seaside for both Eemshaven and Delfzijl.

Since water pressure acts as a stabilizing force on the seaside levee slope, the use of the higher water levels associated with the 1-year flood event may be an unconservative assumption in terms of levee crest settlements. To address this issue, additional numerical analyses were performed assuming mean high water level (i.e. El. +1.93m NAP for both Eemshaven Delfzijl) and mean low tides water level (i.e. El. -0.7m NAP for Eemshaven and El. -1.85m NAP for Delfzijl) to evaluate its influence on dynamically induced crest settlements. The water levels are shown schematically on Figure 43.

Results of the sensitivity analyses on the water level are shown on Figure 44 for Eemshaven and Figure 45 for Delfzijl. The figures plot contours of post seismic crest settlement for the 1-year flood event (upper illustration), mean high water level (illustration in the middle) and mean low tides water level (lower illustration). As shown on these figures the crest settlements are not significantly affected for the water levels considered.

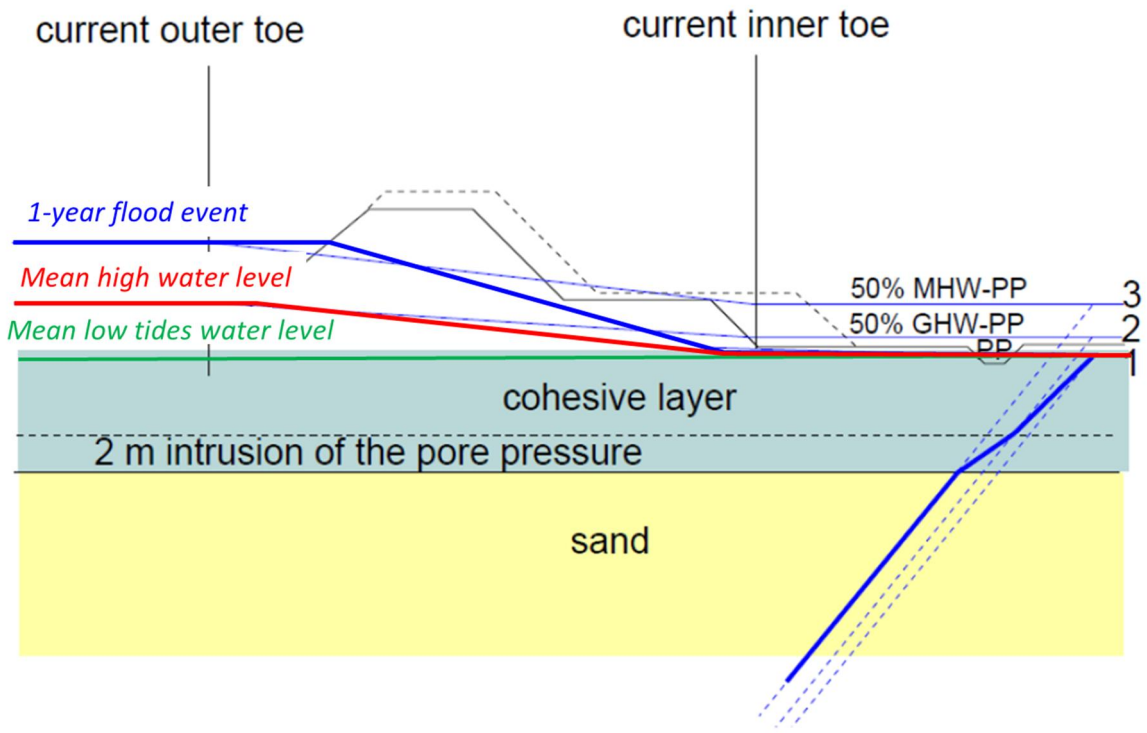

Figure 43. Schematization of 1-year flood event (blue line), mean high (red line) and mean low tides (green line) water levels.

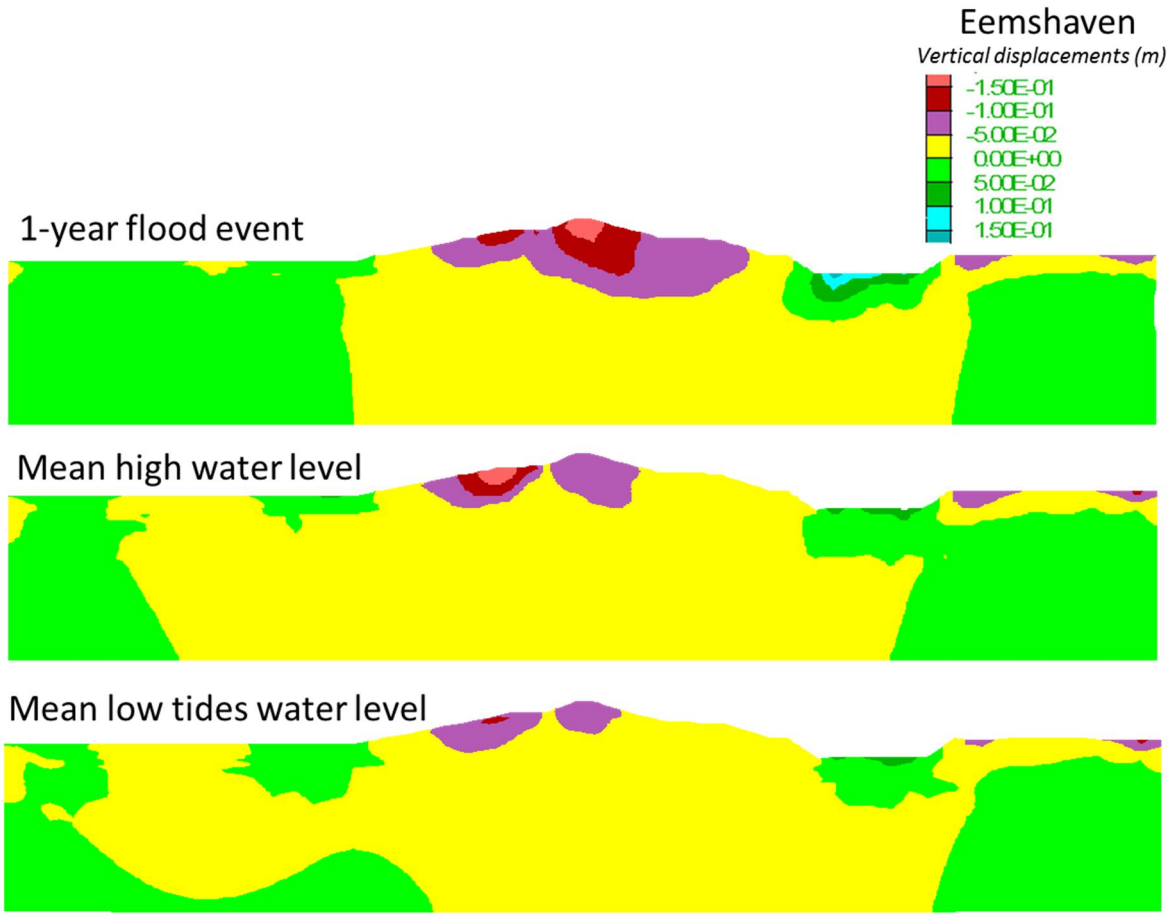

Figure 44. Contours of residual vertical displacements in Eemshaven for 1-year flood event (blue line in Figure 43), mean high (red line in Figure 43) and mean low tides (green line in Figure 43) water level conditions.

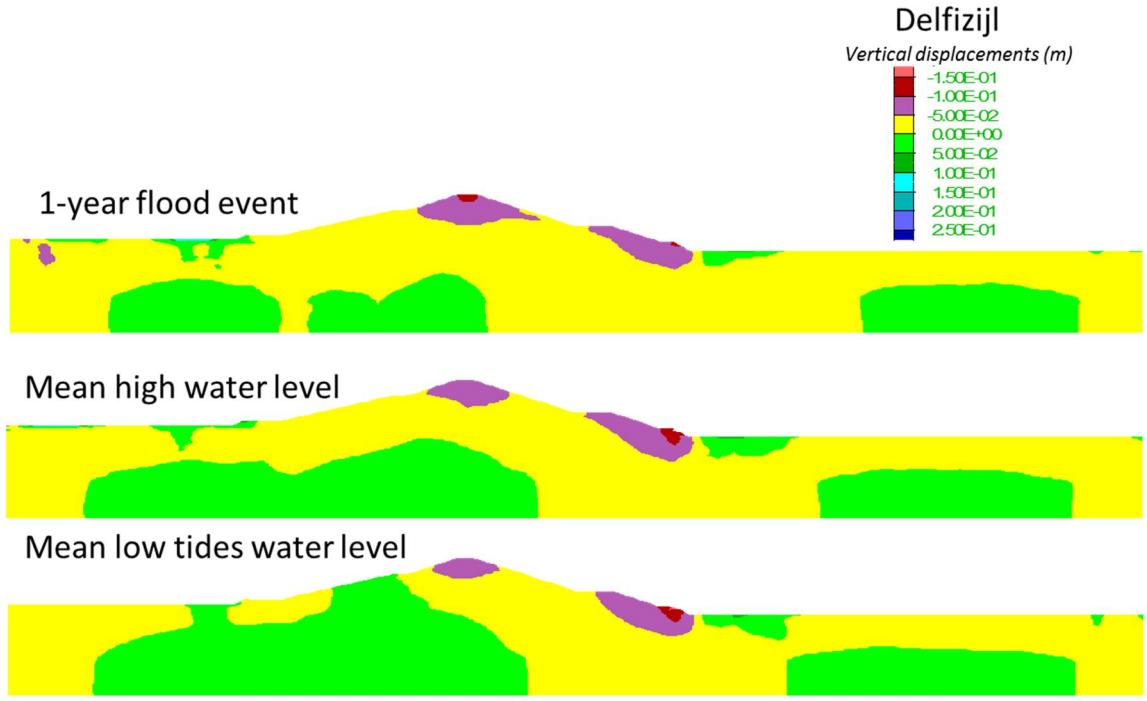

Figure 45. Contours of residual vertical displacements in Delfzijl for 1-year flood event (blue line in Figure 43), mean high (red line in Figure 43) and mean low tides (green line in Figure 43) water level conditions.